Experimentelle Physik

Near-Field Coupling in Hybrid Integrated Photonic Circuits

Inaugural-Dissertation
zur Erlangung des Doktorgrades
der Naturwissenschaften im Fachbereich Physik
der Mathematisch-Naturwissenschaftlichen Fakultät
der Westfälischen Wilhelms-Universität Münster

vorgelegt von
Nico Gruhler
aus Stuttgart

2018

Dekan:	Prof. Dr. Michael Klasen
Erster Gutachter:	Prof. Dr. Wolfram H. P. Pernice
Zweiter Gutachter:	Prof. Dr. Rudolf Bratschitsch
Tag der mündlichen Prüfung:	17.12.2018
Tag der Promotion:	______________________

Contents

Abstract vii

List of Abbreviations ix

1. Introduction 1

2. Silicon Nitride as Basic Passive Integrated Photonics Platform 5

2.1. Silicon Nitride for On-Chip Photonic Structures . . . 5
2.1.1. Silicon Nitride Optical Properties . . . 6
2.1.2. Integrated Optics . . . 7
2.2. Basic Integrated Photonic Circuits . . . 10
2.2.1. Ring Resonators . . . 11
2.2.2. Mach-Zehnder Interferometers . . . 14
2.2.3. Slot Waveguides . . . 16
2.3. Fabrication Process for Silicon Nitride Circuits . . . 17
2.3.1. Electron-Beam Lithography Systems and Resists . . . 19
2.3.2. Dry Etching . . . 20
2.4. Characterization of Silicon Nitride Integrated Photonic Devices . . . 21
2.4.1. Measurement Setup . . . 21
2.4.2. Coupling of Light to and from Integrated Circuits . . . 23
2.4.3. Quantification of Propagation Losses with High-Q Ring Resonators . . . 26
2.4.4. Mach-Zehnder Interferometers . . . 30

3. Near-Field Coupling to a Collective System: Atom Clad Waveguides 31

3.1. Properties of a Rubidium Atom Vapor . . . 31
3.2. Atom-Light Interaction in Integrated Photonics . . . 33
3.3. Fabrication Adaption for Silicon Nitride Devices Coupled to an Atom Vapor . . . 35
3.3.1. Silica Window Substrate for a Vacuum Chamber . . . 36
3.3.2. Borosilicate Glass Substrate for a Vapor Cell . . . 38
3.4. Simulations of Atom Clad Waveguides . . . 38
3.5. Measurement Setup for Atom Clad Waveguides . . . 41

3.6. Experimental Results of the Integrated Atom-Light Interaction . . . 43
3.6.1. Enhancement of the Grating Coupler Efficiency by Utilizing Metal Mirrors . . 43
3.6.2. Atomic Cladding Waveguide Spectroscopy . . . 45
3.6.3. Mach-Zehnder Interferometers for Measurements of the Induced Phase Shift . . 47
3.6.4. Cavity Enhanced Interaction in Ring Resonators . . . 51
3.6.5. Atom Clad Slot Waveguides . . . 57
3.7. Summary and Outlook . . . 62

4. Near-Field Coupling to and from Single Elements 65
4.1. Coupling to Graphene - 2D Carbon Material . . . 66
4.2. GaSe Multilayer as Single-Photon Source . . . 67
4.3. DBT Molecules as Single-Photon Source . . . 69
4.4. Summary of Further Coupling Schemes Realized on the Si_3N_4 Platform . . . 71
4.5. Conclusion . . . 73

5. Integrated Optics in the Long Wave Infrared Regime 75
5.1. Introduction to LWIR Photonics and Materials . . . 75
5.2. Integrated LWIR Photonics Applications . . . 77
5.3. Silicon as Integrated Photonics Reference Material Platform . . . 79
5.3.1. Fabrication of Silicon Devices . . . 79
5.3.2. Characterization of Silicon Devices in the C-band . . . 82
5.4. Diamond as Integrated Photonics Material Platform . . . 83
5.4.1. Diamond Properties and Photonic Applications . . . 83
5.4.2. Fabrication of Diamond Devices . . . 88
5.4.3. Characterization of Diamond Devices in the NIR Regime . . . 91
5.4.4. Functionalization of Diamond Circuits . . . 93
5.5. LWIR Characterization of Silicon and Diamond Devices . . . 96
5.5.1. LWIR Measurement Setup . . . 96
5.5.2. Characterization of Silicon Devices . . . 97
5.5.3. Characterization of Diamond Devices . . . 102
5.6. Summary and Outlook . . . 109

6. Conclusion 113

A. Appendix 117
A.1. Refractive Indices and Dispersion . . . 117
A.2. Detailed Derivation of Ring Resonator Properties . . . 119
A.3. Sample Preparation and Fabrication Parameters . . . 123
A.3.1. Basic Si_3N_4 Devices . . . 123

A.3.2. Si_3N_4 Devices on Silica Window Substrate for a Vacuum Chamber 124
A.3.3. Si_3N_4 Devices on Borosilicate Glass Substrate for a Vapor Cell 126
A.3.4. Basic Silicon Devices 128
A.3.5. Suspended Silicon Devices for LWIR Applications 129
A.3.6. Basic Diamond Devices 131
A.3.7. Diamond on AlN Devices for LWIR Applications 132
A.3.8. Suspended Diamond Devices for LWIR Applications 133
A.4. PEC Parameters 136
A.5. Etching Process Details and Recipes 139
A.5.1. Si_3N_4 Etching Process 139
A.5.2. Etching Recipes 140
A.6. Wafer Dicing Saw 144
A.7. Basic Measurement Setup Components 147
A.8. Simulation Details for Atom Clad Waveguides 148
A.9. Atom Clad MZIs: Fit Parameters 153
A.10. Mechanical Facet Polishing 155
A.11. Details on Optical Components of the LWIR Setup 157

Bibliography **161**

Zusammenfassung in deutscher Sprache **203**

List of Publications **209**

Curriculum Vitae **211**

Acknowledgments **213**

Abstract

The use of optical fiber telecommunication system in the modern information age emphasizes the role of optical system for the technological progress. In recent years, integrated optical circuits have attracted a lot of attention for the implementation of compact communication and computational systems. These circuits consist of dielectric waveguides, which enable the total internal reflection of a light beam. Near-field coupling of guided modes in integrated photonic circuits to additional elements via the evanescent field is a key factor in many applications. The confinement of strong optical fields on a sub-wavelength scale enables strong interactions in hybrid circuits. This is for example used in quantum photonic circuits where single photon sources are coupled to integrated waveguides and the signal is detected via the coupling to superconducting nanowires or in computational photonic circuits where coupling to a phase-change material cell is utilized as an all-optical memory element. As the waveguide mode reacts very sensitive to any changes in its surroundings, the coupling mechanism via the evanescent field is specifically beneficial for sensing and referencing applications. The interaction between optical modes and electron transitions in atoms plays for example not only an important role for cavity quantum electrodynamics experiments but also as a frequency standard. Instead of coupling to atoms, the study of the absorption spectra of molecules is of high interest for chemical sensing and analysis.

In the first part of this work, the coupling of an optical mode in an integrated photonic circuit to a thermal rubidium atom vapor in the visible regime is studied. In the second part, the extension of the usable spectral range of integrated circuits to the long wave infrared (LWIR) regime, which encloses the fingerprint region of many molecules, is presented. Furthermore, the development of the used material platforms is discussed.

A high-quality Si_3N_4 platform is introduced where low-loss waveguides with an attenuation of 21 dB/m and ring resonators with a quality factor above 1×10^6 in the near-infrared (NIR) at a wavelength of around 1550 nm are realized. This platform is adapted for device operation in the visible regime where the coupling to the D2 line of a thermal rubidium vapor is studied. By the out-of-plane access to the circuits through a transparent substrate the development of very compact vapor cells for the atom-light interaction is enabled. The interaction strength is determined by evaluating the linear absorption spectrum and the induced phase shift is obtained by employing integrated Mach-Zehnder interferometers (MZIs). Thereby, a comprehensive description of the interaction is gained. A theoretical model is developed which agrees very well to the obtained data and which is used for understanding and predicting the response of devices based on the atom-light interaction.

Furthermore, the enhanced interaction by the use of ring resonators is studied and the contribution of the induced phase shift and attenuation to the resonator response is discussed. As a last point, the possible enhancement of the interaction by the use of slot waveguides is evaluated where the main part of the mode is confined in a free space between two dielectric strips.

Due to its material absorption the Si_3N_4 platform is not suitable for the extension of the usable spectral regime to the LWIR region for future spectroscopic sensing of molecules. A suspended silicon platform is developed with a waveguide attenuation of 0.5 dB/mm in the NIR regime and which is used for the first presentation of transmission through silicon-based integrated photonic circuits at a wavelength of 8 µm with an estimated propagation loss of 1 dB/mm.

An even broader spectral range can be accessed by using diamond as a device material. Due to its large electronic band gap, the transparency window of diamond starts close to the ultraviolet and stretches all the way to the far-IR with only an absorption band around 3-6 µm. The surface functionalization of diamond waveguides for protein detection in the NIR regime is studied as an example for life-science applications and the extension to the LWIR regime for future sensing applications is presented. By using a suspended diamond platform, the first combination of devices operating in the visible ($\lambda = 650$ nm), NIR ($\lambda = 1550$ nm) and LWIR ($\lambda = 8$ µm) regime on a single sample is realized. Therein, an attenuation of 8.9 dB/mm in the NIR and 9.8 dB/mm in the LWIR regime is achieved. Such a broadband usability of the diamond platform widely opens the door for a combination of sensing schemes on a single photonic chip, which has so far been unattainable. The development of the LWIR regime for integrated photonic circuits also paves the way for the miniaturization of general optical systems in this technologically important waveband.

List of Abbreviations

AFM	Atomic force microscopy
AFP	Alpha-fetoprotein
ALD	Atomic layer deposition
AlN	Aluminium nitride
BSG	Borosilicate glass
C-band	Conventional band
CAD	Computer-aided design
CFN	Center for Functional Nanostructures
CMOS	Complementary metal-oxide-semiconductor
CNT	Carbon nanotube
CVD	Chemical vapor deposition
DAQ	Data acquisition unit
DBT	Dibenzoterrylene
DOI	Diamond on insulator
EBL	Electron-beam lithography
EIT	Electromagnetically induced transparency
ER	Extinction ratio
FEM	Finite element methods
FF	Fill factor
FIB	Focused ion beam
FSR	Free spectral range
FWHM	Full width half maximum
HF	Hydrofluoric acid
HMDS	Hexamethyldisilazane
HSQ	Hydrogen silesquioxane

HWHM	Half width half maximum
IC	Integrated circuit
ICP	Inductively coupled plasma
INT	Institute of Nanotechnology
IPA	Isopropyl alcohol
IR	Infrared
LPCVD	Low-pressure chemical vapor deposition
LWIR	Long-wave infrared
MBE	Molecular beam epitaxy
MIBK	Methylisobutylketone
MZI	Mach-Zehnder interferometer
NIR	Near-infrared
PCD	Polycrystalline diamond
PEC	Proximity effect correction
PECVD	Plasma-enhanced chemical vapor deposition
PL	Photoluminescence
PMMA	Polymethyl methacrylate
PSF	Point spread function
PVD	Physical vapor deposition
QCL	Quantum cascade laser
QED	Quantum electrodynamics
RF	Radio frequency
RIE	Reactive ion etching
SCD	Single crystalline diamond
SEM	Scanning electron microscope
SNR	Signal-to-noise ratio
SNSPD	Superconducting nanowire single photon detector
SOI	Silicon-on-insulator
TE	Transverse electric

TM Transverse magnetic
TMAH Tetramethylammonium hydroxide
TPA Two-photon absorption

UHV Ultra-high vacuum
UV Ultraviolet

WGM Whispering gallery mode

1 Chapter 1. Introduction

Coupling of guided modes in nanophotonic circuits to surrounding elements via the evanescent field is an integral part of many applications in the field of integrated optics. In this thesis the potentials and capabilities of such coupling schemes with the focus on sensing processes are studied and a novel platform for ultra-broadband device operation from the visible to the long infrared spectral regime on a single sample is presented.

Optical devices and optical systems have always played a crucial role in the history of science and technology. In particular, the modern information age would not have been possible without the development of optical fiber telecommunication. Light guiding is the central element for confining and transmitting light over a broad variety of length scales. Initially used for long-distance fiber communication at extremely high data rates [1–4], optical interconnects have been introduced at ever shorter length scales due to increasing bandwidth demands and decreasing costs [5]. For communication between different server racks and boards such interconnects are already commercially available and widely in use [6, 7]. Additionally, optical interconnects in between single chips [8–11] as well as on-chip optical connections between otherwise electronic integrated components are intensely studied [12–15].

In parallel to optical interconnects, integrated optical circuits based on light guiding in on-chip dielectric waveguides have been developed. In analogy to electronic integrated circuits, the introduction of photonic circuits led to the miniaturization of optical experiments. Such optical experiments are often based on free-space optics using bulk components like mirrors and lenses. Thus, they typically suffer from limitations, for example in the long-term stability of the setup and the need to realign the components and refocus the light beam. Moreover, their physical size limits the scalabilty and thus also the complexity as well as the possibility of developing compact handheld systems. In contrast, nanophotonic integrated circuits enable the miniaturization and simplification of large complex optical systems with an enhanced stability and reliability. A very small device footprint and the possible mass production of devices lead to lower production costs. Additionally, a higher bandwidth for on-chip communication and computation is realizable with a low energy consumption and heat dissipation [16–20].

Considerable progress in the field of integrated photonics has led to the realization of a multitude of devices by complementary metal-oxide-semiconductor (CMOS) compatible fabrication techniques. This includes a large variety of passive and active integrated components for classical (e. g. lasers [21–24], modulators [25–28], filters [29–32] and detectors [33–36]) as well as quantum communication and computational systems [37–42].

The passive integrated photonics material platform itself is however not sufficient to fulfill all demands on copmlex circuits especially concerning the manipulation of a light beam and the tunability of integrated systems. Hence, the coupling of additional elements to guided modes via the evanescent field is a key factor enabling a major part of cutting-edge photonic applications and fundamental research. This is exemplarily notable for quantum photonic circuits where single-photon sources are coupled to the integrated platform [43–47] and light is manipulated in beam splitters utilizing the coupling between two waveguides [40, 48, 49] or in tunable phase-shifters based on the sensitivity of the field to its surroundings [50]. Single photons are eventually detected by e. g. coupling to a superconducting nanowire single photon detector (SNSPD) placed on top of a waveguide [51–53].

Moreover, near-field coupling to additional elements plays an important role not only in quantum photonic circuits but also in classical communication and computing applications. A lot of attention has been attracted by coupling of phase-change materials cells to photonic integrated circuits for all-optical memory elements [54, 55], switches [56], basic abacuses [57] and most recently as on-chip photonic synapse in neuromorphic systems [58–60]. An additional intensively researched field is the coupling to 2D materials which might for example satisfy the need for broadband fast modulation of optical signals [61]. Therein, graphene-based hybrid devices are mostly used for absorption [62, 63] or phase modulation [64], but can also be employed as a detector [65, 66] or even a combination of both [67]. The discovery of further mono- and multilayered semiconductors has opened the door for novel single-photon sources that can also be coupled to waveguides [68–79]. Thereby, they can find their way into the above mentioned quantum photonic circuits.

Most applications mentioned so far are based on light coupling to a single element or well defined solid-state system. In addition, the coupling to a collective system like a thermal atomic vapor opens up new possibilities for integrated photonic circuits. Typically, ultra cold atomic gases are used for extremely precise measurements in referencing and sensing tasks [80–83] as well as for strong atom-photon coupling in nanophotonic devices for cavity quantum electrodynamics (QED) experiments [84–87]. However, ultra cold atomic gas experiments usually require large apparatus. In contrast, using thermal atomic vapors offers less precision, but enables the miniaturization of devices and on-chip integration. The light-atom interaction offers for example the possibility of fast all-optical modulation and switching in integrated circuits via electromagnetically induced transparency (EIT) and the Autler-Townes effect [88–90]. Additionally, two-photon absorption (TPA) in combination with resonators can be utilized for on-chip modulation and routing for example in complex ring resonator arrays [91–93]. The integration of an atomic vapor with nanophotonic circuits might also be used as a future chip-scale Doppler-free frequency reference with good long term stability [90].

Before, vapors have been used for additional functionality of optical circuits. But waveguides can also be used to sense and measure, using the reverse approach that a guided mode reacts sensitively to a change in its surroundings. Detection based on integrated photonic circuits benefits from a very strong optical field confined in a small volume. The sensitivity is further increased by a long interaction length along the waveguide compared to optical sensors based on single or multiple reflections at an optical interface. This way, basic linear spectroscopy measurements have been implemented within nanophotonic circuits [94, 95]. This has paved the way for various on-chip sensing applications. Not only spectrometric detection of atom gases has been carried out but also integrated optical sensors for molecules have been enabled [96, 97] as well as bio-photonic sensors via the functionalization of integrated circuits [98]. Detection applications are in particular important for the mid infrared and long-wave infrared (LWIR) regions as many molecules exhibit a unique complex absorption structure within this spectral interval [99]. Thus, it is typically referred to as the *fingerprint region*. However, a special material platform is needed for photonic integrated circuits, which exhibits optical transparency and enables total internal reflection in this wavelength regime. A further sensing scheme is based on the surface functionalization of integrated waveguides. By using click-chemistry systems, the binding of e. g. specific proteins to the surface can be detected via the evanescent field. For such life-science applications a biocompatible material platform is favorable in order to ensure long-term stability.

Within this work several material platforms are presented in order to meet the requirements of specific hybrid devices utilizing the near-field coupling to additional elements. Silicon nitride (Si_3N_4) serves as a main platform in the visible and near-infrared (NIR) spectral regime due to its transparency range (∼0.3-5.3 µm) and low intrinsic losses, which enable very high quality circuits. In contrast, due to its bandgap, silicon is limited to wavelengths above 1.1 µm and is used as a reference material in the NIR regime and for the extension of the integrated photonics platform up to a wavelength of 8 µm in the LWIR region. Finally, diamond is studied for integrated photonic devices in the NIR and LWIR regime as it offers a transparency range from close to the ultraviolet (UV) up to the far infrared region, which is in combination with its biocompatibility very promising for sensing applications.

The development and characterization of the high quality Si_3N_4 platform is discussed in **Chapter 2**. First, the fundamentals of integrated photonic circuits and some elementary devices that are used throughout the thesis are introduced. Secondly, the principal fabrication procedure for these circuits, the basic measurement setup for the device characterization and finally the experimental evaluation of the platform and the devices are presented.

The Si_3N_4 platform is used for the interaction of light with a thermal rubidium (Rb) vapor via the evanescent field. This is described in **Chapter 3**. The material platform is further adjusted and optimized regarding the specific requirements of the light-atom coupling. In particular, the rubidium D_2 line is used for the experiments described here. Spectroscopic measurements with basic waveguides are employed for the evaluation of the interaction strength. In addition to the attenuation, the phase change induced in the waveguide mode by the atoms at the electron transition is extracted via the response of Mach-Zehnder interferometers (MZIs). This way, a comprehensive description of the

interaction is gained, which is fundamental for the development of functional devices. As a basic step towards all-optical modulation and routing, the response of ring resonators exposed to the atom vapor is studied. Thereby, a strong interaction between the waveguide mode and the surrounding atoms is achieved. In addition, a further enhancement of the interaction by the use of slot waveguides is analyzed. The experimental results are compared to theoretical predictions by introducing the susceptibility of the atom vapor in simulations of the optical circuits. This model agrees very well with the recorded data and the expected response of future devices can be simulated.

The presented Si_3N_4 integrated photonics platform now also serves as a basis for a major part of the experimental activity within our research group. This includes the development of complete single-photon circuits for quantum photonic networks, which consist of sources, light manipulation and single-photon detectors. A short overview of the coupling of selected elements to integrated circuits is given in **Chapter 4**. As an introduction to the coupling of layered materials, the placement of a graphene flake on a waveguide is discussed. This leads to the coupling of single-photon sources within a layered GaSe sheet into integrated circuits. As an alternative integrated single photon source the use of dibenzoterrylene (DBT) molecules is discussed. Additionally, electrically driven carbon nanotube (CNT) single-photon sources are briefly described as well as superconducting nanowire single-photon detectors, which form the counterpart to the integrated single-photon sources. With the development of on-chip single-photon sources and detectors two fundamental building blocks of quantum photonic circuits are realized.

As mentioned before, in terms of sensing applications for spectroscopic measurements the extension of the integrated photonics platform from the visible wavelength regime used for the light-atom interaction to the LWIR regime is of great interest as it covers the fingerprint region of many molecules. Thus, in **Chapter 5** diamond is introduced as a material platform. First, the diamond on insulator (DOI) platform is described and characterized, which is typically used for application in the visible and NIR regime. The biocompatibility of diamond is exploited in the NIR regime by the surface functionalization of integrated photonic ring resonators. Thereby, antigen coupling of alpha-fetoprotein (AFP) and the binding of streptavidin to biotin is optically detected on-chip. In order to reach the fingerprint region, diamond on aluminium nitride (AlN) as well as suspended diamond is introduced as a new versatile integrated photonics platform. This enables device operation covering a broad spectral range from the visible (and potentially UV) up to the LWIR regime, which might even be extended to the very far infrared region in case of suspended diamond. Additionally, silicon-on-insulator (SOI) and suspended silicon are presented for device operation in the NIR and LWIR region and serve as a comparison for the diamond circuit performance. The diamond platform is characterized in the visible regime (600-800 nm) and along with the silicon platform in the NIR regime at 1550 nm. For both platforms the functionality of integrated photonic circuits in the LWIR regime around a wavelength of 8 µm is presented.

2 Chapter 2.

Silicon Nitride as Basic Passive Integrated Photonics Platform

In this chapter, the basic properties of Si_3N_4 as well as some fundamental integrated devices and the their fabrication process are discussed. First, an introduction to Si_3N_4 as an integrated photonics material is given along with basics about dielectric waveguides. This includes numerical simulations of the guided modes. Furthermore, the fabrication process for the standard Si_3N_4 integrated photonics platform is explained. The development of this basic fabrication process has already begun in the work preceding this thesis [100]. Here, it is further optimized and adjusted in order to fulfill the requirements of the experiments presented in the following chapters. Besides, the measurement setup used for the characterization of integrated circuits is described. Last, some basic devices which are used throughout this thesis and their experimental evaluation are presented. The performance of high-quality Si_3N_4 circuits fabricated by the described procedure has also been published in Ref. [101].

2.1. Silicon Nitride for On-Chip Photonic Structures

Originating in the electronics industry and the fabrication of integrated circuits (ICs), silicon and especially SOI wafers with a Si layer on a SiO_2 intermediate layer are widely used for integrated photonic circuits. High-quality SOI wafers are commercially available and most importantly they are compatible with standard CMOS manufacturing techniques [16, 102, 103]. The large contrast in the refractive index between Si and SiO_2 of $n = 3.45$ to $n = 1.44$, both at a wavelength of $\lambda = 1.55\,\mu m$, provides a tight confinement of the optical mode in silicon waveguides and therefore enables compact circuits with a small device footprint [104–106]. There is, however, a limitation in the accessible wavelength range when using silicon waveguides. Due to a rather small bandgap of 1.1 eV silicon photonic devices are restricted to wavelengths above 1.1 µm [107]. For most devices in communication applications this is sufficient as the wavelengths between 1.53 µm and 1.57 µm of the conventional band (C-band) are employed for infrared optical communication. This originates in a

very low material absorption of silica fibers at $\lambda \approx 1.55\,\mu m$, which shifted the operation wavelength of lightwave systems from historically 0.8 µm and 1.3 µm [108, 109]. However, for applications in the visible wavelength regime silicon cannot be used. Instead, Si_3N_4 is used as a waveguide material for the devices presented in the first part of this work. This has the advantage that it can be applied for nanophotonic circuits operable in the visible as well as in the NIR regime while maintaining a high device quality with low propagation losses and good CMOS-compatible structuring capabilities.

2.1.1. Silicon Nitride Optical Properties

Most important for the optical properties of Si_3N_4 is its wide bandgap of ~5 eV, which provides a transparency window spanning from the visible regime, close to the UV, to infrared (IR) wavelengths (~0.3-5.3 µm) [110, 111]. It also prevents two-photon absorption (TPA) in the NIR regime relevant for communication applications and causes a low free carrier concentration. This leads to reduced absorptive losses, which can impair device operation, e. g. in SOI circuits [112–114]. Additionally, the refractive index of Si_3N_4 around 2 is large enough, compared to air and SiO_2, to enable tight optical confinement in waveguides and thus dense device integration [115, 116]. Moreover, it exhibits a rather small thermo-optic coefficient of $(dn/dT) \approx 2.45 \times 10^{-5}\,K^{-1}$, which is one order of magnitude smaller than in silicon ($\sim 1.8 \times 10^{-4}\,K^{-1}$) and leads to a lower sensitivity to temperature fluctuations [117–119]. Si_3N_4 films produced by low-pressure chemical vapor deposition (LPCVD) exhibit a very precise thickness, a uniform refractive index and a low surface roughness. However, LPCVD Si_3N_4 layers typically exhibit a high tensile stress, which limits the layer thickness to ~0.5 µm as thicker films are likely to exhibit cracks [120]. In order to exploit the third order nonlinear susceptibility $\chi^{(3)}$ of Si_3N_4, the growth of thicker layers by using plasma-enhanced chemical vapor deposition (PECVD) with dual frequency reactors or LPCVD including thermal annealing cycles has recently been developed [121, 122]. Thereby, a layer thickness up to ~1 µm (necessary for dispersion engineering) with a nonlinear index coefficient of $n_2 = 2.4 \times 10^{-15}\,cm^2/W$ has been reported, which can be used for the generation of frequency combs via four-wave-mixing for wavelength division multiplexing and data transmission at very high data rates [111, 121, 123–127].

For the realization of photonic devices studied in this work, commercially available Si_3N_4 wafers from Rogue Valley Microdevices[1] are utilized, which consist of a stochiometric Si_3N_4 layer on a thermal SiO_2 layer on top of a Si substrate. Two different layer thickness configurations are used to ensure single mode waveguiding in the particular spectral region. A 340 nm Si_3N_4 layer on 3.3 µm SiO_2 is used for NIR applications, while devices designed for the visible regime are based on a 200 nm Si_3N_4 layer on a 2.0 µm SiO_2 buffer. According to the manufacturer's specifications these films exhibit a relative thickness tolerance and uniformity within a wafer of both ±5 % and contain a high tensile stress of ~0.8 GPa. The refractive index and dispersion formula of Si_3N_4 and all other materials used within this thesis are listed in App. A.1.

[1] Rogue Valley Microdevices, Medford, OR 97504, USA

2.1.2. Integrated Optics

In order to understand the principle of near-field coupling schemes in integrated optics, the basics of photonic light guiding are reviewed. In general, light confinement in a specific structure is achieved by guiding light in a material with a higher optical density compared to its surroundings. The most prominent example is glass fibers used for fast long-distance communication with very low losses [2, 128, 129]. Integrated photonic circuits combine these advantages with the possibility to build complex optical systems on a microchip. Therein, the central elements for guided light propagation are waveguides typically consisting of a rectangular shaped high-refractive index material on a low-refractive index substrate. Two examples for so called channel waveguides that are used within this thesis are shown in Fig. 2.1. For a ridge waveguide as shown in (a) the waveguide material is completely etched, while it is only partially etched for a rib waveguide (b). Also, a potential cladding of the waveguide needs to exhibit a lower refractive index with respect to the waveguide material.

In a simple ray-optics picture the optical confinement can be easily explained by total internal reflection where a light beam is completely reflected at an interface to an optical less dense material (e. g. $n_1 > n_2, n_0$ in Fig. 2.1) as long as the angle of incident is below the critical angle. However, besides this descriptive picture of light guiding, a rigorous electromagnetic analysis based on Maxwell's equations is needed to describe properties and effects such as field profiles and mode coupling [130–132]. Using the translation symmetry along the waveguide (defined as the z-direction) the analysis can be simplified and the z-dependence can be separated from the other spatial coordinates. Thus, simple plane waves of angular frequency ω are valid solutions to the wave equation for the electric ($\vec{E}$) and magnetic ($\vec{H}$) field:

$$\begin{aligned} \vec{E}_\nu(\vec{r},t) &= \vec{\mathcal{E}}_\nu\,(x,y)\, e^{\mathrm{i}\left(\tilde{\beta}_\nu z-\omega t\right)} \\ \vec{H}_\nu(\vec{r},t) &= \vec{\mathcal{H}}_\nu\,(x,y)\, e^{\mathrm{i}\left(\tilde{\beta}_\nu z-\omega t\right)}. \end{aligned} \tag{2.1}$$

The mode index ν labels the different possible solutions, $\tilde{\beta}_\nu$ is the complex propagation constant and $\vec{\mathcal{E}}_\nu$ and $\vec{\mathcal{H}}_\nu$ are the electric and magnetic field profiles of a particular mode. Given by the waveguide

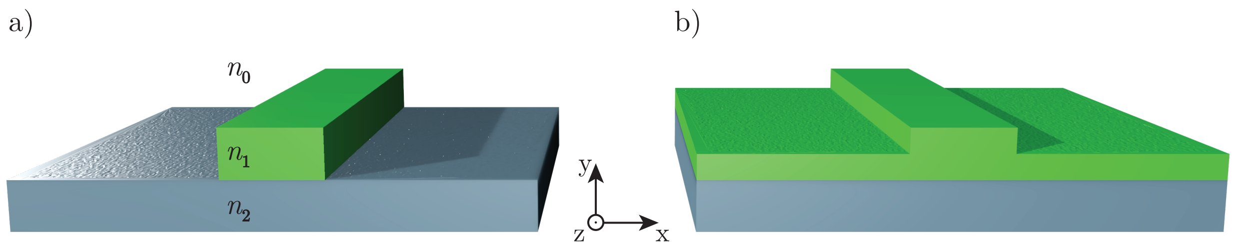

Figure 2.1.: Sketch of a ridge (a) and a rib (b) waveguide. In order to enable light guiding via total internal reflection the waveguide refractive index needs to be larger than those of the surrounding materials: $n_1 > n_0, n_2$.

cross-section geometry, the propagation space is confined in the transverse directions and hence the field patterns have to satisfy the conditions of a two-dimensional cavity. For such a finite-sized cavity there is only a finite number of modes which in case of a waveguide are referred to as *guided modes*. The mode index ν generally labels the number of intensity nodes in the waveguide cross-section. Every guided wave is a superposition of these modes as they are mutually orthogonal and linearly independent.

Each waveguide mode is fully characterized by its field pattern and the propagation constant at a certain wavelength. The propagation constant for a certain mode is related to the vacuum wavenumber $k = {}^{2\pi}/_{\lambda}$ via the *effective refractive index* or *mode index* $\tilde{n}_{\mathrm{eff},\nu}$:

$$\tilde{\beta}_\nu = k \cdot \tilde{n}_{\mathrm{eff},\nu} = \frac{2\pi}{\lambda}(n_{\mathrm{eff},\nu} + \mathrm{i}n'_{\mathrm{eff},\nu}). \tag{2.2}$$

The real part of the mode index $n_{\mathrm{eff},\nu}$ determines the phase velocity of the guided wave whereas the imaginary part $n'_{\mathrm{eff},\nu}$ accounts for propagation losses due to absorption and scattering. By inserting the complex mode index into Eq. (2.1) the exponential decay of the optical intensity along the waveguide is obtained:

$$I(z) = |E(z,t)|^2 = |\mathcal{E}(z)|^2 \cdot |e^{i({}^{2\pi}/_{\lambda}(n_{\mathrm{eff}}+\mathrm{i}n'_{\mathrm{eff}})z-\omega t)}|^2 = |\mathcal{E}(z)|^2 \cdot e^{-\frac{4\pi}{\lambda}n'_{\mathrm{eff}}z}. \tag{2.3}$$

This leads to an *attenuation coefficient* $\alpha = {}^{4\pi}/_{\lambda} \cdot n'_{\mathrm{eff}}$, which corresponds to a decay length of $l = \alpha^{-1}$. Thus, the intensity decreases along the propagation direction according to Beer's law. In contrast to the phase velocity, the propagation speed of a guided optical pulse is determined by the group refractive index n_{g}, which differs from the effective refractive index due to wavelength dispersion. It is derived as

$$n_{\mathrm{g}}(\lambda) = n_{\mathrm{eff}}(\lambda) - \lambda\frac{\partial n_{\mathrm{eff}}}{\partial\lambda}. \tag{2.4}$$

Besides the distinction of the modes by their mode index ν, they are also classified by their longitudinal field component. In a *planar waveguide* with optical confinement in only one transverse direction, the guided modes are distinguished in transverse electric (TE) and transverse magnetic (TM) modes. For a TE mode the z-component of the electric field vanishes ($\mathcal{E}_z = 0$) and from the wave equations for a planar waveguide it follows that $\mathcal{E}_y = \mathcal{H}_x = 0$. The only non-vanishing components are $\mathcal{E}_x$, $\mathcal{H}_z$ and $\mathcal{H}_y$. Similarly, for a TM mode $\mathcal{H}_z = 0$ and $\mathcal{H}_y = \mathcal{E}_x = 0$ is obtained with non-vanishing $\mathcal{H}_x$, $\mathcal{E}_z$ and $\mathcal{E}_y$. For a channel waveguide this is not strictly true. Due to the restriction also in the second transverse direction, there is also a field contribution in the other component. However, for many modes one of the two longitudinal components is significantly smaller than the other and hence the modes are TE-like and TM-like. Yet, in order to maintain better readability the modes are labeled as TE and TM modes throughout the course of this thesis.

Mode simulation

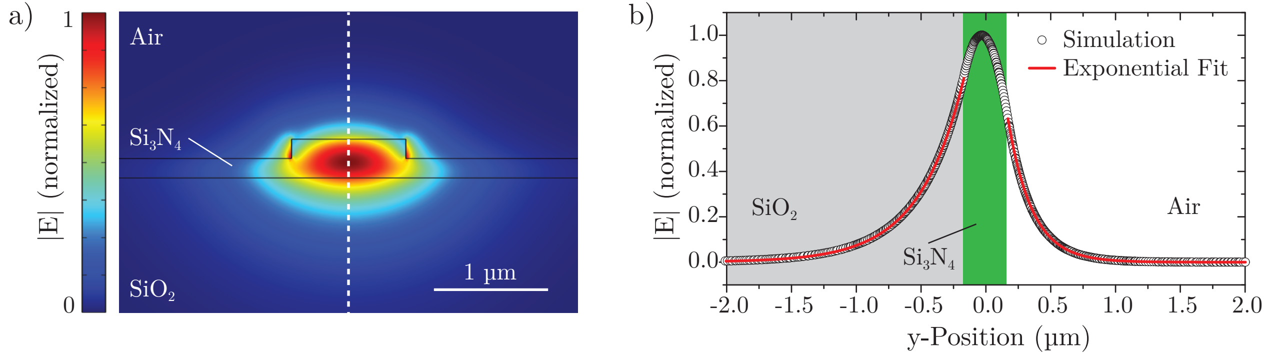

Figure 2.2.: a) Simulated electric field of the TE_0 mode in a half etched 340 nm Si_3N_4 waveguide for a wavelength of 1.55 µm. b) Electric field strength along the dashed line in (a). Outside of the waveguide the field decays exponentially with a decay length of 186 nm in air and 345 nm in the silica substrate. The part of the field outside of the Si_3N_4 waveguide is called the evanescent field.

For most channel waveguide geometries it is not possible to find an analytic expression for the effective index and the field profile. Therefore, finite element methods (FEM) calculations are used within COMSOL Multiphysics[2] in order to simulate the waveguide modes. In Fig. 2.2 a) the simulated electric field distribution of the fundamental TE_0 mode in a typical Si_3N_4 ridge waveguide on SiO_2 is shown at a NIR wavelength of 1550 nm. For this simulation a rib waveguide with an etching depth of 170 nm and a waveguide width of 1 µm is considered. Such a waveguide is later used for the realization of high-quality circuits. The mode exhibits an effective index of $n_{\mathrm{eff}} = 1.56$ and the main part of it is confined within the waveguide. In Fig. 2.2 b) it is shown that the field outside of the waveguide decreases exponentially with a decay length in the order of 100 nm. The confinement of the mode in the waveguide and the ratio of the field outside is determined by the refractive index of the material system and the chosen waveguide geometry. Through this so-called *evanescent field* the waveguide mode is sensitive to its surroundings. Thereby, it enables near-field coupling to other systems in the close vicinity of the waveguide.

The influence of the waveguide geometry on the guided modes is simulated for a varying waveguide width. This *geometric dispersion* is plotted in Fig. 2.3 a) for the same Si_3N_4 waveguide as above. In order to determine the cutoff in the effective mode index for which no more guided mode is supported in the waveguide, not only the refractive index of the SiO_2 substrate has to be considered but also the remaining Si_3N_4 layer. Thus, a simulation of the modes in slab waveguide consisting of a 170 nm Si_3N_4 layer on a SiO_2 substrate is performed. Only a single mode with an effective index of 1.47 is supported in this structure, which serves as a cutoff for the Si_3N_4 rib waveguide with a corresponding height of the remaining Si_3N_4 layer. This cutoff is shown as the dashed line in the graph. For a width below ∼1.2 µm only the fundamental TE_0 mode is guided while for a waveguide width of e. g. 3 µm the

[2] Comsol Multiphysics GmbH, 37073 Göttingen, Germany

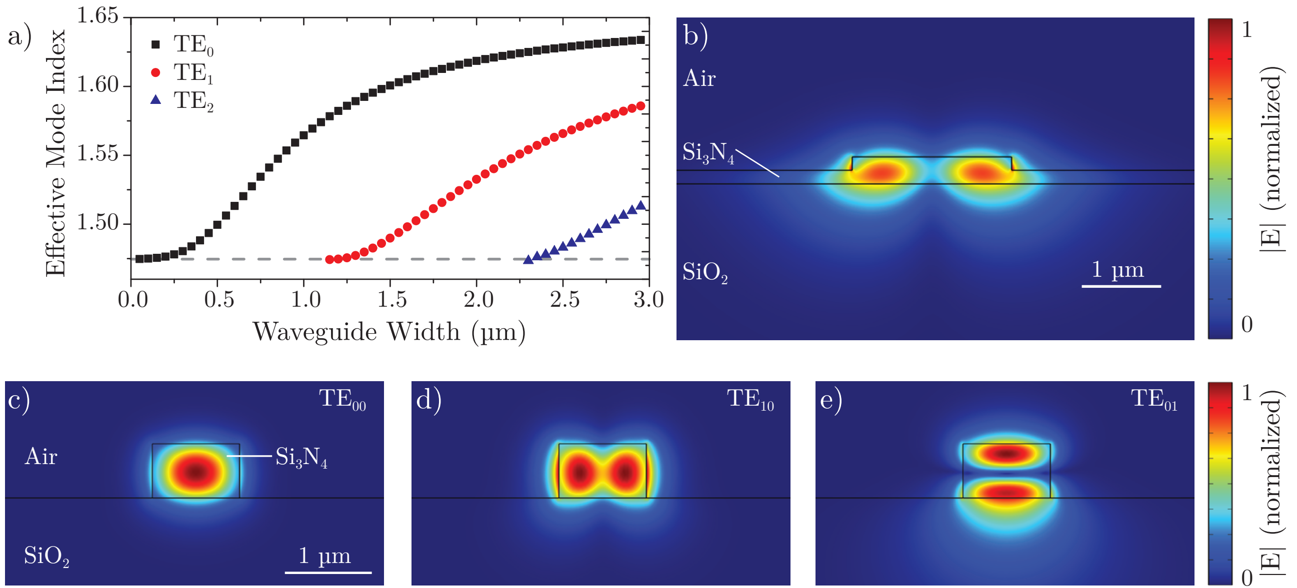

Figure 2.3.: Simulation results of the guided modes in Si_3N_4 waveguides at $\lambda = 1.55\,\mu m$. a) Effective refractive index of the guided modes in a 340 nm thick half etched rib waveguide. The dashed line indicates the cutoff. Below this cutoff the modes are not anymore supported by the waveguide. b) Electric field profile of the TE_1 mode for a waveguide width of 2 µm. c) - e) Simulated mode profiles of a 870nm Si3N4 ridge waveguide with a width of 1.4 Îijm. The fundamental TE mode is shown in (a). Due to the waveguide dimensions the higher order modes can not only be spread in the x-direction (e. g. TE10 in (d)) but also in the y-direction (e. g. TE01 in (e)).

higher order modes TE_1 and TE_2 are also supported. As an example, the electric field profile of the TE_1 mode for a waveguide width of 2 µm is displayed in Fig. 2.3 b). Hence, by using such simulations a single mode waveguide geometry can be found.

Typically, the waveguide height and its aspect ratio only allow for the intensity maxima of higher order modes to be spread only in the x-direction. In this case only a single mode index is used, which is maintained throughout the thesis. However, for a larger waveguide height, the nodes of the higher order modes can be located in both transverse directions. Only in such a case the modes are labeled by two indices. An example is shown in Fig. 2.3 c)-e) for the electric field distribution of three modes in a 870 nm thick and 1.4 µm wide Si_3N_4 waveguide. In (d) and (e) the first higher order TE mode is spread in the x- and y-direction respectively.

2.2. Basic Integrated Photonic Circuits

The dielectric waveguides introduced above are the fundamental building blocks for integrated circuits. In this section three basic integrated photonic devices are introduced, which are used throughout this thesis. Ring resonators are employed for the characterization of waveguide properties of different material systems and in spectroscopic measurements of the atom-light interaction. In order to determine phase shifts and attenuation variations Mach-Zehnder interferometers are used. Additionally, slot

waveguides are studied in order to obtain a strong optical field in a free space between two waveguide strips for enhanced near-field coupling.

2.2.1. Ring Resonators

Optical cavities are an integral part for many integrated photonics applications. The intra-cavity circulation of light leads to a field enhancement and the wavelength selectivity of those resonators [133]. Due to light interference with itself only wavelengths satisfying a certain resonance condition are supported. While the optical power for these wavelengths is enhanced by constructive interference, it is strongly suppressed for all other components. Typical applications exploiting those properties include filters and routers, e. g. in optical telecommunications [134], as well as cavity-enhanced spectroscopy [135], nonlinear devices [136–139] and the enhancement of spontaneous emission based on the Purcell effect [140, 141]. In recent years the development of *microcavities* with small modal volumes and high quality factors opened up new research opportunities like cavity optomechanics [142] and strong-coupling cavity QED [143, 144]. Besides the classical Fabry-Pérot interferometer with two parallel reflecting surfaces [145], other resonator geometries have been studied for this purpose. These include photonic-crystal cavities, which provide extremely small modal volumes [146–148] and whispering gallery mode (WGM) cavities, which offer very high quality factors usually at the cost of larger modal volumes [149]. As indicated by its name, common WGM resonator designs include rings, disks or spheres, wherein light can circulate [150–153]. Within this work solely ring resonators are studied. They can be conveniently fabricated in a single lithography step together with the surrounding circuitry.

The sketch of the basic configuration of a ring resonator which is evanescently coupled to a bus

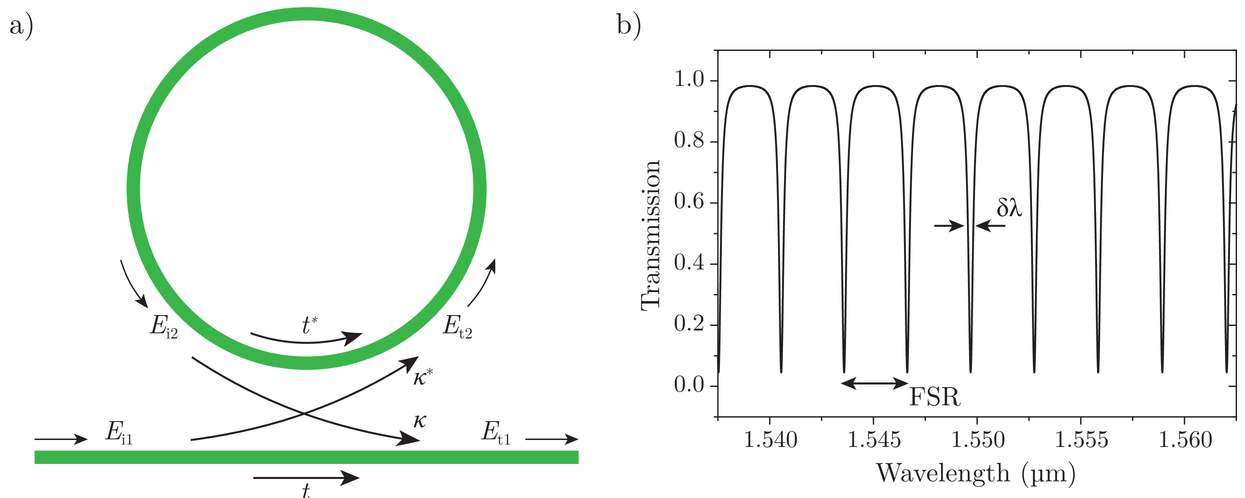

Figure 2.4.: a) Sketch of a ring resonator coupled to a bus waveguide indicating the coupling coefficients t, κ and the field amplitudes of the incoming E_i and transmitted E_t light. b) Theoretical transmission spectrum based on Eq. (2.6) using $A = 0.9, t = 0.85, n_\mathrm{eff} = 1.56, r = 80\,\mu\mathrm{m}$.

waveguide, is displayed in Fig. 2.4 a). Light is coupled between the modes in the ring and the bus waveguide due to the overlap of the fields. This is described by the coupling and transmission coefficients κ and t. Herein, the coupling strength depends on the distance between the ring and bus waveguide as well as the interaction length, which is influenced by the ring radius. For identical waveguides the coupling is symmetric with the coefficients satisfying $|\kappa|^2 + |t|^2 = 1$. Considering a steady-state framework, the coupling between the field amplitudes E is described by the following matrix relation [132, 153]:

$$\begin{pmatrix} E_{\mathrm{t1}} \\ E_{\mathrm{t2}} \end{pmatrix} = \begin{pmatrix} t & \kappa \\ -\kappa^* & t^* \end{pmatrix} \cdot \begin{pmatrix} E_{\mathrm{i1}} \\ E_{\mathrm{i2}} \end{pmatrix}. \tag{2.5}$$

The input field E_{i2} is directly linked to the second output field by $E_{\mathrm{i2}} = A \cdot e^{\mathrm{i}\theta} E_{\mathrm{t2}}$ where $A = e^{-\alpha/2 L}$ is the loss factor and $\theta = 2\pi n_{\mathrm{eff}}/\lambda L$ the collected phase during one roundtrip. Here, all losses occurring in the ring are included in the attenuation coefficient α and the length of the ring is given by $L = 2\pi r$ with the ring radius r. Setting the input amplitude E_{i1} to 1 and expressing the complex transmission coefficient by $t = |t|e^{\mathrm{i}\phi_t}$, the transmitted power is derived as

$$P_{\mathrm{t1}} = |E_{\mathrm{t1}}|^2 = \frac{A^2 + |t|^2 - 2A|t|\cos(\theta + \phi_t)}{1 + A^2|t|^2 - 2A|t|\cos(\theta + \phi_t)} \tag{2.6}$$

and the circulating power as

$$P_{\mathrm{i1}} = |E_{\mathrm{i2}}|^2 = \frac{A^2(1 - |t|^2)}{1 + A^2|t|^2 - 2A|t|\cos(\theta + \phi_t)}. \tag{2.7}$$

Based on Eq. (2.6) the transmitted power is plotted in Fig. 2.4 b). The dips in the spectrum correspond to the ring resonances which are obtained for wavelengths satisfying the resonance condition

$$\theta_{\mathrm{r},m} + \phi_t = 2\pi \frac{n_{\mathrm{eff}}}{\lambda_{\mathrm{r},m}} L + \phi_t = 2\pi m, \quad m \in \mathbb{N}. \tag{2.8}$$

The spectral separation between two adjacent dips is called free spectral range (FSR). It can be derived from the resonance condition by $\lambda_m - \lambda_{m+1}$ as

$$FSR(\lambda) \approx \frac{\lambda^2}{n_{\mathrm{g}}(\lambda)L + \lambda} \tag{2.9}$$

with the group refractive index n_{g} of the intra-cavity mode. Additionally, the full width half maximum (FWHM) of a resonance dip is denoted by $\delta\lambda$. The ratio between maximal (in between resonances) and minimal (on resonance) transmitted power is expressed by the extinction ratio (ER) as

$$ER_{\mathrm{dB}} = 10 \log_{10} \left(\frac{P_{\mathrm{max}}}{P_{\mathrm{min}}} \right). \tag{2.10}$$

Using the resonance condition (Eq. (2.8)), the transmitted power on resonance is calculated as

$$P_{\mathrm{t1,r}} = \frac{(A-|t|)^2}{(1-A|t|)^2}. \tag{2.11}$$

Thus, at so-called *critical coupling* the roundtrip loss matches the coupling strength (from $A = |t|$ follows $1 - A^2 = |\kappa|^2$) and no optical power is transmitted in the bus waveguide. Therefore, the ER reaches its maximum. This case is typically used for efficiently filtering a certain wavelength or if a maximum intensity in the ring is required.

Another important parameter is the *quality factor* Q of a ring resonator. It is defined in terms of the dissipated energy per cycle with respect to the energy stored by the resonator [154, 155]. However, in most cases it can be accessed experimentally by the width of the resonance dip:

$$Q = \omega \frac{\text{stored field energy}}{\text{dissipated power}} = \frac{\lambda_{\mathrm{r}}}{\delta\lambda} \tag{2.12}$$

where ω is the angular frequency of the wave. The stored energy and the loss can also be expressed in terms of the intensity and by using Eq. (2.3) the quality factor is linked to the attenuation coefficient in the following way:

$$Q = \omega \frac{I}{\mathrm{d}I/\mathrm{d}t} = \omega \frac{I}{\lambda\omega/2\pi n_{\mathrm{g}}\,\mathrm{d}I/\mathrm{d}z} = \frac{2\pi n_{\mathrm{g}}}{\lambda\alpha} \quad \Leftrightarrow \quad \alpha_{\mathrm{dB}} = \frac{10}{\ln(10)}\frac{2\pi n_{\mathrm{g}}}{\lambda Q}. \tag{2.13}$$

Thereby, ring resonators are used for the characterization of the waveguide performance. However, only for a non-coupled ring resonator its *intrinsic* Q-factor is reached which corresponds to the actual propagation losses. Coupled to a bus waveguide, a *loaded* Q-factor is determined, which represents a combination of propagation losses and losses due to coupling to the waveguide. By increasing the gap between bus waveguide and ring, the resonator is only very weakly coupled and values close to the intrinsic Q can be reached.

It is also possible to extract the loss factor A and the transmission coefficient $|t|$ of the coupling matrix directly by using Eq. (2.6). The ER of a measured ring spectrum is extracted and by using the transmitted power on resonance (Eq. (2.11)) as well as in between resonances for destructive interference at $\theta + \phi_t = (2n+1)\pi$, $n \in \mathrm{N}$, it is derived as

$$ER = \frac{P_{\mathrm{t1,max}}}{P_{\mathrm{t1,min}}} = \left(\frac{(A+|t|)(1-A|t|)}{(1+A|t|)(A-|t|)}\right)^2. \tag{2.14}$$

As a second quantity the *finesse* $\mathcal{F} = FSR/\delta\lambda$ is extracted from a recorded spectrum. As it relates the separation between resonances (and therefore the resonator size) to the resonance width, it is used as a measure for the cavity resolution. By using the phase for which the transmitted power in Eq. (2.6)

reaches the half maximum, the following relation is derived:

$$\cos\left(\frac{\pi}{\mathcal{F}}\right) = \frac{2A|t|}{1 + A^2|t|^2}. \tag{2.15}$$

The combination of these two equations allows for extracting A and $|t|$ from the finesse and the ER of a ring resonator. A full derivation of both parameters can be found in App. A.2. However, as both parameters appear symmetrically in Eq. (2.6), a further study is needed to distinguish between them. In order to do so, the relation between them is monitored when the coupling conditions are changed. The coupling strength is for example decreased by increasing the gap between ring and bus waveguide. As mentioned before, in case of critical coupling the ER exhibits its maximum and A equals $|t|$. For a stronger coupled ring it is $A > |t|$, which is also called the *over-coupled* regime. Else, for a ring further away from the bus waveguide, the ring is *weakly coupled* and it is $A < |t|$.

A further feature of ring resonators is typically only observed for very sharp resonances. Instead of single resonance dips they exhibit a doublet structure [156, 157]. This can be explained by considering additional counter-propagating modes in the ring instead of a single unidirectional mode. Coupling between the modes is based on scattering effects and it can be included in the ring description by replacing the 2×2 coupling matrix in Eq. (2.5) by a 4×4 matrix, which includes back scattering in the coupling mechanism [158, 159]. This leads to the excitation of counter-propagating symmetric and antisymmetric modes with differing resonance frequencies. It can be illustrated by a different field distribution of the modes in the coupling region to the bus waveguide, which causes a slight variation in the effective mode index and therefore in the resonance wavelength. In fact, due to the presence of the straight bus waveguide, the rotational symmetry of the ring is broken, which leads to a splitting of the originally degenerate modes [159, 160]. However, this resonance splitting is only obsereved for very high-Q ring resonators, where the splitting is not masked by the width of the resonance.

2.2.2. Mach-Zehnder Interferometers

On-chip interferometers are an important tool for detecting small variations in the phase or amplitude of a light beam. This is for example used for the characterization of phase shifters [50, 161, 162] or to detect the motion of an opto-mechanical resonator, which can be employed for sensing applications [163–165]. Vice versa by coupling a tunable element to one of the interferometer arms, they are also applied as on-chip ultra-fast modulators [25, 62]. A sketch of an integrated version of a MZI is presented in Fig. 2.5 a). Using a beam splitter, a waveguide is divided in two arms of different length that are afterwards recombined again. The interference at the recombination only depends on the relative phase difference between the two arms. Light is either fully transmitted into the output waveguide in case of constructive interference or it is fully or partially scattered out of the device for total or partial destructive interference [166].

The output of such an interferometer can be calculated from the combination of the fields in the different arms. With an input mode $\vec{E}_{\text{in}} = \vec{\mathcal{E}}_0 e^{i\phi}$ and assuming a perfect 50/50 splitting, the output

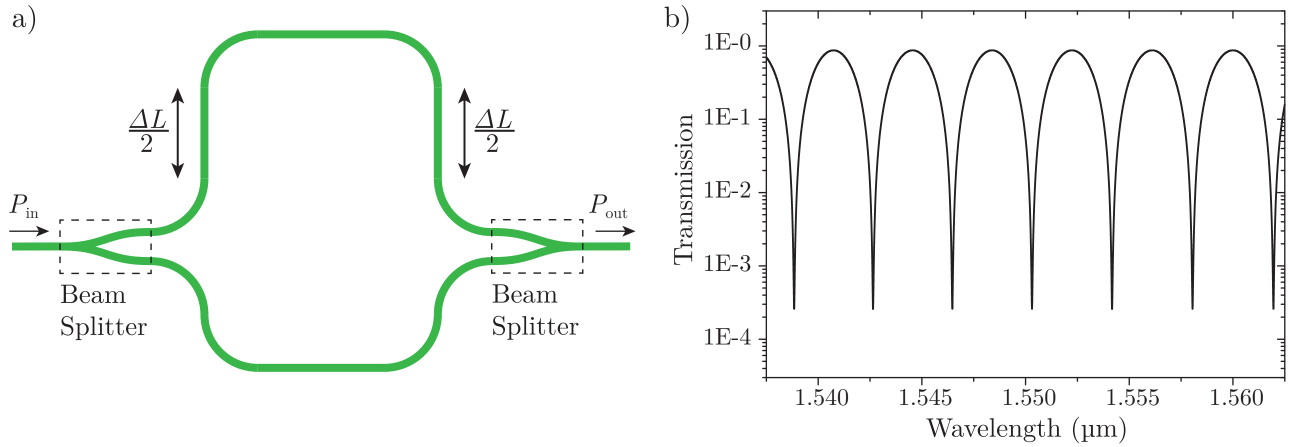

Figure 2.5.: a) Sketch of a MZI in which the waveguide is splitted in two arms of different length and recombined again. The phase and attenuation difference determines the interference spectrum. b) Theoretical transmission spectrum based on Eq. (2.17) using a perfect 50/50 splitter, $\Delta L = 400\,\mu\mathrm{m}, n_{\mathrm{eff}} = 1.56, \alpha = 0.75\,\mathrm{dB/mm}$. The spectrum exhibits an ER around 38 dB.

field is obtained as

$$\vec{E}_{\mathrm{out}} = \frac{1}{2}\vec{\mathcal{E}}_0 A_1 e^{\mathrm{i}\beta L_1 - \mathrm{i}\omega t} + \frac{1}{2}\vec{\mathcal{E}}_0 A_2 e^{\mathrm{i}\beta L_2 - \mathrm{i}\omega t}, \tag{2.16}$$

where $A_{1,2} = e^{-\alpha/2 L_{1,2}}$ is the loss factor in the two arms with the length $L_{1,2}$ and $\beta = 2\pi^{n_{\mathrm{eff}}}/\lambda$ is the real part of the propagation constant of the mode. The ratio between the loss factors is introduced as $A = {A_1}/{A_2} = e^{-\alpha/2 \Delta L}$ and the length difference between the two arms is ΔL. With $P \propto |\vec{E}^2|$ the output power is derived by

$$P_{\mathrm{out}} = \frac{1}{4} P_{\mathrm{in}} A_2^2 \left(1 + A^2 + 2A\cos(\Delta\phi)\right), \quad \Delta\phi = 2\pi \frac{n_{\mathrm{eff}}}{\lambda}\Delta L. \tag{2.17}$$

An unbalanced splitting ratio can be treated as an additional variation in A_1 and A_2. An example for this transmission spectrum is plotted in Fig. 2.5 b). It can be seen that even for destructive interference the transmission is non-zero. This is caused by the attenuation and splitting imbalance between the two arms. The ER between maximal and minimal transmitted power quantifies the ratio between the field amplitudes:

$$ER = \frac{P_{\mathrm{out,max}}}{P_{\mathrm{out,min}}} = \left(\frac{1+A}{1-A}\right)^2. \tag{2.18}$$

Therefore, an additional phase shift in one of the arms can be observed by a shift in the interference spectrum and a change of the attenuation is observed by a variation in the ER.

Integrated Beam Splitters

In the description of an MZI above, so called *Y-splitters* are used as a beam splitter as well as a combiner. In general, beam splitters distribute light from one or several input channels into several

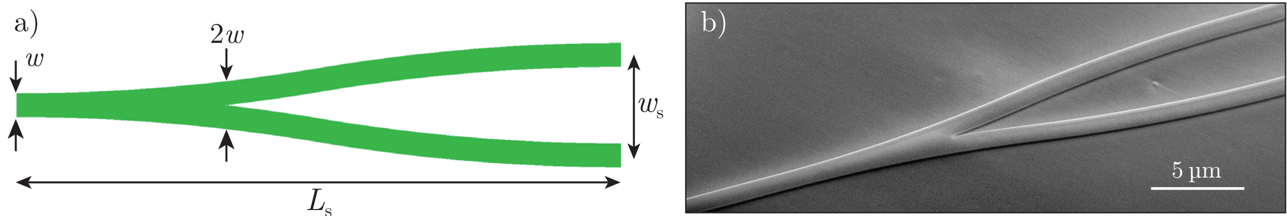

Figure 2.6.: a) Design of a Y-splitter with a waveguide width w, a splitter length L_s and a splitter width w_s. b) SEM micrograph of an integrated Y-splitter with $w = 1.15\,\mu m$, $L_s = 30\,\mu m$ and $w_s = 5\,\mu m$. Picture was taken under an angle of 45°.

output channels. Very often 50/50 beam splitters are implemented, which divide light coming from one input port equally into two output ports. This can be realized by a Y-splitter as depicted in Fig. 2.6 a) where the input waveguide is separated into two output waveguides when its width is doubled. Due to their symmetrical geometry Y-splitters provide very balanced splitting (cf. Sec. 2.4.4) [167, 168]. Moreover, they offer a very good performance over a wide spectral range and are robust concerning fabrication tolerances. Therefore, exclusively this splitter design is used within this thesis. A scanning electron microscope (SEM) micrograph of an integrated Y-splitter is shown in Fig. 2.6 b). Alternative beam splitters include multimode interference splitters, which enable $N \times M$ splitters with multiple input and output channels and an arbitrary coupling ratio [169–171], as well as directional couplers, which allow for precise control of the splitting ratio between typically two input and two output ports at a specific wavelength [172, 173].

2.2.3. Slot Waveguides

Instead of solid core rib or ridge waveguides also *slot waveguides* can be used for light guiding [174, 175]. They exhibt the interesting property that their mode confinement is below the diffraction limit [176].

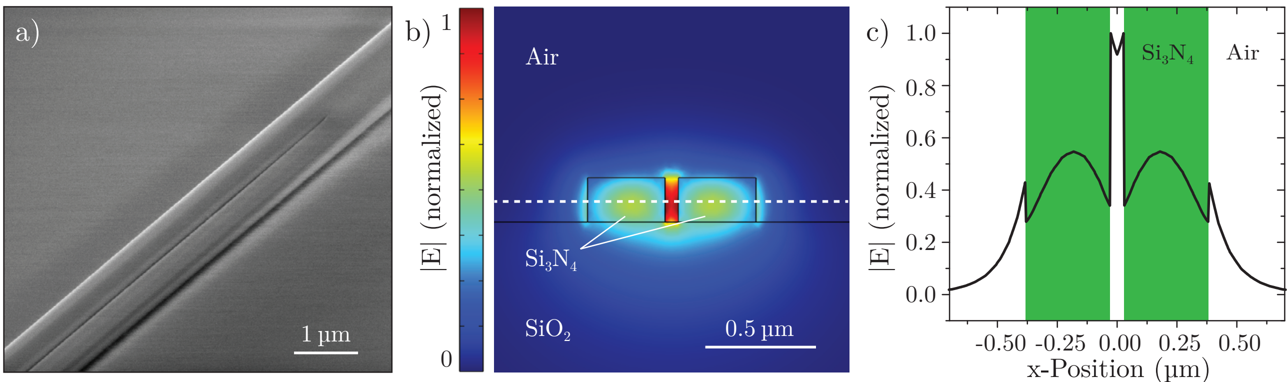

Figure 2.7.: Slot waveguide realized on a 200 nm thick Si_3N_4 platform. Two Si_3N_4 strips with a width of 350 nm are placed next to each other with an narrow gap of 60 nm in between them. a) SEM micrograph of a fabricated slot waveguide, taken under an angle of 45°. The slot is then recombined in order to form a solid core waveguide. b) The simulated electric field profile of the TE_0 mode exhibits its maximum in the slot region. The field strength along the dashed line is presented in (c).

This is realized by using two dielectric strips which are separated by a small slot of lower refractive index. Due to the boundary conditions the electric field exhibits a large discontinuity at the interface to the slot. If the separation between the two strips is smaller than the evanescent decay length of the mode, this leads to a highly increased field amplitude in the slot region. This high optical intensity outside of the dielectric strips is utilized for very efficient light-matter interactions [177, 178]. However, the enhanced field in the vicinity of the interface between the slot and the dielectric strip typically leads to a larger propagation loss compared to solid core waveguides due to increased scattering losses at the sidewall roughness [179–181]. In this thesis only a horizontal configuration with two waveguide strips separated by a small air gap is used. An example for such a configuration is shown in Fig. 2.7. The SEM micrograph in (a) shows a slot waveguide fabricated from a 200 nm high Si_3N_4 layer. The two 350 nm wide strips are separated by a 60 nm gap. In such a structure only a single TE mode is supported with its maximal field amplitude located in the slot region. The simulated electrical field of this mode is presented in panel (b) as well as the field strength in (c) along the indicated dashed line. The field amplitude in the slot is much higher compared to the field amplitude in the strips.

2.3. Fabrication Process for Silicon Nitride Circuits

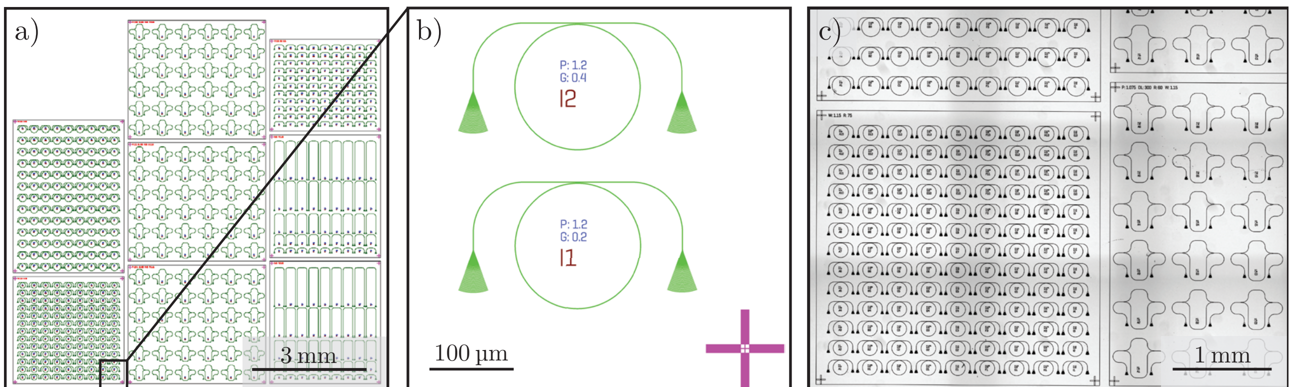

Figure 2.8.: a) Overview of a chip design. b) Enlarged part of the circuit design showing two ring resonators and a global alignment marker used in multi-step lithography processes. c) Optical micrograph of a part of the fabricated circuits featuring ring resonaotrs and MZIs[3].

Integrated circuits for photonics as well as for electronics are commonly fabricated by either electron-beam lithography (EBL) or photolithography [183, 184]. Such lithography processes allow for the fabrication of fine structures down to the nanometer size while at the same time large areas up to wafer-scale size can be processed. Complex designs in terms of the circuit shape and the usage of multiple material layers are realizable by employing several successive lithography steps in combination with etching processes or material deposition. In the photolithography process large areas are exposed simultaneously through a photomask which leads to very short exposure times and therefore low

[3] Image stitching performed by using Fiji [182]

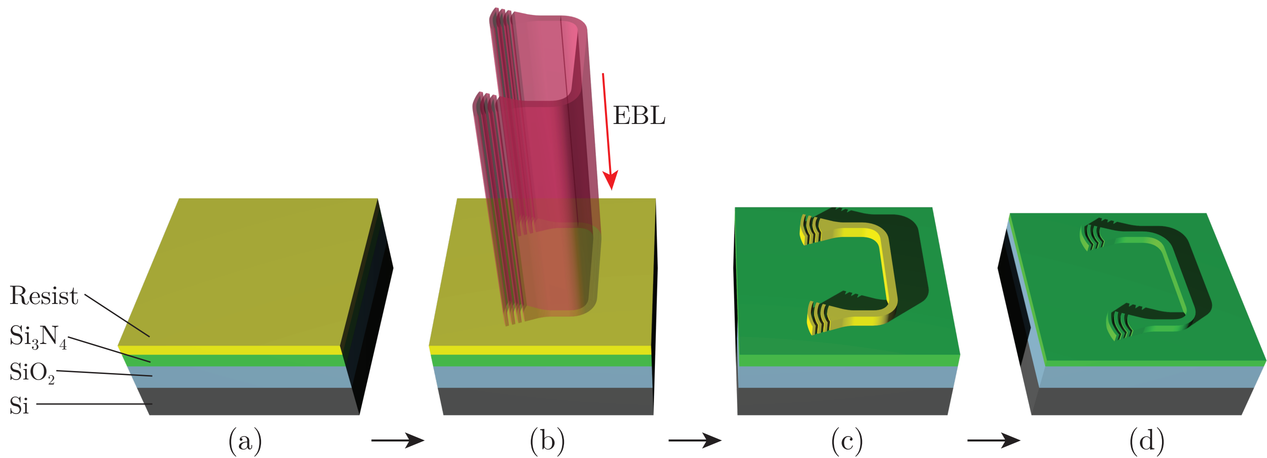

Figure 2.9.: Overview of the basic fabrication steps for Si_3N_4 devices. An EBL resist is spin coated onto the Si_3N_4 / SiO_2 / Si substrate (a). In the EBL step predefined areas of the resist are exposed (b) so that they are insoluble during the chemical development of the resist. Therfore a resist mask is created (c), which is transferred into the substrate via dry etching. After the etching step the resist is removed and the Si_3N_4 circuit is completed (d).

fabrication costs. Thus, this method is preferred for mass production of integrated circuits. However, the photomask itself is typically fabricated by EBL and the minimum feature size is limited by the wavelength of the utilized light. Even if the use of next generation extreme UV light sources for photolithography is considered [185], the spatial resolution using an electron beam for the exposure is usually better [186, 187]. Typical kinetic energies used in EBL vary between 30 and 125 kV, which corresponds to wavelengths of a few pm. The actual resolution is however limited by the chemical properties of the EBL resist and scattering processes of the accelerated electrons in the resist and substrate layers. In contrast to the photolithography process, the exposure in EBL is performed by raster-scanning an electron beam over the desired areas, leading to longer exposure times but enabling maskless lithography with a high resolution.

The circuit design is carried out with a computer-aided design (CAD) software in a Python[4] environment based on the gdsCAD and Shapely packages for the creation of planar geometric objects. An example for such a circuit design is shown in Fig. 2.8 along with a zoom in on one of the ring resonator devices as well as an optical micrograph of the fabricated structures. An overview of the process from the design to the fabricated circuit is shown in Fig. 2.9 for a Si_3N_4 rib waveguide. The Si_3N_4 chip is spin coated with an EBL resist (a). Then the circuit design is transferred into the resist by EBL exposure of the defined areas (b). If a negative tone resist is used, only the exposed parts remain on the chip after the development step (c). Thus, a mask for the subsequent dry etching step is created, which is used to selectively etch the uncovered Si_3N_4 region. Finally, the resist is removed and the desired circuit is obtained (d). In addition to the fabrication explanation in the following sections, a detailed description of all fabrication steps and process parameters including the substrate

[4] Python Software Foundation, Wilmington, DE 19801, USA

preparation is given in App. A.3.

In between the fabrication steps, the resist thickness as well as the device layer thickness during the etching process are monitored in order to ensure consistent fabrication results. This is done via white light reflectometry in two different setups: a Mikropack NanoCalc 2000[5] system at the Institute of Nanotechnology (INT)[6] and a Filmetrics F20 Thin-Film Analyzer[7] system in the Center for Functional Nanostructures (CFN)[8] cleanroom are used. Moreover, EBL methods are used to fabricate complex structures by employing several consecutive lithography steps. This requires careful alignment of the lithography system to existing on-chip structures. Within this work, this is realized by placing alignment crosses on the sample. Large *global* markers are placed in the corners of a chip in order to define a chip coordination system (shown in the corner of the enlarged design picture in Fig. 2.8). If a very precise alignment is needed, additional small *local* markers are placed in close vicinity of the device that should be processed.

2.3.1. Electron-Beam Lithography Systems and Resists

For the lithography process a resist is deposited on a substrate typically via spin coating, which is then exposed in certain areas by an electron beam and subsequently developed in a chemical treatment. Thereby, a mask is created on the substrate which can be either transferred into the substrate via etching or which is used to deposit a new material layer on the substrate that stays within the unmasked areas by using a *lift-off* process in which the mask is dissolved.

EBL resists are classified regarding their behavior when exposed. Within this work the *positive tone* resists ZEP520A[9] and polymethyl methacrylate (PMMA) are used as well as the *negative tone* resists ma-N 2043[10] and hydrogen silesquioxane (HSQ). When a positive resist is exposed by an electron beam, its long molecule chains are broken by energized electrons into small ones and the exposed parts become soluble in a developer. The other way around the initial short chain molecules of negative resists are cross-linked by the electron beam exposure and a developer selectively removes the parts which have not been exposed [188]. For the fabrication of photonic circuits typically negative tone resists are used because a smaller area has to be exposed leading to considerably shorter exposure times compared to positive tone resist. The photonic circuits in Si_3N_4 within this work are in general defined by using the ma-N 2403 resist since it enables the fabrication of fine features down to a size of 50 nm with a low surface roughness [189, 190]. Additionally, an adhesion promoter is applied between the ma-N 2403 resist and the Si_3N_4 substrate. Due to OH-bonds at the Si_3N_4 surface a hydrophilic surface is obtained, which exhibits a poor wetting and adhesion of an unpolaric resist. Adhesion can be

[5] Ocean Optics, Largo, FL 33777, USA
[6] Institute of Nanotechnology, KIT Campus North, Eggenstein-Leopoldshafen, BW 76344, Germany
[7] Filmetrics Inc., San Diego, CA 92121, USA
[8] Center for Functional Nanostructures, KIT Campus South, Karlsruhe, BW 76131, Germany
[9] Zeon Corporation, Chiyoda-ku, Tokyo 100-8246, Japan
[10] Micro resist technology GmbH, Berlin, BE 12555, Germany

enhanced by e. g. using hexamethyldisilazane (HMDS) or titanium-based TI Prime[11], which in both cases results in excellent resist adhesion. A monolayer of TI Prime can be conveniently deposited just by spin coating before the resist is applied. Therefore, this is the method of choice for ma-N 2403 adhesion promotion. Similarly, the adhesion of HSQ is poor on e. g. silicon and diamond surfaces. In this case it cannot be improved by HMDS, TI Prime and also SurPass 3000 and 4000[12]. However, depositing a thin layer of around 5 nm SiO_2 on the substrate results in very good resist adhesion.

The exposures are performed at two EBL systems: a 30 kV Raith e_LiNE system[13] at the INT is mainly used for large patterns like contact pads or cover layers and a 50 kV JEOL JBX-5500ZD[14] at the CFN is used for photonic circuits and fine structures due to a better spatial resolution and very good stitching and alignment procedures[15]. For the EBL exposure of fine structures, especially if they are densely packed or in the vicinity of larger structures, it is important to consider and correct proximity effects in the exposure. Due to forward scattering in the resist and back scattering in the different substrate layers, the area where electrons are deposited is widened. Consequently, parts of a pattern with many surrounding structures are exposed with a higher effective dose than isolated structures or points at the border of large structures [191, 192]. This effect can be compensated by applying a proximity effect correction (PEC). Thereby, the area dose is adjusted over the whole structure, so that a uniform effective dose is achieved for all parts of a pattern independent of their surroundings [193]. The detailed PEC parameters which are used for the different resists and substrates are given in App. A.4.

An important characteristic of the EBL process is the sidewall roughness of the fabricated structures as this greatly influences the attenuation in waveguides. One source for this is the roughness of the etching mask. In order to reduce the surface roughness of the ma-N 2403 resist for Si_3N_4 devices, the sample is heated up after the development step. During this so called *reflow* process, the resist surface flattens and it slightly shrinks at the top surface while the bottom surface stays attached to the Si_3N_4 substrate and does not change size [194]. Here, an optimized reflow process of 110 °C for 2 min on a hotplate is used. If very fine features like the tip of a Y-splitter are included in the circuitry, the reflow temperature is decreased to 100 °C. Hence, a smooth resist surface is obtained which enables high-quality Si_3N_4 waveguides.

2.3.2. Dry Etching

In order to transfer an EBL resist mask into the underlying device layer of a chip, dry or wet etching methods are employed. Within this work, dry etching is used for the structuring of photonic circuits. In such a system a gas mixture is led into an etching chamber where a plasma is started by a radio frequency (RF) field. Due to the potential difference between stage and etching chamber, the ions are

[11] Microchemicals GmbH, Ulm, BW 89079, Germany
[12] DisChem Inc., Ridgway, PA 15853, USA
[13] Raith GmbH, Dortmund, NRW 44263, Germany
[14] JEOL Ltd., Akishima, Tokio 196-8558, Japan
[15] The JEOL EBL system is operated by Silvia Diewald at the Nanostructure Service Laboratory (NSL) within the CFN.

accelerated towards the sample where etching occurs by a combination of a chemical reaction of the plasma with the substrate and physical sputtering [195]. In the process a high etching selectivity of the substrate in contrast to the resist as well as vertical sidewalls of the fabricated photonic structures are desirable. Moreover, surface damage, roughness and contamination have to be minimized in order to obtain high-quality circuits. Therefore, the gas mixture, pressure and power of the etching recipes are optimized regarding the propagation losses of the waveguides.

Within this work two dry etching systems are used. An Oxford 100 Plasmalab inductively coupled plasma (ICP) system at the CFN for mainly chlorine based plasmas is used for etching of e. g. Si and Cr layers and an Oxford 80 Plasmalab[16] reactive ion etching (RIE) system at the INT for flourine based plasmas is used for etching of e. g. Si_3N_4 and diamond layers. For the fabrication of Si_3N_4 devices a CHF_3/O_2-based plasma is used at the RIE. Last, the ma-N 2403 resist is removed in an oxygen plasma. Further details about the etching processes and parameters are given in App. A.5.

2.4. Characterization of Silicon Nitride Integrated Photonic Devices

2.4.1. Measurement Setup

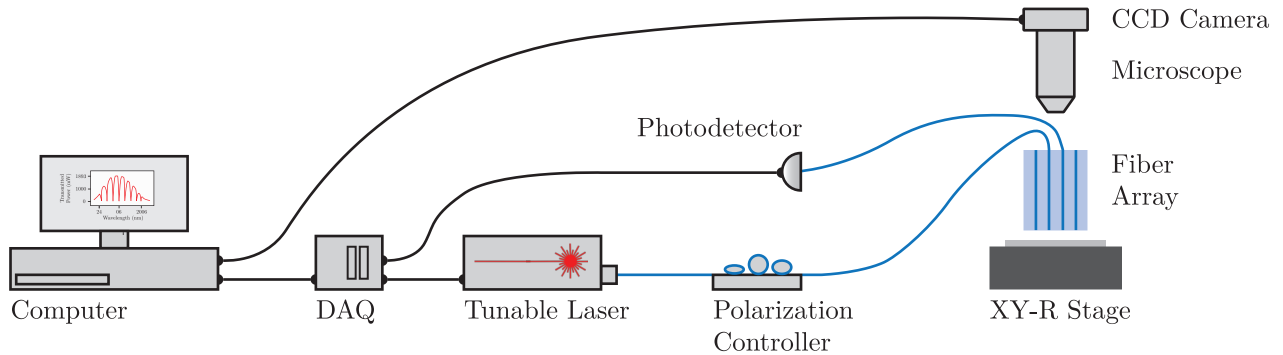

Figure 2.10.: Schematic view of the basic setup used for transmission measurements through on-chip circuits. The sample is aligned to a fiber array and a spectrum is recorded by sweeping a tunable laser while recording the detector signal.

A sketch of the setup used for the recording of transmission spectra of integrated photonic circuits is schematically depicted in Fig. 2.10. A fiber-coupled continuous wave tunable laser source (e.g., from $\lambda = 1500\,\text{nm}$ to $1630\,\text{nm}$) and a low-noise photodetector with variable gain are used to obtain the spectrum of a device by sweeping the laser and simultaneously recording the detector signal. As the light-coupling to the chip via grating couplers (see next section) depends on the polarization, a fiber polarization controller based on stress induced birefringence is placed in line behind the laser. A data acquisition unit (DAQ) is used to trigger the laser and achieve synchronization with the detector

[16] Oxford Instruments, Abingdon, OX13 5QX, United Kingdom

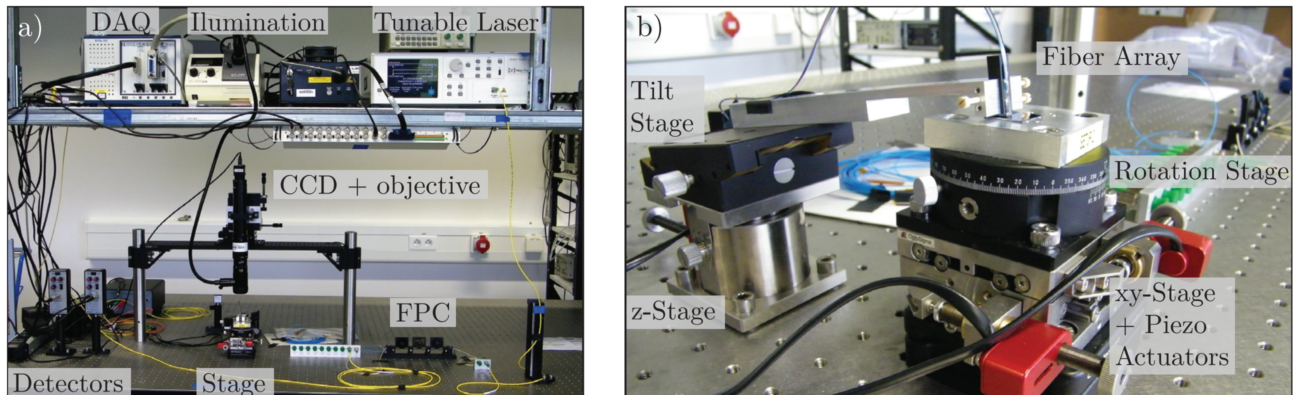

Figure 2.11.: a) Photograph of the measurement setup and a close up (b) of the stage. The sample is placed on a rotation stage on top of a xy-stage. The fiber array is mounted on a tilt stage on top of a z-tower in order to adjust the distance between the fiber array and the sample.

data. It is controlled via Python[17] and LabView[18] programs. A detailed list of the used components is included in App. A.7. For accurate measurements with a high coupling efficiency the integrated devices have to be carefully aligned to the fiber array. For this purpose the sample is placed on a revolving plate and a piezo-driven xy-stage (see Fig. 2.11 b)). The mounted fiber array is fixed to a tilt stage on top of a z-tower, which allows to minimize the distance between the fiber array and the chip without contact. The alignment of the chip to the fiber array is monitored via a CCD-camera with a microscope objective, which is placed above the fiber array (see Fig. 2.11 a)).

The fiber array which is used to access the integrated circuits consists of several fibers aligned in an

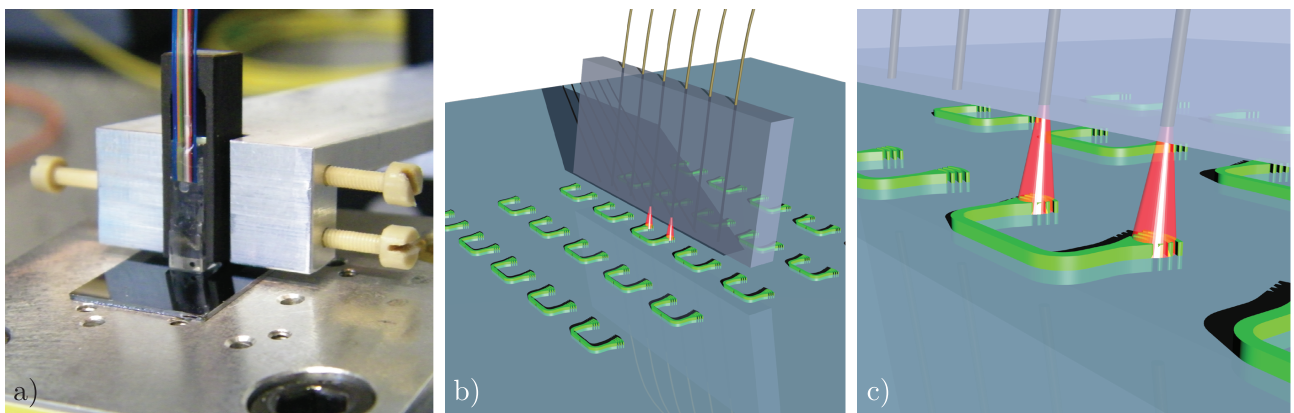

Figure 2.12.: a) Photograph of the fiber array placed very closley above the sample. b) Sketch of the coupling between the fiber array and integrated devices. By moving the sample many devices can be conveniently measured one after the other. c) Light coming form a fiber is coupled into a device and the transmitted signal is collected by a second fiber. The coupler spacing is adjusted to the fiber separation.

[17] Python Software Foundation, Wilmington, DE 19801, USA
[18] National Instruments Corporation, Austin, TX 78759-3504, USA

array with a fixed separation and embedded in a glass cover. Therefore, it enables fast characterization of on-chip devices by conveniently coupling light from an external source to the integrated circuits and by collecting the output from the ciruits [196]. This coupling principle with the help of a fiber array is presented in Fig. 2.12. Panel (a) shows a photograph of the fiber array very closely placed above a photonic chip. As shown in the sketch in panel (b) many devices on a chip can be quickly accessed one after the other by placing the chip on a translational stage in order to align a specific device to the fiber array. In the enlarged picture in panel (c) light coming from one of the fibers is coupled into a device and the transmitted light is collected at the output coupler via a second fiber. Within this work fiber arrays with a fixed fiber-fiber spacing of 250 µm are used exclusively and the distance of the on-chip grating couplers is adjusted accordingly. In order to increase the coupling efficiency, the fiber array is typically tilted by 8° [197]. Thus, in order to enable a very narrow approach of the fiber array to the chip surface while working under the respective tilt angle, its tip is cleaved also under and angle of 8°. Eventually, both the chip position as well as the polarization are optimized in such a way to achieve maximal optical transmission.

2.4.2. Coupling of Light to and from Integrated Circuits

Coupling of light between the external fibers and the integrated photonic circuits is a key element for the characterization of integrated devices throughout this work. Ideally, the coupling scheme should enable highly efficient coupling over a broad spectral range while providing fast and reliable access to any on-chip device. Currently employed approaches do typically not fulfill these requirements simultaneously. One technique is to couple light directly into a waveguide via a cleaved facet. This *butt-coupling* or *end-fire* approach allows for highly efficient coupling over a broadband spectral regime [198–200]. However, careful alignment of an external fiber or objective to the facet and elaborated cleaving and polishing of the facet are required to fully exploit this method. Additionally, only access to waveguides from the side of the chip is gained, which limits the number of on-chip devices. In contrast, out-of plane coupling schemes allow to access arbitrarily placed devices on a chip. On the one hand these include prism-coupling at any chosen waveguide position, which still requires precise adjustment of a prism to a waveguide [201, 202]. On the other hand coupling via a Bragg grating enables fast addressing of many different devices [203–206]. The later method is employed within this work for accessing devices in the visible and NIR regime via *focusing grating couplers*. These are introduced in detail below. A further rather recent coupling method might combine the advantages of butt-coupling with out-of plane coupling schemes. In order to do so, an out-of plane pointing bend is 3D-printed at a tapered end of a waveguide [207], similar to 3D-printed optical interconnects [208, 209]. Thereby, out-of plane coupling via the end facet of the 3D structure is enabled with the possibility to directly shape the facet e. g. as a lense. With ongoing development work, this might present a future coupling alternative.

The advantage of focusing grating couplers is that arbitrarily placed on-chip devices can be accessed

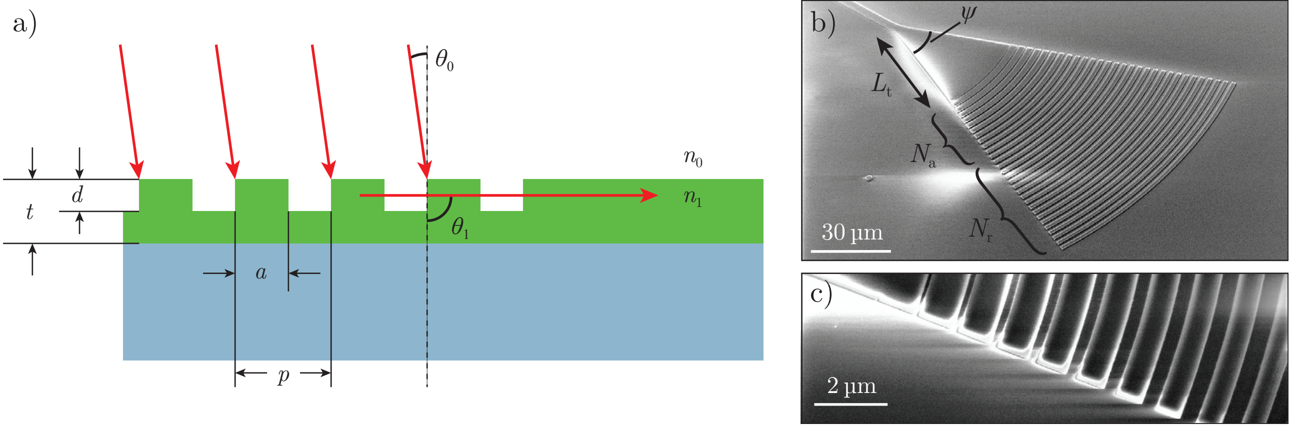

Figure 2.13.: a) Sketch of a grating coupler cross section in a device layer of thickness t and etch depth d where light is diffracted at a grating of period p and fill factor $FF = a/p$ to coupler it into a waveguide. b) SEM micrograph of a coupler with opening angle $\psi = 40°$, taper length $L_t = 16\,\mu m$, $N_r = 20$ regular and $N_a = 10$ apodized gratings. c) Magnified view of the apodization where the FF is increased to the front of the coupler in order to facilitate a smooth transition.

fast and reliably. They exhibit a spectral bandwidth around 30-50 nm and despite their modest coupling efficiency (∼−6 dB per coupler), high powers within the circuits can be achieved by an increased input power. Their basic coupling principle can be explained by the Bragg-diffraction description [132], which is illustrated in Fig. 2.13 a). The device layer of thickness t is etched to a depth d in order to form a grating with period p and width a. In order to excite a guided mode at a certain wavelength by light falling onto the grating under a certain angle, a period that fulfills the Bragg-condition is required:

$$p\left(n_1 \sin(\theta_1) - n_0 \sin(\theta_0)\right) = m\lambda, \quad m \in \mathbb{N}. \tag{2.19}$$

Thereby, the periodic dielectric perturbation accounts for the difference in the propagation constants and enables coupling of light into the waveguide. This condition is also derived by the coupled mode theory in the guided-wave model [130, 210]. Considering the in-plane propagation within waveguides and the effective mode index of the propagation, a direct relationship for the required period at a certain wavelength is obtained:

$$p\left(n_{\text{eff}} - n_0 \sin(\theta_0)\right) = m\lambda, \quad m \in \mathbb{N}. \tag{2.20}$$

However, since this model is technically only valid for weakly disturbed waveguides (e.g., by a surface grating) a rigorous simulation approach is required to get a fully quantitative description. The coupling efficiency is influenced by the overlap of the mode profiles of the incoming and scattered light. An example for a grating coupler is shown in the SEM micrograph in Fig. 2.13 b). With the help of the curved gratings as well as the triangular shape of the coupler the diffracted light from the incoming

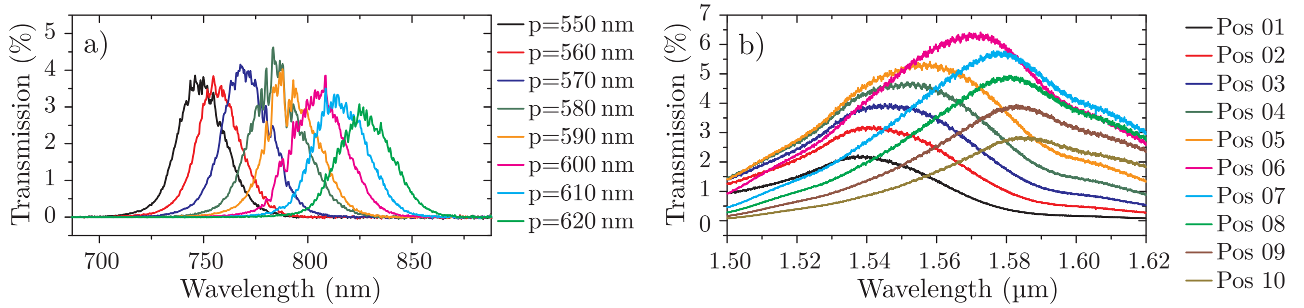

Figure 2.14.: Transmission spectra of a waveguide terminated by two grating couplers. a) By varying the grating period, the transmitted wavelength is shifted. b) In the NIR regime the couplers exhibited a transmission bandwidth (FWHM) around 75 nm. By adjusting the coupler position below a fiber facet, the spectrum can be slightly shifted leading to an increased bandwidth. Each step corresponds to device movement by approximately 1 µm.

beam with a width of approximately 10 µm is focused to the much smaller waveguide width around 1 µm. The mode overlap is also influenced by the fill factor (FF) of the grating. By using *apodized grating couplers* (i.e., an adjustment of the grating at the front of the coupler) a better matching of the mode profiles is achieved as well as a smooth transition between the gratings and the taper to the waveguide [211, 212]. This limits back reflections at the interface and thus suppresses Fabry-Pérot fringes in the device transmission. Within this work the apodization is realized by a linear increase of the FF over ten additional bars at the front of the grating (see Fig. 2.13 c)).

The transmission spectrum through a simple waveguide terminated by two couplers is presented in Fig. 2.14. In panel (a) the shift of the transmitted wavelength by a variation of the grating period in accordance to Eq. (2.20) is shown in the visible wavelength regime. The transmission spectrum exhibits a Gaussian-like shape with a FWHM of up to 75 nm in the NIR regime (b). The different curves in this graph correspond to an optimization of the device position below the fiber array. The transmission decreases when the device is moved from its optimal position indicated by the magenta line (Pos 06). Therefore, careful alignment of the fiber array to the devices is necessary. Additionally, its central peak experiences a slight spectral shift causing a modest increase in the transmission bandwidth by 10 nm. Here, a coupling efficiency of a single grating coupler of typically 20-30 % is reached. More advanced coupler designs have been demonstrated in order to enable a considerably higher coupling efficiency around 80 %, but require a more complex fabrication process [212–214].

Two further characteristics of the grating couplers are displayed in Fig. 2.15. Typically, Si_3N_4 circuits are fabricated on a SiO_2 on Si substrate. Light that is falling onto the grating coupler partly passes the grating, enters the SiO_2 layer and is to a certain degree reflected at the SiO_2 / Si interface (see Fig. 2.15 a)). This leads to an interference effect in the material stack which strongly decreases the coupling efficiency when an interference node is located at the grating. In Fig. 2.15 b) it is shown that this interference effect leads to minima in the transmission spectrum e. g. at a wavelength of 700 nm and 785 nm (marked by the grey shaded areas). In this case a fully etched 200 nm Si_3N_4 layer

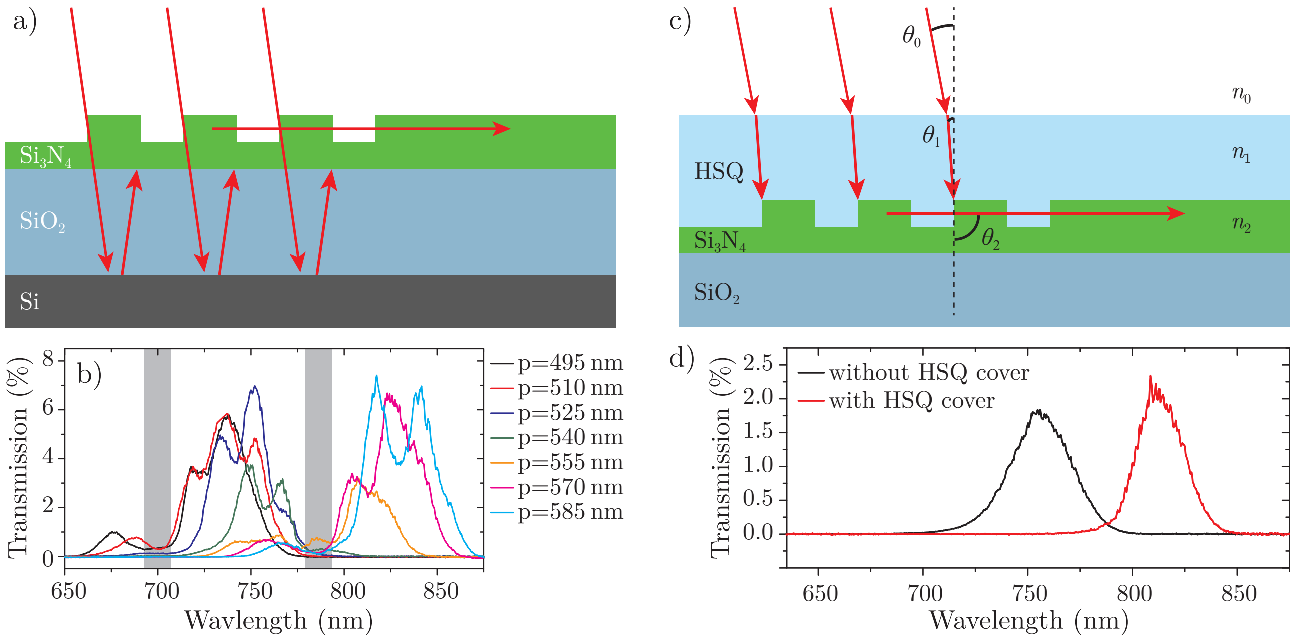

Figure 2.15.: a) Due to reflections at the underlying SiO_2 / Si interface an interference pattern in the material stack is formed. b) If an interference node is located at the grating position, the transmission spectrum exhibits a minimum. c) Sketch of a grating coupler embedded in an HSQ layer. When including the HSQ top surface, the coupling condition does in principle not change. However, typically the beginning of the waveguide is also covered by HSQ, which leads to a shift in the effective mode index and therefore also in the transmission spectrum (d).

on a 2 µm SiO_2 on 525 µm Si substrate is used. In contrast, the spectra in Fig. 2.14 a) are obtained from 150 nm thick Si_3N_4 devices on a sole 500 µm SiO_2 substrate. Thus, the interference layer in the substrate is missing and a consistent transmission is observed for all curves. In the further scope of this work the couplers are often embedded in an HSQ layer as shown in Fig. 2.15 c). Regarding the HSQ surface ($n_0 \sin(\theta_0) = n_1 \sin(\theta_1)$), the Bragg-condition in Eq. (2.20) does in principle not change. However, typically not only the coupler but also the beginning of the waveguide is embedded in the HSQ cover. This causes a shift in the effective index of the guided mode, which in turn leads to a shift in the coupling condition. At a wavelength of around 780 nm a red-shift of the transmission spectrum around 55 nm is expected, which is confirmed by the recorded spectra presented in Fig. 2.15 d).

2.4.3. Quantification of Propagation Losses with High-Q Ring Resonators

As explained in Sec. 2.2.1, in addition to their application in routing, filtering and power enhancement, ring resonators can be conveniently utilized for characterizing the waveguide properties. For devices in the NIR half etched rib waveguides with a width of 1.15 µm and a ring radius of $r = 75$ µm are fabricated from a 340 nm Si_3N_4 layer. An example of such a ring coupled to a bus waveguide of the same dimensions and terminated by two grating couplers is shown in the SEM micrograph in Fig. 2.16 a). Several ring resonators with varying gap g between the ring and bus waveguide are

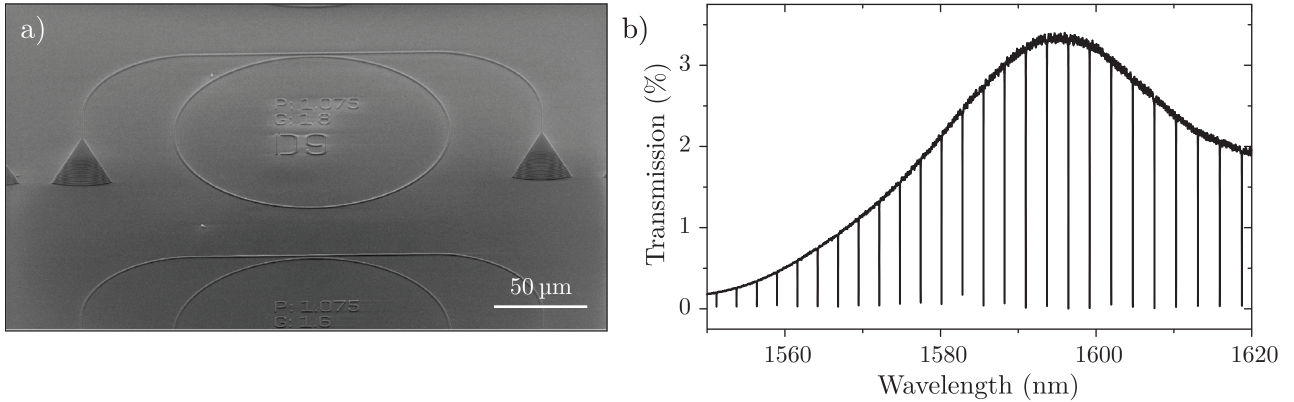

Figure 2.16.: a) SEM micrograph of a ring resonator with a radius of 75 µm coupled to a bus waveguide on the Si_3N_4 platform. b) Transmission spectrum of a ring resonator close to critical coupling. The Gaussian-like envelope is caused by the grating couplers and the dips correspond to the ring resonances.

fabricated and the transmission spectrum is recorded. Fig. 2.16 b) shows the transmission spectrum of a nearly critically coupled ring resonator for a gap size of $g = 1.2$ µm. The Gaussian-like envelope is caused by the grating couplers and the dips correspond to the ring resonances. The ring resonances of this device exhibit an ER of approximately 23 dB.

A typical course of the average quality factor for an increasing gap is shown in Fig. 2.17 along with a zoom-in on high-Q resonances. In panel (a) the quality factor in the NIR regime increases with increasing gap due to a decreased coupling strength until it approaches its intrinsic value for very weakly coupled rings. The standard deviation for the high-Q resonances is quite large whereas it vanishes behind the data points for the rings with a gap below 1.2 µm. This is caused by a decreased ER and therefore lower signal-to-noise ratio (SNR) and by the double structure of high-Q resonances, which makes a fit to the resonance more challenging. An average quality factor of 1.04×10^6 is reached for a very weakly coupled ring corresponding to a propagation loss of 34 dB/m as explained in Sec. 2.2.1. The quality factor is extracted from the data by fitting a Lorentz curve to the resonance as shown in Fig. 2.17 b). Here, a very high-Q resonance is presented, which exhibits a double structure (cf. Sec. 2.2.1). Thus, a fit function containig two Lorentzian curves is used to extract the resonance properties. The quality of the Si_3N_4 photonics circuits, however, can be enhanced by a further fine tuning of the reflow process for the EBL resist (see Sec. 2.3.1). Thereby, a maximal quality factor of 1.6×10^6 is achieved at still only 85 % transmission on resonance for a ring reasonator with a gap of 2.4 µm to the bus waveguide and an radius of 140 µm. This quality factor corresponds to a very low attenuation coefficient of 21 dB/m [101].

Similarly, the circuit quality is determined in the visible spectral regime. For these devices, 180 nm thick Si_3N_4 ridge waveguides with a width of 800 nm and a ring radius of 80 µm are used. A ring resonance along with the Lorentz fit to the resonance is presented in Fig. 2.17 c) for a gap of 0.2 µm to the bus waveguide. The resonance exhibits a quality factor of $Q = 9.6 \times 10^4$ and an ER of 12 dB, which

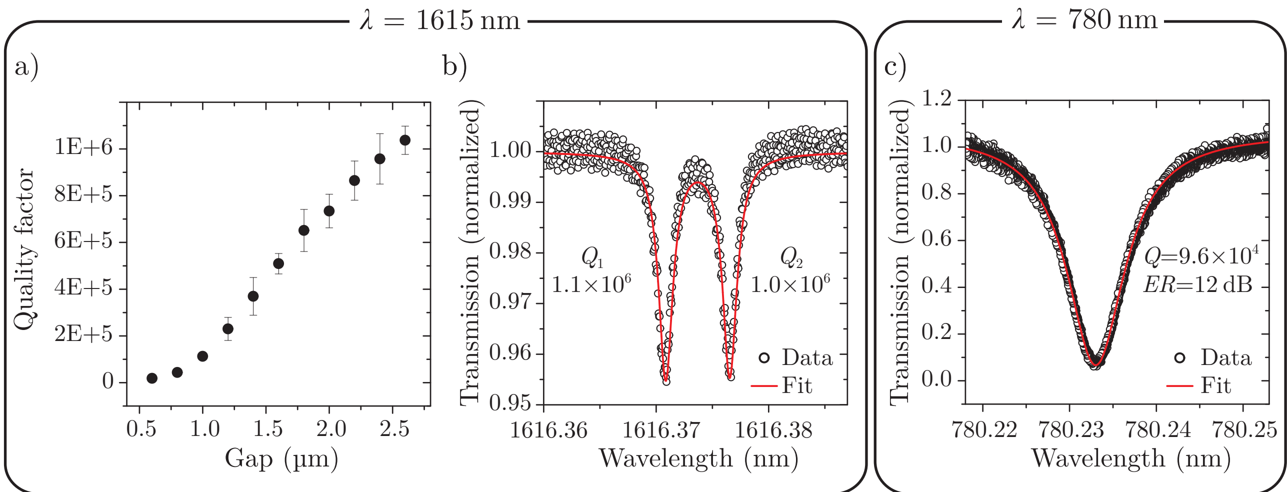

Figure 2.17.: Evaluation of ring resonances in the NIR ((a) and (b)) and in the visible (c) wavelength regime. a) The quality factor increases with increasing gap to the bus waveguide until it is close to the intrinsic value. Each data point corresponds to the average Q obtained from up to ten resonances from a single device. Error bars represent the standard deviation. b) Very high-Q resonances exhibit a double structure due to mode splitting. c) In the visible regime a Q of almost 1×10^5 is reached for a ring resonance with an ER of 12 dB close to critical coupling.

means that it is close to critical coupling. By extracting the attenuation and transmission coefficients from the finesse and ER (cf. App. A.2) an intrinsic propagation loss of 1.1 dB/cm is achieved.

In order to compare the circuit quality to other research results, several factors have to be considered. In the C-band around a wavelength of 1550 nm there are two approaches for high-quality Si_3N_4 devices. Either highly delocalized optical modes within extremely thin films and high aspect ratio waveguides or highly confined modes in thicker films are used. However, all circuits with an extremely low propagation loss require two additional processing steps. On the one hand, by applying a complete SiO_2 cladding, buried waveguides are used to decrease scattering losses caused by the sidewall and surface roughness of the waveguide [215]. On the other hand, an annealing step of the fabricated circuits at typically 1100-1200 °C for several hours is used to minimize the material absorption by a reduction of absorbing hydrogen bonds [216]. An overview of recently published results of Si_3N_4 waveguide and cavity properties is given in Tab. 2.1.

For highly delocalized optical modes a propagation loss of 0.32 dB/m was achieved in an only 40 nm high and 11 µm wide waveguide. The extreme delocalization requires however a very large bending radius of 9.65 mm. Thereby, a ring resonator quality factor of 42×10^6 was realized [219]. Since highly confined modes in Si_3N_4 waveguides are used within this work, a comparison to other waveguides of a similar geometry is more informative. As mentioned above, very high quality factors are only realized by buried waveguides with an additional annealing step. Thereby, a ring resonator quality factor of 7×10^6 with a corresponding propagation loss of 4.2 dB/m was realized [220]. Of particular interest are three publications in which Si_3N_4 circuits without an annealing step are considered, even though

Wavelength	Waveguide dimension	Attenuation coefficient	Cavity type	Quality factor	Bend radius	Annealing	Buried waveguides	Ref.
1550 nm	80 nm × 2.8 µm	2.91 dB/m	Ring	7×10^6	2 mm	Yes	Yes	[217, 218]
1580 nm	40 nm × 11 µm	0.32 dB/m	Ring	42×10^6	9.65 mm	Yes	Yes	[219]
1540 nm	644 nm × 900 nm	6.5 dB/m	Ring	1.5×10^6	20 µm	Yes	Yes	[194]
1555 nm	910 nm × 1.8 µm	4.2 dB/m	Ring	7×10^6	115 µm	Yes	Yes	[220]
1530 nm	400 nm × 8 µm	235 dB/m	Ring	1.5×10^5	60 µm	No	Yes	[221]
1530 nm	400 nm × 8 µm	6 dB/m	Ring	6×10^6	60 µm	Yes	Yes	
1568 nm	400 nm × 8 µm	2 dB/m	Ring	2×10^7	240 µm	Yes	Yes	
1568 nm	300 nm × 3 µm	-	Ring	2.7×10^6	300 µm	No	Yes	[222]
1554 nm	600 nm × 3 µm	2.1 dB/m	Finger-shaped	1.4×10^7	950 µm	Yes	Yes	
1554 nm	900 nm × 2 µm	290 dB/m	Ring	5.2×10^4	100 µm	No	Yes	[223]
1590 nm	**340 nm × 1.15 µm 170 nm rib**	**21 dB/m**	**Ring**	$\mathbf{1.6 \times 10^6}$	**100 µm**	**No**	**No**	**[101]**
660 nm	150 nm × 1.5 µm 4 nm rib	0.5 dB/cm	-	-	2 mm	No	Yes	[224]
632 nm	200 nm slab	0.1 dB/cm	-	-	-	Yes	No	[225]
780 nm	230 nm × 700 nm	1.33 dB/cm	-	-	-	No	No	[226]
532 nm	230 nm × 1 µm	0.1 dB/cm	-	-	-	No	Yes	
655 nm	200 nm height	-	Disk	4×10^6	100 µm	No	No	[227, 228]
780 nm	**180 nm × 800 nm**	**1.1 dB/cm**	**Ring**	$\mathbf{9.6 \times 10^4}$	**80 µm**	**No**	**No**	**-**

Table 2.1.: Waveguide and cavity properties of integrated optical Si_3N_4 circuits for device operation in the visible and NIR regime. Results obtained within this work are printed in bold.

buried waveguides are still used. Thus, a quality factor of 1.5×10^5 was realized for a $r = 60$ µm ring and a propagation loss of 23.5 dB/m was deduced. After an annealing step at 1100 °C, the ring exhibited a quality factor of 6×10^6 and a corresponding propagation loss of 6 dB/m [221]. Also, in Ref. [222] the quality factor of a buried $r = 300$ µm ring could be increased from originally 2.7×10^6 by one order of magnitude through an annealing step at 1200 °C. This underlines the role of the annealing step for extremely high-Q devices. Furthermore, only recently a not annealed ring resonator has been presented with a ring radius of 100 µm, which exhibited a quality factor of 5.2×10^4 and a propagation loss of 290 dB/m [223]. Taking into account that within this work no annealing step for the Si_3N_4 circuits is employed and that the use of buried waveguides would prevent evanescent coupling to other system in the close vicinity of the waveguide, the circuit quality is to our knowledge among the highest reported results. Hence, high quality Si_3N_4 photonic circuits in the C-band can be fabricated, which enable very good device performances.

In the visible regime for a wavelength around 530-780 nm a propagation loss of 0.5-3 dB/cm was achieved in typically 150-200 nm high Si_3N_4 waveguides. By using a cladding around the waveguide and a tiny etch depth of only 4 nm, a propagation loss of 0.5 dB/cm has been reported [224]. However, this requires a very large bend radius above 2 mm. Furthermore, by using a non-annealed waveguide without a cladding and a size of 230 nm × 700 nm at a wavelength of 780 nm a propagation loss of

1.33 dB/cm was achieved [226]. Additionally, in order to employ high-Q resonators in the visible regime, microdisks are typically used with the advantage that, compared to ring resonators, there is no inner sidewall which might cause scattering losses. Hence, a quality factor of up to 4×10^6 was reached in such microdisks at a wavelength of 655 nm [227, 228].

2.4.4. Mach-Zehnder Interferometers

In order to use MZIs as phase or attenuation sensitive devices, they should exhibit very good properties in terms of balanced splitting of the optical mode in the two arms and low intrinsic propagation losses in the arms. In order to evaluate these properties the ER of the spectrum is considered as explained in Sec. 2.2.2. In Fig. 2.18 a) the optical micrograph shows some MZIs fabricated on the half etched 340 nm Si_3N_4 platform for device operation in the NIR regime. The corresponding transmission spectrum is presented in Fig. 2.18 b). The FSR of 4.2 nm between the interference fringes is caused by the path difference of 300 µm between the two MZI arms. In order to obtain MZIs of high quality, the splitter geometry is varied and an optimal length of 30 µm for a width of 5 µm is found. Furthermore, the reflow temperature is reduced from 110 °C to 100 °C in order to avoid damaging the fine tip of the Y-splitter. This way the spectrum exhibits an ER exceeding 40 dB, which covers the full spectral range of the grating couplers.

By using Eq. (2.18) the splitting ratio of the Y-splitter can be deduced, when perfect combination of the two MZI arms is assumed. Considering loss-free waveguides an ER of 40 dB corresponds to a splitting ratio of $^{50.5}/_{49.5}$ in the Y-splitter. The introduction of a propagation loss of 37 dB/m (see previous section) in the waveguides and the path difference of 300 µm between the arms leads to an uncertainty in the splitting ration of ±0.1 %. This is due to the possibility that the slightly larger part of the divided mode is directed into either the longer or the shorter arm of the MZI. In summary, the fabrication methods enable the implementation of very balanced Y-splitters and the realization of very high quality MZIs, which are well suited for detecting small phase shifts of the waveguide mode in one of the arms.

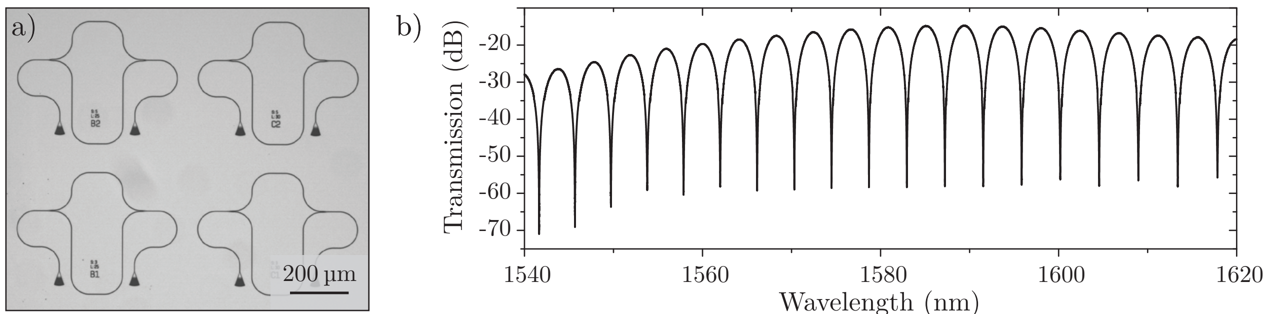

Figure 2.18.: a) Optical micrograph of MZIs on the Si_3N_4 platform. The path difference of 300 µm causes a FSR of 4.2 nm as shown in the transmission spectrum shown in (b). With an optimized splitter geometry and reflow temperature a very good ER of up to 40 dB is obtained over a rather broad spectral regime.

Chapter 3.

3 Near-Field Coupling to a Collective System: Atom Clad Waveguides

The coupling of a waveguide mode to a thermal rubidium vapor via the evanescent field is presented in this chapter. First, the basic rubidium properties with regard to the light-atom interaction and possible applications of this interaction implemented in integrated photonic devices are discussed. The modifications and fabrication of the Si_3N_4 photonics platform in order to meet the specific requirements for the atom vapor integration are addressed next. Moreover, the susceptibility of the atom vapor surrounding a waveguide is included in the simulations of the supported modes. Finally, the measurement setup utilized for the atom vapor integration is described and the experimental results obtained from various photonic devices are discussed. They are also compared to theoretical predictions from numerical simulations. This project was realized in cooperation with Ralf Ritter in the group of Prof. Dr. Tilman Pfau at the University of Stuttgart[1]. The measurements of the device response in presence of the atom vapor were performed by Ritter. Furthermore, the results of this project have been published in Ref. [229–231].

3.1. Properties of a Rubidium Atom Vapor

Rubidium (Rb) belongs to the alkali metal group of the periodic table. The elements of this group exhibit very similar characteristic properties, like a high reactivity and a weak metallic bond. This is mainly caused by a single electron in an s-orbital as their outermost electron shell. Naturally occurring rubidium comprises two isotopes: ^{85}Rb with a relative abundance of 72.2 % and ^{87}Rb with a relative abundance of 27.8 %. While the ^{85}Rb isotope is stable, ^{87}Rb is weakly radioactive, decaying via β^- to ^{87}Sr with a half-life of 4.9×10^{10} years. Rubidium is (under standard conditions) a solid, very soft metal with a low melting temperature of 39 °C and can be easily vaporized [232, 233]. Most of the optical applications which utilize rubidium atoms are based on specific electron transitions between

[1] 5th Institute of Physics, University of Stuttgart, Stuttgart, BW 70569, Germany

energy levels of the term diagram. Within this thesis the coupling to the atom vapor is focused on the D2 line transition between the $5^2S_{1/2}$ and $5^2P_{3/2}$ states[2]. Thus, the term diagram of rubidium is briefly explained in the following, based on Ref. [234–236].

The spectra of alkali atoms are similar to the simple spectra of one-electron atoms. This is caused by their single weakly bound outer electron, the so-called *valence electron*. All other electrons are in closed shells and these electrons are as a rule more strongly bound and closer to the nucleus than the valence electron. Also closed shells are spherically symmetric and their total angular momentum vanishes. Thus, the alkali atoms can be described by a picture in which the valence electron is located at a rather large distance r from the center and moves in the electrostatic field of the nucleus, which is for the most part screened by the electrons in the closed shells. In this way, the many-body problem can be reduced to a single-particle system closely related to the single-electron atom. In contrast to the single-electron atom, an effective potential $V_{\text{eff}}(r)$ is used for the valence electron. At small electron-nucleus distances the effective potential approaches the unscreened nuclear potential $\sim{-Ze^2}/r$ (with the atomic number Z), whilst the nucleus is screened by Z-1 electrons in the closed shells for large distances resulting in a potential $\sim{-e^2}/r$ as for a single unit of nuclear charge. The shape of this effective potential is illustrated in Fig. 3.1 a) as a transition between the two extreme cases. The potential is not anymore proportional to $1/\mathrm{r}$ and thus, contrary to e. g. the hydrogen atom, the l-degeneracy for the orbital angular momentum l is lifted.

In order to obtain a precise picture of the term diagram further corrections to the energy levels have to be considered. In the *fine structure* the spin-orbit interaction is considered. The energy levels are corrected by $-\vec{\mu}_S\vec{B}_L$, the relative orientation of the magnetic moment associated with the spin $\vec{S}$ in the magnetic field induced by the orbital angular momentum $\vec{L}$. This is described by the total angular momentum $\vec{J} = \vec{L} + \vec{S}$ with its magnitude J in the interval $|L - S| \leqslant J \leqslant |L + S|$. Within the fine structure relativistic effects are also taken into account. This is the correction of the kinetic energy according to the special relativity and of the potential energy by the *Darwin term* due to the uncertainty in the electron position. The total effect of the fine structure is a correction of the energy levels, which only depends on the principal quantum number n and the total angular momentum number J. An additional correction of the energy levels is caused by QED effects. Vacuum fluctuations influence the interaction strength of the electron with the potential of the nucleus. This is called the *Lamb shift*.

The energy levels of the term diagram are further splitted by the *hyperfine structure*. The atomic nucleus possesses a mechanical angular momentum, also called nuclear spin $\vec{I}$. Connected with the angular momentum is a magnetic momentum $\vec{\mu}_I$, which interacts with the magnetic field at the site of the nucleus induced by the electron angular momentum $\vec{J}$. Similar to the fine structure this leads to an additional magnetic energy of $-\vec{\mu}_I\vec{B}_J$. Thus, a new total angular momentum $\vec{F} = \vec{J} + \vec{I}$ is introduced

[2] The notation of the electron states corresponds to $n^{2S+1}L_J$, where n is the principal quantum number, S is the spin quantum number, L is the orbital angular momentum quantum number, which follows the numbering S, P, D, F, G for $L = 0, 1, 2, 3, 4$, and J is the total angular momentum quantum number

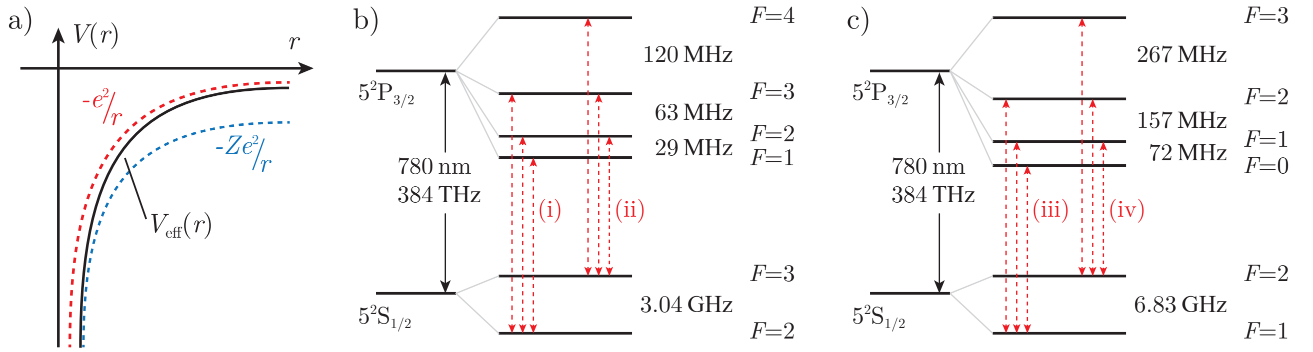

Figure 3.1.: a) The effective potential $V_{\text{eff}}(r)$ experienced by the valence electron as a transition between the unscreened potential of the nucleus at close distances (indicated in blue) and the potential which is screened by Z-1 electrons at large distances (indicated in red). The hyperfine structure of the states contributing to the D2 line are presented for Rb^{85} in (b) and Rb^{87} in (c) including the energy differences between the levels. The red dashed arrows indicate the optical transitions of the D2 line. Visual spacing between the levels are not to scale. Precise data on energy levels can be found in [237–242]

.

with its quantum number F taking the values $|J-I| \leqslant F \leqslant |J+I|$. In the case of rubidium the nuclear spin is $I = 3/2$ for Rb^{87} and $I = 5/2$ for Rb^{85}. For the $5^2S_{1/2}$ ground state of the D2 transition J is $1/2$ and thus, $F = 1,2$ for Rb^{87} ($F = 2,3$ for Rb^{85}), while $J = 3/2$ for the $5^2P_{3/2}$ excited state and $F = 0,1,2,3$ ($F = 1,2,3,4$ for Rb^{85}).

The term diagram hyperfine structure of the states contributing to the D2 line of rubidium are depicted in Fig. 3.1 b) and c), where the energy splitting according to the F-states is also indicated. These states are further degenerated with respect to the z-component of F (labeled by m_F) by a degree of $2F+1$. The red dashed lines indicate the optical transitions contributing to the D2 line. According to the selection rule the change in the total angular momentum is $\Delta F = 0, \pm 1$. Within these lines, the transitions between the m_F states depend on the polarization. Linear polarized light causes π transitions with $\Delta m_F = 0$, while circular polarized light causes $\sigma^{\pm}$ transitions with $\Delta m_F = \pm 1$. As shown in the term diagram, the energy splitting between the levels of the ground state is much larger compared to the levels of the excited state. Thus, the transitions from a single ground state level to the exited states is generally experienced as a single broad line in the spectrum. In this way, there are typically four peaks (or dips) visible in the D2 line spectrum, which correspond to the transitions from the Rb^{85} $S_{1/2}$ $F = 2$ (labeled as (i)), $F = 3$ (ii) and Rb^{87} $S_{1/2}$ $F = 1$ (iii), $F = 2$ (iv) to the $P_{3/2}$ states.

3.2. Atom-Light Interaction in Integrated Photonics

Interfacing atomic gases with nanophotonic devices has the potential to miniaturize and incorporate applications based on atom-light interactions, such as referencing, sensing, routing and switching as

well as nonlinear optical systems. For ultra precise measurements e. g. in metrology [81–83] and for strong atom-photon coupling in cavity QED [87, 243, 244] typically ultra cold atoms have to be used. For example, in atomic clocks the frequency of electronic transitions of atoms is used as a feedback control for an electronic oscillator [80, 245, 246]. Further exceptional applications are realized by the use of *Rydberg atoms*, where one of the atom's electrons is excited into very high, very closely spaced energy states. This for example enables a *Rydberg blockade*, where an excitation of such an atom in a cavity by a first photon causes a shift in the energy levels and blocks the transmission of a second photon [247]. Furthermore, dipolar interaction between Rydberg atoms have been utilized for the realization of a Rydberg blockade between two atoms seperated by a large distance of up to 10 µm [248, 249]. Such atom-based controlled quantum dynamic procedures might act as a basic tool in quantum information precessing networks with neutral atoms [250–255]. Regarding the integration of the atom-light interaction, the strong coupling regime has been explored by coupling of cold atoms to nanophotonic cavities [84, 85] and photonic crystal waveguides [86]. However, ultra cold atom experiments usually require rather large apparatus. While progress on the miniaturization of such devices has been reported [83, 256], their scaling and handling with integrated photonic networks remains challenging.

Although using thermal atomic vapors offers less precision and control, the low technical complexity and potential for miniaturization enables their integration with scalable nanophotonic networks. The miniaturization of thermal atomic vapor based devices has been realized by utilizing small vapor cells e. g. in magnetometry [257–259], spectroscopy [260] or atomic clocks [261, 262]. For the coupling of an atom vapor to confined light fields several approaches exist such as tapered nanofibers [263–265], hollow core fibers [266–268], and integrated hollow waveguides (anti-resonant reflecting optical waveguides (ARROWs)) [94, 269, 270]. Here, we employ solid core integrated waveguides for the atom-light interaction [90, 95, 229], which offer the advantage of a rather simple fabrication of complex circuits. The atom-light interaction based on guided light modes benefits from a very strong optical field confined in a small volume. The sensitivity is further increased by a possible long interaction length along the waveguide.

On-chip atomic spectroscopy is the most straightforward application of interfacing atoms with integrated circuits [94], which can also be transfered to sensing schemes beyond atomic vapors. This is closely related to exploiting the electron transitions of the atoms as an on-chip frequency standard for photonic applications [271]. For a further increase in referencing precision, Doppler free schemes based on counter-propagating beams might be introduced also for on-chip circuits [90, 272].

The integration of an atom vapor also enables the use of various nonlinear effects for photonic applications. This includes the realization of slow light on a chip [273], phase switching [274], as well as the opening of a transparency window in an electron transition [273], which might satisfy the need for fast all-optical modulation and switching in information processing circuits. The opening of such a transparency window for all-optical switching at low beam powers [88] is based on electromagnetically induced transparency (EIT) [275, 276]. This scheme utilizes a three level system with two allowed

transitions, where a pump beam is tuned to one of the transitions and the probe beam to the other. Absorption of the probe is caused either by a direct transition or via a combination of both transitions. The probability amplitudes for the two paths interfere destructively and cause a transparency window in the center of the absorption line. A V-type three level scheme is for example provided by the combination of the D2 ($5^2S_{1/2}$ to $5^2P_{3/2}$, 780 nm) and D1 ($5^2S_{1/2}$ and $5^2P_{1/2}$, 795 nm) transitions in rubidium. In contrast, the opening of a transparency window at higher beam powers in the strong coupling regime is based on the Autler-Townes effect and can be exploited for all-optical modulation [90]. This behavior is the AC equivalent of the Stark effect when the field is tuned in resonance to an electron transition frequency. It is caused by an effective coherence of the third transition which develops as a result of the coherent driving of the two allowed transitions [277, 278].

As a further nonlinear effect two photon absorption in combination with a nanophotonic cavity can be employed for all-optical modulation or routing applications [91]. For example, the rubidium two photon transition $5^2S_{1/2} \rightarrow 5^2P_{3/2} \rightarrow 4^3D_{3/2}$, consisting of the D2 line at 780 nm followed by a transition at 1529 nm, is used in such schemes. When a cavity, e. g. a ring resonator, tuned to the second transition and exposed to a rubidium vapor is irradiated by light corresponding to the D2 transition, an absorbing channel is enabled at its resonance wavelength due to electrons inhabiting the $5^2P_{3/2}$ sate. By turning the absorbing channel on and off, the propagation of light tuned to the ring resonance is switched between a through and a drop port due to the Zeno effect [279–281]. This can be further extended by introducing atom-light interactions in complex ring resonator arrays, in which routing of light along its edge states has been realized [93]. In such a network the introduction of a dissipation channel at a certain location leads to an all-optical variation of the light routing. It has been further proposed to introduce strong photon-photon interactions mediated by for example atoms in these resonator arrays [92].

Here, we study the integration of a thermal atomic rubidium vapor with several integrated photonic devices based on solid core Si_3N_4 waveguides. Linear spectroscopic measurements with basic waveguides are employed for the evaluation of the interaction strength. Additionally, the phase change induced in the waveguide mode by the atoms at the electron transition is extracted via the response of Mach-Zehnder interferometers. As a basic step towards all-optical modulation and routing the response of ring resonators exposed to the atom vapor is studied. Furthermore, slot waveguides are introduced as a possibility for an enhancement of the interaction strength.

3.3. Fabrication Adaption for Silicon Nitride Devices Coupled to an Atom Vapor

In order to utilize the high quality Si_3N_4 platform introduced in Chap. 2 some adaptions are made for meeting the requirements of the atom vapor integration. First of all, for the light-atom interaction a chip is mounted on the side of a vapor chamber or cell with its surface, which contains the nanophotonic circuits, on the inside of the chamber. Thus, there is no direct access to the circuits from the top of the

grating couplers, as typically used in our measurement setup (see Sec. 2.4.1). In order to couple light to and from the integrated circuits, a transparent substrate is used instead of silicon and a free space laser beam is focused from the outside of the vapor chamber through the substrate onto a grating coupler. However, a considerable part of the beam passes through the photonic layer and enters the chamber where it excites the atoms leading to a strong unwanted background fluorescence. A silica spacer is therefore deposited on the grating couplers with a subsequent metalization step on top of the spacer. This effectively blocks the beam from entering the chamber and additionally increases the efficiency of the grating coupler as it reflects the beam. This is further discussed in Sec. 3.6.1. The silica spacer is additionally utilized for covering all parts of the circuit which should not be exposed to the atom vapor. Thereby, the interaction region is well defined.

Two different platforms are used for interfacing rubidium atoms with nanophotonic circuits. These two platforms are presented in Fig. 3.2 a)-c). The first one consists of a thick silica window for vacuum chambers, onto which a 180 nm Si_3N_4 layer was deposited. After structuring the circuits this window can readily be mounted into a custom made flange via a metal seal and connected to an ultra-high vacuum (UHV) chamber. The drawback of this method is that the vacuum chamber can be hardly moved and thus, for accessing different on-chip devices or for varying the input beam angle the laser beam alignment and focal spot have to be readjusted. As a second generation platform a Si_3N_4 on borosilicate glass (BSG) substrate is used[3]. After the device fabrication the chip is bonded to a vapor cell with a rubidium reservoir. Due to its small size, this system offers an easier temperature control of the atom vapor inside as well as a high flexibility in terms of the sample positioning by simply moving the cell itself. The required fabrication steps for both platforms are discussed in the following sections. A precise description of all steps and process parameters is given in App. A.3.2 and A.3.3.

3.3.1. Silica Window Substrate for a Vacuum Chamber

The silica window for a vacuum chamber requires specific precautions for the spin coating and EBL steps due to its dimensions (4 mm thick, 3.8 cm diameter). A picture of a structured vacuum window is shown in Fig. 3.2 a), where mainly the metal mirrors are visible in the center of the sample. The available stage adapters of the JEOL EBL system do not allow for samples of this size and therefore the e_LiNE system is used, even though it suffers from a lower precision when a large pattern, which is stretched over several write fields of the system, is exposed. In order to minimize the effect of misaligned write fields, the EBL resist is switched from the negative tone ma-N 2403 to the positive tone ZEP 520A resist for structuring the photonic circuits. As the transparent substrate is nonconductive, an additional electrically conductive layer of Espacer 300Z[4] is spin coated to avoid charging effects during the EBL exposure. Otherwise, the charging of the sample surface would lead to a strong deflection of the electron beam during the exposure. A custom made clamp is used to ensure an

[3] The Si_3N_4 layer for both platforms was deposited using a PECVD process by iX-factory; now Micronit GmbH, Dortmund, NRW 44263, Germany.
[4] Showa Denko K. K., Minato-ku, Tokyo 105-8518, Japan

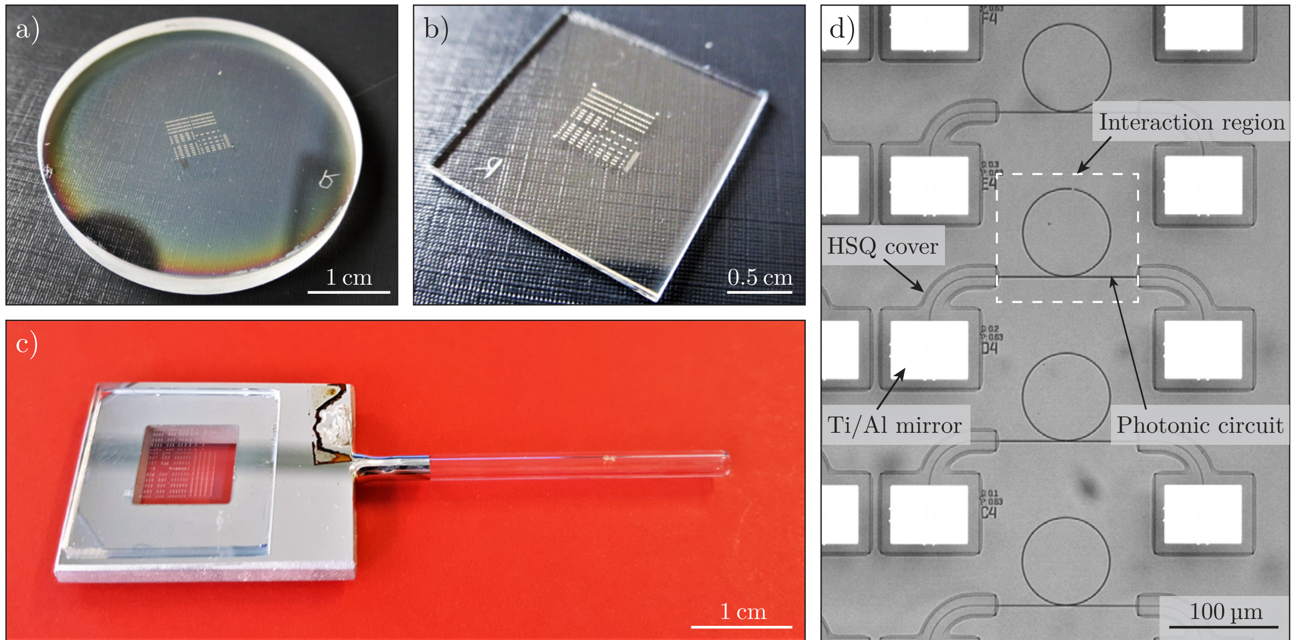

Figure 3.2.: a) Picture of a structured vacuum window that can be mounted to the side of a UHV chamber. b) A structured BSG substrate, which can be bonded to a small glass vapor cell as shown in (c). On the right side of the cell a glass tube is attached as a Rb reservoir. d) Optical micrograph of ring resonators coupled to a bus waveguide. The grating coupler and parts of the waveguide are covered by an HSQ layer, leaving only a part of the photonic circuit bare, so that these parts (marked by the dashed rectangle) interact with a surrounding atom vapor. On top of the HSQ cover at the position of the grating couplers there are Ti/Al mirrors placed.

electrical contact from the sample surface to the EBL stage. This procedure is used for every EBL exposure with transparent substrates. After the exposure the Espacer layer is removed by rinsing the sample with water before the resist is developed. Subsequently, the photonic structures are transferred into the Si_3N_4 layer via standard dry etching.

In a second EBL process HSQ FOX-15[5] is used to create an approximately 700 nm thick spacer on the grating couplers and all parts of the photonic circuits, which should be protected from the atom vapor. In a third EBL exposure a PMMA mask is created for the metalization step. Molecular beam epitaxy (MBE) deposition of a 5 nm Ti layer followed by a 100 nm Al layer with a subsequent lift-off process of the PMMA mask in acetone is used for the fabrication of the metal mirrors on top of the HSQ spacer above the grating couplers. The alignment of the three EBL steps is ensured by the use of large global markers around the pattern, which are fabricated in the first step alongside the photonic structures. The placement of the HSQ spacer and the metal mirrors is exemplarily shown in Fig. 3.2 d) for some ring resonator devices.

[5] Dow Chemical Company, Midland, MI 48667, USA

3.3.2. Borosilicate Glass Substrate for a Vapor Cell

The second generation of samples are used for the assembly of small vapor cells via anodic bonding. They are fabricated from a 180 nm Si_3N_4 layer on a 1.1 mm thick transparent BSG substrate. A structured sample is depicted in Fig. 3.2 b). They are cut in 20x20 mm^2 pieces by using the wafer saw and the JEOL system is used for all EBL exposures. An important step for the vapor cell fabrication is the bonding process of the photonic sample to the cell. This can be realized via anodic bonding between a Si_3N_4 layer and a BSG cell [282–284]. By using a positive tone EBL resist only a small area around the structures is exposed and subsequently etched. Thereby, the Si_3N_4 layer stays on the remaining sample area and is used for the bonding process. However, quite often after dry etching of the photonic circuits there are resist leftovers at the edge of the sample that are hard to remove due to the heat development during etching, which impede the bonding process. Thus, direct bonding of the BSG substrate to an aluminum layer on the frame of the cell is employed via alumina (Al_2O_3) formation [285–287]. For realizing this procedure, the negative tone ma-N 2403 resist is used, resulting in the removal of the Si_3N_4 layer everywhere on the BSG substrate apart from the photonic structures. This results in an excellent bond for the vapor cell fabrication[6]. The complete vapor cell with bonded chip and tube for the Rb reservoir is shown in Fig. 3.2 c).

The fabrication of the spacer and the metal layer on top of the grating couplers follows the description in the last section. Only an additional cleaning procedure in piranha solution is introduced directly after the fabrication step of the photonic structures in order to remove any small resist residuals on the waveguides. For the first generation of samples described in the previous section, an accumulation of the alkali atoms [288] on the sample surface is observed, which leads to a deterioration of the photonic circuits within days up to weeks of usage. In order to protect the photonic Si_3N_4 circuits on the BSG substrate against chemical deterioration by the aggressive alkali atoms, the structures are covered in a final step with an approximately 7 nm thick alumina coating via atomic layer deposition (ALD). Since a bare BSG substrate is required for the bonding process, a frame along the edge of the sample is covered during the ALD procedure. With such a alumina protection coating the devices are usable for several months without further degradation of their performance.

3.4. Simulations of Atom Clad Waveguides

The response of nanophotonic circuits in the presence of rubidium atoms at the D2 transition is simulated based on the calculation of the effective index of refraction of the atom vapor. Thereby, the dynamics of the transmission spectrum obtained in various configurations can be studied, the experimental results can be verified and predictions for further devices can be made. The complex refractive index of the atom vapor $\tilde{n}_{\mathrm{Rb}} = n_{\mathrm{Rb}} + i n'_{\mathrm{Rb}}$ is calculated from the effective susceptibility χ of the atoms via $\tilde{n}_{\mathrm{Rb}} = \sqrt{1+\chi}$.

[6] The bonding step of the sample to the cell was done by the glassblowing workshop at the University of Stuttgart.

The following description of the derivation for the susceptibility is adopted from Ref. [289, 290]. It is based on the method developed for attenuated total internal reflection, where the reflection of light from an interface between a dielectric and an atom vapor is investigated [291–294]. In this method the optical Bloch equations are solved with a boundary condition of total dephasing when an atom hits the interface. Additionally, the dynamics of the atom vapor with respect to the waveguide mode have to be considered. Outside of the waveguide the field decays exponentially in the transverse direction. Thus, the interaction time of the atoms surrounding the waveguide and the optical field is finite and typically lower than the lifetime of the excited state. This results in the so called *transit-time broadening* of the spectrum. Also the movement of the atoms along the beam direction has to be considered. As the propagation constant of the waveguide mode is larger than for a free space beam, this leads to an *enhanced Doppler broadening*. It can be shown that the first order susceptibility of the atom vapor is given by [289]:

$$\chi(\Delta) = \frac{N}{\hbar\epsilon_0}\sum_i A_i \sum_{F,F'} \frac{C^2_{F,F'}d^2}{2(2I+1)} \int_{-\infty}^{\infty} dv_z \int_0^{\infty} dv_t \frac{2M(v_z,v_t)}{-2\pi\Delta - k_z v_z - i(2\pi G/2 - i k_t v_t)}, \tag{3.1}$$

where N is the atom density, ϵ_0 the vacuum permittivity, and $\hbar$ the reduced Planck constant. The first sum over i runs over the two rubidium isotopes Rb^{85} and Rb^{87} with the respective occupation ratio A_i according to their natural abundance. The second sum runs over all considered transitions from a state with total angular momentum F to an excited state with F'. The transition strength of a specific hyperfine transition is denoted with $C^2_{F,F'}d^2$, where $C^2_{F,F'} = \sum c^2_{m_F,m'_F}$ is the sum of the relative transition strengths of each Zeeman transition (here only π transitions with $\Delta m_F = 0$ are considered due to linear polarized light) and d is the reduced matrix element in $\langle F, m_F \| e\vec{r} \| F', m'_F\rangle = c_{m_F,m'_F}\langle L \| e\vec{r} \| L'\rangle = c_{m_F,m'_F} d$. The factor $2(2I+1)$ accounts for the degeneracy of the ground state of the particular isotope with the spin I of the nucleus. It is assumed that the population is evenly distributed among those ground-state Zeeman sublevels. The atomic velocities along the beam propagation direction z and the transverse direction t are v_z and v_t, M is the Maxwell-Boltzmann velocity distribution for each direction, k_z and k_t represent the propagation constants in beam and transverse direction, G is the natural FWHM linewidth, and Δ is the frequency detuning from the specific transition frequency. The imaginary part of Eq. (3.1) is related to the absorption coefficient and takes the form of a Voigt function as it basically is the convolution of a Lorentzian and a Gaussian function.

The equation for χ is valid in the case of a low vapor density, as used in the experiments here. For its calculation the atom density, which is equivalent to the temperature, as well as the propagation constant in the direction along the beam and in transverse direction is required. In terms of the waveguide properties (see Sec. 2.1.2), this is the effective propagation constant of the mode $\beta = k \cdot n_{\text{eff}}$ along the propagation direction and the inverse evanescent decay length perpendicular to the propagation for the transverse direction. In order to extract these values, the mode supported

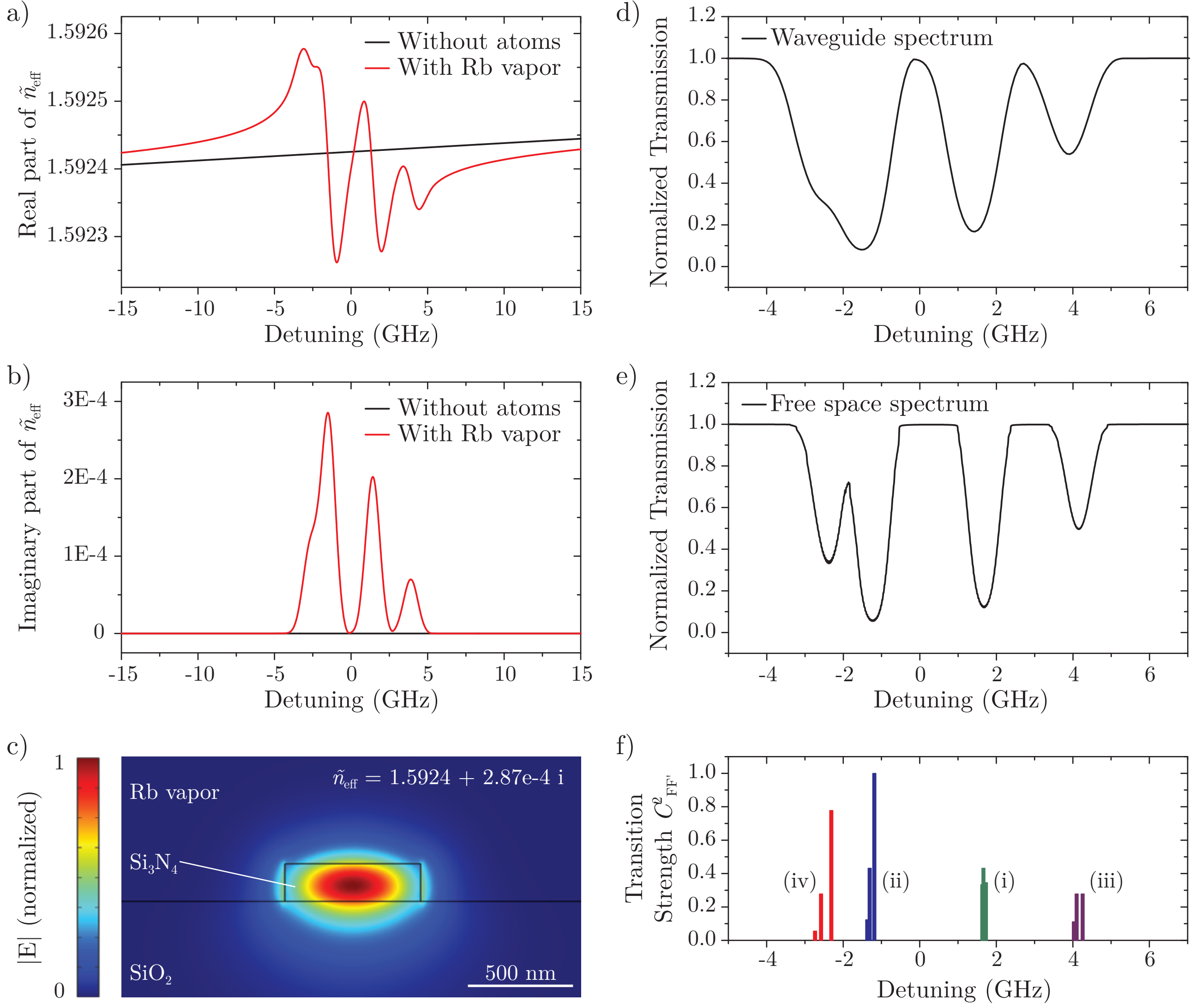

Figure 3.3.: Simulation results of an atom clad Si_3N_4 waveguide. The real part (a) and the imaginary part (b) of the effective mode index is shown when scanning over the rubidium D2 line (red line) and is compared to its value without the presence of the atoms (black line). A detuning of zero corresponds to the center of the D2 line at $\nu_c = 384.23\,\text{THz}; \lambda_c = 780.24\,\text{nm}$. The mode profile obtained by FEM simulations of the waveguide surrounded by rubidium atoms is shown in (c). From the attenuation data the normalized transmission spectrum of a waveguide (d) compared to the free space case (e) is calculated. Due to the transit time and enhanced Doppler broadening the absorption dips in the waveguide spectrum are much wider, which results in a larger overlap of the lines. The spectral position and strength of all hyperfine transitions are shown in (f). They can be grouped in four sets according to the transitions from the different ground states to the excited states.

by a specific waveguide geometry is modeled by COMSOL FEM simulations and the decay length is obtained from a fit to the evanescent field outside of the waveguide as described in Sec. 2.1.2. With these values the susceptibility and thus the effective index of refraction of the atom vapor surrounding the waveguide is calculated. In a further step, the atom vapor is included in the waveguide mode simulation as a surrounding cladding material with the respective complex index of refraction. Thereby, the complex effective mode index is simulated, where the variation in the real part leads to a phase shift of the mode and the complex part represents the absorption of the beam. However, this also leads to a small change in the mode field and thus, slightly changed values for the propagation constant and decay length are extracted. In a further step the atom susceptibility and subsequently the effective waveguide mode index are recalculated using these new propagation parameters.

The results of this simulation are presented in Fig. 3.3 for a 180 nm x 650 nm Si_3N_4 waveguide surrounded by a rubidium atom vapor at a temperature of 150 °C. In subfigure (a) and (b) the real and imaginary part of the effective mode index are presented. When scanning over the D2 line of rubidium, the presence of the atom vapor leads to an oscillation of the real part around its original value without the atoms. This leads to a phase shift of the beam at the atom transition. The imaginary part, which represents the beam attenuation, exhibits peaks corresponding to the hyperfine transitions in the atom vapor. The resulting mode profile with the complex effective mode index from the FEM simulation is shown in panel (c). The information about the attenuation can now be used to calculate the transmission spectrum through the waveguide with a light-atom interaction length of e. g. 50 µm as depicted in panel (d). The width of the transitions is increased due to transit time broadening and enhanced Doppler-broadening because of the increased propagation constant in the waveguide. For comparison a typical simulated absorption spectrum of a free space beam by rubidium atoms is presented in (e), which is not influenced by transit time broadening but only by normal Doppler-broadening. As the spectrum consists of several hyperfine transitions, the transitions strengths as well as the spectral position of all transitions contributing to the D2 line of rubidium are given in (f). The spacing between the lines in the four sets (i - iv, see also the term diagram in Fig. 3.1 in Sec. 3.1) is so narrow that typically only these four peaks (or dips) are obtained. Further details on the atom susceptibility and transition strength as well as all used parameters for the calculation and the details on numerical implementation are given in App. A.8. Also the magnitude of the change in attenuation and propagation with several iterations of the simulation are presented in the appendix.

3.5. Measurement Setup for Atom Clad Waveguides

In order to evaluate the light-atom interaction and to study the response of atom-based photonic devices, a transmission spectrum through the integrated circuits which are exposed to a rubidium atom vapor has to be recorded. A schematic view of the utilized measurement setup for the characterization of the devices is shown in Fig. 3.4. A free space tunable laser source is used and the input beam is focused via a lense on the grating coupler. After passing the device, the output beam from a second

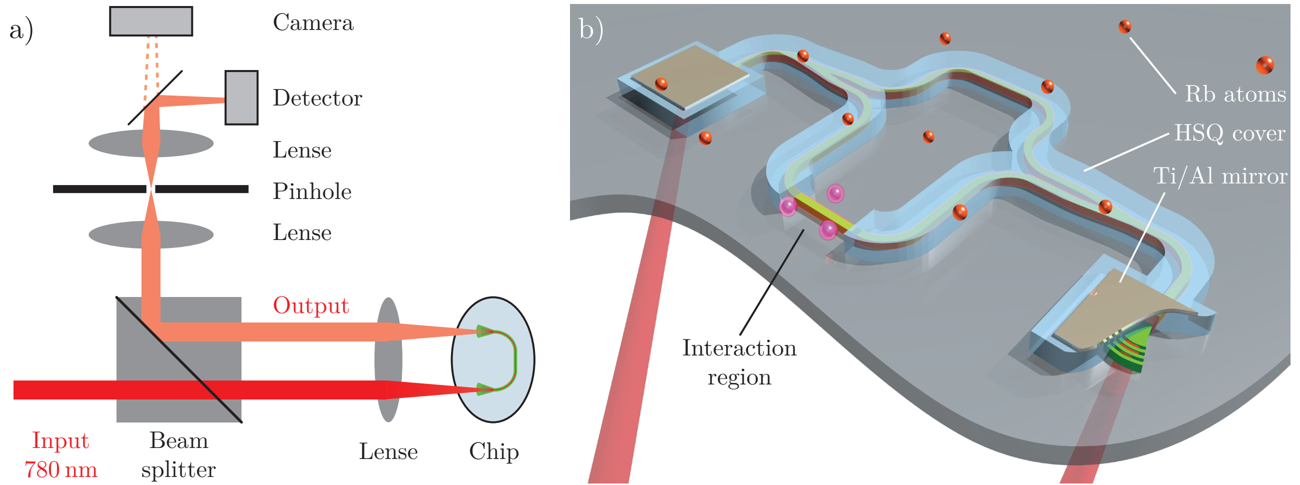

Figure 3.4.: a) Schematic view of the setup used for characterizing integrated photonic devices in the presence of an atom vapor. A free space laser is used to couple to the devices through the substrate. This is also shown in the sketch of a single device surrounded by an atom vapor in b). Only a well defined part of the waveguide is not covered by HSQ and atoms in this interaction region can be excited by the waveguide mode.

grating coupler is collected via the same lense. The output beam is separated from the input path by using a beam splitter and sent to the detector (photomultiplier tube). An additional lense in combination with a pinhole is used to select the precise area from which light is collected. Alternatively, by removing the mirror the sample can be viewed by a CCD camera for alignment purposes. In Fig. 3.4 b) a sketch of an integrated device exposed to the atom vapor is shown. Light is coupled through the transparent substrate into the integrated circuit via a grating coupler and also the output from the second grating coupler is collected through the substrate. Most of the waveguide is protected from the atom vapor by an HSQ cover. Only a specific part of the waveguide is not covered and in this way a well defined interaction region for the waveguide mode with the rubidium atoms is obtained. Furthermore, at the position of the grating couplers a metal mirror is placed on top of the HSQ cover. This metal mirror prevents the input beam that is focused onto the grating coupler from entering the chamber. Otherwise many atoms would be excited by this beam causing a strong unwanted background fluorescence. Additionally, it increases the efficiency of the grating couplers as the input beam is reflected after passing the grating coupler and the mirror on the output coupler reflects the part of the beam, which is scattered in the upward direction.

The chip is mounted to the side of a UHV chamber or to a vapor cell and a rubidium reservoir is attached to either system. By heating up this reservoir an atom vapor inside the chamber or cell is generated that surrounds the integrated devices. But only atoms in the close vicinity of the bare waveguide are excited and contribute to the light-atom interaction. By controlling the rubidium temperature the atom density of the vapor is adjusted. In case of the vacuum chamber a heating coil is placed around the structured vacuum window. Thereby, the window and the photonic structures are

kept at a higher temperature then all other parts of the chamber in order to diminish the probability of atoms condensing on the window surface. In contrast to the vacuum chamber, the vapor cell is much smaller and thus the temperature control of the complete cell is much easier. Furthermore, the vacuum chamber is fixed on an optical table and for addressing different devices the laser beam has to be readjusted by the optical components of the setup. Contrarily, the vapor cell can conveniently be moved around, e. g. on a translation stage, and various devices can be accessed without altering the beam alignment. Also the input angle of the beam can be adjusted by simply tilting the vapor cell. This can be used to compensate an offset in the grating period of the coupler in order to maximize the coupling efficiency for the specific wavelength of approximately 780 nm at the D2 line of rubidium.

3.6. Experimental Results of the Integrated Atom-Light Interaction

In this section various different devices interacting with a rubidium atom vapor are introduced. The strength of the interaction is discussed in terms of attenuation of a waveguide mode as well as the induced phase shift, when scanning over the rubidium D2 line. The alteration of the response of ring resonators due to the attenuation and the phase variation caused by the atoms is studied and a possible enhancement of the interaction by the use of slot waveguides is discussed.

3.6.1. Enhancement of the Grating Coupler Efficiency by Utilizing Metal Mirrors

The main purpose of the metal mirrors on top of the HSQ spacer above the grating couplers is to prevent that the input beam enters the space where the atom vapor is enclosed. Besides, they have the side effect that light is reflected, causing an interference with the incoming beam. This can be utilized for increasing the efficiency of the grating couplers. The basic effect is similar to the interference process observed in an underlying SiO_2 buffer layer when using standard silicon wafers as discussed in Sec. 2.4.2. A critical point for the interference is the thickness of the HSQ spacer between the grating coupler and the metal mirror. An appropriate thickness is crucial for obtaining constructive interference at the position of the grating coupler. In this way, the coupling efficiency can be increased while it might even be inhibited for a thickness which causes destructive interference.

A simple calculation of the interference effect based on a single reflection of the beam at the metal mirror gives an optimal spacer height of 680 nm for an interference maximum at a wavelength of 780 nm with the adjacent minima at $\lambda = 650$ nm and 970 nm. However, in order to obtain the actual optimal parameters an experimental study of the effect is carried out. The photonic structures are fabricated from a 180 nm Si_3N_4 layer on a 500 µm silica substrate. A simple geometry of two grating couplers directly connected by a waveguide is employed. The structures are covered by an approximately 730 nm thick HSQ layer via spin coating. Using the standard measurement setup (see Sec. 2.4.1) a transmission of approximately 2 % is obtained. Next, the chip is turned upside down and the transmission when accessing the devices by the fiber array through the transparent substrate is recorded. Due to 500 µm thick substrate the distance to the fiber array is increased and the beam is

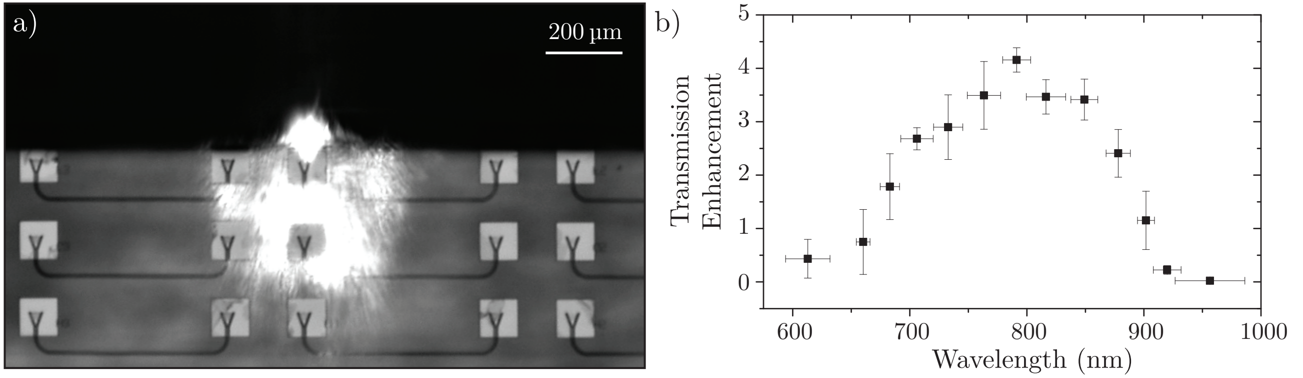

Figure 3.5.: a) Optical micrograph of the chip in the measurement setup. The black part at the top is the fiber array which is used for coupling light to the devices. The actual device which is accessed is hidden below the fiber array. The bright squares are the metal mirrors that are placed on the HSQ spacer and the chip is turned upside down for coupling light to the devices through the substrate. The large bright spot is a reflection of the input light beam from one of the fibers of the array at a wavelength around 800 nm. b) The enhancement of the transmission greatly depends on the wavelength. For constructive interference at the coupler position the transmission is increased (e. g. at a wavelength around 780 nm), while it is inhibited for destructive interference.

quickly diverging when leaving the fiber. Thus, a decrease in the transmission down to ∼0.15 % is caused.

In a further EBL step a PMMA mask is created and a metal layer is deposited on the chip. Thereby, a mirror is placed at the grating coupler position on top of the HSQ spacer. This can be seen in the optical micrograph of the chip in Fig. 3.5 a). For evaluating the interference effect caused by the metal mirrors, many devices with varying period of the grating couplers are fabricated. The transmission is recorded and compared to the case without the mirrors. An increase in transmission of up to 0.6 % is observed. The resulting enhancement factor depending on the wavelength transmitted by the coupler is presented in Fig. 3.5 b). The x-error represents the variation in the wavelength, which is best transmitted by a coupler with a certain period. In this case a grating period from 450 nm to 750 nm in steps of 25 nm is used. For each grating period there are several devices that are evaluated and the variation in the device transmission is shown by the y-error. There are several uncertainties in the experimental realization compared to the simple model of a single reflection. The HSQ layer thickness is measured after spin coating on a flat surface at the side of the chip. The height of the devices however leads to a larger layer thickness around the structures. Also the overall layer thickness decreases when the sample is heated up on a hotplate. In addition, the 180 nm high photonic devices are embedded within the HSQ layer rather then being completely below the layer. The EBL exposure might also slightly change the refractive index of the HSQ spacer and several reflections instead of a single one might contribute to the interference effect. Despite these constraints a transmission enhancement very much alike the calculated spectral positions of the interference extrema is obtained with a maximum enhancement around the desired wavelength of 780 nm. Thus, the layer thickness of the HSQ spacer is kept for all further samples presented in the following sections.

3.6.2. Atomic Cladding Waveguide Spectroscopy

In this first experiment, the light propagation in an atom clad waveguide is investigated. Here, we use a 1.1 µm wide and 180 nm high solid core Si_3N_4 ridge waveguide on the vacuum window platform. A meander geometry is chosen for the waveguide between the grating couplers and the HSQ cover defines an interaction length of 1.2 mm. This waveguide layout is shown in the optical micrograph of the sample in Fig. 3.6 a). A free space Gaussian beam is used to couple light to the integrated circuit via the grating couplers and a total transmission of 0.25 % is obtained in the absence of rubidium atoms. By heating up a rubidium reservoir connected to the vacuum chamber an atom vapor around the waveguide is included. The sample is typically kept at a temperature that is 20 K higher than the one of the reservoir in order to avoid atom condensation on its surface. However, thereby it is hardly possible to determine the precise temperature of the atom vapor above the sample surface. The atom density is extracted from a fit of the theoretical model to the data and the corresponding temperature is calculated by using the vapor pressure curve (see App. A.8). By scanning the input beam over the spectral range of the Rb D2 line a basic linear absorption spectrum of the atom vapor is recorded. A weak laser power of 50 nW is used for the data acquisition, which is well below the saturation power of the atoms.

The obtained normalized transmission spectrum for different atom densities is presented in Fig. 3.6 b), where the light color curves represent the recorded data. With increasing atom density (increasing reservoir temperature) the absorption dips deepen. This can be expressed in terms of the optical depth, where an optical depth of 1 corresponds to an attenuation of the beam by $1/e$. Thus, an optical depth of 0.53 is reached for an atom density of $11.4\,\mu m^{-3}$. The line shape of the spectrum shows a distinct deviation from the conventional Rb D2 spectrum because of the enhanced width of the absorption lines. As explained in Sec. 3.4, this is caused by the enhanced Doppler broadening due to the effective propagation constant in the waveguide and by the limited transit time of the atoms traveling through the evanescent field. By fitting a Voigt profile to the Rb^{85} $5^2S_{1/2}$ $F = 2 \rightarrow 5^2P_{3/2}$ transition for $N = 5.8\,\mu m^{-3}$, an overall width of 879 MHz is obtained. The theoretical model described above can be used to calculate the transmission spectrum via the equation for the transmitted power P:

$$P = P_0 \cdot e^{-\frac{4\pi}{\lambda}\mathrm{Im}(\tilde{n}_{\mathrm{eff,Rb}})L}, \tag{3.2}$$

with the input power P_0, the interaction length L, and the complex effective mode index $\tilde{n}_{\mathrm{eff,Rb}}$ in the presence of the Rb vapor calculated for this particular waveguide geometry. This model is fitted to the data with the atom density N as the only free parameter. As shown by the dark color lines in Fig. 3.6 b) this model fits very well to the experimental data. For an atom density of $5.8\,\mu m^{-3}$, the residuals R are depicted in panel (c) showing a deviation of the model from the data of less than 5 %. This model can thus be used to extrapolate the response of the system for e. g. higher Rb reservoir temperatures.

In Fig. 3.6 d) the optical depth for the system employed here is shown as a heatmap for a temper-

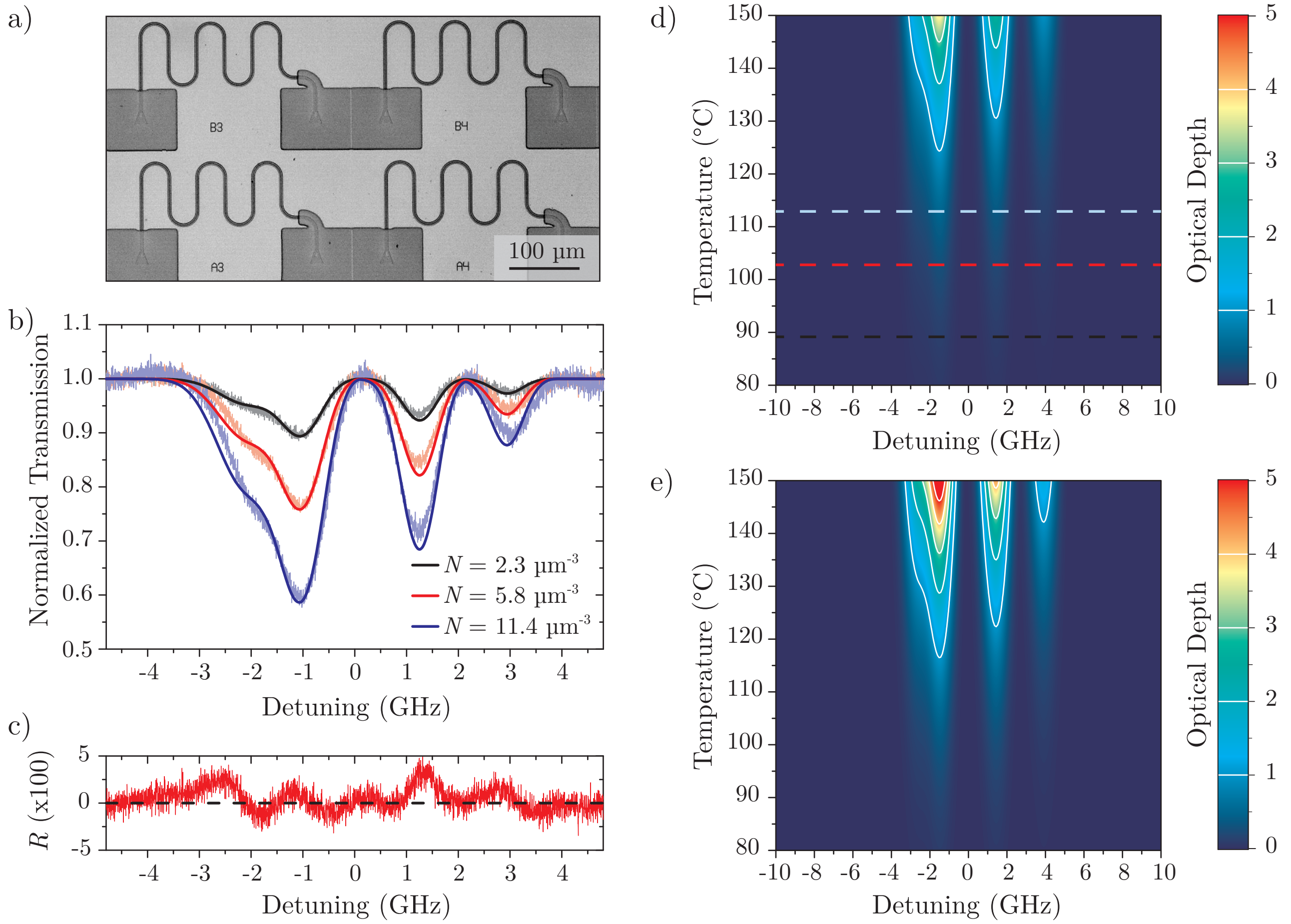

Figure 3.6.: a) Optical micrograph of the basic circuits used for the spectroscopy measurements. An interaction length of 1.2 mm is not covered by the HSQ spacer. Note that the metal mirrors are not yet placed at the coupler positions. b) Recorded spectra for an increasing Rb temperature (increasing atom density). The fit of the theoretical model to the data is given by the dark colored lines and shows a very good agreement of the model to the data. c) The calculated residuals R for an atom density of 5.8 µm^{-3} shows a deviation of less than 5 % between the model and the experimental data. d) The model is used to extrapolate the response of the system at higher temperatures by calculating the optical depth. The dashed lines at 89 °C, 103 °C and 113 °C correspond to the spectra shown in (b) for the different atom densities. e) By decreasing the waveguide width from 1.1 µm to 600 nm the ratio of the field which interacts with the atoms is increased. Thus, an optical depth of 1 can already be achieved at a Rb temperature of 116 °C instead of 125 °C in (d).

ature range from 80 °C to 150 °C. The positions of the spectra depicted in panel (b) are indicated by the dashed lines at the temperature corresponding to the particular atom density. From the plot it can be extracted that an optical depth of 1 would be reached at a temperature of 125 °C for the Rb^{85} $5^2S_{1/2}$ $F = 3 \rightarrow 5^2P_{3/2}$ transition. This can be used as a measure for the interaction strength. As the waveguide mode interacts with the atom vapor via the evanescent field, the proportion of the field being outside of the actual waveguide in the atom vapor is an important factor for the interaction. A ratio of 20.1 % of the mode field which interacts with the Rb vapor for the particular geometry used

here is extracted from numerical simulations. The rather large waveguide width of 1.1 µm is chosen to ensure proper fabrication results despite the limitations of the used EBL system. Decreasing this width to 600 nm, which is still above the cutoff for the fundamental TE mode, the proportion in the evanescent field increases and a ratio of 24.2 % of the mode field interacts with the surrounding atoms. The optical depth is recalculated for this geometry and depicted in Fig. 3.6 e). In this case an optical depth of 1 can already be achieved at a rubidium temperature of 116 °C. This is comparable to the optical density of 1.6 reported for a 200 nm × 500 nm Si_3N_4 waveguide at a temperature of 135 °C with a larger interaction length of 1.5 mm in Ref. [95]. There, a total line width of 1.1 GHz is obtained, compared to a smaller width of 879 MHz achieved here.

As shown in this section a distinct absorption spectrum of the rubidium atom vapor is already obtainable at a weak laser power and for a low atom density by using integrated photonic circuits with a small device footprint. In addition, the interaction can be further enhanced by simple alterations of the waveguide geometry.

3.6.3. Mach-Zehnder Interferometers for Measurements of the Induced Phase Shift

The transmission spectra obtained by basic waveguides in the previous section solely depend on the attenuation induced by the Rb vapor surrounding the waveguide. However, as discussed in Sec. 3.4, not only the imaginary part of the effective mode index is influenced but also the real part exhibits a fluctuation around its original value without the atoms when scanning over the Rb D2 line. In order to extract the magnitude of this variation integrated MZIs are employed. A shift in the real part of the effective mode index directly translates to a phase shift of the mode and such a phase shift is easily detectable by an MZI. The basic properties of these integrated interferometers are discussed in Sec. 2.2.2. Here, the same platform and waveguide dimension as for the absorption spectroscopy measurements is used. The waveguide is splitted in two arms, which exhibit a length difference of $\Delta L = L_2 - L_1 = 2.2\,\text{mm}$. The two arms are joined together again and the waveguide is terminated by an output grating coupler. Most of the device is covered by an HSQ layer, leaving only a $L_{\text{Rb}} = 2\,\text{mm}$ large part of the longer MZI arm uncovered, which defines the interaction region to the atom vapor. An optical micrograph of the device is shown in the inset of Fig. 3.7.

The presence of the atoms causes an additional attenuation as well as a phase shift in the longer arm of the interferometer. The additional attenuation in the arm leads to a further unbalance in the field amplitudes of the two arms. This is mainly influencing the ER of the transmission spectrum. Thus, an alteration of the MZI spectrum due to the additional absorption would primarily be observed when the spectral position of the Rb D2 line coincides with an interference maximum or minimum of the MZI spectrum. On the contrary, an additional phase shift in one arm leads to a spectral shift of the spectrum. When a fixed wavelength on the slope between a maximum and minimum is chosen and a phase variation shifts the spectrum, this directly translates into an intensity variation at the interferometer output. By considering the complex effective mode index, the MZI output can be

calculated as the combination of the fields of the two arms:

$$T_{\mathrm{MZI}} = |\mathcal{E}_1 e^{\mathrm{i}(\beta_1 L_1 + \Phi_0)} + \mathcal{E}_2 e^{\mathrm{i}[\beta_1 (L_2 - L_{\mathrm{Rb}}) + \tilde{\beta}_{\mathrm{Rb}} L_{\mathrm{Rb}}]}|^2, \tag{3.3}$$

where $\mathcal{E}_{1,2}$ are the field amplitudes of the respective interferometer arm, $\beta_1 = n_{\mathrm{eff}} {}^{2\pi}/_{\lambda}$ is the propagation constant of the mode in the waveguide covered by HSQ and thus protected from the atom vapor, $\tilde{\beta}_{\mathrm{Rb}} = \beta_{\mathrm{Rb}} + \mathrm{i}\beta'_{\mathrm{Rb}} = {}^{2\pi}/_{\lambda}(n_{\mathrm{eff,Rb}} + \mathrm{i}n'_{\mathrm{eff,Rb}})$ is the complex propagation constant of the waveguide in the presence of the atom vapor, and Φ_0 is a phase offset induced by e. g. fabrication imperfections especially in the waveguide splitter and by the temperature dependent change of the optical length of the arms. With this equation the transmitted power of the MZI is calculated as:

$$P_{\mathrm{MZI}} = \frac{P_{\mathrm{in}}}{4}\left(1 + 2Ae^{-\beta'_{\mathrm{Rb}} L_{\mathrm{Rb}}} \cos(\Phi') + A^2 e^{-2\beta'_{\mathrm{Rb}} L_{\mathrm{Rb}}}\right), \tag{3.4}$$

with the input power P_{in}. Note that an unbalanced splitting and any difference in the field amplitude of the two MZI arms without the atoms, due to e. g. the waveguide attenuation in the arms of different length is not considered as a separate factor, but is included in the ratio $A = {}^{\mathcal{E}_2}/_{\mathcal{E}_1}$ of the field amplitudes. The total phase difference Φ' is given by $\Phi' = (L_2 - L_1 - L_{\mathrm{Rb}})\beta_1 + \Phi_0 + L_{\mathrm{Rb}}\beta_{\mathrm{Rb}}$. Thus, a variation in $n_{\mathrm{eff,Rb}}$ leads to a phase shift of the MZI.

When recording an MZI spectrum in the presence of the Rb atom vapor around the waveguide, Eq. (3.4) is used to fit the theoretical model to the data. For the MZI properties P_{in}, A, and Φ_0 are free parameters, while for the interaction with the atom vapor the atom density N is the only free parameter. In Fig. 3.7 the MZI transmission spectra are presented for an increasing rubidium temperature. For these measurements a laser power of 280 nW is used. As visible in the data on the left side, the spectral position of the Rb D2 line is located on the slope of the MZI transmission and the signal variations are mainly caused by the phase shift induced by the atoms at the electron transitions. A zoomed in view on the spectrum is given on the right side and again the theoretical model (dark colored lines) fits well to the experimental data. The fit parameters are discussed in App. A.9.

From the transmission spectrum of the MZI the additional phase shift induced in one of the arms can be extracted. It is derived from Eq. (3.4) as

$$\begin{aligned} \Delta\Phi =& \beta_{\mathrm{Rb}} L_{\mathrm{Rb}} - \beta_0 L_{\mathrm{Rb}} \\ =& \cos^{-1}\left(\frac{{}^{4P_{\mathrm{MZI}}}/_{P_{\mathrm{in}}} - 1 - A^2 \exp(-2\beta'_{\mathrm{Rb}} L_{\mathrm{Rb}})}{2A\exp(-\beta'_{\mathrm{Rb}} L_{\mathrm{Rb}})}\right) - \beta_1(L_2 - L_1 - L_{\mathrm{Rb}}) - \Phi_0 - \beta_0 L_{\mathrm{Rb}}, \end{aligned} \tag{3.5}$$

where β_0 is the propagation constant of the waveguide without the HSQ cover and in the absence of the atom vapor. From the spectra in Fig. 3.7, the additional phase shift is extracted and presented in Fig. 3.8 a). As a comparison also the calculated phase shift is shown as the dark colored lines. Here, a phase shift of 0.15π is induced by the atom vapor at a temperature of 124 °C over an interaction length of 2 mm. The phase shift is caused by the variation in the real part of the effective mode index

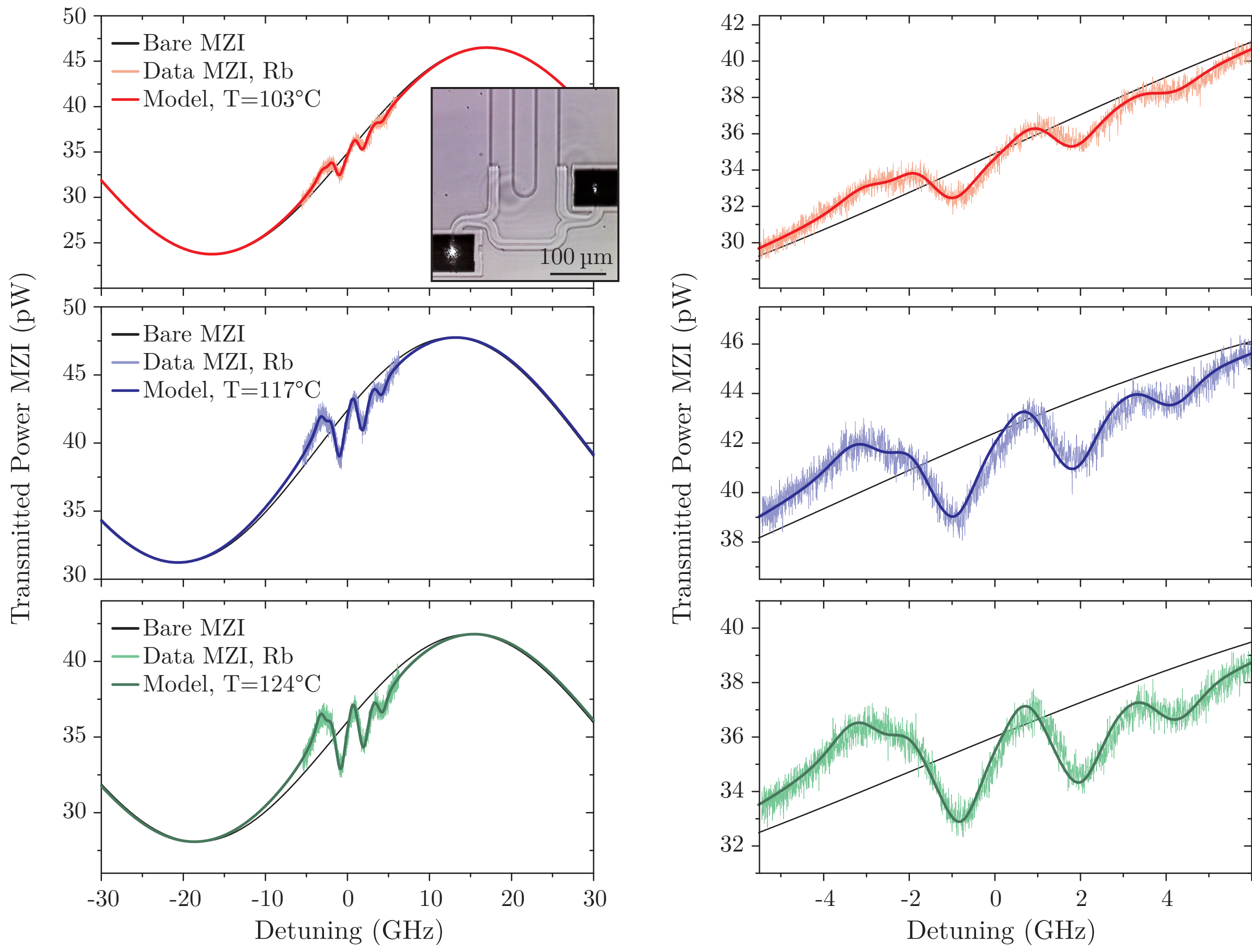

Figure 3.7.: Response of an MZI when one of the arms is interacting with a Rb vapor. On the left side the MZI transmission is shown for increasing temperature (from top to bottom) of the Rb vapor. On the right side a zoom in on the region of the D2 line is shown. The black line represents a reference for an MZI without atoms adapted to the specific device transmission. Light colored lines are the recorded spectra and the dark colored lines are a fit of the theoretical model to the data. For the red line a temperature of 103 °C (with a corresponding atom density $N = 5.8\,\mu m^{-3}$) is observed, for the blue line 117 °C ($N = 13.9\,\mu m^{-3}$), and for the green line 124 °C ($N = 21.0\,\mu m^{-3}$). The inset shows an optical micrograph of the device, where the upper meander-shaped arm is not covered by HSQ. On the left coupler the bright input spot is visible and on the right coupler the transmitted output light.

for the atom clad waveguide (see panel (b)). Hence, it closely follows the curve shape of the effective mode index with respect to the value without the atom vapor. Similar to the previous section, the theoretical model is used to extrapolate the MZI response and thus the induced phase shift at higher temperatures. In this way, it can be inferred that a phase shift of π would be induced at a rubidium vapor temperature of 162 °C as shown in Fig. 3.8 c). Additionally, the same calculation is carried out for a geometry with a decreased waveguide width of 600 nm but the same interaction length. The result is shown in panel (d) and in this case a phase shift of π would already be achieved at 152 °C.

With the help of the MZIs, the influence of the atom vapor on the real part of the effective mode

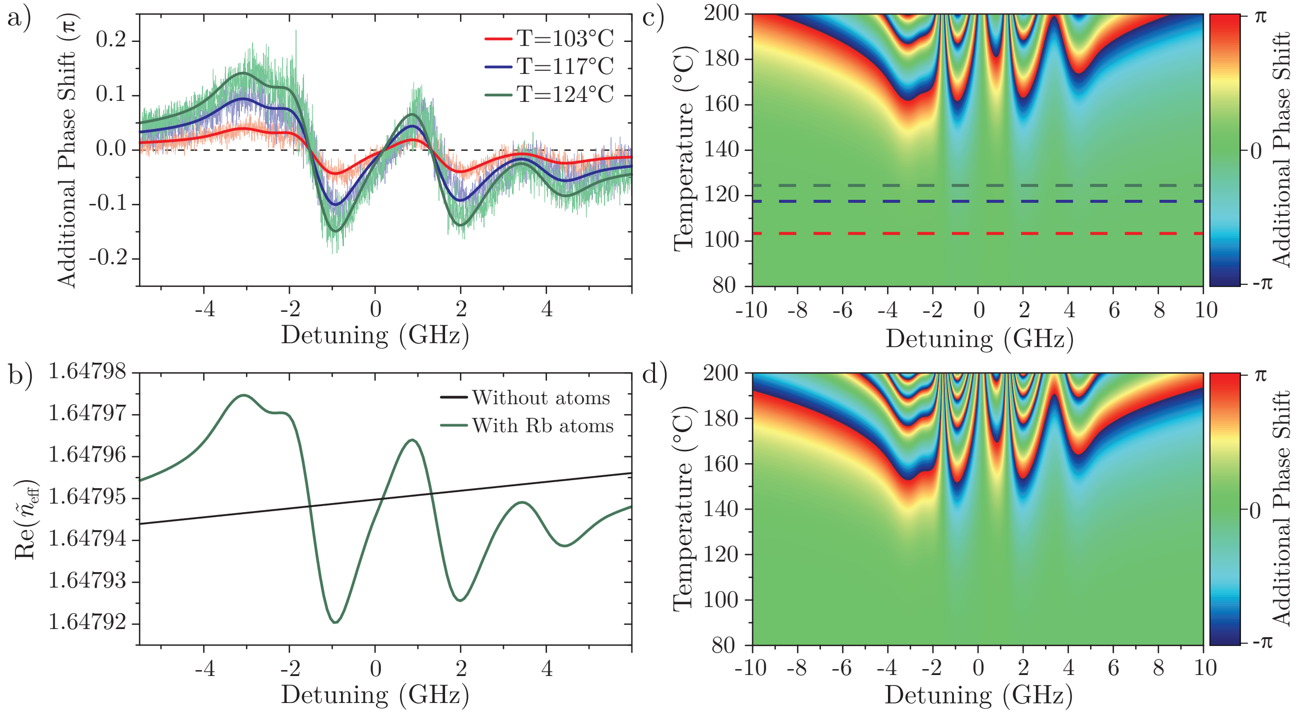

Figure 3.8.: a) From the MZI transmission spectra the additional phase shift caused by the presence of the atom vapor is extracted. Light color lines are the experimental data and dark color lines the fit of the theoretical model. The phase shift is caused by the variation of the effective mode index due to the atom vapor. This simulated variation is shown in (b) for $T = 124\,°\text{C}$. The black line is the reference without the atom vapor. Clearly the phase shift follows the shape of the effective mode index. c) The theoretical model is used to extrapolate the phase shift with increasing Rb vapor temperature. The dashed lines indicate the position of the spectra in (a). For a temperature of 162 °C a phase shift of π is expected. d) By reducing the waveguide width to 600 nm, the ratio of the field interacting with the atom vapor is increased and a phase shift of π can already be achieved at 152 °C

index is separated from the attenuation and the induced phase shift is extracted. This is important for the fundamental understanding of the response of devices, where both parameters contribute equally to the signal. This is for example the case for microcavities, where a cavity resonance can be strongly modified by the atom vapor. The response of integrated ring resonators is studied in the following section. Furthermore, inducing a phase shift by the atom vapor might be directly employed for implementing tunable devices or phase switches via the atom vapor density. The simultaneous attenuation of the atoms might however impede this application. Therefore, a wavelength on the wings of the outer absorption lines should be chosen where the off-resonant phase shift is still present, while the attenuation is already at a very low level. For example, a modulation scheme based on an induced cross-phase shift with a fast response time below 5 ns [274] could be transferred to the integrated photonics platform for future devices.

3.6.4. Cavity Enhanced Interaction in Ring Resonators

Coupling a two level atom to a resonator plays an important role for various applications like cavity QED and on-chip all-optical modulation and routing. Here, integrated photonic ring resonators are used to study the interaction with a surrounding atom vapor. The response of such a cavity in presence of the atoms strongly depends on the alteration of both real and imaginary part of the effective mode index, when scanning over an electron transition. Furthermore, the cavity quality and thus its resonance width plays an important role for the strength of the interaction. The vapor cell platform described in Sec. 3.3.2 is utilized for the experimental realization. This brings the advantage of increased photonic circuit quality, better waveguide protection from the Rb atom vapor, enhanced temperature control of the vapor cell and easier usability of the system due to its very compact size.

A sketch of the device layout is shown in Fig. 3.9 a), where a ring resonator is coupled to a bus waveguide. Light is coupled to and from the photonic circuit via grating couplers through the transparent substrate and an HSQ cover defines the interaction region to the atom vapor. Not only the ring but also a small part of the bus waveguide in the coupling region to the resonator is exposed to the atom vapor. Optical micrographs of the device are shown in Fig. 3.9 b) and c). In this micrographs, as an overlay and colored in red, the light from the atom interaction recorded by the CCD camera is shown. At the position of the left grating coupler (which is masked by the black rectangle of the metal mirror) the spot of the input laser beam is visible, while at the right grating coupler the scattered output light can be observed. The laser beam is tuned to the D2 line of rubidium and thus the atoms surrounding the waveguide are excited and the photoluminescence can be recorded.

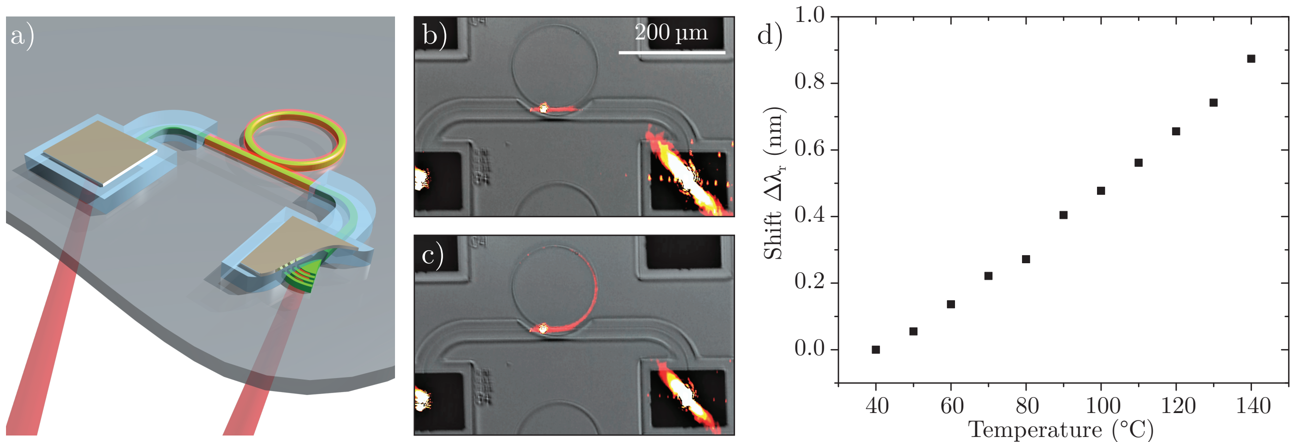

Figure 3.9.: a) Sketch of the ring resonator device, where the atoms interact to the mode in the ring as well as to a small part of the straight bus waveguide. b), c) Optical micrographs of the device with a colored overlay of the detected light for the atom interaction. When the ring is detuned from the D2 line, no light is entering the resonator and only atoms along the straight bus waveguide are excited (b). When the ring is in resonance to the D2 line, light is entering the ring and also excites atoms there. d) By increasing the sample temperature the resonances wavelength λ_r can be shifted via the thermo-optical effect. Thereby, the resonances can be tuned to a desired spectral position.

In panel (b) the resonance wavelength of the ring resonator is detuned from the D2 line and therefore no light is entering the ring resonator and subsequently only atoms along the straight bus waveguide are excited. Contrarily, the ring resonator in panel (c) is tuned in resonance to the Rb D2 line, light is able to enter the resonator and also atoms along the ring are excited. Due to the absorption of the atom vapor the signal decreases along the ring. The presence and the excitation of the atoms make it easily observable if light is able to enter the ring when the resonator is tuned to the laser wavelength at the Rb D2 transition.

The spectral position of the ring resonances is a crucial element when studying the cavity enhanced atom-light interaction. Thus, it is necessary to be able to tune the resonances to an arbitrary position. In particular, the resonator spectrum has to be shifted by at least its FSR. As the vapor cell is heated up for the atom-light interaction, this can simultaneously be used for tuning the ring resonances. The *thermo-optical* effect refers to the temperature dependence of the refractive index. As optical devices react sensitively to even small changes of the refractive index, this can greatly impact the precise cavity properties of the ring resonator. The thermo-optical effect is generally described by a linear approximation for the refractive index as $n(T) = n(T_0) + \gamma \cdot \Delta T$, with the thermo-optical coefficient γ. Compared to silicon ($\gamma_{\mathrm{Si}} = 1.8 \times 10^{-4}\,\mathrm{K}^{-1}$) the thermo-optical coefficients of Si_3N_4 ($\gamma_{\mathrm{Si_3N_4}} = 2.45 \times 10^{-5}\,\mathrm{K}^{-1}$) and SiO_2 ($\gamma_{\mathrm{SiO_2}} = 0.95 \times 10^{-5}\,\mathrm{K}^{-1}$) are roughly an order of magnitude smaller [117–119] and therefore they are less sensitive to temperature fluctuations, but heating a sample still significantly impacts the device characteristics. Thus, the shift in the refractive index of Si_3N_4 as well as of the BSG substrate leads to a variation in the effective mode index and hence in the spectral resonance position. The influence on the effective mode index has to be described by an effective thermo-optical coefficient: $n_{\mathrm{eff}}(T) = n_{\mathrm{eff}}(T_0) + \gamma_{\mathrm{eff}} \cdot \Delta T$.

The shift of a ring resonance is recorded by placing the sample on a temperature stage and monitoring the resonance wavelength. The resulting graph is presented in Fig. 3.9 d). From this curve the effective thermo-optical coefficient is extracted as $\gamma_{\mathrm{eff}} = 1.8 \times 10^{-5}\,\mathrm{K}^{-1}$. The specific waveguide geometry and ring resonator dimension lead to a FSR of 0.62 nm and by a temperature increase of approximately 70 K a shift of the resonance wavelength by one FSR is realized. When studying the influence of the atom vapor the sample is kept at a high temperature that tunes the resonance wavelength to the Rb D2 transition. The Rb reservoir temperature is however kept at a lower temperature in order to avoid unnecessary Rb condensation on the sample surface.

For investigating the ring resonator response in the presence of the atom vapor, the resonator properties are studied first. Here, a ring with a radius of $r = 80\,\mu\mathrm{m}$ (length $L = 2\pi r$) and a gap of 200 nm to the bus waveguide is utilized, where a 100 µm long part of the straight waveguide is also not covered by HSQ. Before the Rb reservoir is heated up and the atom vapor is led to the sample surface for the first time, the ring resonances exhibit a quality factor of $\sim$44000. However, when exposed to the atom vapor, the quality factor (detuned from the Rb D2 line) decreases significantly. This strongly indicates that despite the 7 nm alumina protection layer, there is a small amount of atom adsorption on the waveguide surface, which causes an additional attenuation of the waveguide

mode. Nevertheless, after the first decrease in the circuit quality no further degradation is observed while using the sample over several months and many cycles of Rb atom vapor exposure. Therefore, the protection layer actually serves its purpose, which is in particular notable when it is compared to the vacuum window platform without the protection layer. In that case the signal is completely lost already after a couple of days.

When exposed to the atom vapor the ring resonator quality factor decreases to ~8000, but is still close to critical coupling with an ER of 10 dB. From these properties an attenuation coefficient of 5.5 dB/mm is extracted corresponding to a round trip loss factor $A = e^{-\alpha/2 L} = 0.73$ and a transmission coefficient $|t| = 0.85$ of the coupling matrix. With these parameters the theoretical transmission of the ring resonator coupled to a bus waveguide can be calculated. As also a certain part with length L_{bus} of the bus waveguide is interacting with the Rb vapor, the signal is always a combination of the ring response and the straight bus waveguide. Thus, the transmitted power (compare Eq. (2.6) in Sec. 2.2.1) is given as

$$P_{\text{t}} = e^{-2\beta'_{\text{Rb}} L_{\text{bus}}} \frac{A^2 e^{-2\beta'_{\text{Rb}} L} + |t|^2 - 2A|t|e^{-\beta'_{\text{Rb}} L} \cos(\theta_{\text{Rb}} + \phi_t)}{1 + A^2|t|^2 e^{-2\beta'_{\text{Rb}} L} - 2A|t|e^{-\beta'_{\text{Rb}} L} \cos(\theta_{\text{Rb}} + \phi_t)}, \tag{3.6}$$

with the complex propagation constant of the waveguide mode in the presence of the atoms $\tilde{\beta}_{\text{Rb}} = \beta_{\text{Rb}} + \mathrm{i}\beta'_{\text{Rb}}$ and the phase $\theta_{\text{Rb}} = \beta_{\text{Rb}} L$.

In order to study the ring resonator response in the presence of the atoms a series of measurements is performed where the ring resonance frequency is thermally tuned to different offset positions (atom-resonator detuning Δ_{AR}) from the center of the Rb D2 line. In Fig. 3.10 the results of these measurements are presented for an atom density of $N \approx 100\,\mu\text{m}^{-3}$. For a better visibility a detuning of zero corresponds to the center of the ring resonance, while the recorded D2 spectra are shifted to the corresponding position on the slope of the resonance according to the thermal tuning of the ring resonance. At this atom density the width of the transitions is additionally increased by self broadening. Hence, when applying the theoretical output model, in a first run the Lorentzian width of the atoms is determined, and in a second run the model is fitted to the data with the atom density and the atom-resonator detuning as the only free parameters. As visible by the dark colored lines in the bottom graphs of Fig. 3.10 the model fits very well to the experimental data.

The specific shape of the response depends largely on the relative position Δ_{AR} to the ring resonance frequency. The spectrum for a nearly off-resonant case (i), for a position on the slope of the ring resonance (iii), and in the center of the resonance (iv) are shown in the zoomed-in graphs. For curve (i) (and similarly for (vi)) the spectrum is mainly influenced by the absorption of the bus waveguide and resembles closely the spectrum of the basic attenuation experiments. This is expected, since there is almost no coupling of the probe light to the ring resonator due to a large atom-resonator detuning. At the slope of the resonance (see curve (iii) as well as (v)) the dispersive nature of the atoms causes a large variation in the transmission. Even a small variation in the real part of the effective mode index and thus in the round trip phase causes a shift of the resonance and thereby a large modulation

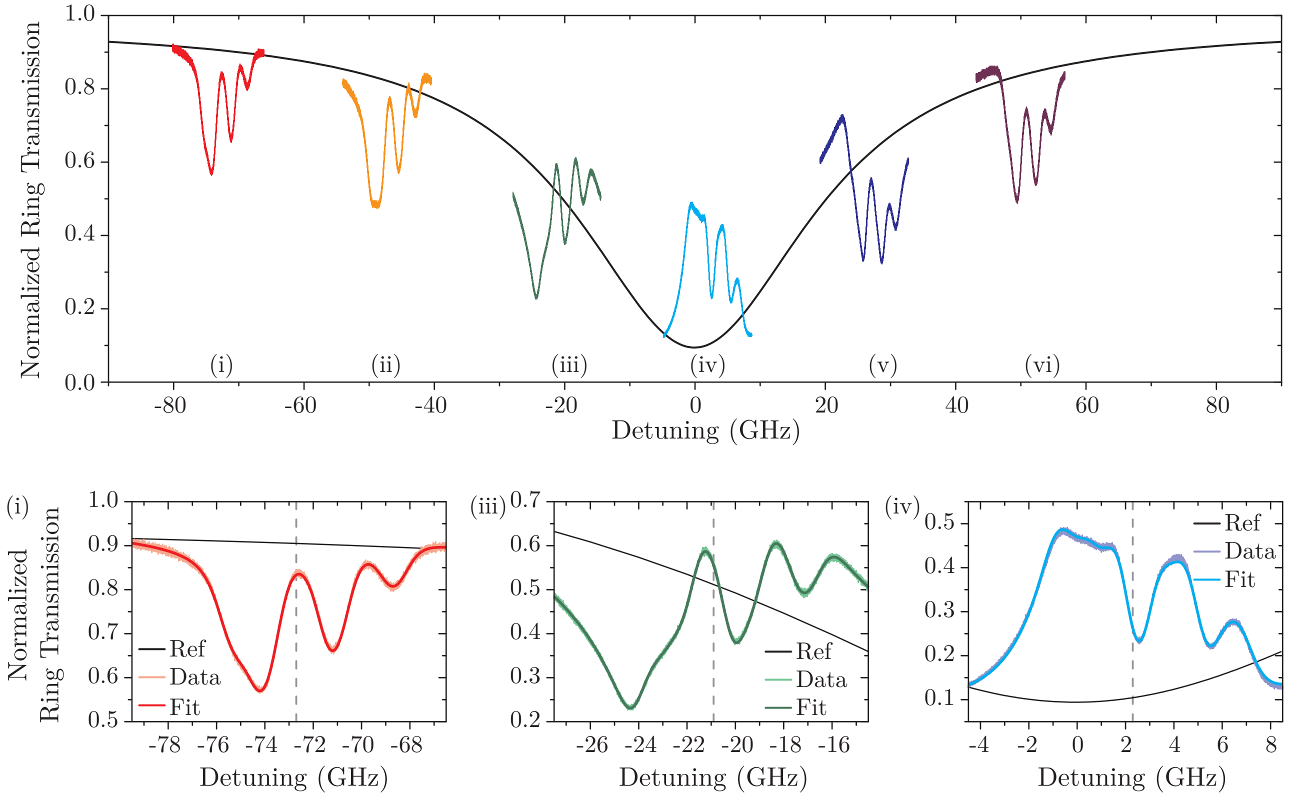

Figure 3.10.: Transmission measurements for various atom-resonator detunings Δ_{AR}. The black curve shows the reference transmission of the ring resonator without atoms as calculated from fit parameters. The superimposed spectra are shifted to the corresponding position on the resonance curve. A zoom in on a spectrum for an off-resonant case (i), on the slope of the resonance (iii), and close to the center of the resonance (iv) are shown with fits of the model (dark colored line). The dashed lines indicate the center of the Rb D2 line.

of the ring transmission. A third characteristic is observed on resonance ($\Delta_{\mathrm{AR}} \approx 0$) as for curve (iv). The additional attenuation in the ring moves the resonator further away from the critical coupling condition and leads to an increase of the transmitted power on resonance. Here, the transmission enhancement amounts to approximately 40 percentage points.

Additionally, the saturation behavior of the atoms interacting with the evanescent waveguide field of the ring resonator is studied. The input power is increased and a sequence of transmission spectra is recorded with the ring being tuned to the atom transition. The Lorentzian linewidth is extracted and the result is presented in Fig. 3.11. From this graph the input power at which saturation occurs is determined by fitting the function $\Gamma_{\mathrm{tot}} = \Gamma_0(1 + P_{\mathrm{in}}/P_{\mathrm{sat}})^{1/2}$ to the data. This yields an initial linewidth $\Gamma_0 = 630\,\mathrm{MHz}$ and a saturation power of $P_{\mathrm{sat}} \approx 5.3\,\mu\mathrm{W}$. The saturation intensity for the atom vapor can be calculated from the initial linewidth via $I_{\mathrm{sat}} = (2\pi^2\hbar c\Gamma_0)/(\sigma_0\lambda)$, with the resonant cross section $\sigma_0 = 1.938 \times 10^{-9}\,\mathrm{cm}^2$ for linear polarized light [237, 295]. Thereby, a saturation intensity of $\sim$260 mW/cm^2 is obtained and the mean intensity of the evanescent field for a given input power is estimated via $I = P_{\mathrm{in}} {}^{I_{\mathrm{sat}}}/{}_{P_{\mathrm{sat}}}$. In this way the intensity scale in Fig. 3.11 is calculated.

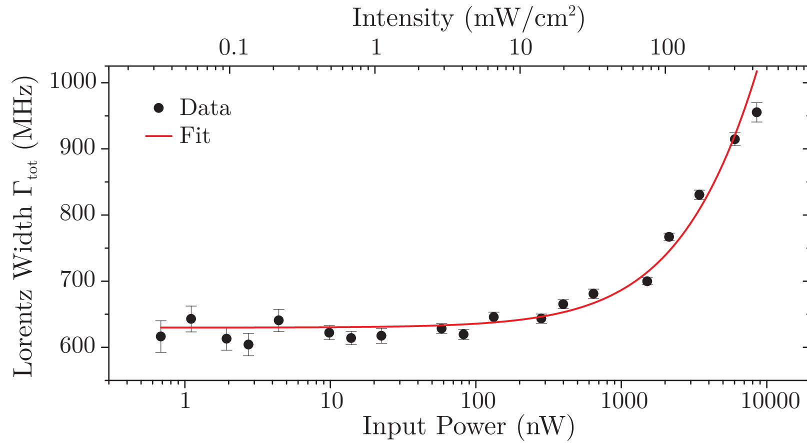

Figure 3.11.: Saturation behavior of the extracted Lorentz width of the spectrum for increasing input power. The red line is a fit of the total width with initial linewidth $\Gamma_0 = 630\,\mathrm{MHz}$ and saturation power $P_{\mathrm{sat}} \approx 5.3\,\mu\mathrm{W}$. From the saturation power, the corresponding mean intensity of the field (top axis) is deduced.

By using numerical simulations the intensity distribution for the waveguide geometry is calculated and the corresponding mode power is extracted. From these data it can be inferred that the saturation intensity at the position of maximal external field is reached for a mode power of $\sim$70 nW. This corresponds to an average photon number of $\langle n \rangle = 0.7$ being in the ring at any time. Furthermore, this can be compared to the quantum numbers as defined in cavity QED [244]. There, the saturation (or critical) photon number n_0 is calculated as

$$n_0 = \frac{\Gamma_\perp^2}{2g_0^2}, \qquad \Gamma_\perp = \frac{\Gamma_0}{2}, \qquad g_0 = \left(\frac{\mu^2 \omega_c}{2\hbar\epsilon_0 V_\mathrm{m}}\right)^{1/2}, \tag{3.7}$$

where $\Gamma_\perp$ is the transverse decay rate and $g_0/2\pi \approx 320\,\mathrm{MHz}$ is the cavity QED coupling parameter calculated from the effective transition dipole moment μ for linear polarized light, the cavity angular frequency ω_c, and the cavity mode volume V_m. Thereby, we estimate the critical photon number as $n_0 \approx 0.5$, which is very close to the average photon number needed for saturation as derived above. Together with the cavity decay rate κ_0, the cooperativity parameter per atom for this system amounts to $C = g_0^2/\Gamma_0\kappa_0 \approx 5 \times 10^{-3}$, which yields a critical atom number of $N_0 = 1/C \approx 200$. This is still rather remote from typical cavity QED experiments and cooperativity values as high as in cold atom experiments are not feasible, but the strong coupling regime with $(n_0, N_0) < 1$ might be approachable by increasing the cavity quality and reducing the mode volume. For example, very small mode volumes can be obtained by using photonic crystal cavities.

In order to study the response of a ring resonator with increasing quality factor in the presence of the atom vapor, the theoretical model of the interaction is employed. In this way, the normalized ring transmission is calculated and the results are presented in Fig. 3.12. For graphs a)-f) a ring resonator with a quality factor of 2.8×10^4 and ER of 10 dB is considered. In a)-c) the ring transmission

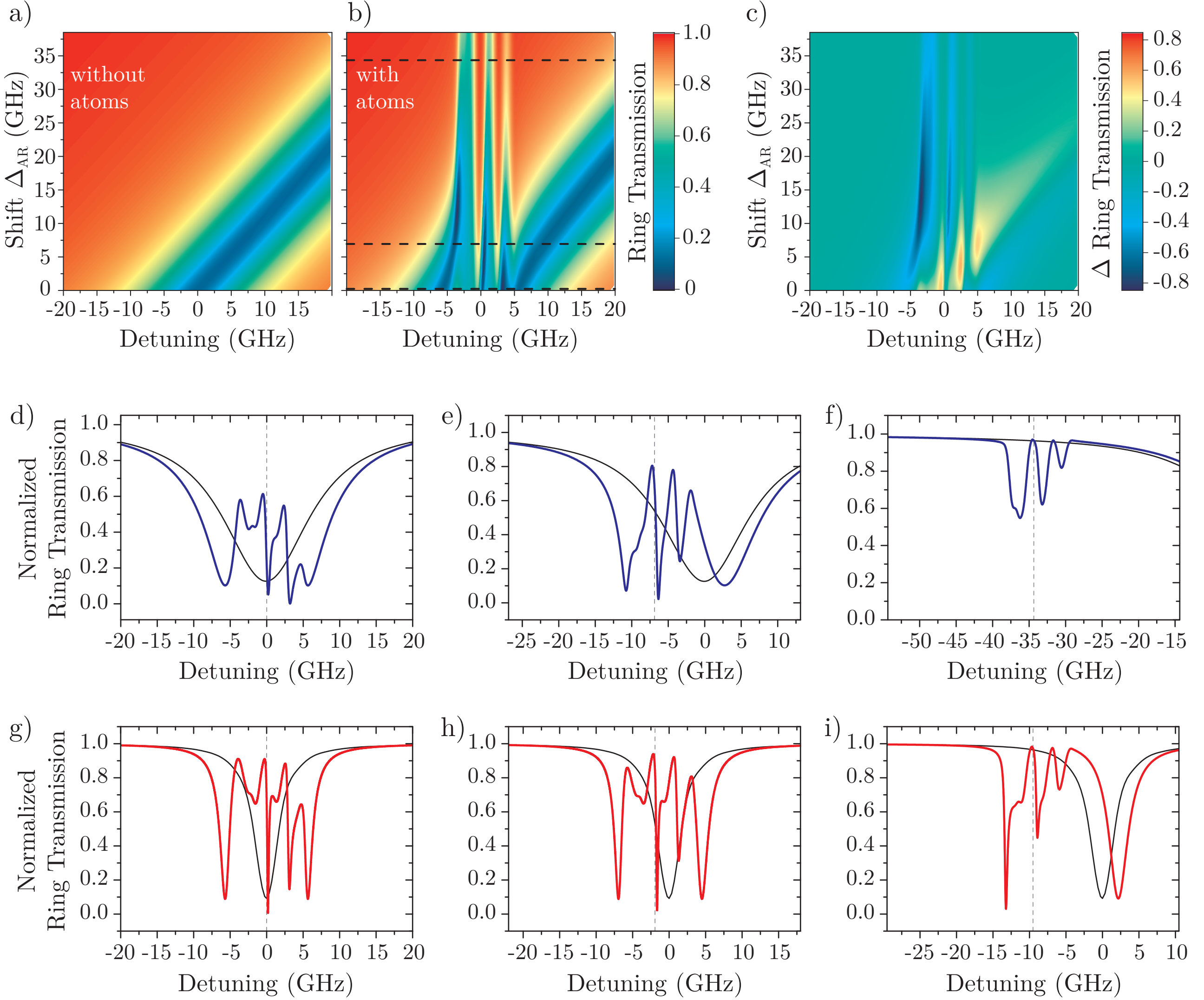

Figure 3.12.: a)-c) Comparison of the ring transmission without and with the atom vapor depending on the detuning from the center of the Rb D2 line and the atom-resonator shift Δ_{AR}. The difference of the transmission in (c) shows that a maximum modulation is achieved at $\Delta_{\mathrm{AR}} \approx 10\,\mathrm{GHz}$, corresponding to a position on the slope of the resonance. Here, a ring with a quality factor of 2.8×10^4 is considered. In d)-f) the ring transmission at the indicated position by the dashed lines in (b) is given. The black line shows the reference transmission of the ring without the atom vapor. Here, zero detuning corresponds to the center of the Rb D2 line, while the vertical dashed lines indicate the atom-resonator shift Δ_{AR}. Similarly, the response of a ring resonator with a high quality factor of 1×10^5 is given in g)-i). For all graphs a Rb temperature of 140 °C is used ($N \approx 50\,\mu\mathrm{m}^{-3}$).

without and with the atoms is compared depending on the detuning from the Rb D2 line and the atom-resonator shift Δ_{AR}. As can be seen in (c) the maximum modulation in the ring transmission due to the presence of the atoms is achieved for an atom-resonator shift of 5-15 GHz, which corresponds to a position on the slope of the resonance (resonance width ~14 GHz). This is also visible from the spectra shown in d)-f) where a position right in the center of the resonance (d), on the slope of the resonance (e), and off-resonance (f) is chosen. On the slope of the resonance a large modulation of approximately 70 percentage points is obtained (transmission dip at ~ -10 GHz in (e)). Similarly, the response is calculated for a ring with a high quality factor of 1×10^5 and ER of 10 dB, also on resonance (g), on the slope (h) and slightly off-resonance (i). As the width of this resonator is in the same order as the transition width, a very strong response is visible and a large modulation of the output signal can be expected when the ring is exposed to the atom vapor. In this case the influence of the phase shift and the attenuation are not anymore clearly distinguishable. Only in (i) the left part of the spectrum is mainly caused by the attenuation in the bus waveguide, while the influence of the real part of the effective mode index at the resonance position is still strong enough to significantly shift the ring resonance.

A ring resonator with a quality factor up to 1×10^5 at a wavelength of 780 nm is realizable as shown in Sec. 2.4.3. However, the protection of the waveguide surface from the atom vapor has to be increased in order to reduce atom adsorption. This might be possible by studying different protection materials and atom desorption can be triggered by high-intensity laser pulses [296–300]. Thereby, an interaction response as discussed above is within reach. Besides increasing the resonator quality or decreasing the cavity mode volume, the interaction between the atom vapor and guided mode can also be enhanced by maximizing the external field e. g. by using slot waveguides.

3.6.5. Atom Clad Slot Waveguides

The waveguide geometry greatly influences the amount of the external field which interacts with a potential atom vapor. By the use of slot waveguides (see Sec. 2.2.3), the area of the maximum field strength can be confined to a region in between two dielectric strips rather than being at the core of a solid waveguide and is thus directly accessible by the atom vapor. A sketch of the device used for coupling to the atom vapor is shown in Fig. 3.13. In (a) it can be seen, that only a short straight part where the slot is located is defined as the interaction area, with a zoom in (b) on the slot where the main part of the mode is confined in. The actual simulated mode profile of an ideal slot geometry with a very strong field confined between the two Si_3N_4 strips is depicted in (c).

For studying the interaction between a mode confined in a slot waveguide and the atom vapor the following geometry on the vapor cell platform is utilized. A 650 nm wide ridge waveguide is splitted into two strips of 400 nm width with a designed slot width from 30 nm to 250 nm in between them. The HSQ cover defines the interaction region to the atom vapor, consisting of the straight slot waveguide with a length of 200 µm. As before, the sample is covered by a 7 nm alumina protection layer. The

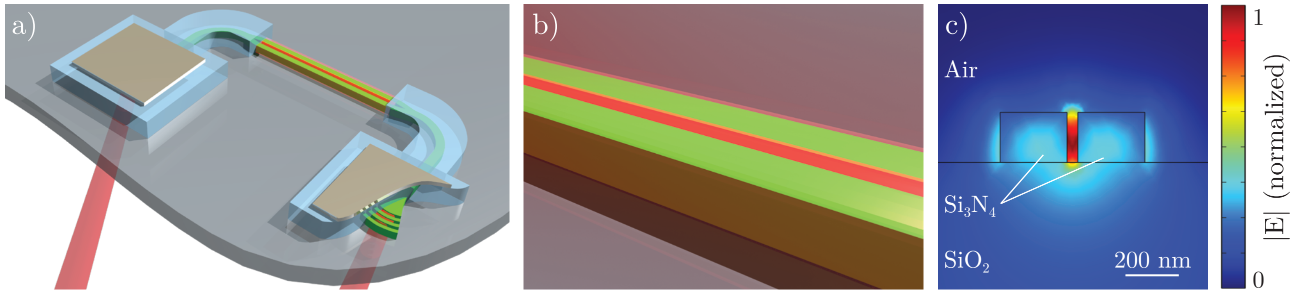

Figure 3.13.: a) Sketch of the slot waveguide device for coupling to an atom vapor with a zoom in on the slot region in (b). The actual simulated mode profile of an ideal slot geometry (c) shows a very strong field confined in the gap between two Si_3N_4 strips.

transmission spectrum for the different slot widths is recorded at an atom density of $N \approx 350\,\mu\mathrm{m}^{-3}$ for an input power of 400 pW, which is well below the saturation power. An example spectrum is shown in Fig. 3.14 a) for a slot width of 75 nm. The width of the absorption lines is greatly increased due to transit time, enhanced Doppler, and self broadening. Thus, in order to extract the spectrum characteristics a series of four Voigt profiles corresponding to the four sets of dipole transitions is fitted to the data. A good agreement of this fit to the data is shown by the red curve in the graph. From these fits, the optical depth as well as the width is extracted. The optical depth depending on the designed slot width is presented in Fig. 3.14 b).

The optical depth should be directly related to the relative part of the optical field that interacts with the atom vapor. For an ideal slot geometry the fraction of the external field is extracted from numerical simulations. The simulation results suggest that a maximum fraction of external field strength is reached for a slot width of approximately 75 nm. However, this clearly differs from the recorded data of the optical width. A main reason for this deviation can be found when studying the fabricated slot geometry. Therefore, onto the sample a thin gold film is deposited as a conductive layer, focused ion beam (FIB) cuts perpendicular to the slot direction are performed and the actual slot waveguide cross section geometry is extracted from SEM micrographs of the cut through waveguides. From these micrographs it is revealed that the slot is only completely open for a designed width larger than 125 nm and it is slightly smaller than designed. Additionally, the slots with a designed size between 50 nm and 125 nm are not completely developed down to the substrate and for a size smaller than 50 nm, there is no slot at all visible. The reason for this are the resolution limit of the EBL resist for very thin slots below 50 nm, the possibility of tiny resist leftovers along the bottom edge of the slot after resist development, and an impeded dry etching process in very small openings.

For each slot size the actual obtained geometry is used for further numerical simulations of the mode profile and the now extracted fraction of the external field is shown in Fig. 3.14 c). The qualitative course of the graph is similar to the one of the optical depth in panel (b) and it can be followed that the external field strength is in fact a main factor for the interaction strength between the guided mode and the surrounding atom vapor. In order to find a quantitative description of not

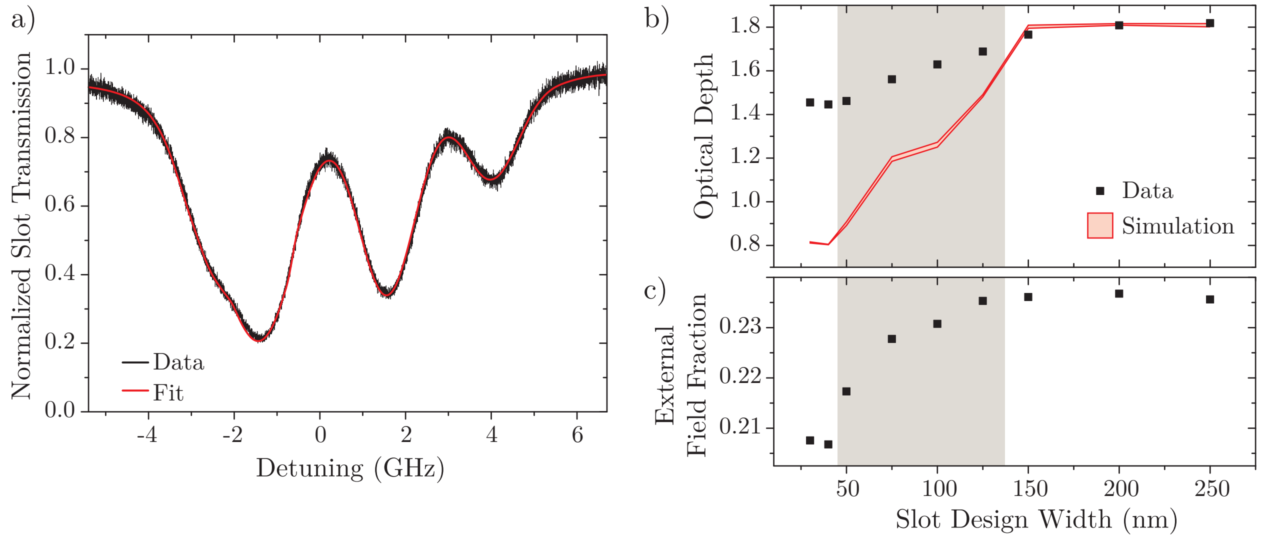

Figure 3.14.: a) Transmission spectrum for a slot waveguide with designed 75 nm gap. The red line is a fit of a series of Voigt profiles to the data. b) Optical depth depending on the designed slot width. The grey shaded region marks the waveguides with not completely open slot. For even smaller slot sizes < 50 nm, there is no gap at all visible between the Si_3N_4 strips. c) Considering the actual waveguide geometry extracted from FIB/SEM micrographs, the fraction of the external field is calculated, which shows the qualitatively same behavior as the optical depth in (b).

only the expected optical depth, but also the transition width and a possible frequency shift a more sophisticated theoretical model is developed by Ralf Ritter[7] and Helge Dobbertin[8]. This model is based on Monte Carlo simulations of atomic trajectories in which the time-dependent optical Bloch equations are solved for each atom. Furthermore, the atom-surface interactions are considered by the introduction of a Casimir-Polder potential. A detailed description of the model and its applications is given in [231]. The resulting optical depth calculated with this model for the specific waveguide geometry and normalized to the experimentally obtained maximum value is shown by the red shaded area in Fig. 3.14 b). Even though the course of the graph is similar to the experimental data, there is still a discrepancy in the quantitative description for the slot geometries with only a partially opened or a completely closed slot. Simply expressed, in this area either the strength of the optical field itself or the atom density in the field is smaller than assumed.

A possible decrease of the optical field strength is discussed in the following. A potential explanation for this effect could be the existence of further optical modes supported by the waveguide geometry that exhibit their maximum strength rather in the waveguide or substrate than in the slot region. Therefore, the supported optical modes for the various slot geometries and their respective effective mode index are numerically simulated. The results are shown in Fig. 3.15 a) and b). In fact, besides

[7] Research group of Prof. Dr. Tilman Pfau, 5th Institute of Physics, University of Stuttgart, Stuttgart, BW 70569, Germany

[8] Research group "Quantenoptik makroskopischer Systeme" of Prof. Dr. Stefan Scheel, Institute of Physics, University of Rostock, Rostock, MV 18059, Germany

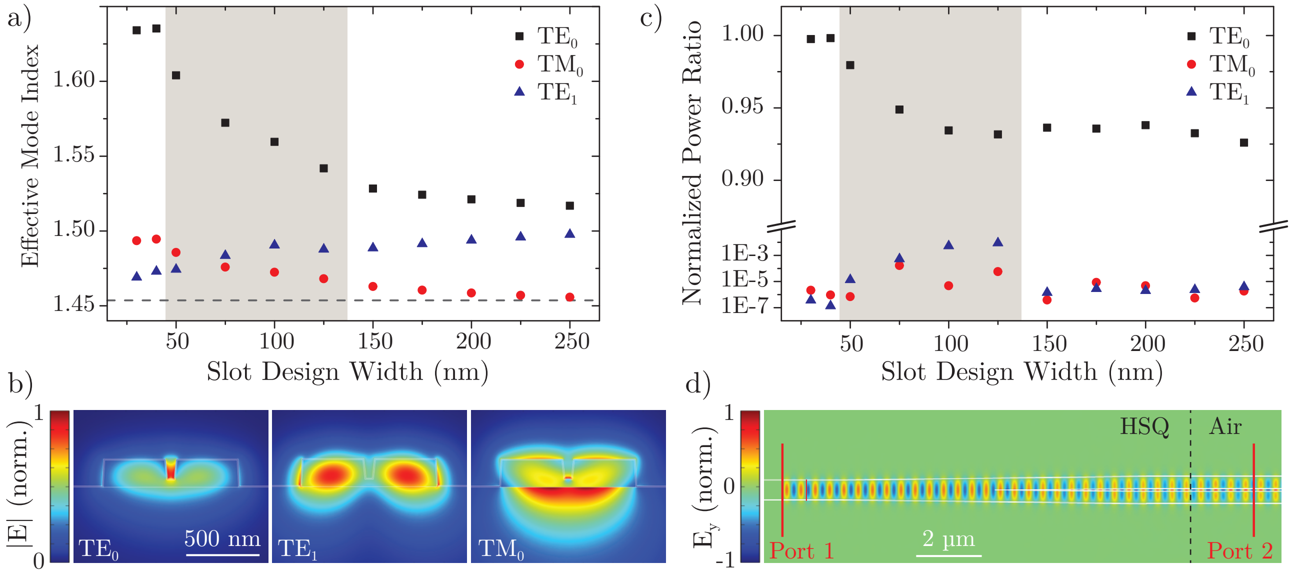

Figure 3.15.: a) Effective mode index of the supported modes in the simulated slot waveguide based on the geometry obtained by FIB/SEM micrographs. The grey shaded area marks the waveguide where the slot is not fully open. For a smaller slot design width there is no slot at all visible. The dashed line indicates the cutoff. b) Simulated mode profiles for a 75 nm slot design width, which is only partially opened during fabrication. Also the ∼7 nm Al_2O_3 protection layer is included in the simulation. c) Simulated fraction of power coupled to the respective modes in the slot waveguide when the fundamental TE mode is considered as the input mode in the ridge waveguide. d) Top view of the 3D model for the transition between ridge and slot waveguide. At port 1 in the ridge waveguide the fundamental TE mode is excited and the power in the different modes at port 2 is monitored. The dashed line indicates the part of the waveguide which is covered by HSQ in order to define the interaction length along the slot waveguide.

the fundamental TE mode there is a second TE and a TM mode supported. However, both modes are rather close to the cutoff (dashed line) and therefore are only weakly guided and are easily lost from the waveguide by scattering. In panel (b) the mode profiles of these three modes are shown for the case of a designed slot width of 75 nm, which is however not fully opened during the fabrication process.

Assuming that these modes are actually supported by the slot waveguide, it is questionable if a significant fraction of the light is coupled to those modes. Hence, a 3D model of the transition between the ridge waveguide and the slot waveguide is employed. In the ridge waveguide a TE and a TM mode are supported, but it is assumed, that light is only coupled to the TE mode via the grating couplers. This is justified as the polarization is adjusted before coupling to the integrated circuit and it is optimized for maximum transmission of the TE mode. In addition, the output of a reference ridge waveguide device without the slot is monitored and only a single transmission peak is observed. In case of coupling to the additional TM mode (with a different effective mode index), a second peak would be visible. Thus, in the model of the transition to the slot waveguide only the TE mode is excited in the ridge waveguide and the power for each mode in the slot region is monitored. The relative power in

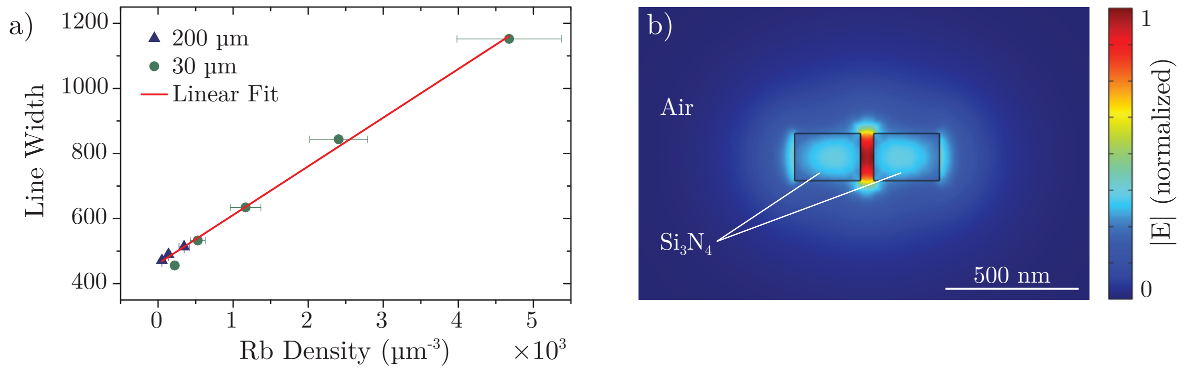

Figure 3.16.: a) Dependency of the Lorentz line width on the Rb density for slot devices with a 30 µm and 200 µm interaction length. b) The mode profile of a suspended slot waveguides shows that a main part of the field is located external from the waveguide.

reference to the input power for each mode is given in Fig. 3.15 c) depending on the designed slot width. The top view of the simulation geometry and the development of the electric field at the transition to the slot waveguide is shown in panel (d) for a slot width of 75 nm as in (b). It can be seen that the vast majority of the input power is coupled to the fundamental TE mode, which is located in the slot region. Only a negligible fraction is coupled to the other modes, which are likely to be eliminated from the waveguide via scattering. Therefore, the reason for the deviation in the interaction strength between the theoretical model and the experimental data for the partially developed slots must be found elsewhere. Employing the theoretical model with an artificially decreased atom density by increasing the adsorption rate of the atoms compared to a negligible desorption (and thereby leaving a thermal equilibrium), indeed shows a better agreement to the data, but it is unclear how such a constructed behavior reflects the real experimental conditions. Hence, further systematic investigations of the interaction in slot waveguides are needed with e. g. varying etching depths and improved fabrication of narrow slots. For example, by using HSQ or ZEP 520A as an EBL resist a better spatial resolution in the exposure can be achieved and increasing the etching time in combination with a higher power should enhance etching results in tiny slots.

Finally, the influence of atom-atom interactions in the evanescent field on the line width is studied. Several transmission spectra with increasing atom density are recorded for the device with a designed slot width of 50 nm and an interaction length of 200 µm as well as 30 µm. The Voigt width is extracted from a fit to the spectrum and the Lorentzian contribution is calculated by assuming a Doppler broadening corresponding to the effective mode index and the cell temperature. The resulting width depending on the atom density is presented in Fig. 3.16 a). The linear increase with the atom density is attributed to self broadening due to resonant dipole-dipole interactions between the atoms [290, 301]. The total width can be described by $\Gamma_{\mathrm{tot}} = \Gamma_0 + \Gamma_{\mathrm{TT}} + \beta_{\mathrm{S}} N$, with the natural line width Γ_0, the transit time broadening Γ_{TT}, the atom density N, and the self broadening coefficient β_{S}. From a linear fit to the data the self broadening coefficient is found as $\beta_{\mathrm{S}} = (1.5 \pm 0.3)10^{-7}\,\mathrm{Hz\,cm^3}$, which agrees to the

value of $(1.10 \pm 0.17)10^{-7}$ Hz cm^3 found in Ref. [294] from total reflection spectroscopy.

In order to further increase the interaction strength, a suspended slot waveguide is considered for future devices. In the fabrication process used here, this can be realized by hydrofluoric acid (HF) etching of the substrate below the waveguide. For example, after the metalization step and subsequent lift off for the mirrors, a fourth EBL step could be carried out for the creation of a PMMA mask that defines windows at the slot waveguide position. This PMMA mask can be directly used as a mask for the wet etching of the substrate below the slot waveguide. Subsequently, after removing the PMMA layer, the alumina protection layer would be deposited as a last fabrication step before the chip is bonded to the vapor cell. By suspending the slot waveguide, the mode is better confined in the slot region, the cutoff is lowered to 1 due to the surrounding air, and the atoms are able to surround the waveguide from all sides. A simulated mode profile is shown in Fig. 3.16 b), for a slot width of 50 nm and a Si_3N_4 strip width of 300 nm. Thereby, a very large fraction of 72 % for the external field can be realized compared to a value of approximately 24 % for the fabricated slot waveguides so far and of 20 % for the employed ridge waveguides.

3.7. Summary and Outlook

In this chapter the near-field coupling in a hybrid device between a guided waveguide mode and a surrounding thermal rubidium vapor has been investigated. A theoretical model was utilized to describe the evanescent atom-light interaction and the experimentally found device responses were compared to the model. In basic linear spectroscopy measurements the attenuation corresponding to the D2 transitions of the Rb atoms was studied. When scanning over the atoms transitions, the absorption is accompanied by a variation also in the real part of the refractive index of the atom vapor. In phase-sensitive measurements via integrated Mach-Zehnder interferometers the induced phase shift in the waveguide mode via the atom vapor was quantified. While exploiting this phase shift at the precise spectral position of the D2 transitions might be limited due to the simultaneous absorption, it can be utilized when choosing a wavelength on the slope of the transition, where the induced phase-shift is still strong and the attenuation subsided already. Thus, integrated optical phase switches and shifters depending on the atom presence are realizable.

In a further step the response of ring resonators surrounded by the Rb atom vapor was studied. Therein, the interplay between both absorptive and dispersive properties of the atoms determine the precise transmission spectrum. The strength of the obtained interaction was also compared to typical cavity QED parameters with an estimation that strong coupling is achievable in future devices. Especially, when increasing the ring quality, a very strong response in terms of the modulation and the spectral shift of the resonance is expected. It was shown that a ring resonator quality factor up to 1×10^5 can be realized in the visible regime, but improvement on the protection of the waveguide from atom adsorption is needed for avoiding a degradation of the cavity quality when exposed to the atom vapor. Furthermore, the migration of the interaction from the visible to the NIR regime around $\lambda =$

1550 nm will be of great interest. For this purpose the two photon transition $5^2S_{1/2} \rightarrow 5^2P_{3/2} \rightarrow 4^3D_{3/2}$ can be used, which consists of the D2 transition followed by a transition at 1529 nm. By irradiating the atom vapor with light corresponding to the D2 line, the intermediate $5^2P_{3/2}$ state is populated and the upper transition is enabled. Thus, the ring response in the presence of a Rb vapor in the NIR can be studied. In this regime a very high ring resonator quality factor of up to 1×10^6 was achieved and a strong interaction of the resonator mode to the atom vapor is expected. By e. g. adding a drop port to the resonator all-optical switching and modulation via the ring is enabled. Additionally, the integration of an atom vapor in ring resonator arrays was proposed, where topological edge states are studied [92, 93]. Furthermore, instead of using ring resonators, photonic crystal cavities offer the advantage of very small resonator mode volumes. Thereby, a potential path to strong coupling to the atom vapor is enabled in future devices.

A further possibility of increasing the interaction strength between the guided waveguide mode and the atom vapor was explored by using slot waveguides. By confining a main part of the mode in the slot region rather than in the solid waveguide core the external field strength can be largely increased. Even though the fabrication process limited the effect here, a huge potential for further improvement was illustrated especially for suspended slot waveguides when the substrate is removed via wet etching. This might also offer the possibility of using a suspended slot waveguide as an opto-mechanical cavity and couple the atom transitions optically to a mechanical resonator. Additionally, it is intended to bend the slot waveguides to ring resonators in order to combine the strong interaction in the slot region with a cavity mode. Similarly, the interaction within double beam photonic zipper cavities can be studied in future circuits [302–305]. These devices consist of two waveguide strips likewise to slot waveguides and a photonic crystal structure is included in the beams. Thereby, an effective photonic crystal cavity for the slot region is realized, which combines a very strong optical field in the slot with a very small cavity mode volume.

Therefore, within the integrated photonics platform presented here a diverse range of devices were realized, which utilize the different aspects of the atom-light interaction. By accessing the photonic circuits via grating couplers through the transparent substrate instead of e. g. coupling via a facet, it is possible to place devices at arbitrary positions on a sample, make use of the complete sample area, and reduce the device footprint. This platform can be employed for (all-optical) switching, modulation and routing based on integrated ring resonators. It can be used to implement attenuation spectroscopy or phase dependent sensing schemes and it can serve as an on-chip Doppler-free frequency reference based on counter-propagating beams in future devices.

Chapter 4.

4 Near-Field Coupling to and from Single Elements

In this chapter, a selection of hybrid integrated photonic circuits that are based on the coupling of single elements to Si_3N_4 waveguides are presented. The main focus is set on the on-chip integration of single photon sources. As an introduction to the use of layered materials the interaction between a waveguide mode and a graphene layer is discussed in the first section. The development of these devices has already begun in the work preceding this thesis [100] and the results have been published in Ref. [101]. The coupling of a quantum emitter incorporated within layered gallium selenide (GaSe) crystals to a Si_3N_4 waveguide is presented in the second section. This project was realized in cooperation with Philipp Tonndorf (in the group of Prof. Dr. Rudolf Bratschitsch at the University of Münster[1]), who transferred the GaSe layer onto the photonic structures and measured the device response. The results have been published in Ref. [79]. An alternative single photon source is presented in the third section by the use of organic-molecule-based quantum emitters. DBT molecules embedded in an anthracene matrix are placed on top of a Si_3N_4 waveguide and the single photon emission into the waveguide is evaluated. This project was realized together with Anna Ovvyan in our research group and in cooperation with Pietro Lombardi in the group of Dr. Costanza Toninelli at LENS Florence[2]. The results have been published in Ref. [306]. In order to give a comprehensive description of the coupling schemes for single photon circuits used in our research group, carbon nanotubes (CNTs) as electrically driven single photon sources and superconducting nanowire single photon detectors (SNSPDs) are briefly discussed in the last section. The main research in these two fields has been carried out by Svetlana Khasminskaya and Simone Ferrari who published their results in Ref. [141, 307–313]. In both cases, the Si_3N_4 material platform (see Chap. 2) which has been developed during the work for this thesis was used for the implementation of the photonic circuits.

[1] Ultrafast solid-state quantum optics and nanophotonics, Institute of Physics, University of Münster, Münster, NRW 48149, Germany

[2] National Institute of Optics (CNR/INO), European Laboratory for Non-Linear Spectroscopy (LENS), Florence, 50019, Italy

4.1. Coupling to Graphene - 2D Carbon Material

The discovery of graphene, a strictly 2D crystal, in 2004 gave rise to a whole new research field, which addresses the properties and applications of atomic monolayer materials [314]. Graphene consists of a single layer of carbon atoms arranged in a honeycomb lattice, which causes its unusual linear electronic dispersion (typically referred to as the cone-like dispersion) around the neutrality points [315]. In this region the dispersion can be described by a 2D Hamiltonian for massless fermions and accordingly graphene mimics the physics of QED at much smaller speed and room temperatures [316–318]. Besides, graphene displays a strong field-effect-transistor behavior [319] with an extremely high charge carrier mobility [320, 321] and current sustainability [322], which are exploited for the realization of high frequency transistors [323–326]. Additionally, graphene shows some unique optical properties including the often stated broadband absorption of 2.3 % of a single graphene sheet [327–329] as well as electrically controllable interband excitations [330–332].

Especially the combination of electronic and optical properties renders graphene interesting for many applications [333], for example as a transparent flexible conductive layer [334–337], as a photodetector [65–67] or an electro-optical modulator [62–64]. The on-chip integration of graphene with nanophotonic circuits is a first step towards near-field coupling between a waveguide mode and a layered material system. Such a system is described in the next section about the coupling of single-photon emitters in GaSe to a nanophotonic waveguide. Placing a material flake on a waveguide offers an enhanced interaction due to the strong optical field confined in the small waveguide and an interaction path along the material sheet. The characterization of the graphene-light coupling is described in this section.

The Si_3N_4 platform is used for the fabrication of high-quality MZIs, which are operated in the NIR regime at a wavelength of 1550 nm. Rib waveguides with an etching depth of 170 nm and a waveguide width of 1.15 µm are used. The induced attenuation of a graphene sheet placed on a waveguide is accessed by evaluating the ER of MZIs where graphene flakes with varying length are arranged on one of the interferometer arms. For this purpose a large graphene layer grown by chemical vapor

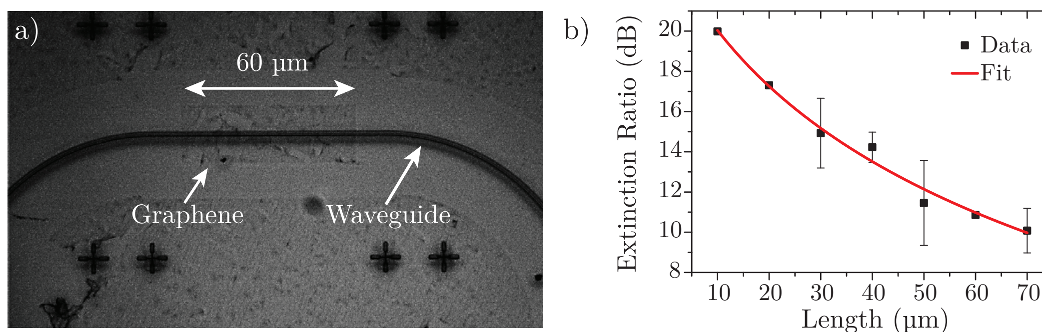

Figure 4.1.: a) Optical micrograph of a 60 µm long graphene flake on top of a Si_3N_4 waveguide. The shape of the flake is structured in an oxygen plasma via a PMMA mask. b) Extinction ratio of a MZI in dependence of the length of the graphene layer which is placed on one of the interferometer arms.

deposition (CVD) is transferred onto a sample by using a stamping technique. With the help of a PMMA mask the graphene layer is structured in an oxygen plasma processing step so that a flake with a certain defined length remains on the waveguide. The optical micrograph in Fig. 4.1 a) shows a 60 µm long graphene layer on top of a waveguide. The extracted ER is depending on the length of the graphene flake. This is presented in Fig. 4.1 b). As described in Sec. 2.2.2, the ER decreases with increasing attenuation in one of the arms. A theoretical curve according to Eq. (2.18) is fitted to the data and an attenuation coefficient for the coupling to the graphene layer of (0.067 ± 0.008) dB/µm is extracted. This agrees well with a theoretical calculation of the optical conductivity of graphene, which is used to simulate the guided modes of a waveguide with a graphene cladding. Thereby, an attenuation coefficient of 0.066 dB/µm is obtained.

With this approach integrated graphene-based nanophotonic devices can be realized. The graphene layer can be contacted electrically and if a gate electrode is added, this configuration can for example be used as a compact fast electro-optical modulator or as a photodetector. The interaction strength can be further increased by using a waveguide geometry which supports a TM mode that exhibits a strong field at the top interface of the waveguide. An alternative geometry consists of a vertically stacked slot waveguide where the graphene layer is placed in the middle of the waveguide sandwich structure. Thereby, the near-field coupling to the waveguide mode can be effectively enhanced as the optical field at the graphene position is increased.

4.2. GaSe Multilayer as Single-Photon Source

Since the discovery of graphene, the search for further 2D materials has attracted a lot of attention due to their exceptional physical properties. In particular transition metal dichalcogenides such as WS_2, MoS_2, WSe_2, $MoSe_2$, and $MoTe_2$ are in the research focus. When thinned down to a monolayer, these semiconductors exhibit a transition in their bandgap from an indirect to a direct one [338–342]. Recently, single-photon sources in several 2D materials have been identified, which represent a new kind of emitter for photonic quantum information systems [68–77]. Single-photon emission is caused by the localization of excitons at quantum dots, impurities or strain induced potential traps within the 2D materials. Similar emitters based on strain-induced confinement potentials have been discovered in layered gallium selenide (GaSe) crystals [78]. GaSe exhibits a layered crystal structure with strong covalent intra-layer bonds and weak (predominant van der Waals) inter-layer bonding. Thin crystals with a thickness in the order of a tens of nanometers can be fabricated by mechanical exfoliation from bulk slabs. Incorporated nanoscale selenium clusters lead to local deformations of the crystal structure. In this way, single-photon emission arises from trapped excitons at the induced potential wells.

In this section, the near-field coupling of single-photon emitters in layered GaSe crystals to pre-fabricated waveguides for the realization of on-chip sources is described. Therefore, Si_3N_4 integrated photonic circuits fabricated from a 200 nm thick device layer on a 2 µm silica-on-silicon substrate are

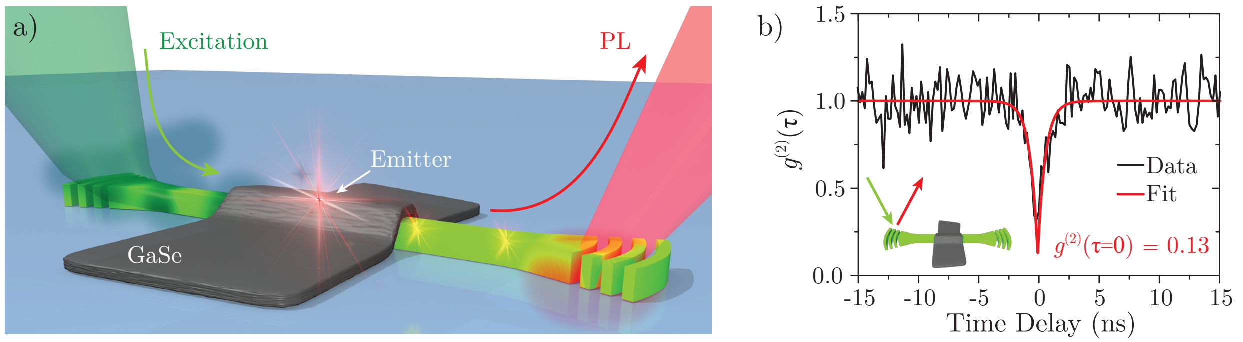

Figure 4.2.: a) Artistic view of the GaSe flake (grey) ontop of the waveguide, which is terminated by two grating couplers. An emitter in the GaSe flake can be excited via the waveguide by light with a wavelength of 532 nm (green arrow). The emitted single photons propagate along the waveguide and can be collected at the grating couplers (red arrow). b) Second order correlation function $g^{(2)}(\tau)$ for excitation and PL detection via one grating coupler (see inset). A $g^{(2)}$ value of 0.13 for zero time delay confirms the emission of single photons.

used. An etching depth of 150 nm is employed for the creation of rib and slot waveguides. The waveguide attenuation is determined by the cut-back method as 4.4 dB/cm. Focusing grating couplers with a coupling efficiency of approximately 25 % for a wavelength of 625 nm are used to access the integrated photonic circuits. Similar to the graphene transfer, a GaSe flake is placed on top of a waveguide with a stamping technique. An artistic view of the configuration is presented in Fig. 4.2 a). Due to the large refractive index of GaSe ($n \approx 3$) compared to Si_3N_4 ($n \approx 2$), in the part which is covered by GaSe the waveguide mode is pulled up into the crystal. Thereby, embedded emission centers in the close vicinity to the waveguide can be efficiently excited by a guided mode. The emitted photoluminescence (PL) signal is collected by the same waveguide and transmitted to the grating couplers at both ends. However, not all of the emitted light is coupled to the waveguide and the PL signal can also be detected directly at the emitter position as well as at folds and the edges of the GaSe layer (due to the crystal thickness of approximately 90 nm the GaSe layer can act as a slab waveguide itself).

To study the PL response of the device, the sample is placed in a helium-flow cryostat ($T = 10$ K) and the excitation is spatially separated from the detection within a reflection-based laser scanning confocal microscope. Light from a continuous-wave laser with a wavelength of 532 nm is used for the excitation and the PL signal at a wavelength of ~625 nm is separated from the input path by a beam splitter. The output signal is filtered with a 560 nm long-pass filter and sent to a monochromator. At the exit slit a Hanbury Brown and Twiss (HBT) setup is attached, which consists of a 50:50 beam splitter and two avalanche phtoto detectors (APDs) with a time resolution of 50 ps. The HBT setup basically compares the relative arrival time of detected photons. Thereby, the second-order correlation function $g^{(2)}(\tau)$ of the PL emission can be recorded, which is used for the light source characterization [343].

Several different configurations are tested in this setup. Direct excitation of an emitter in the

GaSe layer on top of the waveguide as well as excitation via the grating coupler and waveguide is combined in all possible ways with PL detection directly from the emitter as well as from both grating couplers. In all configurations $g^{(2)}(\tau = 0)$ is well below 0.5, which confirms the single-photon behavior of the emission and the coupling thereof to the integrated photonic circuits. The $g^{(2)}(\tau)$ signature for excitation and detection via the grating couplers and the waveguide is presented in Fig. 4.2 b) with $g^{(2)}(0) = 0.13$. Furthermore, in this experiment a lower limit for the coupling efficiency of the emitter into the waveguide of 3.5 % and a minimum internal quantum yield of the emitter of 17 % is estimated. Additionally, the single photon emission under pulsed excitation is confirmed. Since GaSe also exhibits electroluminescence, these emitters are of particular interest for fully integrated quantum photonic circuits. It should be possible to pump and control the single-photon emitters electrically [344–346], which eliminates the challenge of on-chip separation of the single-photon signal from an optical pump beam. For deterministic positioning of the single-photon emitters, an artificial strain profile could be used to induce their creation [347–349]. This could be realized by a side or surface grating along the waveguide, which could additionally enhance the coupling efficiency. In conclusion, novel single-photon emitters in GaSe layers which are evanescently coupled to waveguides offer a promising approach for sources in integrated quantum photonic circuits.

4.3. DBT Molecules as Single-Photon Source

Molecular emitters represent an alternative platform for single-photon sources, which attract increasing research interest [350–353]. The fluorescence in molecules is caused by a simple quantum process where an absorbed photon causes an electron excitation of the molecules. The recombination of the resulting electron-hole pair via the emission of a photon is detected as the fluorescence signal. However, in many molecules the excited states decay via non-radiative phonon relaxations [354]. Single-photon emission from molecules can be obtained if a single highly fluorescent molecule is selected for the excitation [355]. These molecular sources can exhibit favorable properties such as a sharp emission, a wide range of tunable photon energies, a high stability, electrically driven emission and the usability at room temperature [356–360]. In order to realize fully integrated quantum photonic circuits, the near-field coupling of molecular sources to waveguides is of particular interest. Thus, the integration of DBT molecules with nanophotonic Si_3N_4 circuits is discussed in this section. As the name indicates, DBT molecules consist of two benzene rings fused with a central thiophene ring. Single-photon emission from DBT molecules with an exceptional photostability has been demonstrated at cryogenic as well as at room temperatures[361–363].

The integrated photonics platform comprises 175 nm thick Si_3N_4 waveguides on a transparent silica substrate. A waveguide width of 500 nm is chosen to ensure single-mode propagation at a wavelength of 785.1 nm. This is the emission wavelength of the molecules. The waveguides are terminated at both ends with a grating coupler for out-of-plane access to the circuits. Similar to the photonic structures used for the interaction with an atom vapor (see Sec. 3.3), the grating couplers are embedded in

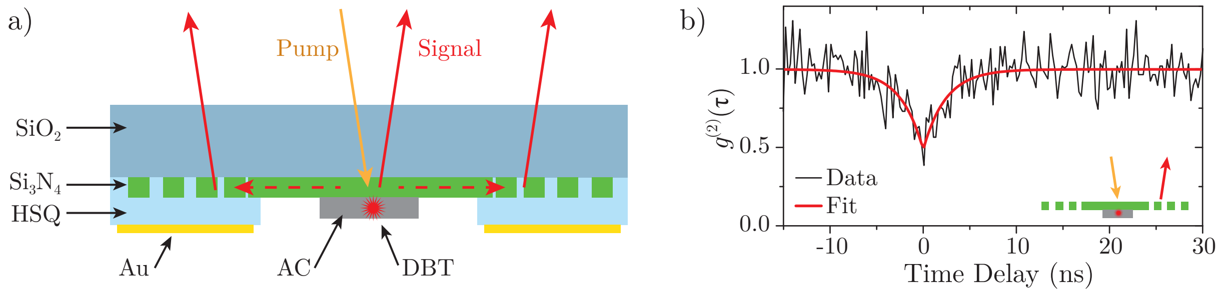

Figure 4.3.: a) Schematic cross-section of the device configuration. The HSQ spacer and gold mirror on top of the grating are used for an enhancement of the coupling efficiency. Here, the case of direct excitation of the DBT molecule via a pump beam is depicted. The signal can be detected directly from the emitter as well as from the two grating couplers. b) $g^{(2)}(\tau)$ signature for direct excitation and detection via a grating coupler (see inset). A $g^{(2)}(0)$ value of 0.49 proves the emission of single-photons.

a 760 nm thick HSQ buffer with a 120 nm Au mirror on top (including a 5 nm Cr adhesion layer). Additionally, an optimized apodization profile for the coupler is used leading to an increased output coupling efficiency through the substrate of 35 %. Single DBT molecules on a waveguide are obtained by embedding them in small anthracene (AC) crystals. This is achieved by drop-wise spin-coating of a DBT in toluene solution, which is strongly diluted with an AC/diethyl-ether mixture. This way, thin AC crystals (with an enclosure of very few DBT molecules) are obtained on the sample. A PL map of the sample is recorded in order to locate emission centers in close vicinity to the waveguides.

For the characterization of the single-photon emission into the waveguide at room temperature the following setup is used: A continuous-wave pump laser at a wavelength of 767 nm is focused onto the sample. Through the same objective as used for the input beam, the emission from the sample is collected. The output signal is separated from the input by a beam splitter and sent through a long pass filter. A specific wavelength of the output is selected by a spectrometer. The signal is either viewed by a CCD camera (for alignment purposes) or sent to an HBT setup (for recording the second order correlation function). A molecular emitter on top of the photonic circuit is either excited directly by a free space beam or by coupling the input light via a grating coupler to the waveguide. For both cases the emission signal is detected directly from the DBT molecule as well as from the output couplers. A schematic cross-section of the device configuration, the excitation beam and the fluorescence signal is presented in Fig. 4.3 a). The main limitation in this setup is the detection of scattered pump light. As the wavelength of the pump beam is rather close to the one of the fluorescence signal, it is challenging to filter the signal. The $g^{(2)}(\tau)$ signature for direct excitation of the emitter and fluorescence detection via one of the grating couplers is shown in Fig. 4.3 b). At zero time delay, a $g^{(2)}$ value of 0.49 is obtained. For direct detection from the molecule a value of 0.33 is obtained. This proves the emission of single photons. The higher value for the coupler output is attributed to a worse signal-to-background ratio than for the direct emission.

As an almost unitary internal quantum yield is obtained for DBT:AC emitters [364], an effective integrated single-photon source at room temperature is realized by this approach. A coupling efficiency

between 20 % and 42 % from the emitter to the waveguide is obtained in this experiment. The variation is caused by a varying distance between emitter and waveguide as well as by the specific in-plane orientation of the molecule dipole with respect to the waveguide mode. In the waveguide the signal is split in the two possible propagation directions but this could be circumvented by the integration of a Bragg mirror in one waveguide direction. Placing a DBT molecule in a slot waveguide could further enhance the coupling efficiency. In terms of scalability, the positioning procedure could be optimized by defining a mask on the sample prior to the spin-coating step of the molecules. Thereby, molecules only attach to the sample surface at predefined locations and excess material can be removed by a lift-off procedure of the mask.

4.4. Summary of Further Coupling Schemes Realized on the Si_3N_4 Platform

In the final section of this chapter two more coupling schemes concerning single-photon circuits are briefly summarized. Both applications use the basic Si_3N_4 platform described in Chap. 2 for the realization of the photonic circuits. First, the use of CNTs as electrically driven integrated single-photon source is described and secondly, on-chip single-photon detectors in the form of SNSPDs are introduced.

The use of CNTs is closely related to the coupling of a graphene layer to a waveguide. A CNT consists of a rolled up sheet of graphene with a certain chiral structure (i.e., the structural offset in the graphene lattice which corresponds to the tube circumference), which causes the specific band profile of the nanotube and thus determines its electrical and optical properties [365, 366]. The use of specific CNTs with well-defined properties is enabled by recent advances in structure-dependent sorting and synthesis of nanotubes [367–369]. Here, semiconducting single-walled carbon nanotubes (sc-SWCNTs) are employed, which show a distinct emission peak at $\lambda \approx 1370\,\mathrm{nm}$. Single-photon emission in CNTs is caused by the recombination of excitons trapped at structural defects or dopants along the tube [370–372]. Such excitions can be generated electrically by impact ionization or carrier injection [373].

In order to contact the CNTs, gold electrodes are placed on the sample with the waveguides in between them. The nanotubes are deposited from a suspension in between the electrodes. A voltage is applied and the CNTs orient themselves perpendicularly to the waveguide as they follow the direction of the electric field between the electrodes during dielectrophoresis. This approach allows for simultaneous nanotube positioning on a large array of devices. A coupling efficiency for the photon emission from the nanotube to the waveguide of $\sim$0.6 is realized [307]. For the evaluation of the nanotube emission the fabricated sample is placed in a liquid-helium cryostat with a base temperature of 1.6 K. The CNTs are driven electrically and the emitted light is collected by the waveguides where it is split equally in both propagation directions. On-chip single photon detectors (see paragraph below) are placed on the waveguide in both directions effectively setting up an HBT configuration. Thereby,

the $g^{(2)}(\tau)$ signature of the CNT source is recorded and a value of 0.49 is obtained for zero time delay [308]. This proves the single-photon emission from sc-SWCNTs as an on-chip source integrated with nanophotonic circuits and single-photon detectors. The minimum $g^{(2)}(0)$ value is limited by the detector performance, by thermal emission from the nanotube as well as by exciton delocalization and lifetime reduction associated with self-heating of the nanotube.

These electroluminescent sources are highly attractive as they do not require optical filtering and provide a tiny device footprint. Additionally, their emission wavelength in a spectral range from the visible to NIR regime can be selected via the nanotube chirality and diameter. An enhancement of the photon emission in combination with a smaller linewidth can be achieved by the integration of CNTs into nanophotonic resonators such as photonic crystal cavities with a small modal volume and a high quality factor [374–379]. Thereby, high-speed light sources operating in the GHz range can be realized [141].

The above mentioned single-photon detectors represent a fundamental building block for the realization of quantum photonic circuits. As a counterpart to integrated single-photon sources, fast and efficient on-chip single-photon detectors are required [380]. SNSPDs are the most promising detection devices as they combine a high temporal resolution, a low dark count rate and a high detection efficiency [381–383]. In contrast to illumination under normal incidence, the integration of these detectors with nanophotonic waveguides leads to light propagation along the nanowire. This results in a drastically increased absorption efficiency due to evanescent coupling of a waveguide mode to the nanowire and it enables compact devices within large-scale integrated circuits [52, 53].

In this paragraph, SNSPDs, which are integrated with nanophotonic Si_3N_4 circuits for efficient detection of single photons at a telecommunication wavelength of 1550 nm, are described. The detectors are fabricated from an approximately 4 nm thick niobium nitride (NbN) film on top of the Si_3N_4 layer. A single meander geometry is chosen for the nanowire with a width between 60 nm and 140 nm. The waveguides and detector patterns are transferred into the respective chip layers and connected to gold contact pads by using several EBL, dry-etching and lift-off steps. The nanowire meander is placed on top of a waveguide and therefore directly in the near-field of a guided mode. The devices are operated inside a liquid-helium cryostat with a base temperature of 1.7 K, which is below the critical temperature of the superconducting nanowires ($T_c \approx 9$ K). The absorption of a photon in the current-biased nanowire leads to a transient breakdown of the superconductivity. The large change in the detector resistance is registered electronically in the readout circuitry as a signal 'click'. For the device characterization the on-chip detection efficiency (OCDE) is measured. It is the product of the absorption efficiency and the internal quantum efficiency. The absorption efficiency is mainly controlled by the coupling strength of a guided mode to the absorptive nanowire on top of the waveguide and the corresponding interaction length [384]. The internal quantum efficiency depends on the kinetics during the breakdown of the superconductivity and thus on the bias current, on the energy of the absorbed photons, and on the nanowire dimensions [383, 385]. By varying the nanowire width and length, an OCDE above 80 %, an internal quantum efficiency close to unity and a minimum

decay time of 5 ns are achieved [312]. Thereby, the suitability of SNSPDs for fast and efficient on-chip detection of single photons is demonstrated.

The presented detection principle is also transferred to a diamond and a silicon integrated photonics platform, which shows the versatility of the SNSPDs [386–389]. The silicon platform is used for the realization of fast detectors with a minimum decay time of 119 ps. This is achieved by using short nanowire bridges across a waveguide, which are placed in a photonic crystal cavity in order to maintain a high detection efficiency.

4.5. Conclusion

In this chapter, the near-field coupling of guided waveguide modes to single elements placed in the evanescent field has been described. This complements the coupling procedure to a collective system represented by the Rb atom vapor, which was discussed in the previous chapter. Through the interaction between a waveguide mode and its surroundings the functionality of the integrated photonics platform can be drastically expanded, which emphasizes the relevance of such coupling schemes. The so far described applications are all based on nanophotonic circuits for device operation in the visible and NIR part of the electromagnetic spectrum. A whole new field for integrated photonic devices can however be developed by extending the usable spectral regime on the infrared side. This is of particular interest for the realization of compact optical sensors enabled by the highly sensitive response of a guided mode to any changes in its environment. Thereby, on-chip devices for molecular spectroscopy and general chemical analyses can be realized. In the following chapter the development of a diamond and a silicon nanophotonic platform meeting the specific requirements posed by this wavelength regime is presented. On these two platforms single-photon detection at long infrared wavelengths might be realizable in future devices via the use of SNSPDs.

5 Chapter 5. Integrated Optics in the Long Wave Infrared Regime

The extension of the wavelength range of integrated photonic circuits from the visible and near infrared regime to the long wave-infrared regime is presented in this chapter. Diamond is introduced as a device material for integrated photonic circuits with diamond on silica for visible and NIR applications and diamond on aluminum nitride as well as suspended diamond for LWIR circuits. Additionally, silicon-on-insulator as well as suspended silicon are studied as a reference material in the NIR and LWIR regime. The fabrication methods for the different material platforms are discussed including the removal of a buffer layer for dree-standing devices, the circuit quality is evaluated and a first step towards sensing schemes based on the device functionalization in the NIR regime is studied. The setup for measurements in the LWIR regime is introduced and the transmission results for the different material platforms at a wavelength of 8 µm are presented. Device operation in this part of the electromagnetic spectrum enables molecular spectroscopy via the evanescent field in future circuits and complements the near-field coupling to an atom vapor in the visible regime (see Chap. 3). Parts of the results presented here have been published in Ref. [390].

5.1. Introduction to LWIR Photonics and Materials

The mid-infrared (mid-IR) wavelength regime is of great interest for integrated photonics because of its wide range of applications in spectroscopic sensing. Typically the mid-IR regime refers to a wavelength interval from 2 µm to 20 µm, with the far-IR region covering even larger wavelengths from 20 µm on. Here we further distinguish this region by labeling the part between 2 µm and 7 µm as mid-IR and from 7 µm to 20 µm as the long-wave infrared (LWIR) region. Both parts form a technologically important wave band [391–393]. On the one hand it encloses two atmospheric windows (3-5 µm and 8-12 µm) of relatively high transparency in the earth's atmosphere [394], which are of particular interest for industrial, atmospheric and security applications, such as thermal imaging and detection,

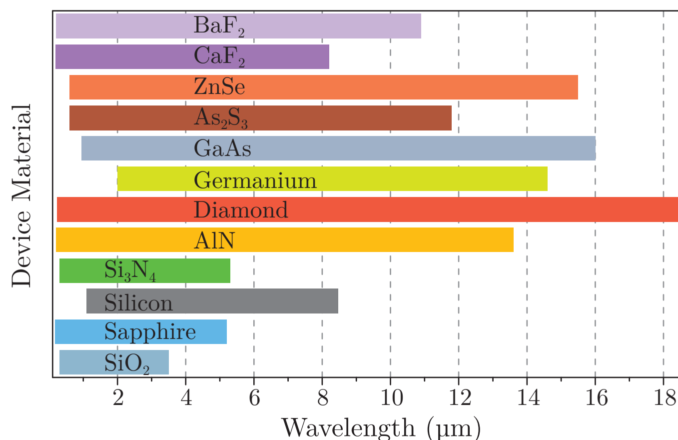

Figure 5.1.: Transparency window for selected materials typically used for integrated photonic circuits and IR components.

communication systems, and infrared homing and countermeasures. On the other hand, it contains the absorption bands of the main chemical bonds as well as the LWIR fingerprint region with the unique spectra of many molecules and functional groups [99]. Therefore, IR optical systems in this wavelength regime and their miniaturization are of great interest for industrial applications as well as for research purposes.

Mid-IR and LWIR optical systems generally require the use of uncommon materials which are transparent in this particular wavelength regime. These materials are often processed by complex fabrication methods, which lead to high production costs. Integrated planar photonic circuits offer an alternative potentially low-cost solution for high-quality optical devices. However, this also depends on the specific selection of device and buffer materials. A selection of typically employed materials for integrated photonic circuits and IR components is presented in Fig. 5.1 based on Ref. [395–405]. The bars represent the transparency window of the different materials. In order to enable IR waveguiding not only the device material, but also the optical buffer to the substrate needs to be transparent for the chosen wavelength and a larger index of refraction for the waveguide compared to the buffer is required to ensure total internal reflection. The transparency of the materials in the IR depends on the onset of phonon excitations. Therefore, light elements like oxygen typically lead to higher phonon frequencies (and limited IR transmission) of e. g. oxides compared to for examples selenides or sulfides.

Typical material platforms for integrated photonic devices in the visible and NIR regime are based on a silica buffer between the device layer and the substrate. This is the case for the wide spread SOI platform as well as for the Si_3N_4 platform introduced as a standard material stack in the previous chapters. Hence, the device operation is limited to a maximum wavelength of approximately 3 µm due to the SiO_2 material absorption. However, if the buffer layer is removed and suspended circuits are obtained, this obstacle is resolved. In this way, suspended silicon devices operating at a wavelength of up to 5.2 µm have been realized with an expected usability up to 8.5 µm [406–415]. Therefore,

suspended silicon is employed here as a reference material in the NIR as well as in the LWIR regime, where the extension of its usable spectral regime up to 8 µm is studied.

Furthermore, chalcogenide (e. g. As_2S_3, ZnSe) and halide (e. g. CaF_2, BaF_2) glasses are common materials for discrete optical LWIR components such as lenses and windows. A range of waveguides have been realized by utilizing these materials [416–423], but they are generally considered not to be compatible with CMOS fabrication processes. However, a hybrid device layout with silicon waveguides indicates that an integration with standard photonic platforms is realizable [424]. Similarly, a Ge-on-Si combination has been used for CMOS compatible processing for mid-IR integrated photonic circuits, in which the Si layer can directly be used as a bottom cladding due to the large refractive index of Ge ($n \approx 4$) [425–430]. One drawback of all silicon based hybrid circuits is that they are limited by silicon's transparency window of 1.1 µm to ∼8.5 µm. Hence, suspended Ge membranes have been employed, which do not depend on the silicon substrate. Thereby, a potentially broadband operation up to ∼14 µm is enabled, but so far only devices with an operational wavelength below 3 µm have been realized on this platform [431, 432].

Diamond offers an alternative versatile material platform for the realization of integrated photonic circuits operating in the LWIR regime. Due to its large bandgap, diamond exhibits a very large transparency window starting close to the UV and stretching into the far-IR. Typically, it only shows an absorption band in the region between 3-6 µm, whose strength is influenced by the diamond growth conditions. In the far IR the material absorption slowly increases up to a wavelength around 500 µm. Thus, diamond offers a potentially ultra broadband device operation unattainable by any other material. However, the choice of substrate might restrict the usable spectral interval because of its limited transparency range. Typically, SiO_2 is chosen as a simple reliable substrate which forms the diamond on insulator (DOI) platform. This is used for applications in the visible as well as NIR regime, but prevents its use in the mid-IR and LWIR region. Here, we introduce aluminum nitride (AlN) as an alternative substrate offering a transparency window from the UV up to around 12 µm. This forms the diamond on aluminum nitride (Di-on-AlN) platform. Only the rather small index contrast of diamond ($n \approx 2.4$) to AlN ($n \approx 2.1$) might limit its usability in terms of the mode confinement. Additionally, fully suspended diamond circuits are presented, which are independent of the choice of substrate. Here, integrated photonic circuits from all three platforms (DOI, Di-on-AlN, suspended diamond) are realized and their performance in the visible, NIR and LWIR regime is evaluated. The diamond properties, fabrication methods and realized integrated photonic devices are reviewed in the beginning of Sec. 5.4.

5.2. Integrated LWIR Photonics Applications

As mentioned above, the mid-IR and LWIR regime plays an important role for thermal imaging, tracing and detection, as well as for communication systems within the atmospheric window. Compared to free-space optical systems built from discrete elements, the introduction of integrated photonic circuits

offers huge advantages in terms of scalability, power consumption and robustness. Low-cost and high-performance circuits can be fabricated in large quantities ideally by CMOS compatible manufacturing methods. Moreover, optical confinement of a light beam in the sub-wavelength scale is provided leading to a strong boost of light-matter interaction and the corresponding signal-to-noise ratio. In the LWIR regime this can be exploited for spectroscopic sensing of molecules and functional groups e. g. for detection of drugs and explosives, for life-science applications and general chemical analyses.

While the interaction to an atom vapor presented above in Chap. 3 utilizes absorption in the visible region of the spectrum based on electronic energy transitions, infrared spectroscopy makes use of molecular vibrations, which give rise to absorption bands in the mid-IR and LWIR regime. These vibrational excitations are briefly discussed in the following paragraphs based on Ref. [433, 434]. Considering a molecule with N atomic nuclei, there are a total of $3N$ degrees of freedom for the motion of the molecule. Three degrees of freedom correspond to the translation of the center of mass and for a non-linear molecule further three degrees of freedom correspond to the rotation of the molecule. This leaves $3N - 6$ internal degrees of freedom corresponding to independent normal modes of vibration. In each normal mode all atoms in the molecule oscillate in-phase and with the same frequency. The relative amplitude may differ in magnitude and direction for each atom, but the center of mass of the molecule does not move and there is no rotation of the molecule.

In a simple model, the atoms can be viewed as masses and the forces connecting the atoms as mass-less springs. If these forces are linear functions of the displacement of the nuclei from their equilibrium position, the molecular vibrations are harmonics, i. e., each atom position is described by a sine or cosine wave. The frequency of a vibrational mode is the first principle observable in IR spectroscopy. Such a vibration frequency depends sensitively on the forces between the atomic nuclei and their masses. The chemical bonds between the atoms are the main factor for these forces but they also include contributions from non-bonding interaction within the molecule and from the molecular environment. In general the frequency of a harmonic vibration increases with the bond strength and decreases with increasing atom masses. Thereby, the frequency distribution of the normal modes of a molecule constitutes a characteristic signature of its chemical composition, structure and electron density distribution in a certain environment. Molecular vibrations can be excited by either inelastic scattering of photons, which is utilized in Raman spectroscopy, or via direct absorption of photons, which is the basis for IR spectroscopy.

When the molecules are irradiated with IR light photons are absorbed when their energy matches the energy difference between two vibrational energy levels and a transition from the initial ground state to the final excited state is induced. Besides the transition frequencies, the intensity of a vibrational band is observable in the spectrum. It is proportional to the probability for a transition between vibrational levels. This is given by the transition dipole moment between the wavefunctions of the vibrational states and the electrical dipole moment operator due to the absorption of a photon. Thus, only transitions with a non-zero dipole moment are called *IR active*. Additionally, the relative orientation of the molecule to the probe light polarization has to be considered. By recording an IR spectrum various

molecules and their functional groups can be uniquely identified. In particular, on-chip spectroscopy using integrated photonic circuits can enable a large enhancement in sensitivity as well as an improved scalability of these devices. This is a driving force for the development of integrated IR devices, which can hugely impact IR optical systems and offers a major growth opportunity for integrated photonic platforms.

5.3. Silicon as Integrated Photonics Reference Material Platform

In this section the silicon material platform for integrated photonic circuits is introduced. First, the standard fabrication process for the realization of circuits operating in the NIR regime is briefly described. Secondly it is discussed how this process is adapted for the realization of suspended silicon integrated photonic circuits suitable for the LWIR regime. The detailed fabrication steps and process parameters can be found in App. A.3.5. The characterization of the platform in the NIR is discussed here, while the device performance in the LWIR is presented in Sec. 5.5.

5.3.1. Fabrication of Silicon Devices

Silicon or rather the SOI platform is the most commonly used material for NIR integrated photonic circuits. It originates from the electronics industry and profits from a wealth of experience in the handling and fabrication of electronic integrated circuits. Here we use commercially available SOI wafers with a device layer thickness of 220 nm on a 3 µm buried oxide layer on a Si substrate[1]. Because of the low etch selectivity of the ma-N 2403 resist compared to the silicon layer in the dry etching step, the ZEP 520A resist with a layer thickness of around 450 nm is used instead in the EBL process. This offers a better etching selectivity and resist resolution, although at the cost of slightly longer EBL exposure times as it is a positive tone resist. After the exposure the resist is developed in xylene and a reflow process on a hotplate is applied directly after development. The duration and temperature of the reflow process are finely tuned to minimize the propagation losses of the fabricated integrated circuits. A baking temperature of 140 °C for a duration of 2:30 min are found as optimal parameters. The pattern is subsequently transferred into the silicon device layer by a chlorine based dry etching process. The gas mixture and flow rates as well as the pressure and applied power are optimized and a recipe based on a Cl_2/HBr plasma is found (see App. A.5). As a last step the remaining EBL resist is removed in an oxygen plasma. Thereby, a fabrication process for high-quality silicon photonic devices operating in the NIR regime is established.

Fabrication Adaption for the LWIR Regime

In order to study the performance of Si devices in the LWIR regime, the oxide substrate has to be removed because of its material absorption and a suspended Si platform is employed. Rib waveguides

[1] Soitec, Bernin, Isère 38190, France

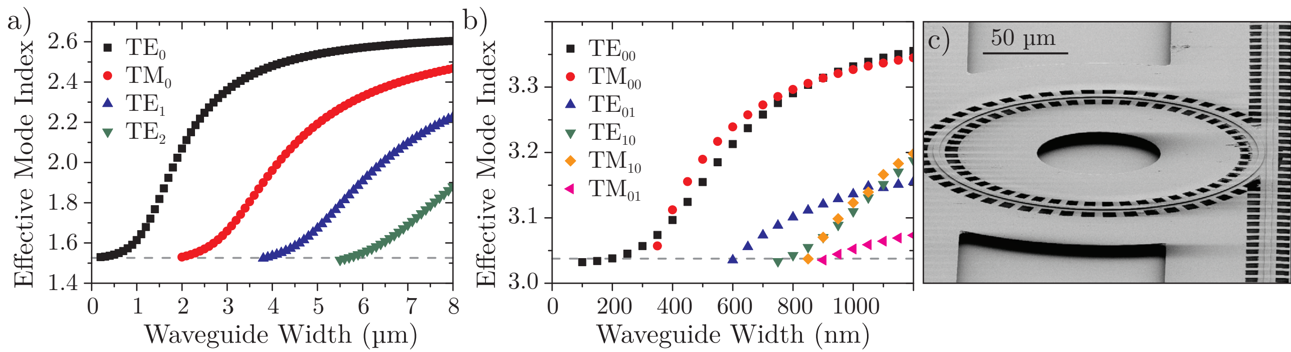

Figure 5.2.: a) Guided modes for $\lambda = 8\,\mu m$ in a 600 nm thick Si rib waveguide supported by a suspended 400 nm Si membrane. b) Same as in (a), only for a wavelength of 1550 nm. In both graphs the dashed line indicates the cutoff between radiative and guided optical modes. c) SEM micrograph of a suspended silicon ring resonator for operation in the LWIR.

with a certain thickness of the remaining Si layer are used. In this remaining Si membrane windows are opened next to the photonic structures. Through these windows the oxide layer beneath the waveguides is dissolved in a wet etching process and free-standing devices are obtained. Numerical simulations show that for a Si layer thickness of 1 µm the waveguide modes at a wavelength of 8 µm can be well confined in the waveguide. The simulated effective mode index of the supported modes is shown in Fig. 5.2 a). Here, a suspended silicon rib waveguide with a height of 600 nm on a 400 nm membrane is considered. For this layer thickness, the number of modes supported by the waveguide can be easily controlled by tuning the channel width. For example, at a width below 2.5 µm only the fundamental TE mode is supported, which simplifies the evaluation of a potential transmission signal, as no other modes have to be considered. If the device layer height is increased to for example 2 µm, guiding of the fundamental TM mode starts at a similar waveguide width as the fundamental TE mode. As it is the aim to use the very same material platform for both the NIR and LWIR regime, the supported modes at a wavelength of 1550 nm are additionally simulated as shown in Fig. 5.2 b). For a waveguide width below 600 nm only the two fundamental TE and TM modes are supported while for a larger width a multitude of higher order modes are additionally guided within the waveguide.

It is difficult to obtain silicon wafers with a device layer thickness of 1 µm. Therefore, wafers with a mean layer thickness of 2 µm±0.5 µm are utilized[2]. However, the uniformity on the wafers is rather poor and shows a variation of up to 500 nm in thickness even within a sample size of 20x20 mm^2. This for example influences the reproducibility of specific devices and might change the device characteristics as a thickness variation leads to a variation of the effective mode index within fabricated circuits. In order to obtain a lower layer thickness, the silicon dry etching recipe is used to thin down the bare samples to a mean silicon device layer thickness of 1 µm. The buried oxide is 5 µm thick, so that when the oxide is removed and suspended structures are formed, the distance to the underlying substrate is large enough to prevent coupling and thus losses to the substrate.

[2] Silicon Materials, Kaufering, BY 86916, Germany

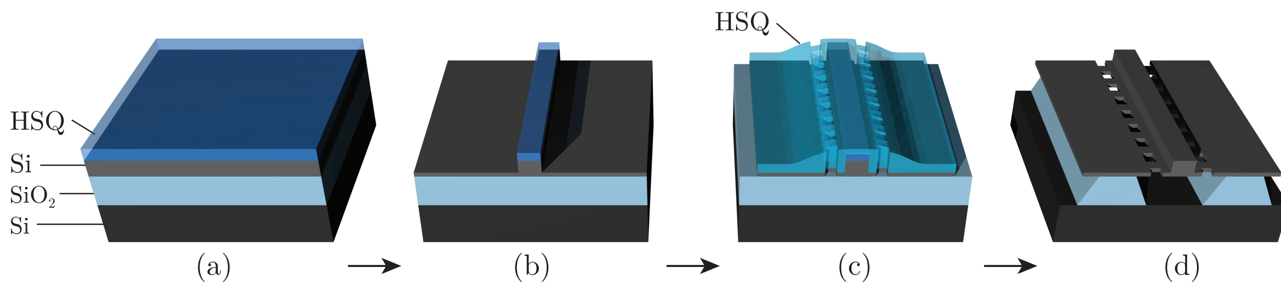

Figure 5.3.: Overview of the fabrication steps for suspended silicon circuits. HSQ is spin coated as EBL resist onto the SOI sample (a). In the EBL step the waveguide area is exposed and the HSQ mask is subsequently transferred into the Si layer via dry etching to form a rib waveguide (b). A second HSQ resist layer is spin coated and a sleeve along the waveguides is exposed. In this sleeve openings along the waveguide are left out during the exposure. Thereby, windows in the mask are created which are transferred into the remaining Si membrane in a further dry etching step (c). As a last step the SiO_2 buffer layer beneath the waveguides is dissolved through the windows in an HF dry etching step, with the side effect that also the remaining HSQ resist is removed. Thus, suspended Si circuits are obtained (d).

An artistic sketch of the process steps for suspended silicon circuits is shown in Fig. 5.3. The fabrication of waveguides from a 1 µm thick silicon layer requires a large selectivity in the silicon etching rate compared to the resist etching rate. This can not be provided by the ZEP 520A resist and thus a 450 nm thick HSQ resist is used, which exhibits a very good etch resistance in the chlorine based plasma (see step (a)). The photonic structures are defined by an EBL process and transferred into the silicon layer via dry etching. The silicon layer is not fully etched but a ∼400 nm thick layer is left on the substrate (see step (b)), which forms the support layer as the buried oxide is removed and the structures are suspended. For realizing such suspended circuits windows are opened in the remaining silicon layer along the whole length of the waveguides with a distance of ∼3.5 µm from the photonic structures. Through these windows the buried oxide in the area of the waveguides can be removed by HF wet etching.

A mask for the windows is defined by a second EBL process again with HSQ as a resist. The remaining HSQ resist on top of the waveguides from the first process step is not removed prior to the second step as it is needed as a protection layer for the waveguides. Without this protection the resist thickness on top of the waveguides in the second spin coating step would be too thin and the waveguides would be attacked during the subsequent dry etching process. The waveguides and remaining HSQ on top forms an approximately 1 µm high barrier in the second spin coating process and a much increased resist thickness is obtained around the waveguide compared to a typically 450 nm thick layer on a flat substrate. This variation in the resist thickness poses a major challenge for the EBL exposure as the required dose directly depends on the resist thickness. In order to define windows close to the waveguide, a wide (∼120 µm) stripe along the waveguide is exposed leaving out only the windows area. Due to the increased resist thickness along the waveguide the inner part of this stripe in close vicinity to the waveguide is exposed with a lower base dose compared to the outer part of the

stripe and both dose values are optimized for achieving fully opened windows while getting a solid mask all around. The HSQ mask is used to transfer the windows into the remaining silicon layer via plasma etching (see step (c)). Thereby, access to the underlying buried oxide layer is gained. In order to couple light from the side of the chip via a waveguide facet, the chip is cut as close as possible to the end facet of the waveguide by the wafer saw. In a subsequent HF wet etching step, the oxide below the area of the waveguides is dissolved through the windows in the remaining silicon layer. This has the side effect that also the HSQ resist on top and around the waveguide is removed (see step (d)). More details on the wet etching are given in the description of the diamond fabrication procedure. An SEM micrograph of a suspended silicon photonic circuit is shown in Fig. 5.2 c) for a 4.5 µm wide and 600 nm high waveguide on a 400 nm silicon support membrane.

5.3.2. Characterization of Silicon Devices in the C-band

In order to evaluate the fabrication process quality, the device performance in the NIR regime is studied first. The 220 nm SOI platform is used to create ring resonators coupled to a bus waveguide with a ring radius of $r = 70\,\mu\text{m}$, a waveguide width of 500 nm and an etching depth of 110 nm. The quality factor of the rings is evaluated and its behavior with increasing gap is presented in Fig. 5.4 a). At a gap of 200 nm the rings are close to critical coupling (ER$\approx$ 15 dB) as shown in the spectrum in panel (b). Light is coupled to the circuits via grating couplers and a transmission of up to 1.2 % is reached at a wavelength around 1600 nm with a grating period of 690 nm. For a very weakly coupled ring with a gap of 300 nm to the bus waveguide an average quality factor of 2.4×10^5 is obtained corresponding to an approximate propagation loss of 3 dB/cm.

These results indicate that the fabrication process is suitable for obtaining photonic circuits with a low propagation loss. A realized ring resonator coupled to a bus waveguide which is terminated by grating couplers is shown in the SEM micrograph in panel (c) with a zoom in on the coupler area. As a positive tone resist is used, a small region around the photonic structures is exposed in the EBL

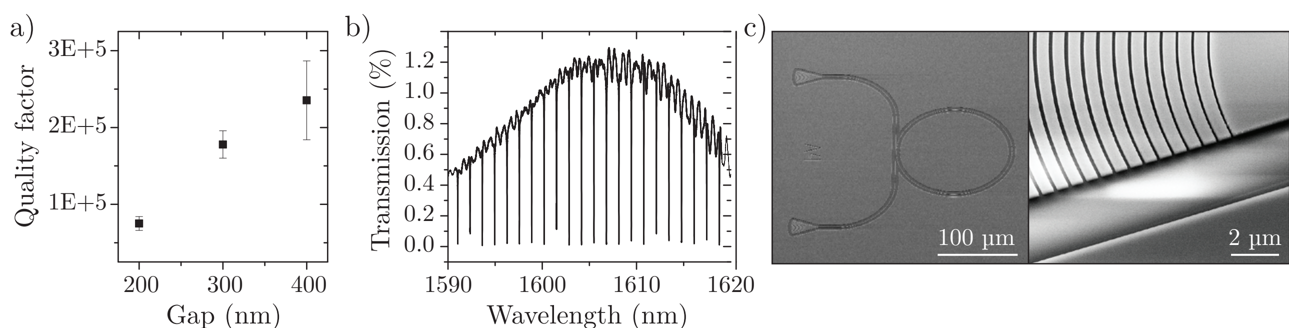

Figure 5.4.: a) In the NIR regime an average quality factor of up to 2.4×10^5 is reached in silicon devices for weakly coupled rings. b) Transmission spectrum of a ring close to critical coupling for a gap size of 200 nm. c) SEM micrographs of a ring resonator and a zoom in on the grating coupler, taken under a tilted view. As a positive tone resist is used, a small area around the structures is exposed instead of the structures themselves.

process rather than the waveguide itself. The same process parameters, such as the etching recipe, are then used for the fabrication of silicon circuits from a micrometer thick device layer for operation in the LWIR spectral region.

5.4. Diamond as Integrated Photonics Material Platform

Before describing the characterization of suspended silicon devices in the LWIR regime, diamond as an integrated photonics material platform is introduced. This offers the possibility of an ultra-broadband device operation starting in the visible regime close to the UV and stretching to the far-IR. In combination with its chemical stability diamond is an ideal material for the fabrication of robust circuits suitable for chemical analyses and life-science applications. The basic diamond material properties are discussed, the fabrication process for integrated photonic circuits is introduced and the device performance in the NIR region is studied. The circuit transmission of both diamond as well as silicon circuits in the LWIR part of the spectrum is then presented in Sec. 5.5.

In recent years tremendous progress has been made in the development of diamond integrated photonic circuits [435–437]. Diamond exhibits several outstanding properties which have attracted broad interest for its use as a versatile material platform. This interest is driven by several factors. Among them are on the one hand the implementation of quantum photonic circuits for the generation, manipulation and detection of quantum states of light that can be realized within a single diamond integrated photonics platform. On the other hand diamond offers a robust platform for sensing of chemicals even in hazardous environments and over a broadband spectral range. Here, the diamond platform is studied in the NIR regime and the realization of devices operating in the LWIR are presented.

5.4.1. Diamond Properties and Photonic Applications

Diamond is an allotrope of carbon with a special crystal structure. Its atoms form a covalent network of sp^3-hybridized orbitals resulting in the diamond lattice, which can be seen as the combination of two face-centered cubic lattices. It is well known as the hardest natural material and offers some very favorable properties for nanophotonic circuits. A large electrical bandgap of 5.5 eV for pristine diamond gives rise to an extremely broad window of transparency starting in the UV at a wavelength of 226 nm and stretching to the far-IR beyond 500 µm, with an absorption band only in the region between about 3 µm and 6 µm [398, 438, 439]. The large bandgap also prevents two-photon absorption in the visible and NIR regime, which is a common source for attenuation in other photonic materials such as silicon [440, 441]. Diamond exhibits a relatively high refractive index around 2.4 in the visible and NIR spectral regime, which provides a large contrast to surrounding optical buffer layers and enables tight light confinement in diamond waveguides [395, 442]. Furthermore, its high thermal conductivity up to 2200 W/mK, a low thermo-optic coefficient around $6 \times 10^{-6}\,\mathrm{K}^{-1}$ and one of the lowest coefficients of thermal expansion enable an efficient dissipation of locally generated heat and

allows to use extreme levels of optical power [443–447]. In combination with a relatively high nonlinear refractive index [123, 448] ($n_2 = 1.3 \times 10^{-19}\,\mathrm{m^2\,W^{-1}}$ in the visible regime), this makes diamond an attractive platform for nonlinear optics [449–451].

Additionally, optically active defects in diamond attract intense research attention. So called *color centers* are defects of the diamond lattice consisting of a carbon vacancy with an adjacent non-carbon atom, which effectively act like isolated artificial atoms in a solid-state system. There are over 500 currently known color centers with an emission spectrum ranging from the visible to the NIR regime. Thereof more than ten color centers have demonstrated single-photon emission, which can be utilized as sources in quantum photonic circuits [435, 452]. Due to the extremely high Debye temperature ($\sim$2000 K) in diamond, color centers such as the extensively studied nitrogen vacancy (NV) and the silicon vacancy (SiV) show a stable emission even at room temperature and a low probability for phonon-assisted dephasing and emission, and thus makes their usage viable under ambient conditions [453–456]. As a further property, color centers offer optically addressable electronic and nuclear spin states with long coherence times. These can be used as quantum memories for the realization of quantum networks mediated by spin-photon entanglement, or as solid-state quantum registers for quantum information processing [457–462].

Besides its versatile optical properties, diamond also offers exceptional mechanical properties. In particular an extremely high Young's modulus of 1100 GPa in combination with a low thermo-elastic dissipation (caused by its high thermal conductivity) enables mechanical resonators operating at high frequencies without significant damping [463–465]. This is not only of furthermost interest for high precision sensing applications [466, 467] but also for the realization of tunable parts in integrated photonic circuits via joined optical and mechanical elements. For example, the position of a movable arm in the vicinity of a waveguide can be altered by electrostatic forces, which induces a local variation of the effective index of the waveguide mode and thus leads to a phase shift [50, 165, 468]. Such phase-shifters are important elements for the development of diamond based quantum photonic circuits [469–471]. As a final building block for quantum photonic circuits, superconducting films can be deposited on top of diamond waveguides for the realization of integrated superconducting nanowire single-photon detectors [386, 387, 472].

For spectroscopic measurements as well as for sensing applications based on the functionalization of photonic circuits, the large transparency range in combination with the relatively high refractive index are the most significant optical properties. Thereby, tight optical confinement in nanophotonic circuits is enabled over a broad wavelength range. Also diamonds durability and biocompatibility makes it an ideal choice for application in harsh environmental conditions. Here, this is exploited for the realization of a diamond photonics platform applicable for circuits in the visible, NIR and LWIR regime.

Growth and Processing of Single and Polycrystalline Diamond

The development of diamond integrated photonic circuits has been enabled by the ongoing progress in the synthesis and processing of CVD diamond, which provides high quality diamond films with reproducible properties [473]. Two types of diamond are used for implementing nanophotonic circuits. Bulk single crystalline diamond (SCD) typically exhibits a high material quality at the cost of more challenging fabrication procedures, while polycrystalline diamond (PCD) offers a better availability of wafer-scale thin films and easier nanofabrication methods.

SCD can only be grown homoepitaxially on existing SCD templates and subsequently has to be cut off from the original diamond [474, 475]. Therefore, no waferscale substrates with thin SCD films are currently available, but rather thick slabs of SCD are obtained, typically limited in size to below $1\,\mathrm{cm}^2$. This requires more advanced transfer, structuring and etching processes for the fabrication of integrated circuits from bulk samples and the small size of the samples limits the scalability of the circuits and their fabrication. However, a high material quality with e. g. a low background fluorescence and a low concentration of color centers can be achieved [476, 477]. Fabrication of nanophotonic circuits from bulk SCD slabs typically involves a process to obtain a thin film by e. g. etch down or lift-off procedures and subsequent structuring processes [478, 479]. Alternatively, nanophotonic structures can be directly obtained from a slab via angle and undercut etching procedures, via focused ion beam milling or the more gentle electron-beam induced etching [480–483]. Recently, a further promising structuring approach emerged based on material modification by direct laser writing with ultrashort pulses [484]. However, all methods for SCD structuring typically require advanced techniques beyond standard CMOS methods. A comprehensive description of fabrication procedures and realized nanophotonic devices can be found in recent review articles [436, 437, 485].

While most of the outstanding properties of diamond are widely preserved also for PCD, the transparency range and the thermal conductivity are deteriorated mainly because of the grain boundaries, which incorporate sp^2 carbon and other impurities [443, 452]. The impurities, as well as induced strain during the growth process, degrade the color center properties [475] while grain boundaries contribute to additional scattering losses. However, in contrast to SCD slabs, thin PCD films can be grown on different insulating substrates with a diameter of up to 6 inch and with very uniform layer thickness after surface polishing. This provides a fabrication friendly platform, which can be structured via standard lithography, dry and wet etching methods. Also the PCD quality can be increased by further progress in high purity diamond deposition with a decreased number of impurities and a controlled incorporation of color centers [486, 487].

The research project on diamond integrated photonic structures is realized in collaboration with the Frauenhofer Institute for Applied Solid State Physics IAF[3]. PCD diamond films are deposited via PECVD [488, 489] in an ellipsoidal 2.54 GHz microwave plasma reactor at a temperature between 600 °C and 850 °C by using 1 % methane in hydrogen at a pressure between 25 mbar and 70 mbar.

[3] The diamond deposition is performed by Georgia Lewes-Malandrakis and Taro Yoshikawa. Surface polishing is done by Dietmar Brink. Christoph Nebel leads the collaboration. IAF, Freiburg, BW 79108, Germany

Choice of Substrate and Layer Thickness

The choice of the substrate and in particular of the buffer layer between the diamond film and the silicon wafer depends on the envisaged application. Basic diamond photonic circuits for the visible and NIR regime are realized on an approximately 600 nm thick film on a 2 µm silica-on-silicon platform. However, as discussed above the buried oxide layer limits the usability to a spectral regime below ∼3.5 µm. Therefore, the oxide buffer layer is replaced by an aluminum nitride (AlN) layer, which enables a photonics platform usable in the visible, NIR and LWIR regime. This platform provides the advantage of a simple fabrication process for photonic structures as they can be defined by a single EBL exposure followed by a plasma etching step. Test devices in the NIR regime are realized using a 600 nm thick diamond film on a 2 µm ALN-on-silicon platform. Yet, this layer thickness is not large enough to support guided modes in the LWIR regime. Thus, a 1.5 µm thick diamond layer on a 5 µm AlN layer on silicon is employed. The increase in the AlN buffer layer thickness is required to minimize coupling of the waveguide modes to the underlying silicon substrate, which causes additional losses.

In order to quantify the coupling losses to the substrate numerical simulations of the layer stack are employed. A 2D cross-section through a 1.5 µm thick diamond slab waveguide on an AlN buffer with variable thickness on a silicon substrate is considered. At an input port in the diamond slab waveguide the fundamental TE mode at a wavelength of 8 µm is excited and its propagation through the slab along a distance of 1 mm is monitored. Due to coupling of the mode to the substrate a certain part of the power in the waveguide is lost. The simulated decrease of the power in the waveguide for an AlN buffer thickness between 1 µm and 6 µm is shown in Fig. 5.5 a). By fitting an exponential decay function to the data (red dashed lines), the attenuation coefficient is extracted, which is presented in panel (b). With increasing buffer thickness the attenuation decreases and for a thickness of 6 µm

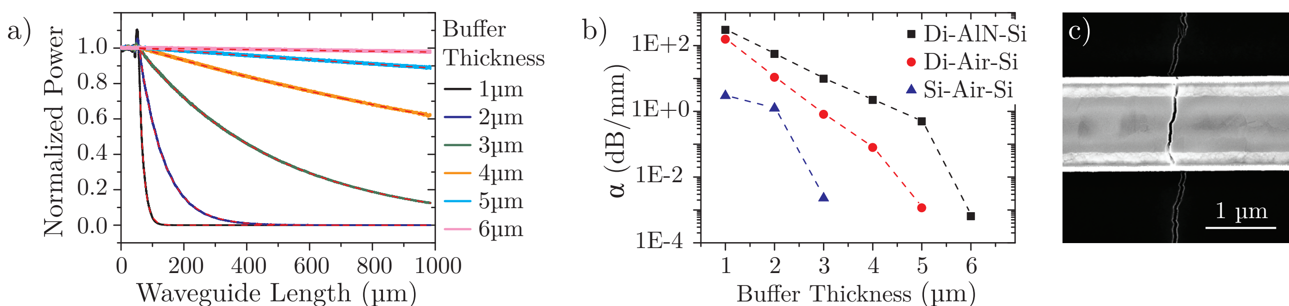

Figure 5.5.: a) The power of a simulated waveguide mode ($\lambda = 8$ µm) in a 1.5 µm thick slab waveguide on an AlN buffer on a silicon substrate decreases due to coupling of the mode through the buffer to the substrate. With increasing buffer layer this effect can be minimized. By fitting an exponential decay function (red dashed lines) to the curves, the attenuation coefficient is extracted, which is shown in (b). The same simulation is applied for the suspended diamond and suspended silicon platform and the results are shown by the red and blue markers. Dashed lines are used to guide the eye. c) The use of a 5 µm AlN buffer leads to highly stressed layers after the diamond deposition. When the diamond layer is etched during the device fabrication the stability of the layers is decreased and cracks in the AlN layer as well as in the diamond waveguides may appear.

the attenuation drops significantly. For a further increase in the buffer thickness, the attenuation is too small to be extracted. For a buffer thickness of 5 µm as employed here, an additional attenuation of 0.5 dB/mm can be expected due to coupling to the substrate. Nevertheless, the buffer thickness is kept at this value since a larger thickness would increase the surface roughness of the AlN layer and impede the diamond growth. While diamond and SiO_2 exhibit a similar coefficient of thermal expansion, the one of AlN is much larger. As diamond is typically deposited at a temperature of 850 °C, highly stressed diamond on AlN layers are obtained when the sample is cooled down after the deposition. By optimizing the process parameters, the deposition temperature for diamond-on-AlN is decreased to 600 °C. Still, the induced stress after cooling down is so high that when the originally 1.5 µm thick diamond layer is etched during the circuit fabrication for more than ∼1.1 µm, the stability of the layers is strongly decreased. Thereby, ruptures in the AlN layer as well as in the circuits and the remaining diamond layer are caused. This is shown in the SEM micrograph in Fig. 5.5 c), where a crack in the substrate crosses a waveguide.

The same simulation is employed for the suspended 1.5 µm diamond platform and the suspended 1 µm silicon platform, where the buffer thickness corresponds to the gap (filled with air) between the device layer and the silicon substrate. The extracted attenuation coefficients are depicted by the red and blue markers in Fig. 5.5 b). Due to the surrounding air buffer, the mode exhibits a higher confinement inside the waveguide and the coupling to the silicon substrate is reduced. For the suspended silicon the confinement is even stronger because of the larger index of refraction compared to diamond. In this case, the attenuation vanishes in the simulations for a 5 µm air buffer layer. Hence, a 1.5 µm thick diamond layer is grown on a 5 µm SiO_2 buffer layer. The buffer layer is removed during the fabrication process in order to obtain suspended diamond circuits. Similarly, a 1 µm silicon layer on a 5 µm silica-on-silicon substrate is used for the fabrication of suspended silicon devices.

Diamond Layer Surface

The diamond surface layer roughness is a main source for scattering losses in waveguides. Due to the polycrystalline growth a very rough surface is obtained as shown in Fig. 5.6 a). Therefore, typically ∼400 nm thicker layers than required are deposited and they are subsequently thinned down to the desired thickness by a chemo-mechanical polishing procedure [490]. However, the magnitude of the surface roughness increases with increasing diamond layer thickness and even after polishing a few 'valleys' remain at some of the grain boundaries. This can be seen at the marked positions in Fig. 5.6 b). Such dips in the surface can create complications in the fabrication process when the thick diamond layer is etched. Along the edge of these dips the field in the plasma etching process is strengthened causing an increased etching rate, which leads to even deeper and broader grooves compared to the flat diamond surface. This is depicted in panel (c). The impact of this effect on the fabrication of suspended diamond structures is discussed in Sec. 5.4.2. Apart from these dips, a very smooth diamond surface is obtained with a root mean square (rms) roughness around 4 nm, which is

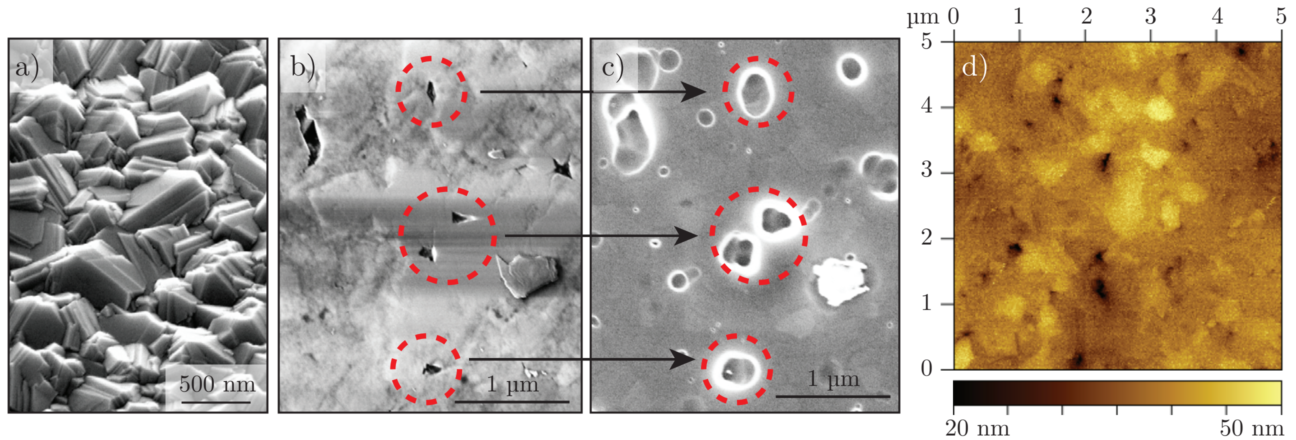

Figure 5.6.: a) Tilted SEM view of an as deposited diamond layer which exhibits a large surface roughness. b) After polishing a smooth surface is obtained. However, there are still some 'valleys' visible, e. g. in the positions marked by the red dashed circles. c) Due to a field enhancement along the edges of the valley in the plasma etching process, these grooves are deepened and widened as shown in the SEM micrograph of the surface after etching. d) AFM micrograph of the polished diamond surface with a rms roughness of 4 nm.

extracted from atomic force microscopy (AFM) micrographs of the surface as shown in Fig. 5.6 d). When diamond is grown on AlN, the roughness of the sputter deposited AlN layer also has to be considered[4]. The surface roughness of the AlN layers increases with increasing layer thickness. While a rms roughness around 2 nm is achieved for 2 µm thick films, this is increased to 6 nm for 5 µm thick layers. Thereby, the AlN-diamond interface is an additional source for scattering losses in this material stack.

5.4.2. Fabrication of Diamond Devices

The fabrication of integrated photonic circuits from the 600 nm diamond on 2 µm buried oxide material stack is rather simple. A 450 nm thick HSQ layer is used as EBL resist. It offers a good selectivity in the plasma etching process as the diamond layer is etched approximately twice as fast as the HSQ resist. However, the HSQ resist adhesion on diamond is very poor, so that 5 nm SiO_2 is deposited on the diamond surface as an intermediate layer, which results in excellent resist adhesion. After the EBL exposure, the resist is developed in MF319 and the structures are subsequently transferred into the diamond layer by an oxygen and argon based plasma etching process, which combines chemical etching and physical sputtering of the diamond layer. An etching depth of ~400 nm is used for the fabrication of diamond rib waveguides with a remaining 200 nm thick diamond layer. As the HSQ resist exhibits silica-like properties it typically remains on top of the structures for applications in the visible and NIR regime.

A fabrication procedure for suspended diamond structures is first developed for 600 nm thick layers

[4] Sputter deposition of AlN layers is performed by EPCOS AG, Munich, BY 81671, Germany

and later on adapted to thicker layers employed for LWIR applications. In order to access the buried oxide buffer underneath the remaining diamond, windows in the diamond layer have to be opened next to the photonic structures, similar to the procedure described in Sec. 5.3.1 for suspended silicon circuits. Therefore, a 10 nm chromium (Cr) layer is deposited on the sample, which serves as a very effective hard mask against the O_2/Ar plasma in the following process. The sample is then spin coated with PMMA and the area of the windows is exposed in a further EBL process. As PMMA is a positive tone resist these windows are opened in the resist layer, which is subsequently used as a mask for wet etching of the Cr layer underneath. Thereby, the windows are transferred to the Cr layer and in the following plasma etching step the windows are etched into the diamond layer until the buried oxide layer is reached. Finally, the oxide beneath the photonic structures is dissolved in an HF wet etching process through the openings in the diamond layer, which also causes the removal of the remaining HSQ cover. After flushing the sample with distilled water, it is directly transferred to a further Cr wet etching process in which the remaining Cr layer is removed and subsequently the sample is immersed in methanol. Because of the now suspended structures the sample has to be dried very carefully to avoid tearing off structures. This can be achieved by placing the sample on a hotplate at 70 °C while there is still liquid methanol on the surface and it is dried by quickly but also very gently blowing it with nitrogen.

Fabrication Adaption for the LWIR Regime

In terms of fabrication the simplest platform for integrated photonic devices operating in the LWIR is diamond on an AlN buffer on a silicon substrate. As the AlN layer provides a buffer to the silicon substrate and enables total internal reflection in the diamond layer, photonic structures can be realized by a single EBL process. A 1.5 µm thick diamond layer on a 5 µm AlN buffer layer is used. Again a 450 nm HSQ resist is used for the exposure. In order to avoid cracks in the substrate an etching depth of 1 µm is targeted, but the resist layer is not thick enough to realize this. Due to the field enhancement in the plasma etching process, the edges of the resist are rather quickly etched. After a diamond etching depth of approximately 500 nm the resist is completely consumed at its sides and the top edges of the diamond waveguides are attacked. This results in a strongly chamfered and very rough top part of the waveguide sidewall which needs to be prevented.

In order to obtain straight sidewalls a combination of an HSQ and Cr hard mask is used. A 10 nm Cr layer is deposited prior to spin coating HSQ. This film replaces the SiO_2 adhesion layer used before and serves simultaneously as effective adhesion promoter and additional etching mask. Now a two-step dry etching procedure is applied. In a first Cl_2 based plasma the Cr layer is etched and in a second step the diamond layer is etched by an O_2/Ar plasma. For accessing devices in the LWIR regime, coupling via the end facet of the waveguides is applied. The chips are cut by the wafer dicing saw and the cut position is placed as close as possible to the waveguide end. Thereby, a distance between the end facet and the side of the chip in the order of a few µm is achieved. Subsequently

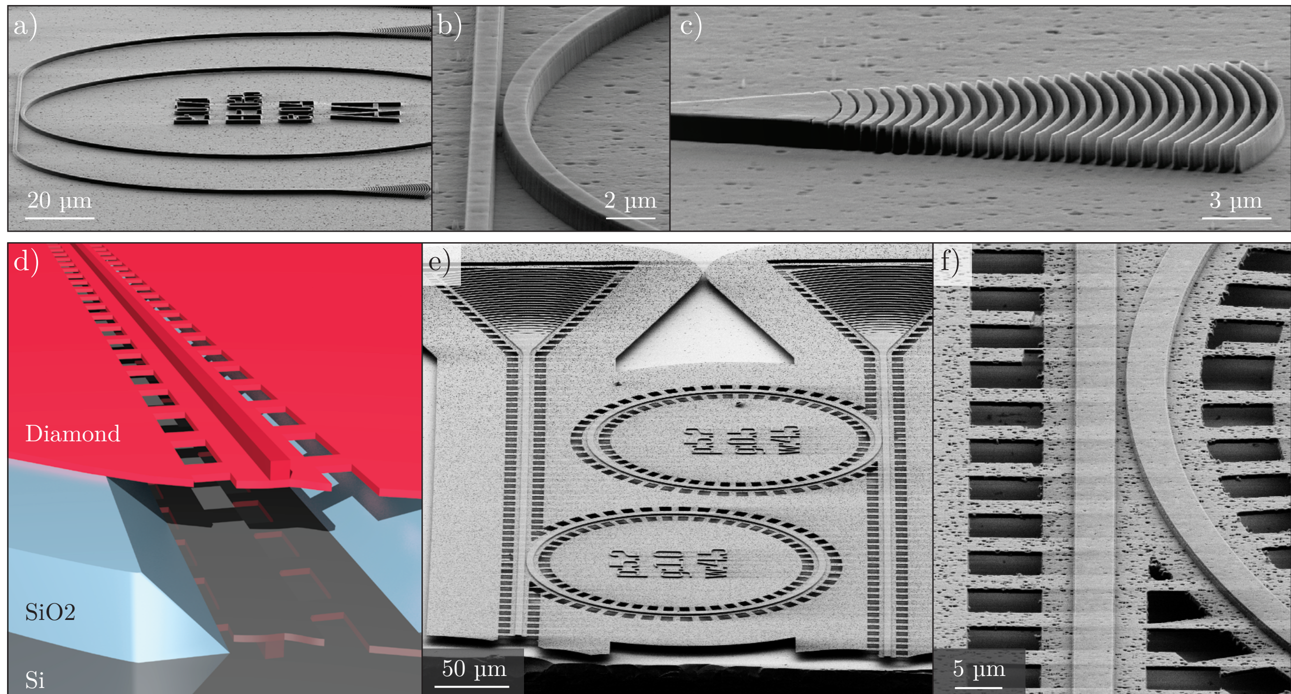

Figure 5.7.: SEM micrographs of diamond integrated photonic circuits fabricated from a 1.5 µm thick layer with an etching depth of 1 µm. For the pictures the sample is tilted under an angle of around 85°. a) Ring resonator with a zoom in on the coupling region between the ring and the bus waveguide (b) and on the grating coupler (c). With a waveguide width of 750 nm, this device is suitable for operation in the NIR and visible regime. d) Model of a suspended diamond waveguide, where the SiO_2 substrate underneath the waveguide is dissolved. e), f) Suspended diamond waveguides with a waveguide width of 4.5 µm, which are suitable for operation in the LWIR regime. The ring resonators (e) are coupled to a bus waveguide, which is terminated on one end by a grating coupler and on the other end by a waveguide facet. A zoom in on the coupling region between the waveguide and ring resonator is shown in (f).

the HSQ cover is removed by an HF dip followed by a wet etch removal of the Cr layer. An example for 1 µm high diamond rib waveguides fabricated by this technique is shown in Fig. 5.7 a) - c). The structures exhibit straight sidewalls at a large aspect ratio (1 µm etching depth and 250 nm width for the gratings), which confirms the suitability of the Cr layer as an additional etching mask.

The realization of suspended diamond circuits is slightly more elaborate since the buffer layer needs to be removed. The sketch of such a suspended diamond waveguide is shown in Fig. 5.7 d). As a starting point a 1.5 µm diamond layer on a 5 µm silica-on-silicon substrate is used. The photonic structures are fabricated as before by the combination of a Cr and HSQ mask and the diamond etching depth is kept at 1 µm. In order to remove the silica buffer, windows in the remaining diamond layer have to be opened. However, the previous approach of a Cr/PMMA proves to be ineffective. At such a large diamond etch depth the 'valleys', strongly enlarged in the etching process, become too deep, so that a deposited 10 nm Cr layer does not provide enough protection. When trying to etch openings into the diamond layer all the grooves are also etched down to the substrate. In a subsequent oxide

removal, HF reaches the buffer not only through the windows but also through all the grooves, which entails a removal of the oxide throughout the full sample area and and detaches the diamond layer from the substrate. While this might present an unconventional way of obtaining a free diamond membrane that contains nanophotonic circuits and might be transferred onto an arbitrary substrate to form a new 'diamond-on-anything' platform, this is unwanted here.

Instead, the use of a second 450 nm HSQ mask, this time with a 5 nm deposited SiO_2 adhesion layer, proves to be an efficient solution. The only drawback is that HSQ is a negative tone resist and therefore (similar to the suspended silicon platform) a large ∼140 µm wide area around the circuits is exposed with some openings in close proximity along the waveguides. Due to the increased HSQ thickness around the waveguides, this area is also divided in two sections. The inner one close to the waveguide is exposed with a lower dose during EBL, while the dose for the outer region is increased. After the mask creation, the windows are transferred into the diamond layer via plasma etching. As before, the chips are then cut by the wafer dicing saw in close proximity to the waveguide end in order to enable coupling of light to and from the sample via the end facet. In the last fabrication step, the oxide substrate below the photonic circuit as well as the HSQ resist is removed by HF etching. Thereby, large suspended diamond photonic circuits are realized with a waveguide length of up to 9 mm. SEM micrographs of the resulting photonic circuits are shown in Fig. 5.7 e) and f). With a waveguide width of 4.5 µm, the devices are suitable for operation in the LWIR regime. The fabrication details for all diamond nanophotonic devices can be found in App. A.3.6 - App. A.3.8.

The waveguide facet quality strongly influences the coupling efficiency for end facet coupling. In order to avoid scattering losses from the facet, it should be as smooth as possible [491]. Therefore, mechanical polishing of the side of the sample, which contains the facet can be applied. This is tested for the diamond and silicon devices before the removal of the oxide buffer layer. The stress in the diamond as well as in the silicon device layer is however too large for successful polishing of the waveguide facet. As soon as the side of the chip is polished far enough and the waveguide is reached, parts of the device layer are ripped off rather then resulting in a polished facet. Hence, the facet is kept as it is after the plasma etching of the photonic structures. The details of this polishing process are discussed in App. A.10.

5.4.3. Characterization of Diamond Devices in the NIR Regime

For the first steps towards protein detection via the surface functionalization of integrated optical circuits (see next section) diamond devices for operation in the NIR regime are used. In addition, the diamond circuit performance can be compared to silicon and Si_3N_4 devices by the characterization of devices in this spectral regime. In this case, integrated photonic circuits are fabricated from a 600 nm diamond layer on a 2 µm SiO_2-on-Si substrate. Ring resonators coupled to a bus waveguide with a ring radius of $r = 60$ µm and a waveguide width of $w = 800$ nm are used. The 600 nm thick diamond layer is etched by 400 nm, leaving a 200 nm support layer. In this support layer windows are opened

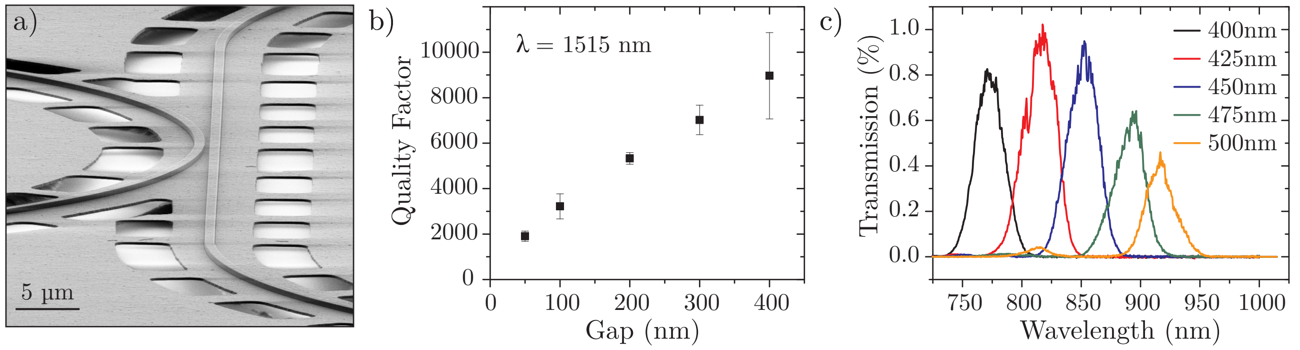

Figure 5.8.: a) SEM micrograph of a suspended ring resonator coupled to a bus waveguide. b) Achieved quality factor with increasing gap to the bus waveguide in the NIR regime. c) Transmission spectra in the visible regime for a grating coupler period between 400 nm and 500 nm.

along the waveguides and the underlying oxide layer is dissolved below the photonic structures via HF etching. The SEM micrograph in Fig. 5.8 a) of the suspended diamond structures shows the coupling region of the ring resonator to the bus waveguide.

The quality factors of the rings for an increasing gap to the bus waveguide are measured before and after underetching the structures. No change in performance is observable, confirming that the fabrication procedure for suspended devices does not compromise the photonic devices. The realized quality factors with increasing gap size at a wavelength of 1515 nm are presented in Fig. 5.8 b). For a weakly coupled ring with a gap of 400 nm to the bus waveguide an average quality factor of $Q = 9000$ is reached, with single resonances exhibiting a quality factor up to 11000. Assuming that the quality factor is close to its intrinsic value, this corresponds to a propagation loss of 4.3 dB/mm. This is close to the best device performance obtained for PCD with standard EBL and dry etching procedures, where an attenuation coefficient of 3.8 dB/mm has been realized [492]. A further improvement of the PCD circuit quality has been reported by employing reactive ion beam angled etching. Thereby, racetrack resonators with a quality factor up to 30000 have been obtained in the NIR regime [480]. However, in that case a PCD sample with a diamond grain size around 50 µm was used, compared to a grain size in the order of 1 µm for the samples utilized here. Therefore, the increased circuit quality is rather caused by the high diamond material quality than the fabrication procedure, as scattering and absorption at grain boundaries, related to sp^2 carbon and doping atoms, is one of the dominating sources for the attenuation in PCD waveguides [493, 494]. Consequently, the device performance of photonic circuits in SCD is even better due to the entirely missing grain boundaries. In this way very low propagation losses for nanophotonic circuits down to 0.3 dB/cm and quality factors of ring resonators up to 1×10^6 have been achieved [450, 495–497].

Using the same diamond platform as above, the transmission through a simple waveguide (width $w = 600$ nm) terminated by two grating couplers is tested in the visible spectral regime. The recorded spectra for a grating period between 400 nm and 500 nm are presented in Fig. 5.8 c). The maximum transmitted power is influenced by the interference effect in the underlying buffer, which is in this

case the gap between the suspended diamond layer and the silicon substrate. Thus, the maximum transmission is achieved at a wavelength around 820 nm corresponding to a grating period of 425 nm, while the transmission decreases for the other devices.

5.4.4. Functionalization of Diamond Circuits

As discussed above, diamond offers very good broadband transmission properties, while being mechanical strong and chemically inert. This makes it an ideal material for analytic optical devices in harsh environments e. g. in life-science applications. An example for such an application is given here by the optical detection of the binding of proteins to a functionalized surface. In particular the binding of avidin to biotin and between the alpha-fetoprotein (AFP) antigen and its antibody is studied. The avidin-biotin complex exhibits one of the strongest bounds occuring in nature and is widely used in biochemical sensing applications like the identification of new drug targets and the addressing and linking of DNA structures [498–501]. AFP is a naturally occurring protein that is associated with carrier functions in fetal blood [502]. It is mainly produced during fetal development near the end of the first trimester and its occurrence rapidly decreases to trace amounts after birth. The AFP concentration is detected via blood or urine samples. While deviations of the AFP concentration from the norm during pregnancy can be an indicator for particular developmental abnormalities of the fetus, an increased concentration in adults is an indicator for certain kinds of liver cancer as well as testicular tumors [503–506]. Hence, simple detection schemes are of high interest for early cancer diagnosis [507–511].

Here, the protein detection via the response of photonic integrated circuits is studied. By using ring resonators it is monitored if binding of a protein to the functionalized waveguide surface causes additional absorption losses and if a phase shift via a slight change of the surrounding refractive index is induced. Therefore, the diamond platform described above, which operates in the NIR regime is utilized. An input waveguide is split into two arms and to each arm a ring resonator is evanescently coupled. The proteins are linked via click-chemistry to only one of the rings and the throughput spectrum of both arms is compared. For the photonic structures, a ring radius of 65 µm, a waveguide width of 800 nm and an etching depth of $\sim$400 nm are chosen and the ring performance before the functionalization is studied. As the diamond layer quality depends on the growth conditions and the polishing procedure, this varies from batch to batch. From the available wafer utilized here, a ring resonator quality factor of only 3500 is achieved at a wavelength of $\lambda = 1600$ nm for a weakly coupled ring with a gap of 400 nm to the bus waveguide. This decreased device quality also limits the visibility of any potential change in the spectrum. For the functionalization ring resonators closer to critical coupling with a gap of 200 nm and 300 nm to the bus waveguide are chosen, which exhibit a quality factor between 2200 and 2800.

The functionalization of the sample surface is realized in cooperation with Mahdi Dadfar in the

research group of Michael Hirtz at the Karlsruhe Institute of Technology[5]. In order to attach biotin (as a linker for avidin binding) or the anti-AFP antibody (as a linker for AFP binding) to the ring surface, the following procedure is used. The sample is cleaned and then treated in a weak oxygen plasma in order to obtain a hydroxyl-terminated surface. The sample is then immersed in a GPTMS ((3-Glycidyloxypropyl)trimethoxysilane) solution, where the GPTMS attaches to the sample surface via its silane group. Now a droplet of either biotin or anti-AFP solved in PBS (Phosphate Buffered Saline) is brought onto the sample surface and biotin or anti-AFP is attached to the GPTMS layer via a reaction between the epoxide functional group of GPTMS and the amine group of biotin or anti-AFP. In order to further block all remaining functional groups of GPTMS, the sample is immersed in a BSA (Bis(trimethylsilyl)acetamide) solution in PBS, which rapidly reacts with compounds containing OH and NH functional groups. Thereby, a system with a specific biotin or anti-AFP linker is realized on the sample surface. In order to study the effect of AFP binding to the antibody (or avidin binding to the biotin marker), AFP solved in PBS (or avidin in PBS) is site specifically brought to the waveguide surface of one of the ring resonators via dip-pen nanolithography with a microcantilever-based microfluidic handling device, while the markers on the second ring remain empty. The binding of AFP to the antibody can be reversed without removing the antibody by immersing the sample in a pepsin in glycin-HCl solution [512].

An optical micrograph of one of the utilized devices for the binding between the antibody and AFP is shown in Fig. 5.9 a). The grating coupler in the middle is used as input and the transmission is recorded at both outer grating couplers. While the whole sample surface is covered by the antibody, AFP is specifically placed on the left ring only, where it binds to the antibody. As AFP is fluorescent in the red light region around 650 nm, the location of the AFP attachment can be verified by taking a fluorescence microscope picture. This is shown in the lower part of panel (a), where an excitation wavelength around 550 nm is used and the signal is filtered for wavelengths above 600 nm. It can be seen, that the main fluorescent signal is obtained from the left ring where the AFP is placed. However, a significant background fluorescence is obtained in particular for the photonic circuits, which is caused by doping of the diamond layer with foreign atoms. Thus, the diamond growth needs to be optimized in order to achieve pure diamond layers and better fluorescence results.

The response of the ring resonators is evaluated by comparing the spectrum of the left ring with AFP or avidin to the right ring with the bare marker. As a further reference the markers on both rings for the devices with a gap of 100 nm are left empty. The ratio of the quality factor between the right and the left ring is shown in Fig. 5.9 b). While a ratio of 1 is obtained for the device with empty markers on both rings, it is slightly decreased for the devices where AFP or avidin is linked to the markers on the left ring. This indicates a slightly increased absorption by the proteins, but regarding the error bars, this trend is not yet significant. AFP or avidin is brought to the sample by solving it in PBS. In a further test the concentration in the solvent is varied and again the quality factors of

[5] Dip-Pen Nanolithography (DPN) and Related Techniques, Institute of Nanotchnology, Karlsruher Institute of Technology, Eggenstein-Leopoldshafen, BW 76344, Germany

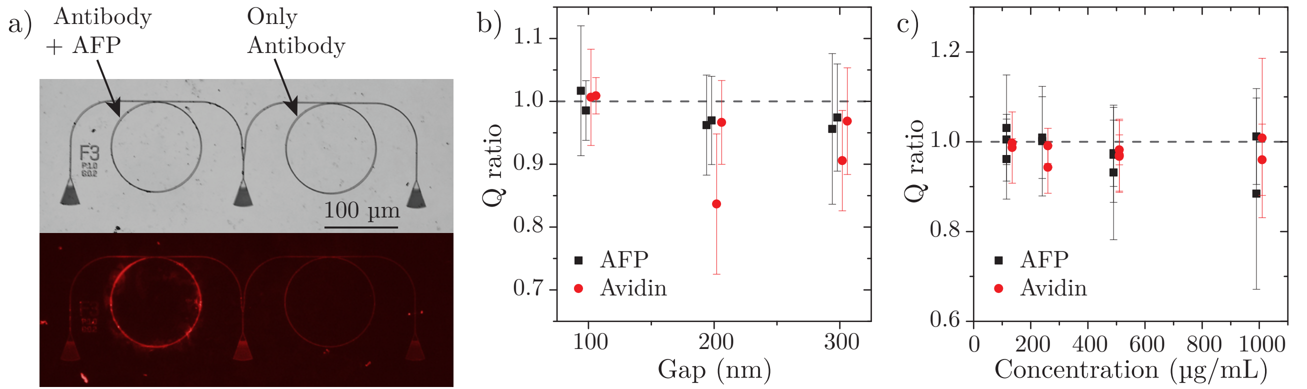

Figure 5.9.: a) Optical micrograph of a test device (top) and fluorescent signal of the same devices (bottom). The stronger signal from the left ring confirms binding of AFP to the antibody only at this site. The background fluorescence is caused by doping of the diamond layer. b) Ratio of the quality factor of the left ring to the right ring. For a gap of 100 nm both rings are left bare without the protein and exhibit the same quality factor, while for a gap of 200 nm and 300 nm the protein is linked to the functionalized surface of the left ring, which leads to a very slight decrease of the quality factor compared to the right ring. c) Ratio of the quality factor of the left ring (with protein) to the right ring (without protein). However, a decrease of the quality factor of the left ring compared to the right ring with increasing protein concentration can not be observed.

the left ring with protein and the right ring without it are compared. The results are presented in Fig. 5.9 c), but no trend of a decreasing quality factor with increasing concentration is observable.

Thus, if the binding of AFP or avidin on top of the waveguide surface changes the properties of the guided mode, the effect is too small to be observed by these experiments. However, the diamond photonic circuit quality of the devices employed here is rather low which might be the limiting factor. Therefore, a further set of experiments is currently conducted, which uses the high quality Si_3N_4 integrated photonics platform introduced in Chap. 2. By using rings with a quality factor around 5×10^5 in the NIR regime, even small changes in the attenuation are more easily detectable. In addition, the spectral position of the ring resonances is monitored in order to detect any phase shifts induced by a variation of the effective mode index. Similarly, the use of MZIs, where the proteins are linked to one of the arms, is aimed at the observation of any induced phase shifts. The results of these experiments are expected to clarify if a detectable increase in absorption or a phase shift is induced on the waveguide mode in the NIR regime by linking AFP or avidin to the functionalized surface.

It has been shown that the absorption as well as the fluorescence of AFP in the visible regime can be increased by antibody linking of metallic quantum dots to the antigen [513, 514]. This might present an alternative detection scheme by using integrated photonic ring resonators in the visible wavelength regime. A future further step is the combination of integrated optical sensors based on the attenuation or induced phase shift with integrated opto-mechanical resonators. Such resonators have already been demonstrated within diamond photonic circuits. High mechanical resonant frequencies above 100 MHz have been realized, allowing operation under ambient conditions as it limits the effect of air damping on the resonator [165, 468, 515]. The mechanical resonance is read out optically and a

change of the resonator mass by binding of e. g. AFP to its surface leads to a shift in the resonance, which is observable in the optical response of the device. Thereby, different detection schemes can be combined on a single integrated photonics platform and by applying a set of different linkers or antibodies to an array of devices (e. g. ring resonators), a sample can be simultaneously employed for examining the occurence of various different substances. In order to test a solution for specific components, a microfluidic channel is ideally directly attached to the sample [512]. Hence, the devices can be easily surrounded by a liquid with real-time monitoring of the optical response. This shows a way for implementing compact multi-purpose optical sensors for life-science applications.

5.5. LWIR Characterization of Silicon and Diamond Devices

The main objective of the diamond and suspended silicon platform presented here, is the extension of the usable wavelength regime to the fingerprint LWIR region. Therefore, the utilized measurement setup as well as the obtained characterization results of the different material platforms are presented in the final section of this thesis.

5.5.1. LWIR Measurement Setup

A schematic of the measurement setup for the characterization of integrated photonic circuits in the LWIR regime is depicted in Fig. 5.10 a). A tunable quantum cascade laser (QCL) is used with a wavelength range between 6.9 µm and 9.3 µm, which can be operated in CW or pulsed mode. The optical isolator prevents back reflections, which can damage the laser module. The beam can be guided to the sample by using a free space path (red line in the figure). In this case a free space polarization controller is used and the beam is focused onto the waveguide facet by a reflective objective. Control over the polarization is important as single mode waveguides, where only the fundamental TE mode is guided, are used. In order to couple to this waveguide mode, the polarization of the input beam has to be adjusted accordingly. The state of the polarization can be verified by placing a free space wire grid polarizer in the beam and monitoring the throughput while rotating the polarizer. Alternatively, the beam can be coupled to a chalcogenide glass fiber (blue line), where the polarization is adjusted by a fiber polarization controller. Using the bare fiber end for coupling light to the facet of a waveguide significantly simplifies the alignment procedure as the position of the fiber can be better controlled than the focal spot of an objective. The output of the end facet of a waveguide is either monitored directly by an IR camera, which is especially useful in the alignment procedure, or it is collected by a further reflective objective and send to a detector. Additionally, the alignment of the sample is monitored from above by either a CCD camera with a microscope objective or also by an IR camera. The top view of a sample, where the end of the waveguide is well aligned to the center of the fiber, is shown in Fig. 5.10 b).

As an alternative to input and output coupling of light via the end facet of the waveguide, the use of grating couplers for out-of-plane access to the photonic circuits is studied. Therefore, waveguides

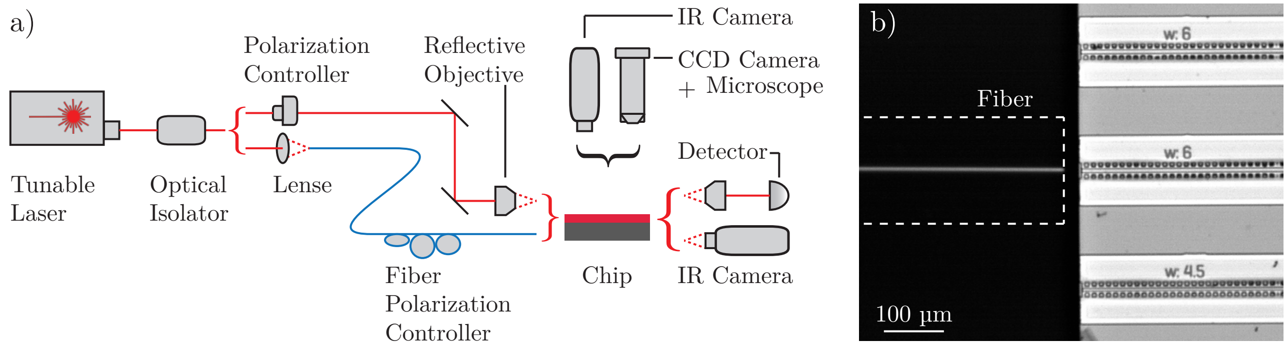

Figure 5.10.: a) Schematic of the measurement setup in the LWIR regime. The beam can be either directed to the sample by using a free space path or by coupling it to a fiber. The output of a waveguide end facet is monitored directly by an IR camera or is collected with an objective and send to a detector. Additionally, the sample can be monitored from above with a CCD camera or also by an IR camera. b) Top view of the end of the fiber aligned to the end facet of a waveguide, taken by the CCD camera. The outline of the fiber is marked by the dashed line.

terminated on one side by a grating coupler and on the other end by a waveguide facet at the side of the chip are fabricated. When using the facet as an input port, the output at the grating coupler is monitored from above by the IR camera. Vice versa, for using the grating coupler as input port, the end of the fiber is mounted on a holder placed above the sample, similar to the fiber array configuration (see Sec. 2.4.1), only with a single fiber. In this case, the output is monitored at the end facet of the waveguide by the IR camera or the detector. For alignment purposes the input fiber holder (or the input objective), the sample itself, as well as the output objective are placed on piezo-driven xyz-stages. The details and the characterization of the individual optical components used in the setup are given in App. A.11.

5.5.2. Characterization of Silicon Devices

For the characterization of suspended silicon waveguides in the LWIR regime, several different devices are fabricated. The most simple design is just a straight waveguide terminated on both sides by its plain facet. Those waveguides exhibit a length of 7 mm and the sample is cut through by the wafer dicing saw as close as possible to the end facets of the waveguide. Thereby, the sample size is decreased to ∼7 mm and the waveguide transmission is recorded by coupling light to the waveguide facet on one side of the sample and collecting the output from the facet on the other side of the sample. A similar design includes an s-shaped bend in order to realize an additional lateral offset of 4 mm. Thus, any stray light from the input beam, which might propagate straight along the sample, can be separated from light guided by the waveguide. Furthermore, waveguides which are terminated only on one side by their facet and on the other side by a grating coupler are included on the sample for testing the out-of-plane access to integrated photonic circuits.

As the alignment of the sample and the waveguide end facets to a fiber is significantly simplified

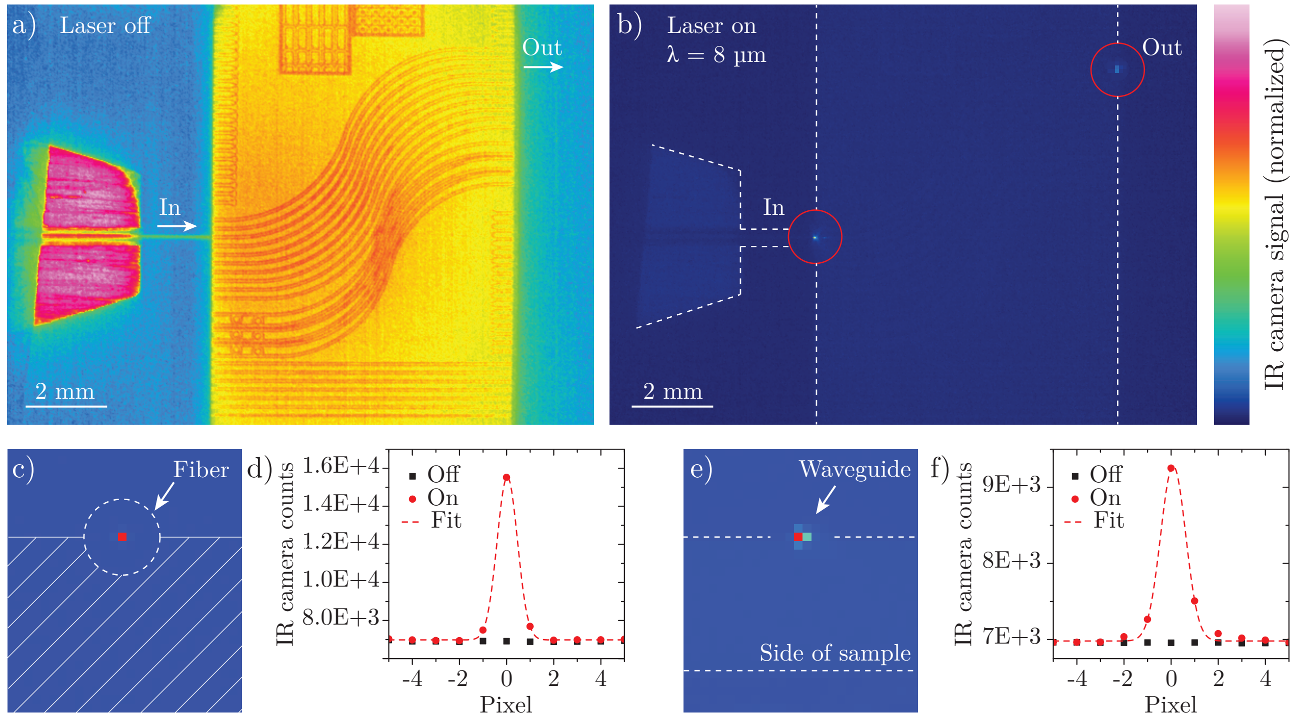

Figure 5.11.: a) Top view of the sample taken with IR camera when tha laser is turned off. On the left side the fiber holder and the end of the fiber, which is located very close to the end facet of a waveguide, are visible. The sample width is 7 mm and the waveguides in the middle exhibit a bend so that the output is shifted from the input by 4 mm in lateral direction. When the laser is turned on (b) a bright spot at the input facet is visible, as light from the fiber is also reflected upwards. At the output only a very weak spot is detected in upward direction as most of the light from the end facet propagates in forward direction. The fiber holder, the end of the fiber and the side of the sample are marked by the dashed lines. c) Front view of the fiber output recorded by the IR camera. The fiber facet is marked by the dashed circle, but as the fiber core is much smaller, only a singe pixel lights up. The striped area marks the fiber holder outline. d) Profile of the detected counts through the fiber facet in (c), when the laser is turned off (black markers) and turned on (red markers). Even though the output spot is very narrow, a Gauss curve can be fitted to the data. e) Front view of the end facet of the waveguide in (b). The output shows that light is transmitted at a wavelength of 8 µm through a suspended silicon waveguide across the whole sample. The dashed lines indicate the size of the sample side. f) Profile of the detected counts through the waveguide end facet in (e), when the laser is turned off (black markers) and turned on (red markers). Again a Gauss curve is fitted to the data. The scale of all IR micrographs is normalized to the minimum and maximum signal within each picture.

compared to the alignment to a focal spot of a lens or objective, the laser beam is coupled to a polycrystalline chalcogenide glass fiber and the fiber end is positioned as close as possible to the waveguide facet. The output is monitored by an IR camera with its focal plane adjusted to the side of the sample containing the waveguide end facet. The sample is also monitored from above by a further IR camera. While the laser is still turned off, the top view of the configuration is shown in Fig. 5.11 a). On the left side of the sample the fiber holder is visible and the fiber is aligned to a waveguide end. In the center of the sample, the s-shaped waveguides from one side of the chip to

the other side are visible. Below these structures, the straight waveguides are placed. The same view when the laser is turned on at a wavelength of 8 µm, is given in panel (b). The outline of the fiber holder, the fiber and the sample are indicated by the dashed lines. A bright spot is now visible at the input position of the waveguide. The fiber core diameter is 12 µm, which is much larger than the 1 µm x 6 µm end facet of the waveguide. A part of the larger mode of the fiber is scattered at the edge of the sample and detected by the IR camera above the sample. At the output position of the waveguide there is also a weak signal visible. When exiting the waveguide most of the light propagates in forward direction and thus only a small fraction is scattered upward to the IR camera. This is, to the best of our knowledge, the very first demonstration of transmission through integrated photonic silicon waveguides at an LWIR wavelength of 8 µm.

The transmission through the waveguide is also confirmed by monitoring the output with an IR camera from the side. First the output directly from the fiber is recorded. This IR micrograph is shown in Fig. 5.11 c), where the dashed circle indicates the outline of the fiber facet, which includes the core as well as the direct cladding. As the mode in the fiber is guided in the small core, the fiber output is mainly recorded by a single pixel of the camera. The profile of the output through this spot is shown in panel (d) and compared to the case when the laser is turned off. Here it can be observed, that the pixels next to the main peak only record a very weakly increased signal when the laser is turned on. According to the specification, one pixel in the micrograph taken by the IR camera with a 40 mm objective corresponds to a distance of 25 µm. Bearing in mind that only three data points contribute to the peak, a Gaussian curve (dashed line) can be fitted to the data, giving a very rough estimation of a mode field diameter equal to approximately 21 µm. The IR camera is very sensitive to small signals and particular care has to be taken for not damaging the camera sensor. Thus, for recording the direct output from the fiber, the laser is driven in pulsed mode with the lowest possible duty cycle of 0.002 % (1 kHz pulse rate, 20 ns pulse width), which corresponds to an average power at the output of the fiber smaller than 1 µW.

Similarly, the light transmitted through the suspended silicon waveguide is detected with the IR camera by monitoring the front view of the side of the sample that contains the end facet of the waveguide. This is depicted in Fig. 5.11 e), with the profile through the spot shown in (f). Thereby, compared to the fiber output, a slightly enlarged mode profile with an approximate width of 26 µm is obtained. However, in order to be able to record the waveguide transmission the average laser power has to be increased by using a duty cycle of 0.2 % (10 kHz pulse rate, 200 ns pulse width). Subtracting the background signal obtained without the laser beam, the output peak from the waveguide can be compared to the fiber output, which gives an estimation for the transmission through the waveguide of $\sim$0.3 %. This includes the coupling to the waveguide as well as the propagation along the waveguide with a total length of 9 mm. Considering the length of the waveguide as well as the large mismatch between the fiber core dimension and the waveguide cross-section, which limits the coupling efficiency, this is a promising result for the photonic circuit performance.

Coupling to and from a waveguide via the end facet requires access to the photonic circuits via the

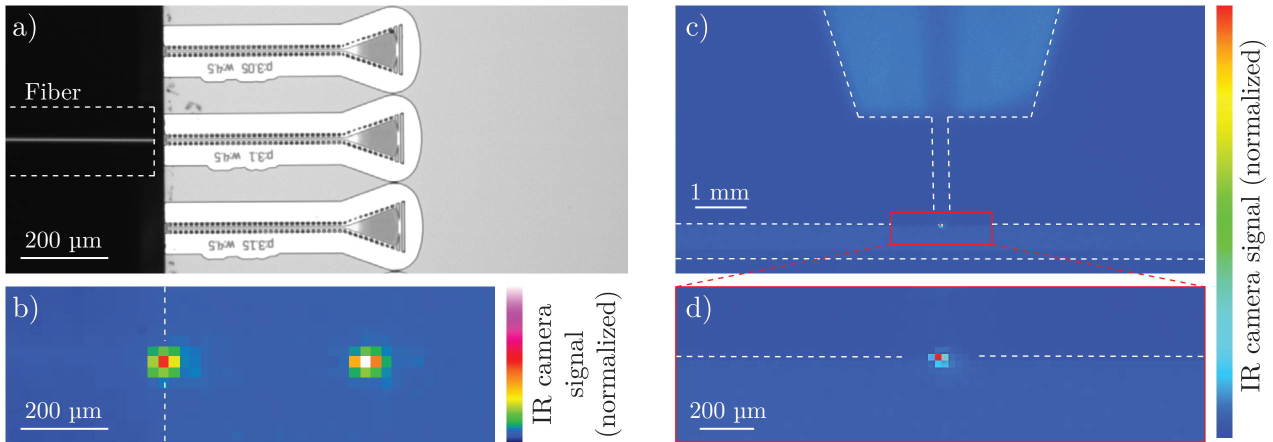

Figure 5.12.: a) Optical micrograph of the suspended silicon waveguides terminated on the left side by a waveguide facet and on the right side by a grating coupler. The fiber end is aligned to the waveguide facet. b) When the laser is turned on ($\lambda = 8\,\mu\text{m}$), a bright spot at the edge of the sample as well as at the position of the grating coupler is recorded by the IR camera. c) The fiber end is placed above the sample and light is coupled to the waveguide via the grating coupler. A bright output spot is detected at the end facet of the waveguide by the IR camera. The outline of the fiber holder and the fiber as well as the side of the sample are indicated by the dashed lines. d) Zoom in on the output at the waveguide end facet.

side of the sample. This limitation for the effectively usable sample area can be avoided by out-of-plane coupling via focusing grating couplers (see Sec. 2.4.2). Therefore, grating couplers are tested in the LWIR regime. Waveguides are fabricated which are terminated on one end by a facet on the side of the chip, but on the other end by a grating coupler. Light can now be coupled from the fiber to the waveguide via the end facet and the output from the grating coupler is monitored with the IR camera from above. An optical micrograph of the configuration taken with the CCD camera is shown in Fig. 5.12 a). The outline of the fiber end is indicated by the dashed lines and it is aligned to a 400 µm long waveguide terminated on the other end by a grating coupler with a grating period of 3.1 µm. The IR micrograph of the same device when the laser is turned on is shown in panel (b). Due to scattering of light from the fiber at the edge of the sample a bright spot at the sample border is visible. The second spot is caused by output coupling of light from the waveguide via the grating coupler in upward direction.

Vice versa, the input coupling via the grating coupler is tested, by placing the fiber above the coupler and monitoring the output at the waveguide facet. In the IR micrograph of the side of the sample in Fig. 5.12 c), the outline of the fiber holder and the fiber above the chip can be spotted in the top part. The side of the sample is marked by the horizontal dashed lines. The output from the waveguide is visible as a bright spot (see enlarged picture in (d)), which vanishes when the laser is turned off or the fiber is misaligned from the coupler position. Comparing the output signal from the waveguide facet to the one directly obtained from the fiber end, a transmission of up to 2 % can be estimated.

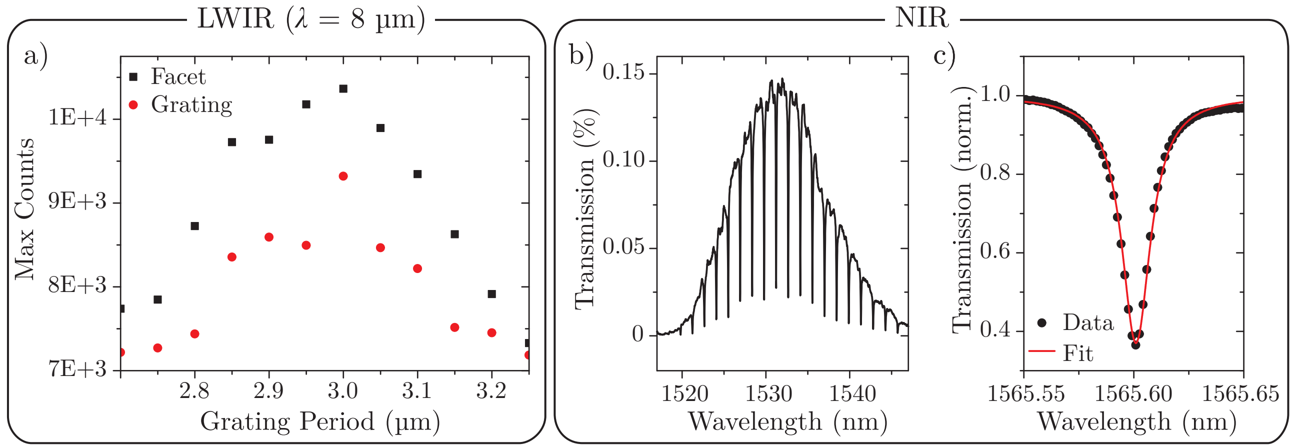

Figure 5.13.: a) Maximum detected counts by the IR camera at the waveguide output for a varying grating coupler period. For the black markers, light is coupled to the waveguide via the end facet and the output is recorded at the grating coupler and for the red markers light is coupled to the waveguide via the grating coupler and the output is recorded at the end facet. b) On the very same sample that contains the circuits for LWIR operation, there are also devices included for operation in the NIR regime. Here a spectrum of a ring resonator close to critical coupling is presented. c) For a more weakly coupled ring a resonance with a quality factor of 1×10^5 and an ER of 4.4 dB is achieved.

Additionally, the output from the grating coupler or the waveguide facet is compared when devices with a varying grating period are used. The maximum detected counts at the output position recorded by the IR camera are shown in Fig. 5.13 a). For both, input coupling via the facet, output at the grating coupler (black squares) and for input coupling via the grating coupler, output at the waveguide facet (red dots), the maximum efficiency for coupling light with a wavelength of 8 µm is obtained for a grating period around 3.0 µm. Shifting the period from this point, where the Bragg condition is fulfilled, decreases the obtained waveguide transmission. It can also be observed, that the input coupling via the facet seems to be slightly more efficient than input coupling via the grating coupler. The coupling efficiency of the grating coupler can however be further enhanced by adjusting its geometrical parameters such as the fill factor.

In a further step, devices which are terminated by a grating coupler on one end and by a facet on the other one are fabricated with a step-wise increase of the waveguide length from 300 µm to 2.1 mm. The decrease of the transmission is recorded in dependence on the waveguide length, but the fluctuations of the results are in the same magnitude as the decrease. This is most likely caused by variations of the waveguide end facet quality, which is obtained in the etching process of the structures. Therefore, only a very rough estimation for the propagation losses of around 1 dB/mm can be given. This nevertheless fits to the observed decrease of the transmission from 2 % for the waveguide with a length of 400 µm to a transmission of 0.3 % for the 9 mm long waveguide across the whole sample. In this case however, the different coupling methods used for the two waveguides are neglected. For a more precise determination of the propagation losses via the cutback method, waveguides with an increasing length in steps of e. g. several mm should be fabricated. And even more important is the

recording of a transmission spectrum by performing a wavelength sweep of the laser and using a fast detector. In this way the ring resonators, which are already implemented on the sample can be evaluated. The necessary steps for such a future evaluation are discussed at the end of the chapter.

On the very same sample that contains the circuits for operation in the LWIR regime, there are also devices for the NIR regime included. For these structures only some geometrical properties like the waveguide width or the grating period are adjusted, but they are fabricated simultaneously to the LWIR devices in the same process including the under-etching of the devices. A transmission spectrum in the NIR C-band of a ring resonator close to critical coupling with a gap of 100 nm to the bus waveguide is shown in Fig. 5.13 b). A high quality factor of up to 1×10^5 is achieved for a weakly coupled ring resonator with a gap of 200 nm to the bus waveguide. Such a resonance is shown in panel (c), which still exhibits an ER of 4.5 dB. This corresponds to an attenuation coefficient of 0.5 dB/mm, which is only slightly larger than the one obtained for devices on the 220 nm thick SOI platform (see Sec. 5.3.2). This is caused by an increased sidewall roughness during the etching procedure as there is no reflow procedure applicable for HSQ resist. Furthermore, this rough sidewall area is much increased as an etching depth of 500 nm is used instead of 110 nm. Also the top surface might be impaired as the device layer is thinned down in a dry etching process prior to the device fabrication. Considering those limiting factors, the circuit quality is still very good.

Previous experimental demonstrations of similar photonic circuits using suspended [412–415] or pedestal [410, 411, 516] silicon waveguides were limited to wavelengths lower than 5.2 µm. At this wavelength ring resonators with a quality factor up to 8100 have been demonstrated [407, 408]. With the photonic circuits presented here, not only device operation in the LWIR regime at 8 µm on a silicon platform is realized, but the platform can simultaneously be used for NIR applications. This enables for example the implementation of a combination of sensing schemes covering a broad spectral range from the NIR to the LWIR regime as there is no limiting factor for transferring the presented device operation to an intermediate wavelength.

5.5.3. Characterization of Diamond Devices

In this section the device performance of diamond integrated photonic circuits in the LWIR regime is discussed. Diamond on aluminum nitride is in terms of the fabrication process a very handy platform. The photonic structures are fabricated in a single lithography step without any need to under-etch the waveguides. As a first test for circuits fabricated from the 1.5 µm thick diamond layer on the 5 µm AlN buffer, devices in the NIR regime are used. At a wavelength around 1550 nm a propagation loss as low as 6.1 dB/mm, obtained from ring resonators ($Q = 6.900$, weakly coupled) as well as by the cutback method, is achieved for the best devices. These preliminary results demonstrate the suitability of this platform for the realization of integrated photonic devices. The slightly increased losses compared to the basic diamond on oxide buffer platform (∼4 dB/mm, see Sec. 5.4.3) are caused by the rather rough interface between AlN and diamond and the increased size of the etched sidewalls.

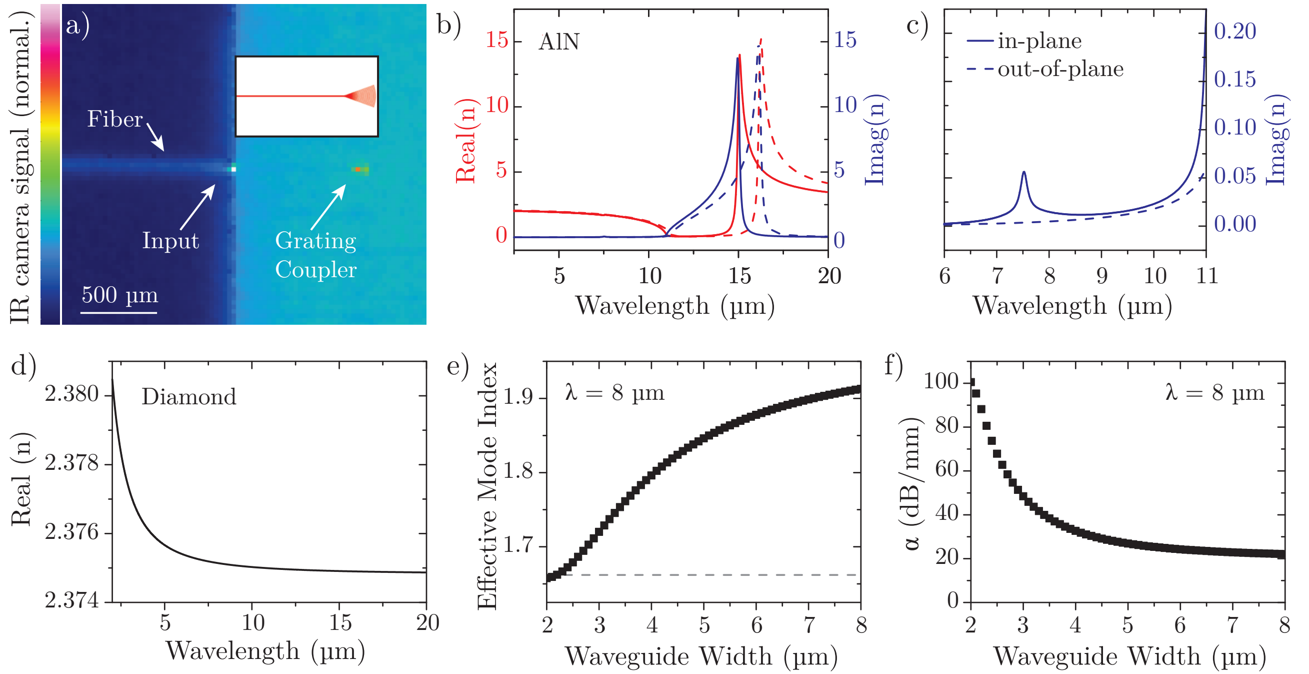

Figure 5.14.: a) IR micrograph of a diamond on AlN waveguide. A bright input spot can bee seen where light from the fiber is coupled to the waveguide via the waveguide end facet. A rather weak output spot can be observed at the grating coupler position. The waveguide design is shown in the inset. b) Real (red) and imaginary (blue) part of the refractive index of AlN obtained by IR ellipsometry. The solid line corresponds to the in-plane value and the dashed line to the out-of-plane value. c) Zoom-in on the imaginary part around a wavelength of 8 µm. d) Similarly, the refractive index of diamond is obtained by ellipsometry. Using these values for the refractive index of AlN and diamond, the effective mode index (e) of the guided modes in the diamond waveguide is simulated. The dashed line indicates the cut-off for the supported modes. f) Additionally, the attenuation coefficient α, which is caused by the imaginary part of the refractive index of AlN, is obtained from the simulations.

When characterizing the devices at a wavelength of 8 µm, transmission can only be recorded for very short waveguides. An IR micrograph of the top view of a 600 µm long waveguide with a width of 6.5 µm, terminated by a grating coupler on one end, is shown in Fig. 5.14 a). On the left side, where light is coupled from a fiber to the waveguide via its end facet, a bright spot is visible and at the position of the grating coupler the output is monitored. The inset in the picture shows the waveguide layout of the tested device. A further increase in the waveguide length quickly leads to the loss of any transmission signal, which indicates a much larger attenuation than expected from the small coupling losses to the silicon substrate or from scattering effects (see Sec. 5.4.1). Therefore, the AlN and diamond optical properties are studied by IR ellipsometry[6]. First, a sample with only 5 µm AlN on a silicon substrate and, secondly, a sample with 1.5 µm diamond on an AlN-on-Si substrate is studied for extracting the optical constants of both AlN and diamond in the IR range.

The obtained real (red line) and imaginary (blue) part of the refractive index for AlN is shown

[6] IR ellipsometry of the samples is performed by J.A. Woollam (J.A. Woollam Co. Inc., Lincoln, NE 68508, USA) with their IR-Vase Mark II instrument.

in Fig. 5.14 b), where the solid line corresponds to the in-plane and the dashed line to the out-of-plane value. This is caused by the birefringence of AlN and the typical column-wise growth structure during sputter deposition. For light guiding along the integrated circuits, the in-plane value is of particular interest. The imaginary part, which corresponds to the material absorption, shows a strong increase from a wavelength of 11 µm to its peak at 15 µm. A detailed view of the imaginary part around 8 µm (see panel (c)) reveals that there is an additional small absorption peak for the in-plane value at 7.5 µm. This experimentally determined complex refractive index of AlN in combination with the obtained refractive index for diamond (see panel (d)) is used to simulate the supported modes in diamond waveguides on the AlN buffer. The resulting effective mode index of the fundamental TE mode at a wavelength of 8 µm is shown in panel (e) and it can be seen that the mode is well supported for the used waveguide width of 6.5 µm. The imaginary part of the AlN refractive index causes absorption in the waveguide and the extracted attenuation coefficient is shown in panel (f). For a small waveguide width, a large part of the mode extends to the AlN buffer, which causes a strong attenuation. For increasing waveguide width, the mode is better confined in the waveguide area and the attenuation decreases to a relatively constant value around 20 dB/mm. This still very large attenuation explains the quickly decaying transmission for a waveguide length in the order of 1 mm. Hence, for the fabrication of LWIR compatible low-loss integrated photonic diamond circuits on an AlN buffer the material quality of the sputter-deposited AlN layer needs to be enhanced. It has been shown that by varying the growth conditions in the deposition process, the absorption peak around 7.5 µm can be avoided [402]. For the future development of diamond on AlN circuits the deposition process has to be improved or another manufacturer for the AlN layers has to be found.

Suspended Diamond Circuits

In contrast to the diamond on AlN platform, suspended diamond circuits are not inhibited by any buffer layer. This makes the platform ideal for very broadband operation from the visible to the far IR regime. The characterization of the platform at a wavelength of 8 µm is presented in the following. Light is coupled from a chalcogenide glass fiber to the waveguide and the transmission through the circuits is recorded by an IR camera. First, the fiber is placed above the sample and light is coupled via a grating coupler to the waveguide. The end facet of a 400 µm long waveguide with a width of 4.5 µm is monitored by the IR camera. A bright spot at the output of the waveguide (see Fig. 5.15 a)) is clearly visible. Here, the horizontal dashed lines mark the side of chip, while the dashed lines above the sample mark the outline of the fiber holder and of the fiber. Additionally, the transmission at the grating coupler is recorded when light is coupled in the reverse direction into the end facet.

An array of devices with varying period of the grating coupler is studied and the transmission trough the devices measured for the two different cases is compared. The maximum counts recorded by the IR camera as a function of the grating period are reported in Fig. 5.15 b) for input coupling via the facet (output via the grating coupler; black squares) and for input coupling via the grating coupler

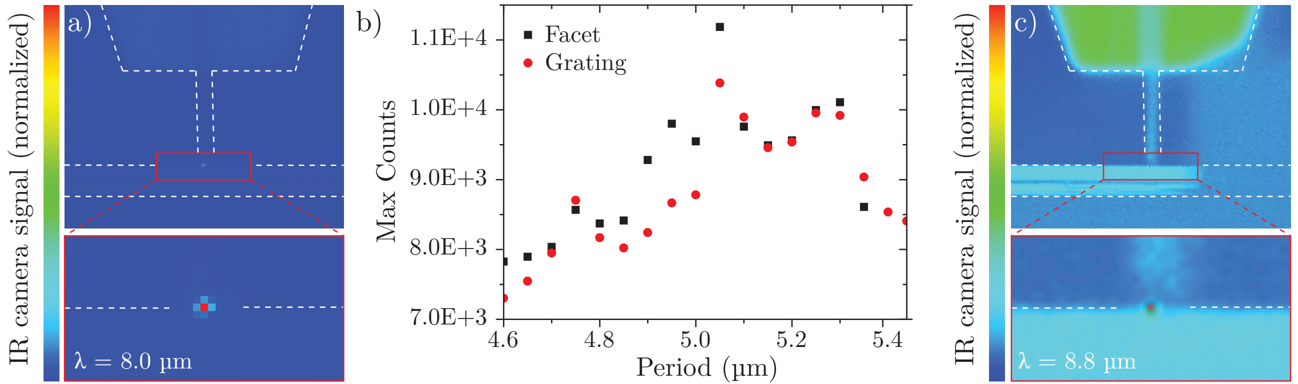

Figure 5.15.: a) IR micrograph of the output at the end facet of the suspended diamond waveguide when light is coupled in via the grating coupler. The horizontal dashed lines mark the side of the sample and above the sample the outline of the fiber holder and fiber are indicated. b) Maximum recorded counts of the IR camera depending on the grating period of the coupler. The black squares correspond to input coupling via the facet (output at the grating coupler) and the red dots to input coupling via the grating coupler (output at the end facet). c) Similarly to the scenario in (a), the transmission at the end facet is monitored when the wavelength is increased from 8.0 µm to 8.8 µm.

(output via the facet; red dots). Thereby, an optimal grating period around 5.1 µm for coupling light at $\lambda = 8$ µm is obtained. The fluctuations of the transmission in this graph are most likely caused by variations of the waveguide end facet quality, which is influenced by the etching process as well as the dicing of the sample where the cut position is placed as close as possible to the end facet. The transmission trough the waveguide is also tested at a wavelength of 8.8 µm (see Fig. 5.15 c)). However, the recorded output power is much weaker than in the previous case, since the largest grating period available on the sample (5.5 µm) is too small for achieving efficient coupling at this wavelength.

In order to determine the propagation losses of the suspended diamond platform at a wavelength of 8 µm, several devices with increasing waveguide length from 300 µm to 2.1 mm are studied. The circuit layout as well as the corresponding recorded IR micrographs for the devices are presented in Fig. 5.16 a). Light is coupled from the fiber via the end facet of the waveguide and the output at the grating coupler position is monitored. Additionally, an SEM micrograph of these structures is displayed in panel (b). The measured transmission as a function of the waveguide length is reported in panel (c) for several devices with a grating period ranging from 4.9 µm to 5.4 µm. The attenuation coefficient corresponding to the decrease of the transmission is extracted from a fit to the data as (9.8 ± 0.6) dB/mm. This is also confirmed by reversing the coupling scheme for input coupling via the grating coupler and recording the output at the waveguide facet.

On the same sample used for the characterization in the LWIR regime, devices for studying the circuit transmission in the NIR and visible regime are included. These are fabricated simultaneously to the LWIR structures in the same process and only geometrical properties in the circuit layout, like the grating coupler period and the waveguide width, are adjusted. The waveguides are terminated by grating couplers and are characterized in the standard NIR measurement setup (see Sec. 2.4.1). In

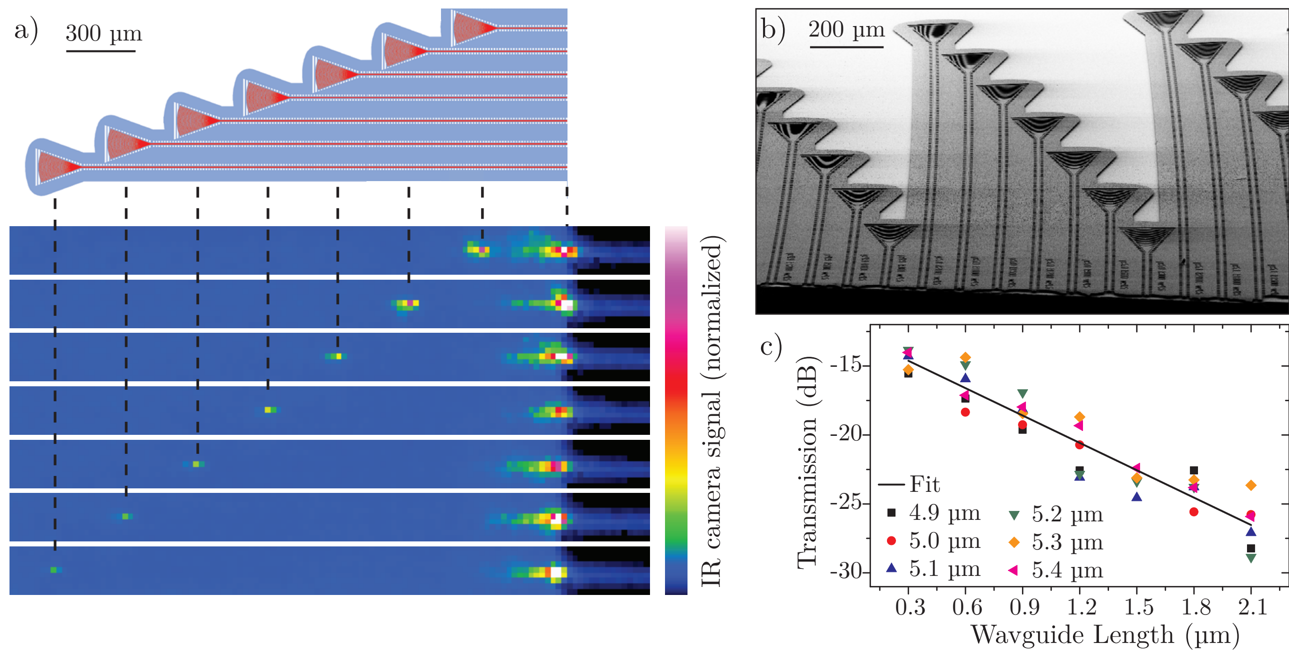

Figure 5.16.: a) Layout and IR micrographs of the devices used for determining the propagation losses via the cutback method. The waveguides in the layout are drawn in red, while the blue area is the mask for under-etching the devices. The IR micrographs are taken for input coupling from the fiber via the waveguide facet on the right side, while the output is recorded at the grating coupler position. b) The SEM micrograph shows the suspended diamond devices used here. c) Device transmission in reference to the signal directly obtained from the fiber end for a grating period between 4.9 µm and 5.4 µm depending on the waveguide length.

order to determine the device quality ring resonators coupled to a bus waveguide as well as devices with increasing waveguide length are studied. The spectrum of a ring resonator with a gap of 100 nm to the bus waveguide close to critical coupling is shown in Fig. 5.17 a). The Gaussian-like envelope of the spectrum with a peak transmission of 2.5 % at a wavelength of 1575 nm is caused by the grating couplers with a period of 860 nm. With increasing gap to the bus waveguide the quality factor of the ring resonators increase until an average Q of 6200 is reached close to its intrinsic value for a very weakly coupled ring at a gap size of 400 nm (see panel (b)). This corresponds to an attenuation coefficient of (8.9 ± 0.8) dB/mm. The attenuation is furthermore determined by using devices with increasing waveguide length and comparing the recorded transmission. The maximum transmitted power depending on the waveguide length between 350 µm and 1.65 mm is shown in Fig. 5.17 c) for devices with a grating coupler period from 840 nm to 900 nm. From a fit to the data an attenuation of (9.4 ± 0.7) dB/mm is extracted in good agreement with the results obtained from ring resonators.

The propagation losses in the NIR regime for suspended diamond circuits are larger than the ones obtained for the the devices fabricated from the standard 600 nm diamond on SiO_2 buffer platform (∼4 dB/mm). Besides the increased etching depth and thus larger uneven sidewall area, this is mainly attributed to variations in the surface roughness of the deposited diamond layer on the different wafers

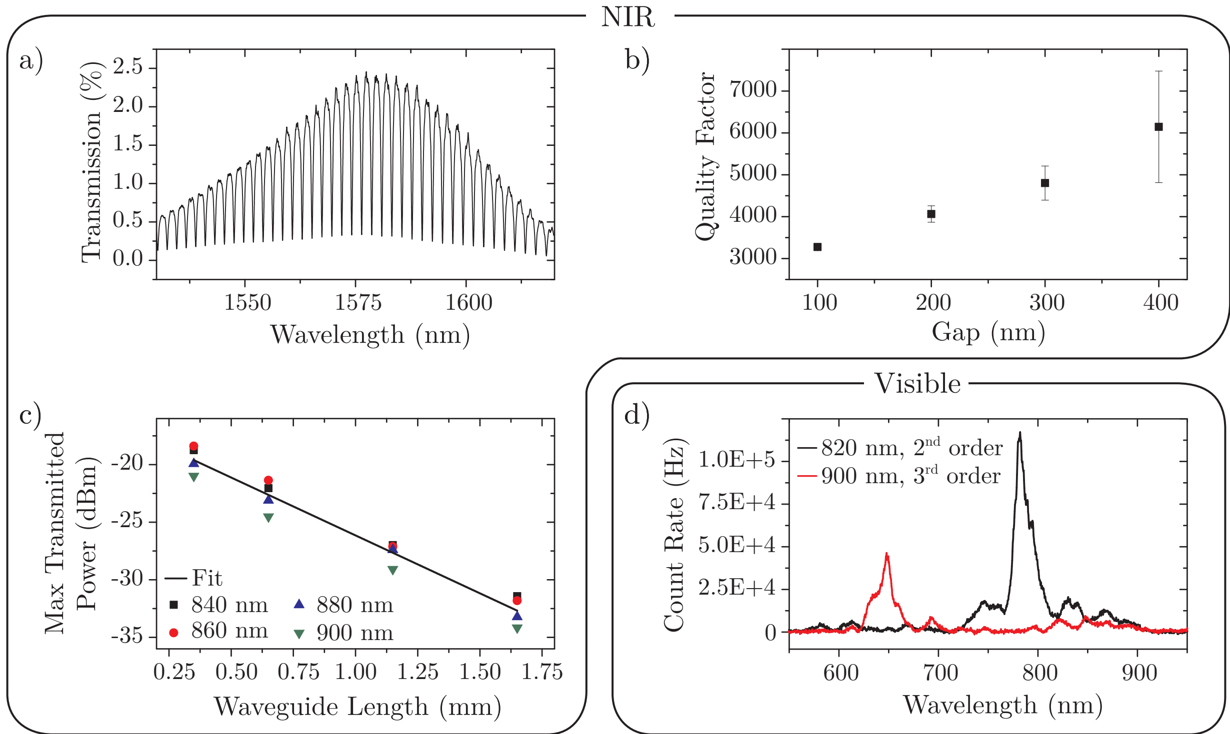

Figure 5.17.: a) Transmission spectrum of a ring resonator in the NIR regime close to critical coupling at a gap of 100 nm to the bus waveguide. b) By increasing the gap size an average quality factor of 6200 is achieved for a very weakly coupled ring at a gap size of 400 nm. c) The maximum transmitted power depending on the waveguide length is plotted and an attenuation coefficient of (9.4 ± 0.7) dB/mm is obtained from the fit. d) Device transmission recorded by a spectrometer in the visible regime at a wavelength of 780 nm, achieved via second order coupling by a grating coupler with a period of 820 nm (black line) and at 650 nm via third order coupling by a grating coupler with a period of 900 nm (red line).

after the polishing procedure. A thicker diamond layer leads to an increased surface roughness after CVD deposition and this is still evident after a reduction of the layer thickness by ∼400 nm during chemo-mechanical polishing. The attenuation in the LWIR regime compared to the NIR regime is very slightly increased. While a reduction of scattering losses due to sidewall and surface roughness is expected because of the larger wavelength, the intrinsic material absorption of PCD grown by CVD in the LWIR region is enhanced [398]. For the platform studied here, both effects balance each other and a similar attenuation coefficient is obtained for both spectral regions.

Besides the characterization of suspended diamond waveguides in the LWIR and NIR regime, the platform is also studied in the visible spectral regime. The transmission spectra in this region are recorded by using a broadband white light source in combination with a spectrometer (see App. A.7). The same devices used for NIR transmission measurements are characterized at visible wavelengths by coupling light into and from the waveguides via the second and third diffraction orders of the grating couplers. Fig. 5.17 d) shows the measured transmission spectra at a wavelength of 780 nm and

650 nm. The spectra do not exhibit a single transmission peak, but rather consist of a combination of several peaks because a multitude of modes are supported by the waveguides at such wavelengths. The propagation loss at a wavelength of 780 nm is estimated via the cutback method as (16.6 ± 2.9) dB/mm. In order to give a comprehensive comparison between all platforms used within this work, the waveguide performance of the material systems in the different wavelength regimes is listed in Tab. 5.1.

The use of suspended diamond waveguides in the mid-IR regime for e. g. spectroscopic sensing has attracted increasing interest during the last years. In a PCD waveguide with a 14 µm x 13.5 µm cross-section, a propagation loss of 12.6 dB/cm at a wavelength of 3.4 µm has been reported [517]. By increasing the waveguide width to 100 µm and above (while keeping the height at 14 µm), light guiding in the wavelength regime between 5.78 µm and 6.35 µm for spectroscopic analysis of molecules has been demonstrated, however without specifying the waveguide attenuation [518, 519].

Only very recently, the extension of this material platform to the wavelength regime between 5 µm and 11 µm has been studied by using 14 µm x 500 µm large waveguides. While the principal suitability for chemical sensing via the evanescent field has been shown, the experimental determination of the waveguide attenuation has not been reported. The presented spectra however show very poor transmission above 7.7 µm [520]. All of these suspended diamond waveguides are supported by a silicon frame with a Si_3N_4 on SiO_2 buffer. In the area where the waveguides are attached to the frame, the substrate layers contribute significantly to the waveguide attenuation in the mid-IR and LWIR regime.

Material platform	Waveguide height	Wavelength	Attenuation coefficient	Ring quality factor	Extinction ratio
Si_3N_4 on SiO_2	180 nm ridge	780 nm	1.1 dB/cm	9.6×10^4	12.0 dB
	170 nm rib on 170 nm membrane	1590 nm	21 dB/m	1.6×10^6	0.7 dB
Si on SiO_2	110 nm rib on 110 nm membrane	1600 nm	3 dB/cm	2.4×10^5	0.8 dB
Suspended Si	500 nm rib on 500 nm membrane	1530 nm	5 dB/cm	1×10^5	4.4 dB
		8 µm	10 dB/cm	-	-
Diamond on SiO_2	400 nm rib on 200 nm membrane	800 nm	-	-	-
		1515 nm	4.3 dB/mm	1.1×10^4	1.3 dB
Diamond on AlN	1 µm rib on 500 nm membrane	800 nm	13.6 dB/mm	-	-
		1550 nm	6.1 dB/mm	6.9×10^3	0.8 dB
		8 µm	-	-	-
Suspended Diamond	1 µm rib on 500 nm membrane	780 nm	16.6 dB/mm	-	-
		1550 nm	8.9 dB/mm	6.2×10^3	0.4 dB
		8 µm	9.4 dB/mm	-	-
		8.8 µm	-	-	-

Table 5.1.: Comparison of waveguide and ring resonator properties of integrated optical circuits based on the different material platforms used within this work.

This effect is slightly reduced by a well confined mode in the rather large waveguide, which also diminishes the influence of scattering losses caused by the very rough waveguide sidewalls. However, a drawback of using such large waveguides is that it also reduces the evanescent field employed for chemical sensing, thus strongly limiting the sensitivity of this platform. Furthermore, the use of a waveguide width above 100 µm enlarges the footprint of the implemented devices and strongly reduces the scalability of this platform for complex photonic circuits.

A much more scalable platform is presented here with a waveguide cross-section of 1.5 µm x 4.5 µm. This holds not only promise for very sensitive spectroscopic detection of molecules via a strong evanescent field, but also enables the realization of complex circuit designs. Many different devices such as beam splitters, interferometers and microcavities like ring resonators or photonic crystal cavities can be integrated on a single compact platform. Furthermore, the demonstrated use of grating couplers allows for out-of-plane access to the circuits and enables the exploitation of the complete sample area. Additionally, the suspended circuits are not inhibited by material absorption of the substrate as they are supported by diamond bridges. The circuits presented here are not only characterized in the LWIR regime at a wavelength of 8 µm, but also at NIR and visible wavelengths, demonstrating the high flexibility of this platform. Furthermore, the range of usable wavelengths could be extended to the far-IR regime by simply increasing the diamond layer thickness and waveguide width. Between the NIR and LWIR spectral regions diamond exhibits an absorption band only from 3 µm to 6 µm, which limits its usability in the mid-IR. The combination of devices over a very broad spectral range from the visible over the NIR to the LWIR regime allows to envision comprehensive detection schemes on a single platform for e. g. spectroscopic measurements in the molecular fingerprint region, sensing of click-chemistry binding processes in the NIR regime, as well as fluorescence detection in the visible regime.

5.6. Summary and Outlook

In this chapter, the extension of the usable wavelength range for integrated photonic circuits to the LWIR regime was studied. Therefore, the silicon and diamond photonic platforms were introduced along with the implementation of fabrication procedures and the characterization in the NIR regime. For the diamond platform, first steps of the waveguide surface functionalization for click-chemistry binding and subsequent detection of proteins in the NIR were discussed. The material platforms were further developed in order to enable transmission measurements at a wavelength of 8 µm for the suspended silicon, the diamond-on-AlN, as well as the suspended diamond platform. While lower propagation losses in the LWIR as well as NIR region are achieved using silicon waveguides, this platform is limited to a wavelength range between 1.1 µm and approximately 8.5 µm. Diamond waveguides displayed a higher attenuation, but their usability also in the visible spectral part was demonstrated and they offer the possibility for increasing the wavelength range on the long side up to potentially the far-IR regime. In particular, the integration of multiple devices operating in very different parts

of the electromagnetic spectrum on a single sample paves the way for for the implementation of complex sensing arrays on a compact and robust platform. Integrated photonic circuits for gas sensing and the coupling to atomic clouds can furthermore profit from suspended waveguides as they can be completely surrounded by a vapor leading to an enhanced interaction.

An important step for the further development of the presented platforms as a suitable candidate for spectroscopic sensing in the fingerprint region, is the recording of transmission spectra by performing a wavelength sweep and simultaneously detecting the transmission by a fast detector. The noise level of the currently available LWIR detector is at an input power level equal to -20 dB m. Even when using the laser in CW mode with an output power of approximately 240 mW, the transmitted power through the integrated circuits is too low to be detected because of the large losses introduced by external optical components as well as the limited coupling efficiency to the integrated circuits. Possible ways to reduce these losses are discussed in App. A.11, where the different parts of the setup are characterized. Most promising is the absolute reduction of the external elements of the setup by just using an optical isolator for protection of the laser modules and for example a ZnSe lens in order to couple the beam to the sample. However, as single mode waveguides for only TE transmission are used, coupling to the integrated devices is highly dependent on the light polarization. Therefore, without using a beam polarization controller, the sample has to be mounted on a revolving stage so that its orientation can be adjusted to the beam polarization. Also the alignment procedure in this case is more challenging compared to coupling via a fiber end. Further improvements on the coupling efficiency to the integrated circuits can be realized by using inverse tapered waveguide ends [521, 522] and by optimizing the waveguide end facet for example by careful FIB milling [523]. In terms of the detector sensitivity the use of a detector cooled by liquid nitrogen instead of water can be considered.

When being able to record a transmission spectrum in the LWIR regime, the response of ring resonators, which are already implemented on the suspended diamond as well as suspended silicon platform can be studied for further characterization of the integrated circuits and for future cavity enhanced spectroscopy measurements [421, 524]. Similar to the enhancement of the light-atom coupling in the visible regime (see Sec. 3.6.5), slot waveguides in the LWIR offer a viable way for achieving strong interactions in the sensing of chemicals, especially as a suspended material platform is already in use here. In addition to absorption measurements, on-chip MZIs can be implemented to enable phase-sensitive detection schemes. Future developments of this work will aim at the further expansion of the usable detection schemes by the implementation of opto-mechanical resonators, which are highly sensitive to the adsorption of single particles. Due to the mechanical properties of diamond, this platform is ideal for the realization of such elements [165].

Instead of coupling to the integrated circuits via the combination of a grating coupler on one and a waveguide facet on the other end, in and output coupling via a grating coupler can be realized by placing two or more chalcogenide glass fibers in an array, which can be aligned to the grating couplers. Thereby, a fast and convenient setup for the characterization of integrated devices can be implemented, similar to the one already employed in the NIR regime (see Sec. 2.4.1). The possibility

of implementing all-optical switching and routing devices in the LWIR regime based on the coupling to a low-loss phase-change material cell could as well be explored [56, 525, 526]. A further integration step can be taken by implementing on-chip photonic detectors for the LWIR regime along with the integrated circuits. For example, the transfer of superconducting nanowire single-photon detectors which are so far employed in the NIR and visible regime [53, 98] to the LWIR regime is of high interest.

As the grain boundaries in PCD are a main source for scattering losses and absorption via material impurities, the transfer of the integrated photonic circuits for the LWIR regime to a very pure SCD platform offers great potential for reducing the propagation losses and achieving high-quality circuits. This can either be realized by using thin suspended diamond membranes obtained from a bulk SCD slab via the thin-down approach or by carving the photonic structures directly from the bulk sample via angled etching techniques. A main advantage of suspended diamond membranes is that circuits can be directly fabricated without suffering from limitations of a highly absorbing buffer layer. Both cases however require rather challenging fabrication methods and the size of available SCD samples is typically limited to around $1\,\mathrm{cm}^2$, while PCD layers can be grown on wafer-scale substrates. An alternative method for the fabrication of photonic circuits from SCD samples has been demonstrated very recently by femtosecond laser writing. Thereby, device operation at a wavlength of $2.4\,\mu\mathrm{m}$ and $8.6\,\mu\mathrm{m}$ was realized [527]. The use of such waveguides for spectroscopic measurements is however limited, as the waveguides are completely buried in the bulk material. For sensing via the evanescent field, a femtosecond laser written diamond waveguide at the material surface needs to be demonstrated. Furthermore, femtosecond laser writing can only induce a small change in the refractive index of the material, resulting in waveguides with shallow mode confinement and a reduced scalability.

The flexibility of the suspended diamond as well as the suspended silicon platform presented here will enable a broad range of applications of integrated photonic devices in the LWIR regime. This is not only of great interest for spectroscopic sensing in the fingerprint region, but also for general miniaturization of optical systems in this spectral region. Hence, it represents an important new field for integrated photonic circuits. Especially the suspended diamond platform provides an exciting perspective as a material on which so far unknown combinations of devices in a spectral range from the visible to potentially even the far-IR regime are realizable.

Chapter 6.

6 Conclusion

In this thesis the potentials and capabilities of integrated photonic circuits for near-field coupling to surrounding elements have been demonstrated. This work was driven by the capacity of integrated circuits to confine strong optical fields on a sub-wavelength scale, which causes a very sensitive response of the guided modes to any changes in the waveguide surrounding. This motivated the development of circuits on several material platforms with the prospect of implementing evanescent-wave coupling schemes covering a huge spectral range from the visible to the LWIR regime. The presented results contain the development of a high-quality Si_3N_4 integrated photonics platform satisfying highest demands on the device performance in the visible and NIR regime and which is used for the coupling to a thermal rubidium vapor. The introduction of silicon photonic circuits enabled low-loss device operation from the NIR to the LWIR regime, which contains the first demonstration of silicon integrated circuits at a wavelength of 8 µm. Moreover, the further development of the diamond integrated photonics platforms was presented. This way, the first realization of photonic circuits for device operation in the visible, NIR as well as LWIR regime combined on a single sample and fabricated within the same structuring process was achieved.

Si_3N_4 integrated photonic circuits serve as a main platform for versatile projects within our research group. Therefore, the development of the basic passive integrated photonics platform was of particular interest. By optimizing the fabrication process (including the EBL exposure, reflow process and dry etching procedure) high-quality circuits were obtained. In the NIR regime at a wavelength of around 1550 nm circuits with a very low propagation loss of 21 dB/m were realized. This enables ring resonators with an average quality factor above 1×10^6 in the weakly coupled regime and a quality factor around 5×10^5 close to critical coupling. By using well balanced y-splitters, MZIs with a very large extinction ratio up to 40 dB were realized suitable for sensitive detection of phase shifts induced in the waveguide. In the visible regime at a wavelength of 780 nm ring resonators with a quality factor of 9.6×10^4 close to critical coupling ($ER = 12\,\mathrm{dB}$) were realized. This corresponds to a low intrinsic propagation loss of 1.1 dB/cm.

The Si_3N_4 platform in the visible spectral regime was used for interfacing a thermal rubidium atom

vapor with the nanophotonic circuits. For ultra precise measurements, for example in metrology and for strong atom-photon coupling in cavity QED, typically ultra cold atoms have to be used which usually requires a rather large setup. On the contrary, using a thermal atom vapor offers less precision and control but the low technical complexity and the potential for miniaturization enables their integration with scalable nanophotonic networks. Here, the coupling of a waveguide mode in a precisely defined interaction region was studied. By out-of-plane accessing of the photonic circuits through a transparent substrate, the production of small and handy vapor cells for the light-atom interaction was realized. Linear absorption spectra were recorded for the determination of the interaction strength and as a demonstration for spectroscopic sensing within integrated photonic circuits. These structures are also suitable for the development of all-optical modulators based on the opening of a transparency window within the electron transition via non-linear effects. Additionally, the induced phase shift by the surrounding atom vapor was determined via MZIs in order to obtain a comprehensive description of the light-atom interaction. A theoretical model for the interaction was implemented, which agrees well with the experimental results and can be used to make further predictions for atom vapor based devices. The combined influence on the absorption and phase was studied in ring resonators that could be used for all-optical switching and routing via two-photon absorption. Therein, an atomic transition in the NIR regime is of particular interest for interfacing high-Q resonators with a thermal atom vapor. In a last step the possibility of increasing the interaction strength by using slot waveguides was studied. Integrating a thermal atom vapor with nanophotonic circuits can also provide a compact on-chip Doppler-free frequency reference based on counter-propagating beams.

The potential of integrated photonic circuits for sensing application shown by coupling to a thermal atom vapor in the visible regime was further extended by the development of an integrated platform usable in the LWIR regime. This spectral part encloses the fingerprint region that is of main interest for chemical sensing and analysis of molecules as well as a technologically important atmospheric window used for communication systems and thermal imaging and detection. A suspended silicon platform was developed for simultaneously implementing devices in the NIR and LWIR regime. At a wavelength of 1550 nm ring resonators with a quality factor up to 1×10^5 and an attenuation of 0.5 dB/mm were realized while a propagation loss of 1 dB/mm was estimated for a wavelength of 8 µm. Thereby, transmission through fully suspended waveguides with a length up to 9 mm was enabled.

For a further spectral extension of integrated photonic circuits, diamond was studied as a device material. The structures were fabricated from PCD layers grown by CVD on wafer-scale substrates. Diamond-on-insulator was used as a platform in the NIR regime (with a propagation loss of 4.3 dB/mm) where the surface functionalization of waveguides for the detection of AFP as an indicator for a certain kind of cancer was studied. This paves the way for implementing integrated photonic sensing of proteins via click-chemistry binding to the waveguide surface for life-science applications. First diamond circuits for device operation in the LWIR regime were based on diamond-on-AlN structures. It could be shown that the large waveguide attenuation of these devices was caused by the nitride buffer properties. A further development of the diamond platform led to suspended circuits,

which enabled device operation in the visible, NIR and LWIR regime on a single sample. For these circuits an attenuation of 8.9 dB/mm and a ring resonator quality factor up to 6200 in the NIR regime as well as an attenuation of 9.8 dB/mm in the LWIR regime at a wavelength of 8 µm was achieved. Coupling to and from the circuits was not only demonstrated via the waveguide end facet but also via grating couplers for out-of-plane access. This platform enables the development of so far unattainable sensing schemes by combining measurements in the visible, NIR ans LWIR regime with the prospect of being expandable even to the far-IR region. Besides its application for spectroscopic measurements in the fingerprint region, the presented diamond platform is a promising candidate for the miniaturization of general optical systems in the LWIR regime, which offers a major growth opportunity for integrated photonic technologies.

A Appendix A.

Appendix

A.1. Refractive Indices and Dispersion

In this section, the refractive indices n and the corresponding dispersion formulas of the materials used within this thesis are given. These are for example employed for the FEM simulations of the optical modes guided along waveguides and their evanescent field. The equations are given for λ in µm.

- Silicon, Si [105, 528]

$$n(\lambda) = \left(1 + \frac{10.6684293\lambda^2}{\lambda^2 - 0.301516485^2} + \frac{0.0030434748\lambda^2}{\lambda^2 - 1.13475115^2} + \frac{1.54133408\lambda^2}{\lambda^2 - 1104^2}\right)^{1/2} \tag{A.1}$$

- Silicon oxide, SiO_2 [106, 529]

$$n(\lambda) = \left(1 + \frac{0.6961663\lambda^2}{\lambda^2 - 0.0684043^2} + \frac{0.4079426\lambda^2}{\lambda^2 - 0.1162414^2} + \frac{0.8974794\lambda^2}{\lambda^2 - 9.896161^2}\right)^{1/2} \tag{A.2}$$

- Silicon nitride, Si_3N_4 [115, 530]

$$n(\lambda) = \left(1 + \frac{2.8939\lambda^2}{\lambda^2 - 0.13967^2}\right)^{1/2} \tag{A.3}$$

- Aluminum nitride, AlN [531]

$$n_e(\lambda) = \left(3.0729 + \frac{1.6173\lambda^2}{\lambda^2 - 0.1746^2} + \frac{4.139\lambda^2}{\lambda^2 - 15.03^2}\right)^{1/2}$$

$$n_\mathrm{o}(\lambda) = \left(3.1399 + \frac{1.3786\lambda^2}{\lambda^2 - 0.1715^2} + \frac{3.861\lambda^2}{\lambda^2 - 15.03^2}\right)^{1/2} \tag{A.4}$$

- Diamond, discrete values from [395, 398] are typically used.
  The diamond layer is also examined by IR ellipsometry and a Sellmeier equation is fitted to the obtained data. This yields the following formula:

$$n(\lambda) = \left(1 + \frac{0.31989\lambda^2}{\lambda^2 - 0.55723^2} + \frac{4.31987\lambda^2}{\lambda^2 - 0.000001894^2}\right)^{1/2} \tag{A.5}$$

- HSQ resist, data obtained from reflectometer measurements

$$n(\lambda) = 1.392 + \frac{0.004}{\lambda^2} + \frac{0.00003}{\lambda^4} \tag{A.6}$$

A.2. Detailed Derivation of Ring Resonator Properties

In this section the derivation of the loss in a ring resonator and the coupling coefficients of a ring coupled to a bus waveguide is described. As stated in the main text, the coupling is characterized by the complex coupling and transmission coefficients κ and t, which satisfy the relation $|\kappa|^2 + |t|^2 = 1$ for symmetric coupling between identical waveguides. The coupling of the field amplitudes is then described by the matrix relation [132, 153]:

$$\begin{pmatrix} E_{\mathrm{t1}} \\ E_{\mathrm{t2}} \end{pmatrix} = \begin{pmatrix} t & \kappa \\ -\kappa^* & t^* \end{pmatrix} \cdot \begin{pmatrix} E_{\mathrm{i1}} \\ E_{\mathrm{i2}} \end{pmatrix}. \tag{A.7}$$

The input field E_{i2} is directly linked to the second output field by

$$E_{\mathrm{i2}} = A \cdot e^{i\theta} E_{\mathrm{t2}} = e^{-\alpha/2L} \cdot e^{i2\pi n_{\mathrm{eff}}/\lambda L} E_{\mathrm{t2}}, \tag{A.8}$$

where A is the transmission factor during one roundtrip (and $1 - A$ being the loss itself) and θ is the collected phase. From these two equations and by expressing the complex transmission coefficient as $t = |t|e^{i\phi_t}$ the transmitted power in the bus waveguide and the circulating power in the ring follow as [532]

$$P_{\mathrm{t1}} = |E_{\mathrm{t1}}|^2 = \frac{A^2 + |t|^2 - 2A|t|\cos(\theta + \phi_t)}{1 + A^2|t|^2 - 2A|t|\cos(\theta + \phi_t)} \tag{A.9}$$

$$P_{\mathrm{i1}} = |E_{\mathrm{i2}}|^2 = \frac{A^2(1 - |t|^2)}{1 + A^2|t|^2 - 2A|t|\cos(\theta + \phi_t)}. \tag{A.10}$$

The characteristic resonances are obtained for wavelengths satisfying the resonance condition

$$\theta_{\mathrm{r},m} + \phi_t = 2\pi \frac{n_{\mathrm{eff}}}{\lambda_{\mathrm{r},m}} L + \phi_t = 2m\pi, \quad (m \in \mathbb{N}). \tag{A.11}$$

Else, destructive interference in the ring is obtained for

$$\theta_{\mathrm{r},n} + \phi_t = 2\pi \frac{n_{\mathrm{eff}}}{\lambda_{\mathrm{r},n}} L + \phi_t = (2n + 1)\pi, \quad (m \in \mathbb{N}). \tag{A.12}$$

Inserting this in Eq. (A.9) the minimum and maximum transmitted power on resonance and in between resonances respectively is

$$P_{\mathrm{t1,min}} = \frac{(A - |t|)^2}{(1 - A|t|)^2} \qquad P_{\mathrm{t1,max}} = \frac{(A + |t|)^2}{(1 + A|t|)^2}. \tag{A.13}$$

Therefore, the ER can be derived as

$$ER = \frac{P_{\mathrm{t1,max}}}{P_{\mathrm{t1,min}}} = \left(\frac{(A + |t|)(1 - A|t|)}{(1 + A|t|)(A - |t|)} \right)^2. \tag{A.14}$$

The finesse $\mathcal{F} = {}^{FSR}/_{\delta\lambda}$ relates the separation between the resonances to the resonance width. Thus, it can also be expressed in terms of the phase $\theta_w + \phi_t$ (corresponding to the half width half maximum (HWHM)) for which Eq. (A.9) reaches the half maximum:

$$\begin{aligned} \frac{\delta\lambda_{\text{HWHM}}}{FSR} &= \frac{\theta_w + \phi_t}{2\pi} \\ \Leftrightarrow \quad \theta_w + \phi_t &= \frac{2\pi \cdot \delta\lambda_{\text{HWHM}}}{FSR} \\ &= \frac{\pi \cdot \delta\lambda_{\text{FWHM}}}{FSR} \\ &= \frac{\pi}{\mathcal{F}}. \end{aligned} \tag{A.15}$$

From the condition that P_{t1} exhibits the half maximum [533]

$$P_{\text{t1}}(\theta_w + \phi_t) = \frac{1}{2}(P_{\text{t1,min}} + P_{\text{t1,max}}), \tag{A.16}$$

it follows that:

$$\begin{aligned} \frac{A^2 + |t|^2 - 2A|t|\cos(\pi/\mathcal{F})}{1 + A^2|t|^2 - 2A|t|\cos(\pi/\mathcal{F})} &= \frac{1}{2}\left(\frac{(A-|t|)^2}{(1-A|t|)^2} + \frac{(A+|t|)^2}{(1+A|t|)^2}\right) \\ \Leftrightarrow \qquad \cos\left(\frac{\pi}{\mathcal{F}}\right) &= \frac{2A|t|}{1 + A^2|t|^2}. \end{aligned} \tag{A.17}$$

From this equation a relation for $A \cdot |t|$ can be derived:

$$A^2|t|^2 - \frac{2}{\cos(\pi/\mathcal{F})}A|t| + 1 = 0. \tag{A.18}$$

Introducing the variable $C = A|t|$, this can be solved as:

$$C_{1,2} = \frac{1}{\cos(\pi/\mathcal{F})} \pm \sqrt{\frac{1}{\left(\cos(\pi/\mathcal{F})\right)^2} - 1}. \tag{A.19}$$

As a solution with $A|t| > 1$ would correspond to a gain medium, this solution is dropped and only the other one is kept, which is now labeled C without an index. Using Eq. (A.14) this leads to:

$$\begin{aligned} ER &= \left(\frac{(A + {}^{C}/_{A})(1-C)}{(A - {}^{C}/_{A})(1+C)}\right)^2 \\ \Leftrightarrow \quad A^2\left(\pm\sqrt{ER}(1+C) - (1-C)\right) &= C\left(\pm\sqrt{ER}(1+C) + (1-C)\right) \\ \Leftrightarrow \quad A_{1,2} &= \left(C\frac{\pm\sqrt{ER}(1+C) - (1-C)}{\pm\sqrt{ER}(1+C) + (1-C)}\right)^{1/2}. \end{aligned} \tag{A.20}$$

In the last step the negative solutions for A were already neglected as they do not correspond to a physical property. As A and $|t|$ appear in the original equations symmetrically the same result would be obtained for $|t|$. Therefore, the two solutions correspond already to A and $|t|$, but it can not be distinguished which one is which. However, by a variation of the gap between ring and bus waveguide, the coupling strength between them can be varied. For $A = |t|$ there is no transmitted power on resonance and the ER exhibits its maximum. Thus, the roundtrip losses matches the coupling strength: $1 - A^2 = |\kappa|^2$. If the ring is closer to the bus waveguide the coupling is stronger and $1 - A^2 < |\kappa|^2$. From this follows $1 - A^2 < 1 - |t|^2$ and $A^2 > |t|^2$. On the other hand, for a larger gap between the ring and the bus waveguide, the coupling strength is smaller than the losses: $1 - A^2 > |\kappa|^2 \Leftrightarrow A^2 < |t|^2$. Therefore, by fabricating rings with varying gap (and thus coupling strength) and monitoring the ER, it can be decided in which coupling regime the ring is located. In this way, the two parameters obtained in Eq. (A.20) can be assigned to A and $|t|$.

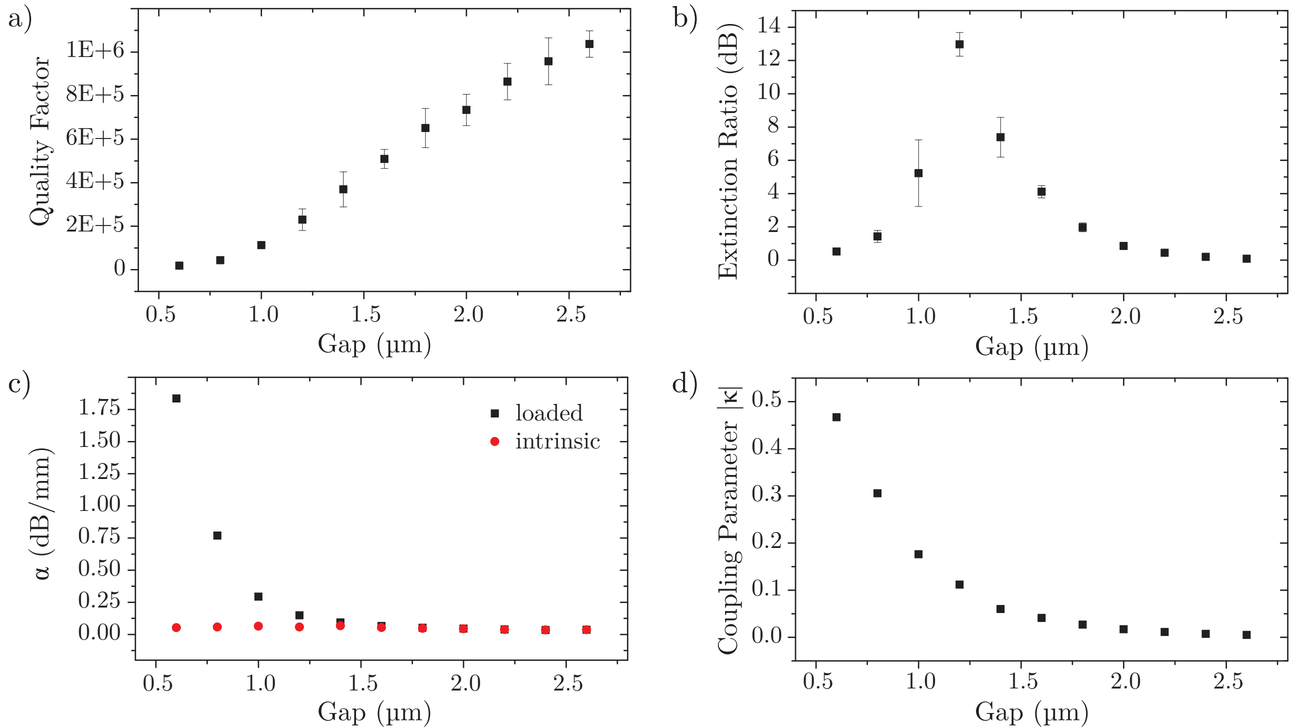

Figure A.1.: a) Quality factor and ER (b) of ring resonators with increasing gap size to the bus waveguide. From the quality factor (or from the ER and finesse) the loaded (intrinsic) attenuation coefficient is extracted (c). As expected both values converge for large gap sizes in the very weakly coupled regime. The strength of the coupling is represented by the coupling parameter $|\kappa|$ (d), which decreases exponentially with increasing gap size.

As an example, this procedure is applied to the data of Si_3N_4 ring resonators in the NIR regime at $\lambda = 1615$ nm. A 1.15 µm wide and 170 nm high Si_3N_4 rib waveguide is used, made from a half etched 340 nm Si_3N_4 layer on SiO_2 on Si. The ring radius is 95 µm and the gap between the ring and the bus waveguide is varied from 0.6 µm to 2.6 µm. The transmission spectrum of each device is recorded

and a Lorentz curve (or a double Lorentz) is fitted to the resonances. Typically ten resonances are evaluated and averaged. The standard deviation from this average is given by the error bars. From the fit, the quality factor Q and the extinction ratio is extracted as well as the finesse. In Fig. A.1 a) the quality factor for increasing gap size is presented. For small gap sizes, the quality factor is loaded due to the coupling to the bus waveguide and for large gap sizes it reaches its intrinsic value when the coupling is very weak. For critical coupling at $A = |t|$, the extinction ration (presented in panel (b)) reaches its maximum. Here, this is the case for a gap size of approximately 1.2 µm. From the loaded quality factor, the propagation losses can be extracted, as described in the main text. Additionally, the intrinsic attenuation coefficient can be extracted from A as described above. Both are shown in panel (c) and as expected the value from the loaded quality factor reaches the intrinsic value for very large gap sizes. Simultaneously the transmission parameter $|t|$ is obtained and thus the coupling parameter $|\kappa|$ can be calculated. As shown in panel (d), the coupling parameter decreases exponentially with increasing gap size. This is caused by the exponentially decaying evanescent field outside of the waveguide. Via this field the ring resonator is coupled to the bus waveguide.

A.3. Sample Preparation and Fabrication Parameters

General basic systems for the sample preparation:

- Ultrasonic cleaner USC 500 THD[1]
- Diener low-pressure plasma system Pico[2]
- SingleWafer spin processor Polos MCD 200[3]

A.3.1. Basic Si_3N_4 Devices

Two material stacks are used for either devices around $\lambda = 1.55\,\mu m$ in the C-band or for devices in the visible wavelength regime around $\lambda = 780\,nm$:

- 340 nm Si_3N_4 on 3.3 µm SiO_2 on 525 µm Si
- 200 nm Si_3N_4 on 2.0 µm SiO_2 on 525 µm Si

The wafers are cut into either 15x15 mm^2 or 20x20 mm^2 samples by the wafer saw. For sawing parameters see App. A.6. If both sides are polished, the backside is marked with a scratched 'R', in order to distinguish between the sides. The fabrication of photonic circuits is realized in the following way:

1. Cleaning of the chip:
   a) Sonicate chip in acetone for 5 min, rinse it with isopropyl alcohol (IPA), blow dry with nitrogen gun.
   b) Oxygen asher: 60 W, 10 sccm[4] O_2, approx. 0.35 mbar, 5 min
   c) Bake on hotplate at 200 °C for 10 min, then cool down the sample on a metal plate for a few seconds
2. TI Prime monolayer coating:
   a) Spin coat approx. 50 µl, 3000 rpm[5], 23 s, 1000 rpms[6]
      After spin coating no residual drops or film of TI Prime should be visible!
   b) Bake on hotplate at 120 °C for 2 min, then cool the sample down on a metal plate for a few seconds
   c) Proceed immediately with spin coating of the main resist following the resist's usual spin coating steps
3. Coating of ma-N 2403: Aim thickness of 340 nm
   a) Spin coat approx. 80 µl
      Step 1: 400 rpm, 3 s, 1000 rpms

[1] VWR International, Radnor, PA 19087-8660, USA
[2] Diener electronic GmbH + Co. KG, Ebhausen, BW 72224, Germany
[3] SPS-Europe B.V., Putten, 3882, Netherlands
[4] The unit sccm stands for standard cubic centimeter per minute (cm^3/min at standard conditions).
[5] The unit rpm stands for rounds per minute.
[6] The unit rpms stands for the acceleration rpm per second.

Step 2: approx. 3400 rpm, 60 s, 1000 rpms (adjust spin speed in order to achieve a resist thickness of 340 nm)

b) Bake on hotplate at 90 °C for 2 min

c) Measure layer thickness with reflectometer, use only halogen lamp to avoid resist exposure

4. EBL exposure at JEOL: 180 µC/cm^2 area dose + PEC
5. Development: 1 min in Microposit™MF-319[7], use distilled water as stopper
6. Reflow procedure on hotplate immediately after development:
   100 °C, 2 min if there are fine features like Y-splitters included in the circuitry
   110 °C, 2 min for all other samples
7. Etching at RIE, detailed recipes in App. A.5
   a) SF_6-based cleaning process before Si_3N_4 etching
   b) Si_3N_4 etching, adjust etching time for desired etching depth. For e. g. a half etched 340 nm rib waveguide an etching time of approx. 3 min is required.
8. Remove residual resist in an O_2 plasma at RIE

A.3.2. Si_3N_4 Devices on Silica Window Substrate for a Vacuum Chamber

The samples consists of a 180 nm Si_3N_4 layer on a 4 mm thick, 1.5 inch diameter silica substrate.

Step I: Photonic circuits

1. Take ZEP 520A and Espacer from refrigerator so that they can warm up for 15 min
2. Cleaning of the chip:
   a) Sonicate chip in acetone for 5 min, rinse it with IPA, blow dry with nitrogen gun.
   b) Oxygen asher: 60 W, 10 sccm O_2, approx. 0.35 mbar, 5 min
   c) Bake on hotplate at 200 °C for 10 min, then cool down the sample on a metal plate for a few seconds
3. Coating of ZEP 520A: Aim thickness of 550 nm
   a) Spin coat approx. 200 µl
      Step 1: 400 rpm, 3 s, 1000 rpms
      Step 2: approx. 1900 rpm, 60 s, 1000 rpms (adjust spin speed in order to achieve a resist thickness of 550 nm)
   b) Bake on hotplate at 170 °C for 2 min
   c) Measure layer thickness with reflectometer, use only halogen lamp to avoid resist exposure
4. Coating of Espacer:
   a) Spin coat approx. 200 µl; 4000 rpm, 40 s, 400 rpms
5. EBL exposure at e_LiNE: 90 µC/cm^2 area dose
6. Rinse for a few seconds with distilled H_2O to remove the Espacer; blow dry with nitrogen gun
7. Development: 50 s in xylene, use IPA as stopper

[7] Microposit™ MF-319 is a developer based on tetramethylammonium hydroxide (TMAH)
Dow Chemical Company, Midland, MI 48667, USA

8. Etching at RIE, detailed recipes in App. A.5
   a) SF_6-based cleaning process before Si_3N_4 etching
   b) Si_3N_4 etching, adjust etching time for desired etching depth. Approximately 165 s are required to fully etch the 180 nm Si_3N_4 layer.
9. Remove residual resist in an O_2 plasma at RIE

Step II: HSQ mask as spacer

1. Take HSQ 15 % and Espacer from refrigerator so that they can warm up for 15 min
2. Cleaning of the chip:
   a) Put chip in acetone for 5 min (no sonication!), rinse it with IPA, blow dry with nitrogen gun.
   b) Bake on hotplate at 105 °C for 1 min, then cool down the sample on a metal plate for a few seconds
3. Coating of HSQ 15 %: Aim thickness of 700 nm
   a) Spin coat approx. 200 µl; approx. 1800 rpm, 60 s, 1000 rpms (adjust spin speed in order to achieve a resist thickness of 700 nm)
   b) Measure layer thickness with reflectometer, use only halogen lamp to avoid resist exposure
4. Coating of Espacer:
   a) Spin coat approx. 200 µl; 4000 rpm, 40 s, 400 rpms
5. EBL exposure at e_LiNE: 300 µC/cm^2 area dose
6. Rinse for a few seconds with distilled H_2O to remove the Espacer; blow dry with nitrogen gun
7. Development: 4 min in MF-319, use distilled water as stopper

Step III: Metal mirrors

1. Take Espacer from refrigerator so that it can warm up for 15 min
2. Cleaning of the chip:
   a) Put chip in acetone for 5 min (no sonication!), rinse it with IPA, blow dry with nitrogen gun.
   b) Bake on hotplate at 180 °C for 2 min, then cool down the sample on a metal plate for a few seconds
3. Coating of PMMA 8.0 : Aim thickness of 800 nm
   a) Spin coat approx. 200 µl; approx. 4000 rpm, 90 s, 1000 rpms (adjust spin speed in order to achieve a resist thickness of 800 nm)
   b) Bake on hotplate at 180 °C for 2 min, then cool down the sample on a metal plate for a few seconds
   c) Measure layer thickness with reflectometer, use only halogen lamp to avoid resist exposure
4. Coating of Espacer:
   a) Spin coat approx. 200 µl; 4000 rpm, 40 s, 400 rpms
5. EBL exposure at e_LiNE: 625 µC/cm^2 area dose
6. Rinse for a few seconds with distilled H_2O to remove the Espacer; blow dry with nitrogen gun

7. Development: 4 min in methylisobutylketone (MIBK) 1:3 IPA, use IPA as stopper
8. MBE of metal layer: 5 nm Ti / 100 nm Al
9. Lift-off of PMMA layer:
   a) Put sample in acetone for several hours. Use syringe to splash the sample for facilitating the process.
   b) Rinse sample with IPA, blow dry with nitrogen gun.

A.3.3. Si_3N_4 Devices on Borosilicate Glass Substrate for a Vapor Cell

The wafers (180 nm Si_3N_4 on BSG substrate) are cut into or 20x20 mm^2 samples by the wafer saw. For sawing parameters see App. A.6. Mark the backside with a scratched 'R', in order to distinguish between the sides.

Step I: Photonic circuits

1. Take Espacer from refrigerator so that it can warm up for 15 min
2. Cleaning of the chip:
   a) Sonicate chip in acetone for 5 min, rinse it with IPA, blow dry with nitrogen gun.
   b) Oxygen asher: 60 W, 10 sccm O_2, approx. 0.35 mbar, 5 min
   c) Bake on hotplate at 200 °C for 10 min, then cool down the sample on a metal plate for a few seconds
3. TI Prime monolayer coating:
   a) Spin coat approx. 50 µl, 3000 rpm, 23 s, 1000 rpms
   After spin coating no residual drops or film of TI Prime should be visible!
   b) Bake on hotplate at 120 °C for 2 min, then cool the sample down on a metal plate for a few seconds
   c) Proceed immediately with spin coating of the main resist following the resist's usual spin coating steps
4. Coating of ma-N 2403: Aim thickness of 340 nm
   a) Spin coat approx. 80 µl
   Step 1: 400 rpm, 3 s, 1000 rpms
   Step 2: approx. 3400 rpm, 60 s, 1000 rpms (adjust spin speed in order to achieve a resist thickness of 340 nm)
   b) Bake on hotplate at 90 °C for 2 min
   c) Measure layer thickness with reflectometer, use only halogen lamp to avoid resist exposure
5. Coating of Espacer:
   a) Spin coat approx. 80 µl; 4000 rpm, 40 s, 400 rpms
6. EBL exposure at JEOL: 180 µC/cm^2 area dose + PEC
7. Rinse for a few seconds with distilled H_2O to remove the Espacer; blow dry with nitrogen gun
8. Development: 1 min in MF-319, use distilled water as stopper

9. Reflow procedure on hotplate immediately after development:
   100 °C, 2 min if there are fine features like Y-splitters or slot waveguides included in the circuitry
   110 °C, 2 min for all other samples
10. Etching at RIE, detailed recipes in App. A.5
    a) SF_6-based cleaning process before Si_3N_4 etching
    b) Si_3N_4 etching, adjust etching time for desired etching depth. Approximately 165 s are required to fully etch the 180 nm Si_3N_4 layer.
11. Remove residual resist in an O_2 plasma at RIE
12. Clean in piranha solution:
    a) Add one part hydrogen peroxide to three parts sulfuric acid and stir
    b) Hold sample in solution for 20 min
    c) Put sample in distilled H_2O; blow dry with nitrogen gun

Step II: HSQ mask as spacer

1. Take HSQ 15 % and Espacer from refrigerator so that they can warm up for 15 min
2. Cleaning of the chip:
   a) Put chip in acetone for 5 min (no sonication!), rinse it with IPA, blow dry with nitrogen gun.
   b) Bake on hotplate at 105 °C for 1 min, then cool down the sample on a metal plate for a few seconds
3. Coating of HSQ 15 %: Aim thickness of 700 nm
   a) Spin coat approx. 200 µl; approx. 1800 rpm, 60 s, 1000 rpms (adjust spin speed in order to achieve a resist thickness of 700 nm)
   b) Measure layer thickness with reflectometer, use only halogen lamp to avoid resist exposure
4. Coating of Espacer:
   a) Spin coat approx. 80 µl; 4000 rpm, 40 s, 400 rpms
5. EBL exposure at JEOL: 450 $\mu C/cm^2$ area dose + PEC
6. Rinse for a few seconds with distilled H_2O to remove the Espacer; blow dry with nitrogen gun
7. Development: 4 min in MF-319, use distilled water as stopper

Step III: Metal mirrors

1. Take Espacer from refrigerator so that it can warm up for 15 min
2. Cleaning of the chip:
   a) Put chip in acetone for 5 min (no sonication!), rinse it with IPA, blow dry with nitrogen gun.
   b) Bake on hotplate at 180 °C for 2 min, then cool down the sample on a metal plate for a few seconds
3. Coating of PMMA 8.0 : Aim thickness of 800 nm
   a) Spin coat approx. 200 µl; approx. 4000 rpm, 90 s, 1000 rpms (adjust spin speed in order to achieve a resist thickness of 800 nm)

   b) Bake on hotplate at 180 °C for 2 min, then cool down the sample on a metal plate for a few seconds
   c) Measure layer thickness with reflectometer, use only halogen lamp to avoid resist exposure
4. Coating of Espacer:
   a) Spin coat approx. 80 µl; 4000 rpm, 40 s, 400 rpms
5. EBL exposure at JEOL: 850 $\mu C/cm^2$ area dose + PEC
6. Rinse for a few seconds with distilled H_2O to remove the Espacer; blow dry with nitrogen gun
7. Development: 4 min in MIBK 1:3 IPA, use IPA as stopper
8. MBE of metal layer: 5 nm Ti / 100 nm Al
9. Lift-off of PMMA layer:
   a) Put sample in acetone for several hours. Use syringe to splash the sample for facilitating the process.
   b) Rinse sample with IPA, blow dry with nitrogen gun.

Step IV: Sapphire protection layer

1. Protect 5 mm frame of the sample with tape. Use a large piece of tape, cut a 10x10 mm^2 window in this piece (photonic structures are within such a 10x10 mm^2 area on the chip). Carefully align and attach the tape to the sample.
2. 5-7 nm Al_2O_3 layer deposition at Picosun SUNALE R-200 Advanced[8] ALD system at the INT.
3. Remove tape and carefully clean frame of the sample with acetone and cotton swab.

A.3.4. Basic Silicon Devices

The wafers (220 nm Si on 3 µm SiO_2 on Si substrate) are cut into either 15x15 mm^2 or 20x20 mm^2 samples by the wafer saw. For sawing parameters see App. A.6. The fabrication of photonic circuits is realized in the following way:

1. Cleaning of the chip:
   a) Sonicate chip in acetone for 5 min, rinse it with IPA, blow dry with nitrogen gun.
   b) Oxygen asher: 60 W, 10 sccm O_2, approx. 0.35 mbar, 5 min
   c) Bake on hotplate at 200 °C for 10 min, then cool down the sample on a metal plate for a few seconds
2. Coating of ZEP 520A: Aim thickness of 450 nm
   a) Spin coat approx. 80 µl
      Step 1: 400 rpm, 3 s, 1000 rpms
      Step 2: approx. 3000 rpm, 60 s, 1000 rpms (adjust spin speed in order to achieve a resist thickness of 450 nm)
   b) Bake on hotplate at 170 °C for 2 min
   c) Measure layer thickness with reflectometer, use only halogen lamp to avoid resist exposure

[8] Picosun Oy, Espoo, FI-02150, Finland

3. EBL exposure at JEOL: 160 µC/cm^2 area dose + PEC
4. Development: 1 min in xylene, use IPA as stopper
5. Reflow procedure on hotplate immediately after development:
   140 °C, 2:30 min
6. Etching at ICP, detailed recipes in App. A.5
   a) O_2 cleaning process before Si etching
   b) Si etching, adjust etching time for desired etching depth. For e. g. a half etched 220 nm rib waveguide an etching time of approx. 25 s is required.
7. Remove residual resist in an O_2 plasma at RIE

A.3.5. Suspended Silicon Devices for LWIR Applications

The wafers (2 µm Si on 5 µm SiO_2 on Si substrate) are cut into either 15x15 mm^2 or 20x20 mm^2 samples by the wafer saw. For sawing parameters see App. A.6. As the device layer exhibits a thickness of 2.0±0.5 µm, this thickness is decreased in a first etching step. The fabrication of photonic circuits is realized in the following way:

Step I: Adjust silicon layer thickness

1. Cleaning of the chip:
   a) Sonicate chip in acetone for 5 min, rinse it with IPA, blow dry with nitrogen gun.
   b) Oxygen asher: 60 W, 10 sccm O_2, approx. 0.35 mbar, 5 min
2. Etching at ICP, detailed recipes in App. A.5
   a) O_2 cleaning process before Si etching
   b) Si etching, adjust etching time so that a mean thickness of 1 µm is obtained.

Step II: Photonic circuits

1. Take HSQ 15 % from refrigerator so that it can warm up for 15 min
2. Cleaning of the chip:
   a) Sonicate chip in acetone for 5 min, rinse it with IPA, blow dry with nitrogen gun.
   b) Bake on hotplate at 105 °C for 1 min, then cool down the sample on a metal plate for a few seconds
3. Coating of HSQ 15 %: Aim thickness of 450 nm
   a) Spin coat approx. 80 µl
      Approx. 4000 rpm, 60 s, 1800 rpms (adjust spin speed in order to achieve a resist thickness of 450 nm)
   b) Measure layer thickness with reflectometer, use only halogen lamp to avoid resist exposure
4. EBL exposure at JEOL: 310 µC/cm^2 area dose + PEC
5. Development: 12 min in MF319, use water as stopper
6. Etching at ICP, detailed recipes in App. A.5
   a) O_2 cleaning process before Si etching

b) Si etching, adjust etching time for desired etching depth so that ∼400 nm of the Si layer are left on the sample.

Step III: Open windows in remaining silicon layer

1. Take HSQ 15 % from refrigerator so that it can warm up for 15 min
2. Cleaning of the chip:
   a) Put chip in acetone for 5 min (no sonication!), rinse it with IPA, blow dry with nitrogen gun.
   b) Bake on hotplate at 105 °C for 1 min, then cool down the sample on a metal plate for a few seconds
3. Coating of HSQ 15 %: Aim thickness of 450 nm
   a) Spin coat approx. 80 µl
      Approx. 4000 rpm, 60 s, 1800 rpms (adjust spin speed in order to achieve a resist thickness of 450 nm)
   b) Measure layer thickness with reflectometer, use only halogen lamp to avoid resist exposure
4. EBL exposure at JEOL:
   Inner part: 240 $\mu C/cm^2$ area dose + PEC
   Outer sleeve: 390 $\mu C/cm^2$ area dose + PEC
5. Development: 12 min in MF319, use water as stopper
6. Etching at ICP, detailed recipes in App. A.5
   a) O_2 cleaning process before Si etching
   b) Si etching, adjust etching time for desired etching depth so that the remaining ∼400 nm of the Si layer in the windows are etched.

Step IV: Chip cutting

1. Cleaning of the chip:
   a) Put chip in acetone for 5 min (no sonication!), rinse it with IPA, blow dry with nitrogen gun.
   b) Bake on hotplate at 105 °C for 2 min, then cool down the sample on a metal plate for a few seconds
2. Coating of S1813 G2 protection layer: 2000 rpm, 90 s, 1000 rpms
3. Bake on hotplate at 105 °C for 2 min, then cool down the sample on a metal plate for a few seconds
4. Cut chip as close as possible to the end facet of the waveguides according to parameters specified in App. A.6.
5. Remove protection coating in acetone (no sonication!), rinse it with IPA, blow dry with nitrogen gun.

Step V: HF underetching (BOE 6:1, rate ∼2 nm/s)

1. Place sample in BOE[9] for 2 h 30 min

[9] As concentrated HF etches SiO_2 too quickly for precise process control, a buffered oxide etch (BOE) is used. A

2. Transfer sample directly to a first H_2O bath, then to a second H_2O bath.
3. Transfer sample to beaker with methanol.
4. Dry sample by placing it directly from methanol bath onto a hotplate at 70 °C and very quickly but also very gently blow dry with nitrogen gun.

A.3.6. Basic Diamond Devices

The wafers (600 nm diamond on 2 µm SiO_2 on Si substrate) are cut into either 15x15 mm^2 or 20x20 mm^2 samples by the wafer saw. For sawing parameters see App. A.6. The fabrication of photonic circuits is realized in the following way:

Step I: SiO_2 deposition

1. Cleaning of the chip:
   a) Sonicate chip in acetone for 5 min, rinse it with IPA, blow dry with nitrogen gun.
   b) Bake on hotplate at 105 °C for 2 min, then cool down the sample on a metal plate for a few seconds
2. Deposition of approximately 5 nm SiO_2 via electron beam physical vapor deposition (PVD)

Step II: Photonic circuits

1. Take HSQ 15 % from refrigerator so that it can warm up for 15 min
2. Cleaning of the chip:
   a) Sonicate chip in acetone for 5 min, rinse it with IPA, blow dry with nitrogen gun.
   b) Bake on hotplate at 105 °C for 2 min, then cool down the sample on a metal plate for a few seconds
3. Coating of HSQ 15 %: Aim thickness of 450 nm
   a) Spin coat approx. 80 µl
      4000 rpm, 60 s, 1800 rpms (adjust spin speed in order to achieve a resist thickness of 450 nm)
   b) Measure layer thickness with reflectometer, use only halogen lamp to avoid resist exposure
4. EBL exposure at JEOL: 310 $\mu C/cm^2$ area dose + PEC
5. Development: 12 min in MF319, use distilled water as stopper
6. Etching at RIE, detailed recipes in App. A.5
   a) Conditioning with diamond etching recipe, 2x5 min
   b) SiO_2 adhesion layer etching, 90 s
   c) Diamond etching in loops with each etching step around 5 min. In between the etching steps use a 2 min cool down period in which the chamber is flushed by argon without igniting a plasma. Adjust total etching time so that 200 nm diamond are remaining on the sample. Typically 15-20 min of total etching time are needed to etch 400 nm of diamond.

common 6:1 BOE solution comprises a 6:1 volume ratio of 40 % ammonuim fluoride (NH_4F) in water to 49 % HF in water. Here, a 6:1 BOE is used from J.T.Baker®, a brand of Avnantor Inc, Center Valley, PA 18034, United States

A.3.7. Diamond on AlN Devices for LWIR Applications

The wafers (1.5 µm diamond on 5 µm AlN on Si substrate) are cut into either 15x15 mm^2 or 20x20 mm^2 samples by the wafer saw. For sawing parameters see App. A.6. The fabrication of photonic circuits is realized in the following way:

Step I: Cr deposition

1. Cleaning of the chip:
   a) Sonicate chip in acetone for 5 min, rinse it with IPA, blow dry with nitrogen gun.
   b) Bake on hotplate at 105 °C for 2 min, then cool down the sample on a metal plate for a few seconds
2. Deposition of approximately 10 nm Cr via electron beam PVD

Step II: Photonic circuits

Begin with waveguide fabrication directly after the Cr deposition in order to avoid oxidation of the Cr layer.

1. Take HSQ 15 % from refrigerator so that it can warm up for 15 min
2. Cleaning of the chip:
   a) Sonicate chip in acetone for 5 min, rinse it with IPA, blow dry with nitrogen gun.
   b) Bake on hotplate at 105 °C for 2 min, then cool down the sample on a metal plate for a few seconds
3. Coating of HSQ 15 %: Aim thickness of 450 nm
   a) Spin coat approx. 80 µl
      4000 rpm, 60 s, 1800 rpms (adjust spin speed in order to achieve a resist thickness of 450 nm)
   b) Measure layer thickness with reflectometer, use only halogen lamp to avoid resist exposure
4. EBL exposure at JEOL: 310 $\mu C/cm^2$ area dose + PEC
5. Development: 12 min in MF319, use distilled water as stopper
6. Etching of Cr layer at ICP, detailed recipes in App. A.5
   After conditioning, etch sample for ∼45 s to fully etch ∼10 nm Cr layer.
7. Etching of diamond at RIE, detailed recipes in App. A.5
   a) Conditioning with diamond etching recipe, 2x5 min
   b) Diamond etching in loops with each etching step around 5 min. In between the etching steps use a 2 min cool down period in which the chamber is flushed by argon without igniting a plasma. Adjust total etching time so that 500 nm diamond are remaining on the sample. Typically 45 min of total etching time are needed to etch 1 µm of diamond.

Step III: Chip cutting

1. Cleaning of the chip:
   a) Put chip in acetone for 5 min (no sonication!), rinse it with IPA, blow dry with nitrogen gun.
   b) Bake on hotplate at 105 °C for 2 min, then cool down the sample on a metal plate for a few

seconds
2. Coating of S1813 G2 protection layer: 2000 rpm, 90 s, 1000 rpms
3. Bake on hotplate at 105 °C for 2 min, then cool down the sample on a metal plate for a few seconds
4. Cut chip as close as possible to the end facet of the waveguides according to parameters specified in App. A.6.
5. Remove protection coating in acetone (no sonication!), rinse it with IPA, blow dry with nitrogen gun.

Step IV: HSQ and Cr removal

1. Place sample in 6:1 BOE for 10 min to remove HSQ
2. Transfer sample directly to a first H_2O bath, then to a second H_2O bath.
3. Transfer sample to beaker with Cr wet etch. Leave in there for 90 s to remove Cr layer. Transfer sample to H_2O bath.
4. Rinse sample with IPA, blow dry with nitrogen gun.

A.3.8. Suspended Diamond Devices for LWIR Applications

The wafers (1.5 µm diamond on 5 µm SiO_2 on Si substrate) are cut into either 15x15 mm^2 or 20x20 mm^2 samples by the wafer saw. For sawing parameters see App. A.6. The fabrication of photonic circuits is realized in the following way:

Step I: Cr deposition

1. Cleaning of the chip:
   a) Sonicate chip in acetone for 5 min, rinse it with IPA, blow dry with nitrogen gun.
   b) Bake on hotplate at 105 °C for 2 min, then cool down the sample on a metal plate for a few seconds
2. Deposition of approximately 10 nm Cr via electron beam PVD

Step II: Photonic circuits

Begin with waveguide fabrication directly after the Cr deposition in order to avoid oxidation of the Cr layer.

1. Take HSQ 15 % from refrigerator so that it can warm up for 15 min
2. Cleaning of the chip:
   a) Sonicate chip in acetone for 5 min, rinse it with IPA, blow dry with nitrogen gun.
   b) Bake on hotplate at 105 °C for 2 min, then cool down the sample on a metal plate for a few seconds
3. Coating of HSQ 15 %: Aim thickness of 450 nm
   a) Spin coat approx. 80 µl
   4000 rpm, 60 s, 1800 rpms (adjust spin speed in order to achieve a resist thickness of 450 nm)
   b) Measure layer thickness with reflectometer, use only halogen lamp to avoid resist exposure

4. EBL exposure at JEOL: 310 µC/cm^2 area dose + PEC
5. Development: 12 min in MF319, use distilled water as stopper
6. Etching of Cr layer at ICP, detailed recipes in App. A.5
   After conditioning, etch sample for ∼45 s to fully etch ∼10 nm Cr layer.
7. Etching of diamond at RIE, detailed recipes in App. A.5
   a) Conditioning with diamond etching recipe, 2x5 min
   b) Diamond etching in loops with each etching step around 5 min. In between the etching steps use a 2 min cool down period in which the chamber is flushed by argon without igniting a plasma. Adjust total etching time so that 500 nm diamond are remaining on the sample. Typically 45 min of total etching time are needed to etch 1 µm of diamond.

Step III: SiO_2 deposition

1. Cleaning of the chip:
   a) Sonicate chip in acetone for 5 min, rinse it with IPA, blow dry with nitrogen gun.
   b) Bake on hotplate at 105 °C for 2 min, then cool down the sample on a metal plate for a few seconds
2. Deposition of approximately 5 nm SiO_2 via electron beam PVD

Step IV: Open windows in remaining diamond layer

1. Take HSQ 15 % from refrigerator so that it can warm up for 15 min
2. Cleaning of the chip:
   a) Put chip in acetone for 5 min (no sonication!), rinse it with IPA, blow dry with nitrogen gun.
   b) Bake on hotplate at 105 °C for 1 min, then cool down the sample on a metal plate for a few seconds
3. Coating of HSQ 15 %: Aim thickness of 450 nm
   a) Spin coat approx. 80 µl
      Approx. 4000 rpm, 60 s, 1800 rpms (adjust spin speed in order to achieve a resist thickness of 450 nm)
   b) Measure layer thickness with reflectometer, use only halogen lamp to avoid resist exposure
4. EBL exposure at JEOL:
   Inner part: 240 µC/cm^2 area dose + PEC
   Outer sleeve: 390 µC/cm^2 area dose + PEC
5. Development: 12 min in MF319, use water as stopper
6. Etching at RIE, detailed recipes in App. A.5
   a) Conditioning with diamond etching recipe, 2x5 min
   b) SiO_2 adhesion layer etching, 90 s
   c) Diamond etching in loops with each etching step around 5 min. In between the etching steps use a 2 min cool down period in which the chamber is flushed by argon without igniting a plasma. Adjust total etching time (∼30 min) so that the remaining 500 nm of diamond in

the windows are etched.

Step V: Chip cutting

1. Cleaning of the chip:
   a) Put chip in acetone for 5 min (no sonication!), rinse it with IPA, blow dry with nitrogen gun.
   b) Bake on hotplate at 105 °C for 2 min, then cool down the sample on a metal plate for a few seconds
2. Coating of S1813 G2 protection layer: 2000 rpm, 90 s, 1000 rpms
3. Bake on hotplate at 105 °C for 2 min, then cool down the sample on a metal plate for a few seconds
4. Cut chip as close as possible to the end facet of the waveguides according to parameters specified in App. A.6.
5. Remove protection coating in acetone (no sonication!), rinse it with IPA, blow dry with nitrogen gun.

Step VI: HF underetching (BOE 6:1, rate ∼2 nm/s)

1. Place sample in 6:1 BOE for 1 h 55 min
2. Transfer sample directly to a first H_2O bath, then to a second H_2O bath.
3. Transfer sample to beaker with Cr wet etch. Leave in there for 90 s to remove Cr layer. Transfer sample to H_2O bath.
4. Transfer sample directly to beaker with methanol.
5. Dry sample by placing it directly from methanol bath onto a hotplate at 70 °C and very quickly but also very gently blow dry with nitrogen gun.

A.4. PEC Parameters

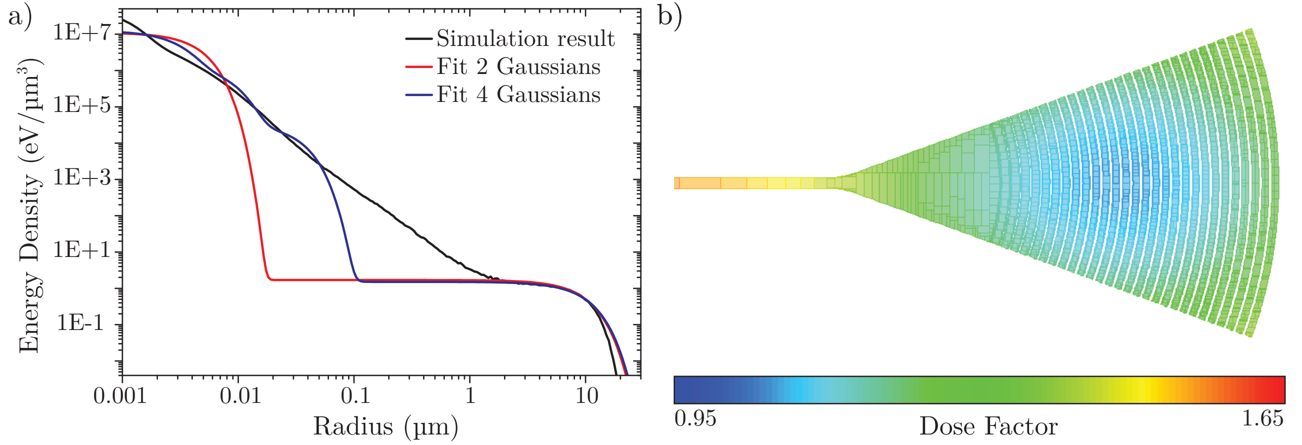

Figure A.2.: a) Point spread function of the deposited energy in dependence of the radius from the beam center for 340 nm maN 2403 on 200 nm Si_3N_4. Due to forward and backward scattering in the different layers the width of the effectively deposited dose is increased. b) Calculated dose factor distribution for a grating coupler, which is required in order to achieve a uniform effective dose.

In order to correct the deposited dose so that a uniform effective dose distribution is achieved, regardless of the structure size and packaging, it is essential to know the electron scattering behavior. Thus, for each material stack a Monte Carlo simulation is performed in which an electron beam with a certain acceleration voltage (here e. g. 50 kV) is considered, which is directed at the substrate. Thereby, the deposited energy at a certain height in the EBL resist on top of the chip material stack is calculated. Due to forward an backward scattering in the different layers, the beam width is broadened. The deposited energy density at a certain distance r from the beam center is typically described by a point spread function (PSF). An example for a material stack of 340 nm maN-2403 EBL resist on top of a 200 nm Si_3N_4 / 2 µm SiO_2 / 525 µm Si substrate is shown by the black curve in Fig. A.2 a).

In order to recalculate the required area dose in the EBL exposure the PSF is described by a mathematical fit using between two and four Gaussian functions. Each Gaussian function is described by its half width parameter σ and is of the form:

$$g_\sigma(x) = \frac{1}{\pi\sigma^2} \cdot e^{-\left(\frac{x}{\sigma}\right)^2}. \tag{A.21}$$

The Gaussian functions are then combined in order to fit the PSF in the following way:

$$PSF(r) = \frac{1}{1+\eta+\nu_1+\nu_2}\Big(g_\alpha(r) + \eta \cdot g_\beta(r) + \nu_1 \cdot g_{\gamma_1}(r) + \nu_2 \cdot g_{\gamma_2}(r)\Big) \tag{A.22}$$

Typically, the forward scattered electrons in the short rang are represented by α, while β describes the backward scattered electrons in the rather long range and η gives the ration between the energy of the

forward and backward scattered electrons. Such a double-Gaussian model gives a reasonable result for the deposited energy, however there is often a deviation of the fit from the simulated deposited energy distribution in the mid range regime. Thus, two further Gaussian functions are added with the width parameters γ_1 and γ_2 and their energy scaling parameter ν_1 and ν_2. Additionally, the normalized function is multiplied by a *scale factor* in order to fit to the simulated distribution. The comparison between the double-Gaussian and a combination of four Gaussian curves is shown by the red and blue curves in Fig. A.2 a). The parameters for the PSF for the different material stacks are given in Tab. A.1. In a later version of the BEAMER[10] software, which is used to create the flow for the EBL exposure, it was also possible to use directly the numerical data of the simulated deposited energy distribution without having to fit a PSF to the data. Based on this data, the dose distribution of a pattern is calculated in order to certain uniform effective dose for all parts of the pattern. An example for such a dose distribution is shown in Fig. A.2 b) for a grating coupler. The dose factors vary from 0.95 to 1.65 in the area of the grating coupler and the beginning of the waveguide.

[10] GenISys GmbH, Taufkirchen, BY 82024, Germany

Material stack	α	β	η	γ_1	ν_1	γ_2	ν_2	Scale factor
340 nm ma-N 2403 / 340 nm Si_3N_4 / 3.3 µm SiO_2 / 525 µm Si	0.0025	9.4037	0.8542	0.0097	0.2549	0.0726	0.1433	1079.42
340 nm ma-N 2403 / 200 nm Si_3N_4 / 2.0 µm SiO_2 / 525 µm Si	0.0029	9.4432	1.4272	0.0079	0.9216	0.0313	0.3588	1100.92
340 nm ma-N 2403 / 200 nm Si_3N_4 / 500 µm SiO_2	0.0028	9.6221	1.2553	0.0082	0.9565	0.0324	0.4888	1029.05
340 nm ma-N 2403 / 180 nm Si_3N_4 / 1.1 mm BSG	0.0029	10.0170	1.1123	0.0080	0.9344	0.0325	0.3759	1015.97
800 nm PMMA / 180 nm Si_3N_4 / 1.1 mm BSG	0.0241	10.2315	1.0997	0.0096	0.6931	0.0852	0.3834	1078.53
750 nm HSQ / 180 nm Si_3N_4 / 1.1 mm BSG	0.0277	10.2234	1.1479	0.0110	0.6240	0.0872	0.4402	1134.55
450 nm HSQ / 650 nm diamond / 2.0 µm SiO_2 / 380 µm Si	0.0138	9.3703	1.3735	0.0047	0.5720	0.0479	0.4542	1163.24
450 nm HSQ / 10 nm Cr / 1.5 µm diamond / 5.0 µm SiO_2 / 625 µm Si	0.0168	9.3349	1.3961	0.0063	0.6591	0.0546	0.4564	1000.31
250 nm PMMA / 10 nm Cr / 400 nm diamond / 5.0 µm SiO_2 / 625 µm Si	0.0024	9.6957	1.0818	0.0358	0.3444	0.0068	0.6034	1037.23
450 nm HSQ / 10 nm Cr / 1.5 µm diamond / 5.0 µm AlN / 625 µm Si	0.0139	7.0608	1.0964	0.0047	0.5726	0.0481	0.4434	1069.02
450 nm HSQ / 1.0 µm Si / 5.0 µm SiO_2 / 500 µm Si	0.0136	9.6761	1.2865	0.0047	0.8322	0.0524	0.4479	1123.54
450 nm HSQ / 220 nm Si / 3.0 µm SiO_2 / 675 µm Si	0.0024	9.7434	1.1393	0.0068	0.5949	0.0477	0.2631	1088.90
400 nm ZEP 520A / 220 nm Si / 3.0 µm SiO_2 / 675 µm Si	0.0087	9.6027	1.3833	0.0034	0.7093	0.0302	0.4580	1199.94

Table A.1.: Parameters for the PEC calculation according to the function in Eq. (A.22)

A.5. Etching Process Details and Recipes

A.5.1. Si_3N_4 Etching Process

As mentioned in Sec. 2.3.2 a CHF_3 based plasma procedure is used to etch Si_3N_4 by fluorine. The direct reactions for the etching steps are [534]

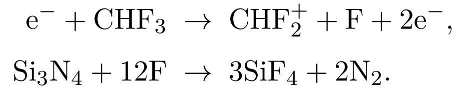

$$\begin{aligned} e^- + CHF_3 &\rightarrow CHF_2^+ + F + 2e^-, \\ Si_3N_4 + 12F &\rightarrow 3SiF_4 + 2N_2. \end{aligned}$$

However, there are two mechanisms which may inhibit this etching process. CHF_3 may decompose to polymer radicals or unsaturated species like CF_2 and C_2F_3 so that a blocking layer is formed through which mass transport of the reactive species is limited [535]. Also unstable silicon compounds might be formed at the surface causing local variations of the etching rate. In order to prevent polymerization on the Si_3N_4 surface, argon can be added to the plasma, which enhances the energetic ion bombardment of the substrate [536]. However, this might increase the surface damage induced by the etching procedure. Alternatively, oxygen can be added to the plasma so that it is energetically favorable to form compounds like CO or CO_2 rather than flourcarbon combinations, which also prevents the formation of a blocking layer [537]. Therefore, a CHF_3/O_2-based plasma is used for Si_3N_4 etching and the gas flow, pressure and power are optimized regarding the propagation losses in waveguides. Additionally, a contamination of the chamber may lead to a very rough surface and the covering of the substrate with a grass-like structure. Thus, before etching of a Si_3N_4 layer, an extensive chamber cleaning process is launched. The detailed Si_3N_4 etching and cleaning process parameters are given below.

A.5.2. Etching Recipes

Oxford Plasmalab 80 RIE at the INT

The RIE system at the INT is used for flourine based plasmas as well as oxygen and argon plasmas. A CHF_3 based plasma is used for the etching of Si_3N_4 layers and an Ar based plasma is used to etch diamond layers. Additionally, an oxygen plasma is used in order to remove remaining ma-N 2403 or ZEP 520A EBL resist on top of the waveguide. All samples which have to be etched are placed on a Si carrier wafer in this system. The cleaning processes are obviously carried out with a completely empty chamber.

Cleaning process directly before Si_3N_4 etching
Three step cleaning process:
Step 1)

- Gas mixture: 50 sccm O_2 / 10 sccm SF_6
- Pressure: 20 mTorr (40 mTorr strike pressure, 100 DC bias minimum, 100 ramp rate)
- Power: 70 W
- Time: 10 min
- Resulting DC bias ≈ 263 V

Step 2)

- Gas mixture: 50 sccm O_2
- Pressure: 20 mTorr (50 mTorr strike pressure, 100 DC bias minimum, 100 ramp rate)
- Power: 100 W
- Time: 5 min
- Resulting DC bias ≈ 360 V

Step 3)

- Gas mixture: 50 sccm O_2
- Pressure: 50 mTorr
- Power: 100 W
- Time: 50 min
- Resulting DC bias ≈ 336 V

Si_3N_4 etching
Before a sample is etched, a 5 min conditioning step is carried out.

- Gas mixture: 50 sccm CHF_3 / 2 sccm O_2
- Pressure: 55 mTorr
- Power: 175 W
- Time: depending on required etching depth
- Resulting DC bias ≈ 430 V

Resulting etching rate:

- Si_3N_4: 0.9-0.95 nm/s
- SiO_2: 0.62 nm/s
- ma-N 2403: 0.4 nm/s

Remove resist

- Gas mixture: 50 sccm O_2
- Pressure: 50 mTorr
- Power: 70 W
- Time: 5 min
- Resulting DC bias ≈ 260 V

Resulting etching rate:

- Si_3N_4: < 0.2 nm/minute
- SiO_2: too small to measure

5-7 nm SiO_2 adhesion layer etching

- Gas mixture: 25 sccm Ar
- Pressure: 10 mTorr (50 mTorr strike pressure, 100 DC bias minimum, 100 ramp rate)
- Power: 200 W
- Time: 1:30 min
- Resulting DC bias ≈ 520 V

Diamond etching

Before a sample is etched, a 5 min conditioning step is carried out.

- Gas mixture: 33 sccm O_2 / 17 sccm Ar
- Pressure: 13 mTorr (45 mTorr strike pressure, 100 DC bias minimum, 100 ramp rate)
- Power: 200 W
- Time: depending on required etching depth
- Resulting DC bias ≈ 560 V

Resulting etching rate:

- Diamond: 20 nm/minute

Chamber cleaning after reactive gases were used

Two step cleaning process:

Step 1)

- Gas mixture: 10 sccm SF_6 / 50 sccm O_2
- Pressure: 60 mTorr
- Power: 100 W
- Time: 15 min

- Resulting DC bias ≈ 255 V

Step 2)

- Gas mixture: 50 sccm O_2
- Pressure: 100 mTorr
- Power: 200 W
- Time: 15 min
- Resulting DC bias ≈ 440 V

Simple chamber cleaning

- Gas mixture: 50 sccm O_2
- Pressure: 100 mTorr
- Power: 200 W
- Time: 30 min
- Resulting DC bias ≈ 440 V

Oxford Plasmalab 100 ICP at the CFN

The ICP system at the CFN is used for chlorine based plasmas. In order to etch Si layers a Cl_2/HBr plasma is used and Cr layers are etched by a Cl_2/O_2/Ar combination. All samples are placed on a Si carrier which is used to load samples from the load lock to the main chamber.

Si etching

Before a sample is etched, a 5 min conditioning step is carried out.

- Gas mixture: 12 sccm Cl_2 / 24 sccm HBr
- Pressure: 10 mTorr
- RF Power: 150 W
- ICP Power: 240 W
- Stage temperature: 20 °C
- Helium backing: Flow: 5 sccm, Pressure: 4.5 Torr
- Time: depending on required etching depth
- Resulting DC bias ≈ 600 V

Resulting etching rate:

- Si: 4.5-5.1 nm/s
- ZEP 520A: 5 nm/s
- HSQ: 0.8 nm/s

Cr etching

Before a sample is etched, a 5 min conditioning step is carried out.

- Gas mixture: 24 sccm Cl_2 / 6 sccm O_2 / 3 sccm Ar

- Pressure: 25 mTorr
- RF Power: 60 W
- ICP Power: 220 W
- Stage temperature: 20 °C
- Helium backing: Flow: 5 sccm, Pressure: 4.5 Torr
- Time: 2:20 min in order to make sure that a 15-20 nm Cr layer is completely etched
- Resulting DC bias ≈ 300 V

Resulting etching rate:

- Cr: 16-19 nm/ min
- HSQ: 2.2-3.2 nm/ min

Chamber cleaning

- Gas mixture: 40 sccm O_2
- Pressure: 20 mTorr
- RF Power: 100 W
- ICP Power: 1000 W
- Stage temperature: 20 °C
- Helium backing: Flow: 5 sccm, Pressure: 4.5 Torr
- Time: 15 min
- Resulting DC bias ≈ 380 V

A.6. Wafer Dicing Saw

In order to cut a wafer into a batch of chips of a certain size, a wafer dicing saw is used. This offers the advantage that with a properly chosen sawing blade and process parameters, the risk of uncontrollably braking a wafer in unintentional directions is avoided, especially if compared to manually scratching a wafer by a diamond tip and subsequently breaking it. Additionally, a single chip can be cut at a precise position by aligning the dicing system to already existing structures on a chip.

Here, a DISCO DAD3350 dicing saw[11] is used. Typically, the system is used in semi-automatic mode, in which several cuts with a certain separation are automatically performed after the alignment of a wafer has been set manually. The samples are placed on the dicing stage by putting them on an adhesion tape (Adwill G260 HP270[12]), which is stretched on a support frame. In order to protect the wafer surface and already existing on-chip circuits from the water cooling of the blade, the sample are covered by a Microposit™ S1813 G2[13] photoresist layer. An approximately 2 µm thick layer is applied by a spin coating process (2000 rpm, 1000 rpms, 90 s) with a subsequent baking step on a hotplate (105 °C, 1 min). After the dicing process the protection layer is simply dissolved in acetone. Typically, a dicing depth is chosen so that 100-250 nm of the substrate is still remaining in order to ensure that the blade is not touching the stage. The chip or wafer can now be broken very easily at the precise cutting position. The dicing blades consist of a bonding material which encloses a certain percentage of diamond crystals of a specific grit size.

Within this work several different substrates and device layers are cut. In order to account for the different material properties, specific dicing blades are used and the process parameters are adjusted. Also if a cut is placed very closely to a photonic circuit, special caution is taken to ensure a very smooth kerf profile. The detailed process parameters are given in the following.

Si and Si_3N_4 device layer on SiO_2 buffer layer on Si substrate

These wafers exhibit a Si or Si_3N_4 device layer thickness up to 2 µm on a 2-5 µm SiO_2 buffer layer on a 375-725 µm Si substrate. For dicing a complete wafer into a batch of e. g. $15 \times 15\,mm^2$ or $20 \times 20\,mm^2$ each cut is made in a single step while a precise cut is performed by a multistep dicing process at the very same position with decreasing blade height.

Wafer dicing:

- Dicing blade: ZH05-SD1500-N1-70[14] hub blade with a kerf width of approximately 50 µm
- Spindle speed: 30×10^3 rpm
- Feed rate: 2 mm/s
- Dicing height: Single step cut with 100 nm remaining substrate height

[11] DISCO Corporation, Ota-ku, Tokyo 143-8580, Japan
[12] LINTEC Corporation, Itabashi-ku, Tokyo 173-0001, Japan
[13] Dow Chemical Company, Midland, MI 48667, USA
[14] DISCO Corporation, Ota-ku, Tokyo 143-8580, Japan; https://www.disco.co.jp/eg/products/catalog/pdf/zh05.pdf

Precise cuts close to existing circuits:

- Dicing blade: ZH05-SD1500-N1-70 hub blade with a kerf width of approximately 50 µm
- Spindle speed: 30×10^3 rpm
- Feed rate: 1 mm/s
- Dicing height: In order to ensure a very smooth kerf profile, a two step process is employed. The first cut is done with a depth of only 30 µm and for the second cut at the very same position the blade height is adjusted so that only 120 µm of the substrate remain.

Si and Si_3N_4 device layer on SiO_2 substrate

In this case, the Si or Si_3N_4 device layer with a thickness up to 340 nm is directly placed on a typically 500 µm thick SiO_2 substrate. As the SiO_2 substrate is harder and more brittle than the Si substrate, a dicing blade with a superior wear resistance and rigidity is used. This is realized by sintered metal powder as bonding agent of the blade.

- Dicing blade: B1A862 SD400 L25 MT38[15] hub-less blade with a kerf width of approximately 120 µm
- Spindle speed: 25×10^3 rpm
- Feed rate: 1.5 mm/s
- Dicing height: Single step cut with 100 µm remaining substrate height

Si and Si_3N_4 device layer on borosilicate glass substrate

In this case, the Si or Si_3N_4 device layer with a thickness of 200 nm is directly placed on a 1.1 mm thick BSG substrate. Due to the large thickness of the substrate, a two step process is used to cut a wafer into smaller pieces.

- Dicing blade: microkerf 2.187-8-30 S16[16] hub-less blade with a kerf width of approximately 200 µm
- Spindle speed: 30×10^3 rpm
- Feed rate: 1 mm/s
- Dicing height: Two step process with 400 µm dicing depth steps. Thus, the first cut is placed at a substrate height of 700 µm and the second cut at a height of 300 µm.

Diamond device layer on SiO_2 or AlN buffer layer on Si substrate

The diamond device layer exhibits a thickness of up to 1.5 µm on an up to 5 µm thick SiO_2 or AlN buffer layer on an up to 675 µm Si substrate. Due to the very hard diamond top layer, a two step process is used to cut a wafer into smaller pieces. In case that a precise cut is placed in close vicinity to integrated circuits, the dicing process is further divided in a multi-step process in order to avoid splintering of the diamond layer.

[15] DISCO Corporation, Ota-ku, Tokyo 143-8580, Japan; `https://www.disco.co.jp/eg/products/catalog/pdf/b1a.pdf`

[16] MINITRON elektronik GmbH, Ingolstadt, BY 85057, Germany; `http://minitron.de/uploads/media/dicbla_01.pdf`

- Dicing blade: B1A862 SD400 L25 MT38 hub-less blade with a kerf width of approximately 120 µm
- Spindle speed: 25×10^3 rpm
- Feed rate: 0.7 mm/s
- Dicing height: In order to avoid splintering of the diamond layer a multi-step dicing process is used. At the beginning three cuts with a depth step size of 30 µm are done and then further cuts are performed with a depth step size of 100 µm until only 250 µm of the Si substrate remain.

A.7. Basic Measurement Setup Components

Here a list of used components for the basic measurement setup used for the recording of transmission spectra is given. For measurements in the NIR C-band the following parts are used:

- New Focus TLB-6600[17] tunable laser, $\lambda = 1510\text{-}1620\,\text{nm}$
- Santec TSL-510[18] tunable laser, $\lambda = 1500\text{-}1630\,\text{nm}$
- Thorlabs FPC030[19] fiber polarization controller
- New Focus 2117 and Focus 2011[17] low-noise, variable-gain semiconducting photodiode detectors

For measurements in the visible regime around a wavelength of 773 nm the following laser and detector are used instead:

- New Focus TLB-6712-P[17] tunable laser, $\lambda = 765\text{-}781\,\text{nm}$
- New Focus 2001[17] low-noise, variable-gain semiconducting photodiode detectors

Additionally, a broadband spectrum in the visible regime can be recorded by using an unpolarized white light source and a spectrometer. This allows for very fast recording of transmission spectra, however their quality is limited by the spectrometer resolution:

- Leukos[20] SM-30-UV white light source with broadband emission from 200 to 2400 nm
- Ocean Optics USB2000+[21] spectrometer, range: 190-890 nm, resolution: 0.3 nm
- Ocean Optics JAZ[21] spectrometer, range: 340-1015 nm, resolution: 0.3 nm
- Ando AQ-6315A[22] optical spectrum analyzer, range: 350-1750 nm, resolution: 0.1 nm

[17] Newport Corporation, Irvine, CA 92606, United States
[18] Santec Corporation, Komaki, Aichi 485-0802, Japan
[19] Thorlabs Inc., Newton, NJ 07860, United States
[20] Leukos, Limoges, NAQ 87280, France
[21] Ocean Optics, Largo, FL 33777, USA
[22] Yokogawa Electric Corporation, Musashino, Tokyo 180-8750, Japan

A.8. Simulation Details for Atom Clad Waveguides

As described in the main text, the atom susceptibility is given as [289–294]:

$$\chi(\Delta) = \frac{N}{\hbar\epsilon_0}\sum_i A_i \sum_{F,F'} \frac{C^2_{F,F'}d^2}{2(2I+1)} \int_{-\infty}^{\infty} dv_z \int_0^{\infty} dv_t \frac{2M(v_z,v_t)}{-2\pi\Delta - k_z v_z - i(2\pi G/2 - ik_t v_t)}. \tag{A.23}$$

The transition strength of a transition between the Zeeman levels of the hyperfine structure is given by the dipole matrix element between the state $|F, m_F\rangle$ and $|F', m'_F\rangle$ as $|\langle F, m_F\|e\vec{r}\|F', m'_F\rangle|^2$. By factoring out the angular dependence this can be expressed by the product of Wigner 3-j and 6-j symbols and a reduced matrix element $d = \langle L\|e\vec{r}\|L'\rangle$ [538, 539]. By calculating the prefactors and Wigner coefficients it can be further reduced:

$$\begin{aligned}\langle F, m_F\|e\vec{r}\|F', m'_F\rangle =& (-1)^{2F'+I+J+J'+L+S+m_F+1} \\ &\times \sqrt{(2F+1)(2F'+1)(2J+1)(2J'+1)(2L+1)} \begin{pmatrix} F' & 1 & F \\ m'_F & -\Delta m_F & -m_F \end{pmatrix} \\ &\times \begin{Bmatrix} J & J' & 1 \\ F' & F & I \end{Bmatrix} \begin{Bmatrix} L & L' & 1 \\ J' & J & S \end{Bmatrix} \langle L\|e\vec{r}\|L'\rangle \qquad (A.24)\\ =& c_{m_F,m'_F}\langle L\|e\vec{r}\|L'\rangle = c_{m_F,m'_F} d \qquad (A.25)\end{aligned}$$

The transition strength of a Zeeman transition is thus given by $c^2_{m_F,m'_F} d^2$. In order to get the transition strength $C^2_{F,F'} = \sum c^2_{m_F,m'_F}$ of a hyperfine transition between F and F' the transition strengths of all contributing Zeeman transitions are summed up. In the case of linear polarized light only the π transitions with $\Delta m_F = 0$ have to be considered. The data for the transition strength $C^2_{F,F'}$ for all transitions of the D2 line are given in table Tab. A.3. The strength $c^2_{m_F,m'_F}$ of the Zeeman transitions (with a factor of $2/3$) can be found in [237, 238].

The reduced matrix element d is calculated via the the expression for the decay rate G and the angular transition frequency ω_0 [295], which can be accessed experimentally.

$$G = \frac{\omega_0^3}{3\pi\epsilon_0\hbar c^3}\frac{2J+1}{2J'+1}|\langle J\|e\vec{r}\|J'\rangle|^2 \tag{A.26}$$

$$\langle J\|e\vec{r}\|J'\rangle = (-1)^{J'+L+S+1}\langle L\|e\vec{r}\|L'\rangle\sqrt{(2J'+1)(2L+1)}\begin{Bmatrix} L & L' & 1 \\ J' & J & S \end{Bmatrix} \tag{A.27}$$

$$\langle J = 1/2\|e\vec{r}\|J' = 3/2\rangle = \sqrt{2/3}\langle L = 0\|e\vec{r}\|L' = 1\rangle, \tag{A.28}$$

for the D2 line of Rb. Thus, an expression for d can be derived:

$$d = \langle L = 0 \| e\vec{r} \| L' = 1 \rangle = \sqrt{3}\sqrt{\frac{3\epsilon_0 \hbar G \lambda^3}{8\pi^2}}. \tag{A.29}$$

The velocity distribution for each direction is given by:

$$g_{v_\mathrm{p}}(v) = \frac{1}{\sqrt{\pi} v_\mathrm{p}} e^{-(v/v_\mathrm{p})^2}, \tag{A.30}$$

with the most probable velocity v_p. Thus, the distribution $M(v_z, v_t)$ in (A.23) is:

$$M(v_z, v_t) = \frac{1}{\sqrt{\pi} v_\mathrm{p}} e^{-(v_z/v_\mathrm{p})^2} \frac{1}{\sqrt{\pi} v_\mathrm{p}} e^{-(v_t/v_\mathrm{p})^2}. \tag{A.31}$$

The most probable velocity at a certain temperature T is calculated via:

$$\frac{1}{2} m v_\mathrm{p}^2 = k_B T \qquad \leftrightarrow \qquad v_\mathrm{p} = \sqrt{\frac{2k_B T}{m}}, \tag{A.32}$$

where k_B is the Boltzmann constant and m is the atomic mass. Note that the different isotopes exhibit different masses.

The number density of the atom vapor at the temperature T (in Kelvin) is calculated via the Nesmeyanov formula for the alkali atoms [540]:

$$N = \frac{133.323 \left(15.88253 - {}^{4529.635}/_{T} + 0.00058663T - 2.99138 \log_{10}(T)\right)}{k_B T}, \tag{A.33}$$

for liquid rubidium at a temperature $T > 39.31\,^\circ\mathrm{C}$.

The expression for χ in (A.23) is implemented in Matlab by replacing the integrals with a sum over the velocity components. All parameters and constants, which are used for the calculation are listed in Tab. A.2 and A.3. As an example for the atom vapor number density and the most probable velocity, their values at a temperature of 150 °C are:

$$N = 84.7\,\mu\mathrm{m}^{-3} \tag{A.34}$$

$$v_{\mathrm{p,Rb85}} = 287.8\,\mathrm{m/s} \tag{A.35}$$

$$v_{\mathrm{p,Rb87}} = 284.5\,\mathrm{m/s}. \tag{A.36}$$

In order to start the simulation of an atom clad waveguide, the propagation constant of a waveguide mode as well as the decay length of the evanescent field outside of the waveguide are extracted from a FEM simulation of the geometry without the atom vapor. For example, a 180 nm high and 650 nm wide fully etched Si_3N_4 ridge waveguide on a silica substrate is considered. The propagation constant

Boltzmann's constant	k_B	$1.380\,650 \times 10^{-23}$ J/K
Planck's constant	$\hbar$	$1.054\,572 \times 10^{-34}$ J s
Vacuum permittivity	ϵ_0	$8.854\,187 \times 10^{-12}$ F/m
Elementary charge	e	$1.602\,176 \times 10^{-19}$ C
Bohr radius	a_0	$0.529\,177 \times 10^{-10}$ m
Electrom mass	m_e	$9.109\,382\,15 \times 10^{-31}$ kg
Atomic mass Rb^{85}	m_{Rb85}	$1.409\,993 \times 10^{-25}$ kg
Atomic mass Rb^{87}	m_{Rb87}	$1.443\,160 \times 10^{-25}$ kg
Natural abundance Rb^{85}	A_{Rb85}	0.7217
Natural abundance Rb^{87}	A_{Rb87}	0.2783
Natural decay rate D2 line Rb	G	6.0666 MHz
Reduced matrix element D2 line Rb	d	$5.177\epsilon_0 a_0$
Center frequency of D2 line Rb	ν_c	384.230 426 6 THz
Center wavelength of D2 line Rb	λ_c	780.241 327 1 nm

Table A.2.: Parameters and constants for the calculation of the atom vapor susceptibility.

Transition	Shift in transition frequency relative to D2 center frequency	Relative transition strength $C^2_{F,F'}$
(i) Rb^{85} $F = 2 \rightarrow F' = 1$	1635.454 MHz	1/3
(i) Rb^{85} $F = 2 \rightarrow F' = 2$	1664.714 MHz	35/81
(i) Rb^{85} $F = 2 \rightarrow F' = 3$	1728.134 MHz	28/81
(ii) Rb^{85} $F = 3 \rightarrow F' = 2$	−1371.29 MHz	10/81
(ii) Rb^{85} $F = 3 \rightarrow F' = 3$	−1307.87 MHz	35/81
(ii) Rb^{85} $F = 3 \rightarrow F' = 4$	−1186.91 MHz	1
(iii) Rb^{87} $F = 1 \rightarrow F' = 0$	4027.403 MHz	1/9
(iii) Rb^{87} $F = 1 \rightarrow F' = 1$	4099.625 MHz	5/18
(iii) Rb^{87} $F = 1 \rightarrow F' = 2$	4256.57 MHz	5/18
(iv) Rb^{87} $F = 2 \rightarrow F' = 1$	−2735.05 MHz	1/18
(iv) Rb^{87} $F = 2 \rightarrow F' = 2$	−2578.11 MHz	5/18
(iv) Rb^{87} $F = 2 \rightarrow F' = 3$	−2311.26 MHz	7/9

Table A.3.: Shift and transition strength of the hyperfine transitions contributing to the D2 line of rubidium.

and the inverse decay length are then used as k_z and k_t in the calculation of the atom susceptibility. As an example, this calculation is done at a rubidium vapor temperature of 150 °C From the susceptibility the complex index of refraction of the atom vapor around the waveguide is calculated. The real and imaginary part are presented in Fig. A.3 a) and b) as the red line. In all these graphs zero detuning

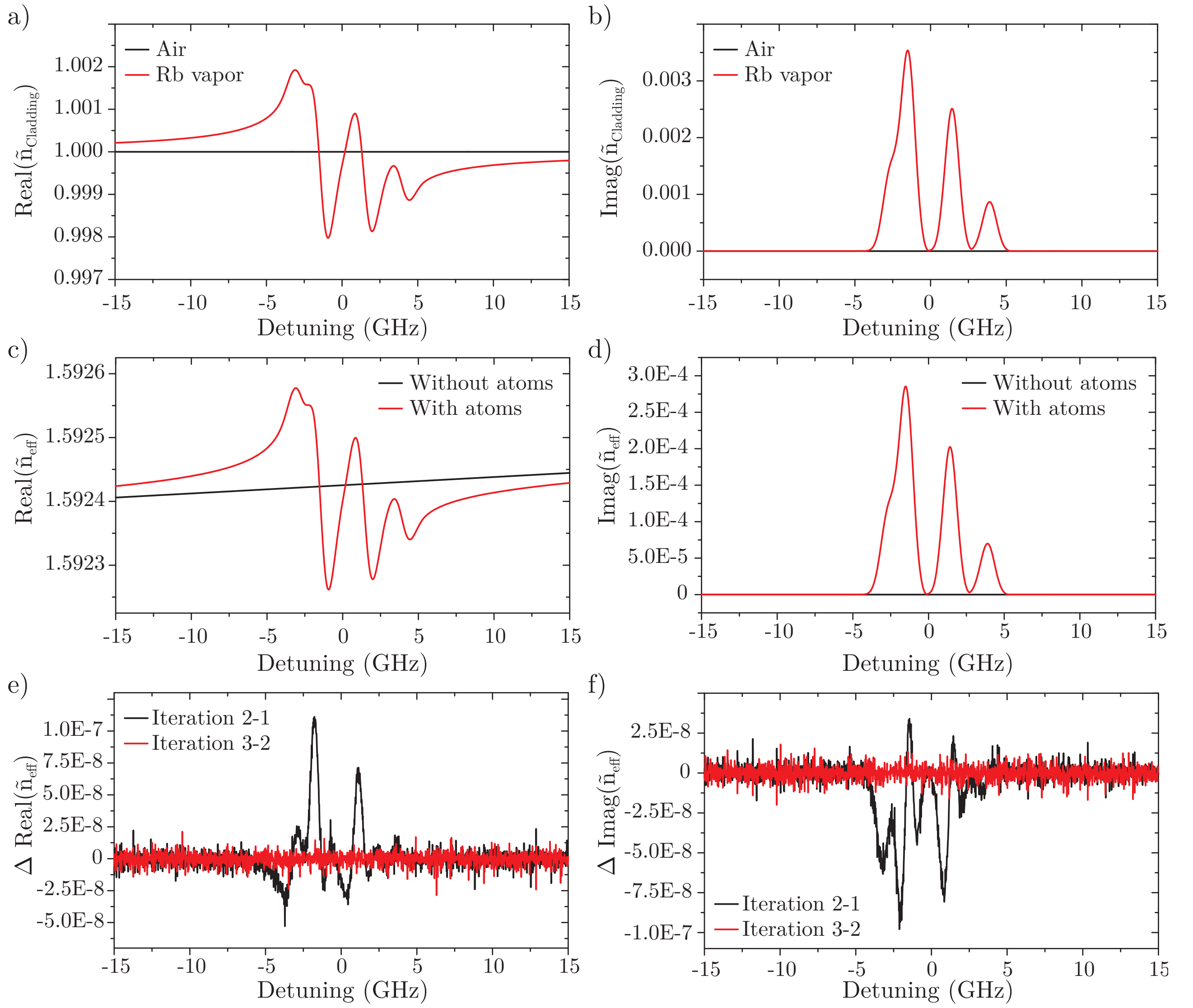

Figure A.3.: a), b) The real and imaginary part of a rubidium vapor around a waveguide are calculated at a temperature of 150 °C. This is used for FEM simulations of the waveguide mode and the complex effective mode index which is presented in c) and d). Several iteration cycles are used for the simulation in order to verify how quickly the solution converges. In e) and f) the complex effective mode index after up to three iteration cycles are compared.

corresponds to the center of the D2 line at approximately 780 nm. The real part (a) oscillates around the value for air when scanning over the transitions of the rubidium D2 line. Its extrema however are not precisely at the same position as the maxima of the imaginary part (b), but rather on the slope of these peaks. This indicates already that the spectral position of the maximum phase shift is slightly altered from the position of maximum absorption.

The rubidium atom vapor is now included in the FEM simulation of the waveguide mode by adding a surrounding layer around the waveguide with the calculated complex refractive index. This leads to

a complex effective index for the waveguide mode as shown in Fig. A.3 c) and d). The shape of the curve of the atom refractive index is now transferred to the effective mode index, where the real part oscillates around the value without atoms and the imaginary part (and thus the attenuation) shows the same spectrum as in (b). With increasing frequency, the real part of the effective mode index without the atom vapor increases due to material dispersion. The maximum in the imaginary part of the effective mode index corresponds to an attenuation coefficient of 20 dB/mm.

Including the atom vapor around the waveguide not only alters the effective mode index at the atom transitions but also the propagation constant linked the the mode index as well as the decay length. This in turn leads to a slight variation in the atom susceptibility and consequently to a slight shift in the effective mode index. Thus, several iterations of this cycle are simulated and the development of the effective mode index is examined. The first iteration uses the k values from the simulation without atoms, the second one uses then the values from the first simulation with atoms and so on. The absolute difference in the real and imaginary part of the effective mode index between the second and first (black line) as well as between the third and second iteration (red line) are presented in Fig. A.3 e) and f). The second iteration leads only to a small change in the order of 10^{-8} (compared to the variation of the effective mode index in the order of 10^{-4} when the atom vapor is included with respect to the case without atoms) and the change due to the third iteration is another four orders of magnitude smaller and is already almost lost in the numerical precision of the calculation and FEM simulation. The resulting effective mode index of the atom clad waveguide thus converges very quickly and only two iterations are used for all the simulations presented here.

A.9. Atom Clad MZIs: Fit Parameters

As described in the main text, the transmitted power of the MZI in the presence of an atom vapor at one of the arms is given by:

$$P_{\mathrm{MZI}} = \frac{P_{\mathrm{in}}}{4}\left(1 + 2Ae^{-\beta'_{\mathrm{Rb}}L_{\mathrm{Rb}}}\cos(\Phi') + A^2 e^{-2\beta'_{\mathrm{Rb}}L_{\mathrm{Rb}}}\right),$$

with the input power P_{in}, the ratio $A = \mathcal{E}_2/\mathcal{E}_1$ of the field amplitudes, and the total phase $\Phi' = (L_2 - L_1 - L_{\mathrm{Rb}})\beta_1 + \Phi_0 + L_{\mathrm{Rb}}\beta_{\mathrm{Rb}}$.

In order to determine the MZI parameters, the spectrum without the atoms or off resonance from the Rb D2 line can be considered. In this case the maximum transmitted power for constructive interference and the minimum transmitted power for destructive interference are used to extract A and P_{in}. The input power here deviates from the laser beam power, because of the coupling process to and from the chip via the grating couplers. Strictly speaking this input power is not a constant due to the Gaussian like transmission spectrum of the grating couplers. However, the width of the grating coupler transmission is in the order of 50 nm, while the scanned region around the Rb D2 line is only approximately 20 pm and thus when being at the peak coupler transmission, a constant input power can be considered. A and P_{in} are extracted from:

$$P_{\max} = \frac{P_{\mathrm{in}}}{4}(1+A)^2 \qquad P_{\min} = \frac{P_{\mathrm{in}}}{4}(1-A)^2.$$

The phase offset Φ_0 is extracted from the spectral position of the interference pattern. The atomic density is the only free parameter for adjusting the influence of the atom vapor to the experimental data. The obtained parameters for the three spectra presented in the main text are given in Tab. A.4. It should be noted that there is a large unbalance in the field amplitudes ratio A. The amplitude in the longer arm of the MZI is approximately ten times smaller than the on in the other arm and it further decreased during the course of the experiment. Thus, a visibility (ER) for the interference pattern is observed, which is much smaller than expected from a 50:50 beam splitter. This can be attributed to the attenuation in the much longer arm compared to the short arm on the one hand, but a much large influence might have atom adsorption on the waveguide in the interaction region on the other hand. The formation of such a (metallic) atom layer leads to a much increased general absorption in this arm. Especially the continuous decrease of the signal during the course of the experiments strongly

Curve	Temperature T	Atomic density N	P_{in}	A	Φ_0
Red	103 °C	5.8 µm^{-3}	138.402 pW	0.099121	-0.120π
Blue	117 °C	13.9 µm^{-3}	156.211 pW	0.105759	-0.185π
Green	124 °C	21.0 µm^{-3}	136.706 pW	0.1664374	-0.064π

Table A.4.: Obtained fit parameters for the atom clad MZI spectra.

hints to atoms sticking to the waveguide surface. Contrary to the used vacuum window platform here, special precautions are taken for the second vapor cell platform to protect the waveguide from the atom vapor.

A.10. Mechanical Facet Polishing

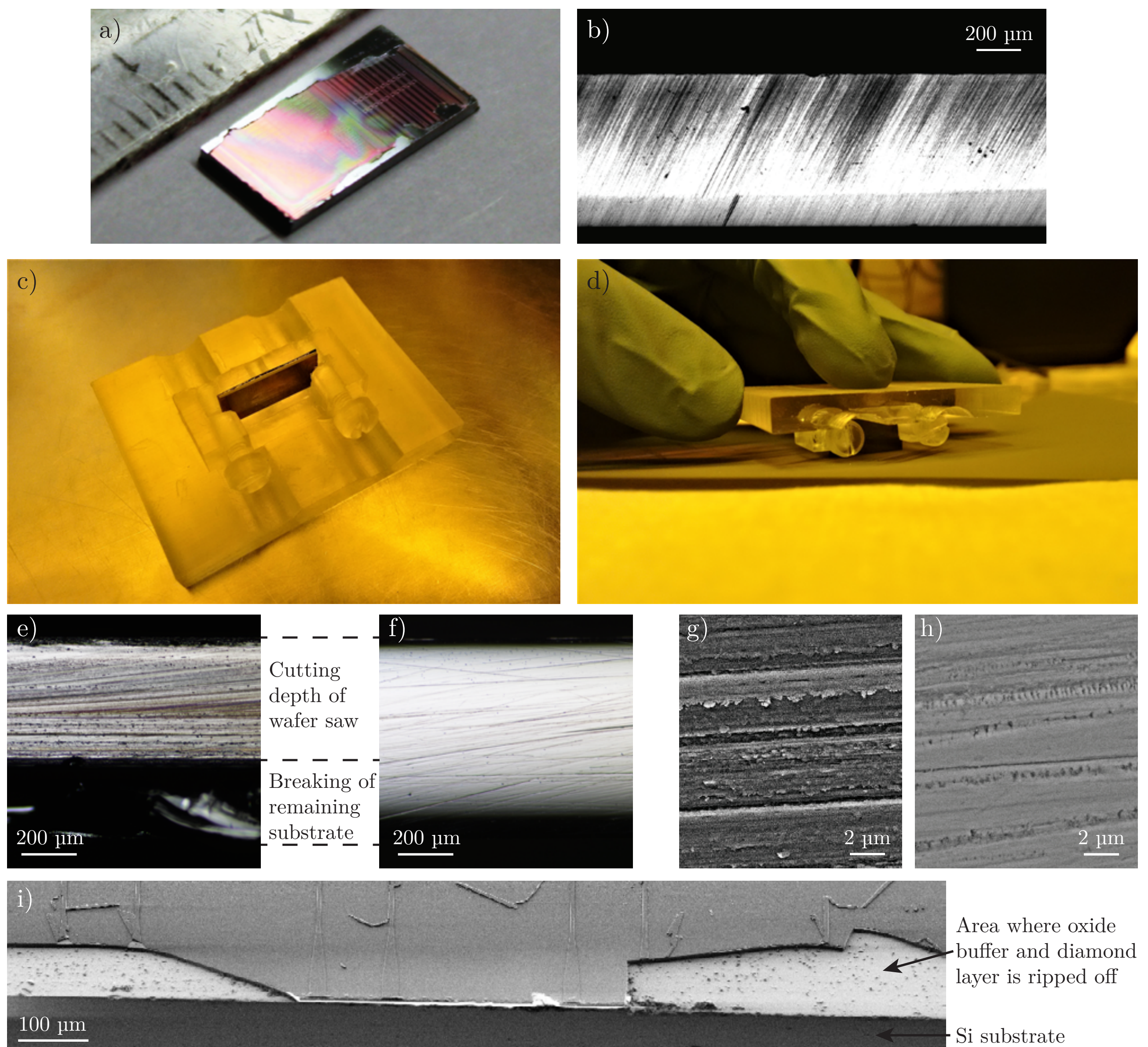

Figure A.4.: a), b) Results of the semi-automatic polishing procedure. The applied forces are rather strong, so that large parts of the diamond device layer as well as the buried oxide layer along the side of the chips are ripped off (a). Th optical micrograph (b) also reveals that there a still depp scratches in the side facet of the chip. c)-i) Process and results of the manual polishing procedure. The sample is fixed in a vertical position in a 3D-printed holder (c) which is used to hold the sample and push it onto the abrasive paper (d). The decreased surface roughness of the sample side facet after polishing can be seen in optical micrographs of the side before (e) and after (f) polishing as well as in SEM micrographs ((g) before and (h) after polishing). However, the polishing process still causes parts of the diamond device layer as well as the underlying oxide buffer layer too be ripped off as shown in the SEM micrograph of the tilted sample edge in (i).

For improving the coupling to and from on-chip circuits vie the end facet of a waveguide, a polishing procedure of the side of the chip and the facet of the waveguide is tested. In order to protect the photonic structures, a ∼2 µm S1813 G2 protection layer is spin coated. In a first test the side of the chip is polished in a semi-automatic process. An abrasive paper is fixed to a quickly revolving plate. The sample is fixed to a mount, so that it is kept in a perpendicular position to the rotating plate. The sample is then lowered onto the plate and the side of the chip is polished. This polishing procedure is rather powerful and in the case of a diamond sample, the applied forces are too strong for the stressed diamond layer and large parts of the diamond layer (which contains the photonic circuits) and the buried oxide layer are ripped off. This can be seen in Fig. A.4 a), where on the side of the chip large parts of the diamond device layer are missing. Also the side view of the chip with an optical microscope as shown in (b) reveals, that the procedure still leaves deep scratches in the surface.

Thus, a much more gentle manual polishing procedure is tested. For this purpose a sample holder is constructed and completely fabricated in a 3D printer[23] which fixes the sample in an upright position (see Fig. A.4 c)). Below the sample is an small empty space, so that the facet is not damaged. This allows to hold the sample vertically and to gently push it onto an abrasive paper, where it is gently moved back and forth to polish its side facet (see Fig. A.4 d)). First an abrasive paper with a grain size of 5 µm is used, then one with a grain size of 1 µm, and as a finishing step a paper with a very fine grain size of 0.3 µm is used in order to obtain a very smooth side facet. The result can be seen in the optical micrographs in panel (e) before and in panel (f) after the polishing procedure. Before the polishing process, the side of the chip is divided in two parts. Down to a certain depth the chip is cut by the wafer dicing saw and the remaining substrate is simply broken at the cut position. After polishing, the side of the chip exhibits a single much smoother facet. This shows, that some of the substrate material is ablated during polishing. A further removal of the still visible scratches could be realized by an extensive polishing with the finest abrasive paper. The decrease of the surface roughness can also be seen in a comparison of the side of the sample in SEM micrographs before (panel (g)) and after (panel (h)) the manual polishing procedure. Even though the manual polishing is much more gentle than the semi-automatic one, the applied forces to the diamond device layer are still too strong. Parts of the dimaond layer along the side of the sample as well as the buried oxide layer beneath are ripped off, which prevents the polishing of the end facet of the waveguides. This can be seen in the SEM micrograph in Fig. A.4 i), where parts of the diamond and oxide layer are missing after the polishing process. Therefore, the polishing of the facet is abandoned and the as-etched facet of the waveguide is kept.

[23] Ember DLP 3D printer, Autodesk, San Rafael, CA 94903, United States

A.11. Details on Optical Components of the LWIR Setup

Here a list of the used components for the LWIR measurement setup is given:

- MIRcat 1300[24] QCL tunable laser, total range: $\lambda = 6.9\text{-}9.26\,\mu\text{m}$

  There are three separate lase modules included in the laser in order to cover this wavelength range: module M1074 ($\lambda = 6.9\text{-}7.63\,\mu\text{m}$), module M1080 ($\lambda = 7.69\text{-}8.4\,\mu\text{m}$), module M1090 ($\lambda = 8.37\text{-}9.26\,\mu\text{m}$).

  The laser can be used in CW mode (240 mW output power at $\lambda = 8\,\mu\text{m}$) or in pulsed mode (210 mW peak power at $\lambda = 8\,\mu\text{m}$, pulse rate: 1-100 kHz, pulse width: 20-500 ns, duty cycle: 0.002-5 %)
- Water chiller for laser cooling: ThermoCube 300[25]
- IR optical isolator FIO-5-8.00[26]
- IR polarization rotator RF-4[26]
- Reflective objective LMM-40X-P01[27]
- Wire grid polarizer WP25H-B[27]
- IR ZnSe lens LA7477-G[27]
- Fiber coupling platform MBT613D/M[27]
- Fiber polarization controller FPC560[27]
- IR chalcogenide glass fibers IRF-Se-12 with FC/B connector at Brewster angle[28]
- Water-cooled IR detector Q-MACS IRDM-DCA 1611060[29]
- IR camera FLIR A655SC, Objective FLIR A6x5SC/ T650SC[30]
- IR camera VarioCAM HDx head 675 S, tele objective 40mm[31]

The minimum laser beam waist is already reached at a distance of 20-30 cm from the laser with a beam diameter of 2-2.5 mm. Thereafter the the beam diameter increases and reaches a value of 3.5-4.1 mm at a distance of 100 cm from the laser. This rather quickly increasing width also limits the device performance of some of the components as discussed in the following. All components are characterized at a wavelength of 8 µm

As a first component, the laser beam is always transmitted through the optical isolater, as already very small back-reflections damage the laser module. First the input and then the output polarizer of the isolater are optimized for maximum transmission. The output polarizer is further fine-tuned for minimum transmission in backward direction by turning the polarizer against beam direction and monitoring the transmission. Turning the isolator back in forward direction a maximum transmission

[24] DRS Daylight Solutions Inc., San Diego, CA 92128, USA
[25] Solid State Cooling Systems, Wappingers Falls, NY 12590, USA
[26] Innovation Photonics, Verona, NJ 07044, USA
[27] Thorlabs Inc., Newton, NJ 07860, United States
[28] IRflex Corporation, Danville, VA 24540, USA
[29] neoplas control GmbH, Greifswald, MV 17489, Germany
[30] FLIR Systems Inc., Wilsonville, OR 97070, USA
[31] InfraTec GmbH, Dresden, SN 01217, Germany

of 45 % is obtained, despite being specified as 76 %.

If a free space path from the laser to the sample is chosen, the free space polarization rotator is needed to adjust the plane of polarization to the waveguide mode. The IR polarization rotator suffers however from a few drawbacks. The axis of rotation of the device is not precisely aligned with the center of the input aperture. Thus, when rotating the device, only a very small effective aperture with a diameter in the order of 1 mm is obtained. This trims the beam and decreases its maximum transmission to 47 %, while is is specified as 83.5 %. Additionally, the output beam is slightly misaligned form the input beam and more significantly the direction of the output beam rotates around the axis of the input beam, when the polarizer is rotated. Hence, the beam alignment needs to be readjusted when the polarization is rotated.

It has to be furthermore considered that the mirrors exhibit a reflection of as specified 94 % and the wire grid polarizer exhibits a transmission of as specified 86 %. In order to avoid additional losses, the number of optical components should be reduced as far as possible. Also the length of the beam path should be as short as possible to avoid a large beam diameter which leads to losses because of the limited aperture size of the used components.

When using a reflective objective to focus the laser beam, the dimensions of the objective play an important role. The objectives used here, exhibit an open input aperture with a diameter of 5 mm. If the beam diameter is larger, the beam is trimmed and the intensity is decreased. Also the inner small mirror leads to a certain amount of beck-reflections into the beam path, which contributes to additional losses. Using a reflective objective to collect light, the inner mirror imposes an obstruction of 22 % of the objective area. The losses are experimentally quantified by focusing the beam with a first objective and directly collecting the light again with a second objective, which leads to a transmission of approximately 25 % through both objectives. Alternatively, a ZnSe lens can be used for focusing the beam, which offers the advantage that a larger transmission is achieved (70 % transmission through a 10 mm ZnSe sample; lens center thickness is 3 mm). However, in contrast to the reflective objectives the focal length depends on the used wavelength and therefore if the wavelength is shifted, the alignment to the focal spot of the optical system has to be readjusted.

Instead of focusing the beam directly onto the end facet of a waveguide, it can be coupled to a fiber, which in turn is used to couple light to the waveguide. This simplifies the alignment of the waveguide significantly, but additional losses are induced by the coupling procedure from the free space beam to the fiber. There is a mismatch between the NA of the lense (0.15, with a focal length of 15 mm and assuming a beam diameter of 5 mm), to the NA of the fiber (0.21). Additionally, the minimum beam waist of the focal spot obtainable by the lens can be calculated. For a beam diameter of 5 mm at a wavelength of 8 µm, a minimum beam waist radius of 15 µm should be achievable. This is however still much larger than the fiber core radius of 6 µm. Using a power-meter the beam power before coupling to the fiber and the fiber output is compared and a transmission of approximately 10 % is obtained, which fits to the area mismatch of the minimum beam waist and the fiber core. This can be increased by using a multimode fiber with a larger core radius. However, the core radius should be as small as

possible to effectively couple to a waveguide with a dimension of approximately 1.5 µm × 4 µm.

An alternative for increasing the coupling efficiency would be using a lens with a smaller focal length. The availability of IR optical components is however limited and therefore this might be rather cost-intensive. Instead, using the reflective objective (with an NA of 0.5) leads to a smaller focal spot, but the limited input aperture and the back-reflections in the center cause a decreased total transmission through the fiber, when this configuration is characterized. A further way to improve the coupling efficiency is to use a beam expander before focusing the beam to the fiber facet. This is tested here, but the attenuation by the additionally used lenses for expanding the beam reverse the positive effect of an enlarged beam diameter so that the achieved transmission through the fiber remains the same as achieved before without the beam expander. A further factor that has to be considered for the coupling to the fiber is that coupling via the Brewster angle is applied. Therefore, the plane of polarization of the input beam needs to be adjusted. However, the losses induced by the free space IR polarizer are larger than the gained coupling efficiency, so that the use of the polarization rotator is renounced. This can be avoided by rotating rather the angled input facet of the fiber than the polarization of the beam, but such a revolving fiber holder is not yet implemented in the setup.

As a last point, the absorption of the laser beam by the humidity needs to be considered. Water vapor exhibits an absorption minimum around a wavelength of 10 µm, but it still contributes to the attenuation of the beam. Therefore, a humidity control in the laboratory would be desirable and fluctuations of the humidity have to be kept in mind as a source for variations in the obtained transmission.

Bibliography

[1] Charles K. Kao. “Nobel Lecture: Sand from centuries past: Send future voices fast.” Nobel Media AB 2014. Web. 13 Mar 2018, URL https://www.nobelprize.org/nobel_prizes/physics/laureates/2009/kao-lecture.html.

[2] H. Venghaus and N. Grote. *Fibre Optic Communication*, vol. 161 of *Springer Series in Optical Sciences*. Springer International Publishing, Cham, 2 edn., **2017**. ISBN 9783319423654. DOI http://dx.doi.org/10.1007/978-3-319-42367-8.

[3] K. Hiraga, M. Yamada, H. Kawakami, S. Matsuo, *et al.*. “2x344 Tb/s propagation-direction interleaved transmission over 1500km MCF enhanced by multicarrier full electric-field digital back-propagation.” In *39th European Conference and Exhibition on Optical Communication (ECOC 2013)*, 1254–1256, **2013**. DOI http://dx.doi.org/10.1049/cp.2013.1691.

[4] D. Hillerkuss, R. Schmogrow, M. Meyer, S. Wolf, *et al.*. “Single-laser 325 Tbit/s Nyquist WDM transmission.” *Journal of Optical Communications and Networking* 4 (10), 715, **2012**. DOI http://dx.doi.org/10.1364/JOCN.4.000715.

[5] R. Kirchain and L. Kimerling. “A roadmap for nanophotonics.”, **2007**. DOI http://dx.doi.org/10.1038/nphoton.2007.84.

[6] A. Alduino and M. Paniccia. “Interconnects: Wiring electronics with light.” *Nature Photonics* 1 (3), 153–155, **2007**. DOI http://dx.doi.org/10.1038/nphoton.2007.17.

[7] M. Paniccia. “Integrating silicon photonics.” *Nature Photonics* 4 (8), 498–499, **2010**. DOI http://dx.doi.org/10.1038/nphoton.2010.189.

[8] D. A. Miller. “Optical interconnects to silicon.” *IEEE Journal on Selected Topics in Quantum Electronics* 6 (6), 1312–1317, **2000**. DOI http://dx.doi.org/10.1109/2944.902184.

[9] D. A. Miller. “Device requirements for optical interconnects to silicon chips.” *Proceedings of the IEEE* 97 (7), 1166–1185, **2009**. DOI http://dx.doi.org/10.1109/JPROC.2009.2014298.

[10] D. A. Miller. “Optical interconnects to electronic chips.” *Applied optics* 49 (25), 70, **2010**. DOI http://dx.doi.org/10.1109/5.867687.

[11] R. Dangel, J. Hofrichter, F. Horst, D. Jubin, *et al.*. “Polymer waveguides for electro-optical integration in data centers and high-performance computers.” *Optics Express* 23 (4), 4736, **2015**. DOI http://dx.doi.org/10.1364/OE.23.004736.

[12] A. Shacham, K. Bergman, and L. P. Carloni. “Photonic networks-on-chip for future generations of chip multiprocessors.” *IEEE Transactions on Computers* 57 (9), 1246–1260, **2008**. DOI http://dx.doi.org/10.1109/TC.2008.78.

[13] M. Asghari and A. V. Krishnamoorthy. “Silicon photonics: Energy-efficient communication.”, **2011**. DOI `http://dx.doi.org/10.1038/nphoton.2011.68`.

[14] A. Rickman. “The commercialization of silicon photonics.”, **2014**. DOI `http://dx.doi.org/10.1038/nphoton.2014.175`.

[15] C. Sun, M. T. Wade, Y. Lee, J. S. Orcutt, *et al.*. “Single-chip microprocessor that communicates directly using light.” *Nature* 528 (7583), 534–538, **2015**. DOI `http://dx.doi.org/10.1038/nature16454`.

[16] B. Jalali and S. Fathpour. “Silicon Photonics.” *Journal of Lightwave Technology* 24 (12), 4600–4615, **2006**. DOI `http://dx.doi.org/10.1109/JLT.2006.885782`.

[17] G. T. Reed. *Silicon photonics: the state of the art.* Wiley, Chichester [u.a.], **2008**. ISBN 9780470025796.

[18] D. A. Miller. “Rationale and challenges for optical interconnects to electronic chips.” *Proceedings of the IEEE* 88 (6), 728–749, **2000**. DOI `http://dx.doi.org/10.1109/5.867687`.

[19] H. Cho, P. Kapur, and K. C. Saraswat. “Power comparison between high-speed electrical and optical interconnects for interchip communication.” *Journal of Lightwave Technology* 22 (9), 2021–2033, **2004**. DOI `http://dx.doi.org/10.1109/JLT.2004.833531`.

[20] Z. Zhou, B. Yin, Q. Deng, X. Li, *et al.*. “Lowering the energy consumption in silicon photonic devices and systems.” *Photonics Research* 3 (5), B28, **2015**. DOI `http://dx.doi.org/10.1364/PRJ.3.000B28`.

[21] D. Liang and J. E. Bowers. “Recent progress in lasers on silicon.” *Nature Photonics* 4 (8), 511–517, **2010**. DOI `http://dx.doi.org/10.1038/nphoton.2010.167`.

[22] T. Creazzo, E. Marchena, S. B. Krasulick, P. K. L. Yu, *et al.*. “Integrated tunable CMOS laser.” *Optics Express* 21 (23), 28048, **2013**. DOI `http://dx.doi.org/10.1364/OE.21.028048`.

[23] Z. Zhou, B. Yin, and J. Michel. “On-chip light sources for silicon photonics.” *Light: Science & Applications* 4 (11), e358–e358, **2015**. DOI `http://dx.doi.org/10.1038/lsa.2015.131`.

[24] D. Liang, X. Huang, G. Kurczveil, M. Fiorentino, *et al.*. “Integrated finely tunable microring laser on silicon.” *Nature Photonics* 10 (11), 719–722, **2016**. DOI `http://dx.doi.org/10.1038/nphoton.2016.163`.

[25] G. T. Reed, G. Mashanovich, F. Y. Gardes, and D. J. Thomson. “Silicon optical modulators.” *Nature Photonics* 4 (8), 518–526, **2010**. DOI `http://dx.doi.org/10.1038/nphoton.2010.179`.

[26] Z. Sun, A. Martinez, and F. Wang. “Optical modulators with 2D layered materials.” *Nature Photonics* 10 (4), 227–238, **2016**. DOI `http://dx.doi.org/10.1038/nphoton.2016.15`.

[27] L. Abdollahi Shiramin and D. Van Thourhout. “Graphene modulators and switches integrated on silicon and silicon nitride waveguide.” *IEEE Journal of Selected Topics in Quantum Electronics* 23 (1), 94–100, **2017**. DOI `http://dx.doi.org/10.1109/JSTQE.2016.2586458`.

[28] A. Govdeli, M. C. Sarihan, U. Karaca, and S. Kocaman. "Integrated optical modulator based on transition between photonic bands." *Scientific Reports* 8 (1), 1619, **2018**. DOI `http://dx.doi.org/10.1038/s41598-018-20097-7`.

[29] F. Xia, M. Rooks, L. Sekaric, and Y. Vlasov. "Ultra-compact high order ring resonator filters using submicron silicon photonic wires for on-chip optical interconnects." *Optics Express* 15 (19), 11934, **2007**. DOI `http://dx.doi.org/10.1364/OE.15.011934`.

[30] Y. Vlasov, W. M. J. Green, and F. Xia. "High-throughput silicon nanophotonic wavelength-insensitive switch for on-chip optical networks." *Nature Photonics* 2 (4), 242–246, **2008**. DOI `http://dx.doi.org/10.1038/nphoton.2008.31`.

[31] B. Redding, S. F. Liew, R. Sarma, and H. Cao. "Compact spectrometer based on a disordered photonic chip." *Nature Photonics* 7 (9), 746–751, **2013**. DOI `http://dx.doi.org/10.1038/nphoton.2013.190`.

[32] B. Shen, P. Wang, R. Polson, and R. Menon. "An integrated-nanophotonics polarization beamsplitter with 2.4 x 2.4 μm^2 footprint." *Nature Photonics* 9 (6), 378–382, **2015**. DOI `http://dx.doi.org/10.1038/nphoton.2015.80`.

[33] D. Ostrowsky, R. Poirier, L. Reiber, and C. Deverdun. "Integrated optical photodetector." *Applied Physics Letters* 22 (9), 463–464, **1973**. DOI `http://dx.doi.org/10.1063/1.1654713`.

[34] S. Assefa, F. Xia, and Y. A. Vlasov. "Reinventing germanium avalanche photodetector for nanophotonic on-chip optical interconnects." *Nature* 464 (7285), 80–84, **2010**. DOI `http://dx.doi.org/10.1038/nature08813`.

[35] X. Gan, R.-J. Shiue, Y. Gao, I. Meric, *et al.*. "Chip-integrated ultrafast graphene photodetector with high responsivity." *Nature Photonics* 7 (11), 883–887, **2013**. DOI `http://dx.doi.org/10.1038/nphoton.2013.253`.

[36] Y.-Q. Bie, G. Grosso, M. Heuck, M. M. Furchi, *et al.*. "A MoTe2-based light-emitting diode and photodetector for silicon photonic integrated circuits." *Nature Nanotechnology* 12 (12), 1124–1129, **2017**. DOI `http://dx.doi.org/10.1038/nnano.2017.209`.

[37] T. D. Ladd, F. Jelezko, R. Laflamme, Y. Nakamura, *et al.*. "Quantum computers." *Nature* 464 (7285), 45–53, **2010**. DOI `http://dx.doi.org/10.1038/nature08812`.

[38] J. L. O'Brien. "Optical quantum computing." *Science* 318 (5856), 1567–70, **2007**. DOI `http://dx.doi.org/10.1126/science.1142892`.

[39] A. Politi, M. J. Cryan, J. G. Rarity, S. Yu, *et al.*. "Silica-on-silicon waveguide quantum circuits." *Science* 320 (5876), 646–649, **2008**. DOI `http://dx.doi.org/10.1126/science.1155441`.

[40] J. C. F. Matthews, A. Politi, A. Stefanov, and J. L. O'Brien. "Manipulation of multiphoton entanglement in waveguide quantum circuits." *Nature Photonics* 3 (6), 346–350, **2009**. DOI `http://dx.doi.org/10.1038/nphoton.2009.93`.

[41] A. Politi, J. C. F. Matthews, and J. L. O'Brien. "Shor's quantum factoring algorithm on a photonic chip." *Science* 325 (5945), 1221, **2009**. DOI `http://dx.doi.org/10.1126/science.1173731`.

[42] P. Sibson, J. E. Kennard, S. Stanisic, C. Erven, *et al.*. "Integrated silicon photonics for high-speed quantum key distribution." *Optica* 4 (2), 172, **2017**. DOI http://dx.doi.org/10.1364/OPTICA.4.000172.

[43] T. Lund-Hansen, S. Stobbe, B. Julsgaard, H. Thyrrestrup, *et al.*. "Experimental realization of highly efficient broadband coupling of single quantum dots to a photonic crystal waveguide." *Physical Review Letters* 101 (11), 113903, **2008**. DOI http://dx.doi.org/10.1103/PhysRevLett.101.113903.

[44] A. Schwagmann, S. Kalliakos, I. Farrer, J. P. Griffiths, *et al.*. "On-chip single photon emission from an integrated semiconductor quantum dot into a photonic crystal waveguide." *Applied Physics Letters* 99 (26), 261108, **2011**. DOI http://dx.doi.org/10.1063/1.3672214.

[45] A. Laucht, S. Pütz, T. Günthner, N. Hauke, *et al.*. "A waveguide-coupled on-chip single-photon source." *Physical Review X* 2 (1), 011014, **2012**. DOI http://dx.doi.org/10.1103/PhysRevX.2.011014.

[46] I. E. Zadeh, A. W. Elshaari, K. D. Jöns, A. Fognini, *et al.*. "Deterministic Integration of Single Photon Sources in Silicon Based Photonic Circuits." *Nano Letters* 16 (4), 2289–2294, **2016**. DOI http://dx.doi.org/10.1021/acs.nanolett.5b04709.

[47] R. N. Patel, T. Schröder, N. Wan, L. Li, *et al.*. "Efficient photon coupling from a diamond nitrogen vacancy center by integration with silica fiber." *Light: Science & Applications* 5 (2), e16032, **2016**. DOI http://dx.doi.org/10.1038/lsa.2016.32.

[48] A. Crespi, R. Ramponi, R. Osellame, L. Sansoni, *et al.*. "Integrated photonic quantum gates for polarization qubits." *Nature Communications* 2, 566, **2011**. DOI http://dx.doi.org/10.1038/ncomms1570.

[49] Z. Lu, H. Yun, Y. Wang, Z. Chen, *et al.*. "Broadband silicon photonic directional coupler using asymmetric-waveguide based phase control." *Optics Express* 23 (3), 3795, **2015**. DOI http://dx.doi.org/10.1364/OE.23.003795.

[50] M. Poot and H. X. Tang. "Broadband nanoelectromechanical phase shifting of light on a chip." *Applied Physics Letters* 104 (6), 061101, **2014**. DOI http://dx.doi.org/10.1063/1.4864257.

[51] X. Hu, C. Holzwarth, D. Masciarelli, E. Dauler, *et al.*. "Efficiently coupling light to superconducting nanowire single-photon detectors." *IEEE Transactions on Applied Superconductivity* 19 (3), 336–340, **2009**. DOI http://dx.doi.org/10.1109/TASC.2009.2018035.

[52] J. P. Sprengers, A. Gaggero, D. Sahin, S. Jahanmirinejad, *et al.*. "Waveguide superconducting single-photon detectors for integrated quantum photonic circuits." *Applied Physics Letters* 99 (18), 181110, **2011**. DOI http://dx.doi.org/10.1063/1.3657518.

[53] W. Pernice, C. Schuck, O. Minaeva, M. Li, *et al.*. "High-speed and high-efficiency travelling wave single-photon detectors embedded in nanophotonic circuits." *Nature Communications* 3 (1), 1325, **2012**. DOI http://dx.doi.org/10.1038/ncomms2307.

[54] C. Rios, P. Hosseini, C. D. Wright, H. Bhaskaran, *et al.*. "On-chip photonic memory elements employing phase-change materials." *Advanced Materials* 26 (9), 1372–1377, **2014**. DOI http://dx.doi.org/10.1002/adma.201304476.

[55] C. Ríos, M. Stegmaier, P. Hosseini, D. Wang, *et al.*. "Integrated all-photonic non-volatile multilevel memory." *Nature Photonics* 9 (11), 725–732, **2015**. DOI http://dx.doi.org/10.1038/nphoton.2015.182.

[56] M. Stegmaier, C. Ríos, H. Bhaskaran, C. D. Wright, *et al.*. "Nonvolatile all-optical 1x2 switch for chipscale photonic networks." *Advanced Optical Materials* 5 (1), 1600346, **2017**. DOI http://dx.doi.org/10.1002/adom.201600346.

[57] J. Feldmann, M. Stegmaier, N. Gruhler, C. Ríos, *et al.*. "Calculating with light using a chip-scale all-optical abacus." *Nature Communications* 8 (1), 1256, **2017**. DOI http://dx.doi.org/10.1038/s41467-017-01506-3.

[58] Z. Cheng, C. Ríos, W. H. P. Pernice, C. D. Wright, *et al.*. "On-chip photonic synapse." *Science Advances* 3 (9), e1700160, **2017**. DOI http://dx.doi.org/10.1126/sciadv.1700160.

[59] L. Wang, S.-R. Lu, and J. Wen. "Recent advances on neuromorphic systems using phase-change materials." *Nanoscale research letters* 12 (1), 347, **2017**. DOI http://dx.doi.org/10.1186/s11671-017-2114-9.

[60] I. Chakraborty, G. Saha, A. Sengupta, and K. Roy. "All-photonic phase change spiking neuron: Toward fast neural computing using light." , **2018**. http://arxiv.org/abs/1804.00267.

[61] S. Yu, X. Wu, Y. Wang, X. Guo, *et al.*. "2D materials for optical modulation: Challenges and opportunities." *Advanced Materials* 29 (14), 1606128, **2017**. DOI http://dx.doi.org/10.1002/adma.201606128.

[62] M. Liu, X. Yin, E. Ulin-Avila, B. Geng, *et al.*. "A graphene-based broadband optical modulator." *Nature* 474 (7349), 64–7, **2011**. DOI http://dx.doi.org/10.1038/nature10067.

[63] C. T. Phare, Y.-H. Daniel Lee, J. Cardenas, and M. Lipson. "Graphene electro-optic modulator with 30 GHz bandwidth." *Nature Photonics* 9 (8), 511–514, **2015**. DOI http://dx.doi.org/10.1038/nphoton.2015.122.

[64] V. Sorianello, M. Midrio, G. Contestabile, I. Asselberghs, *et al.*. "Graphene-silicon phase modulators with gigahertz bandwidth." *Nature Photonics* 12 (1), 40–44, **2018**. DOI http://dx.doi.org/10.1038/s41566-017-0071-6.

[65] F. H. L. Koppens, T. Mueller, P. Avouris, A. C. Ferrari, *et al.*. "Photodetectors based on graphene, other two-dimensional materials and hybrid systems." *Nature Nanotechnology* 9 (10), 780–793, **2014**. DOI http://dx.doi.org/10.1038/nnano.2014.215.

[66] I. Goykhman, U. Sassi, B. Desiatov, N. Mazurski, *et al.*. "On-chip integrated, silicon-graphene plasmonic Schottky photodetector with high responsivity and avalanche photogain." *Nano Letters* 16 (5), 3005–3013, **2016**. DOI http://dx.doi.org/10.1021/acs.nanolett.5b05216.

[67] N. Youngblood, Y. Anugrah, R. Ma, S. J. Koester, *et al.*. "Multifunctional graphene optical modulator and photodetector integrated on silicon waveguides." *Nano Letters* 14 (5), 2741–2746, **2014**. DOI http://dx.doi.org/10.1021/nl500712u.

[68] P. Tonndorf, R. Schmidt, R. Schneider, J. Kern, *et al.*. "Single-photon emission from localized excitons in an atomically thin semiconductor." *Optica* 2 (4), 347, **2015**. DOI http://dx.doi.org/10.1364/OPTICA.2.000347.

[69] C. Chakraborty, L. Kinnischtzke, K. M. Goodfellow, R. Beams, *et al.*. "Voltage-controlled quantum light from an atomically thin semiconductor." *Nature Nanotechnology* 10 (6), 507–511, **2015**. DOI http://dx.doi.org/10.1038/nnano.2015.79.

[70] Y.-M. He, G. Clark, J. R. Schaibley, Y. He, *et al.*. "Single quantum emitters in monolayer semiconductors." *Nature Nanotechnology* 10 (6), 497–502, **2015**. DOI http://dx.doi.org/10.1038/nnano.2015.75.

[71] M. Koperski, K. Nogajewski, A. Arora, V. Cherkez, *et al.*. "Single photon emitters in exfoliated WSe2 structures." *Nature Nanotechnology* 10 (6), 503–506, **2015**. DOI http://dx.doi.org/10.1038/nnano.2015.67.

[72] A. Srivastava, M. Sidler, A. V. Allain, D. S. Lembke, *et al.*. "Optically active quantum dots in monolayer WSe2." *Nature Nanotechnology* 10 (6), 491–496, **2015**. DOI http://dx.doi.org/10.1038/nnano.2015.60.

[73] A. Branny, G. Wang, S. Kumar, C. Robert, *et al.*. "Discrete quantum dot like emitters in monolayer MoSe2: Spatial mapping, magneto-optics, and charge tuning." *Applied Physics Letters* 108 (14), 142101, **2016**. DOI http://dx.doi.org/10.1063/1.4945268.

[74] C. Palacios-Berraquero, M. Barbone, D. M. Kara, X. Chen, *et al.*. "Atomically thin quantum light-emitting diodes." *Nature Communications* 7, 12978, **2016**. DOI http://dx.doi.org/10.1038/ncomms12978.

[75] T. T. Tran, K. Bray, M. J. Ford, M. Toth, *et al.*. "Quantum emission from hexagonal boron nitride monolayers." *Nature Nanotechnology* 11 (1), 37–41, **2016**. DOI http://dx.doi.org/10.1038/nnano.2015.242.

[76] C. Palacios-Berraquero, D. M. Kara, A. R.-P. Montblanch, M. Barbone, *et al.*. "Large-scale quantum-emitter arrays in atomically thin semiconductors." *Nature Communications* 8, 15093, **2017**. DOI http://dx.doi.org/10.1038/ncomms15093.

[77] G. Grosso, H. Moon, B. Lienhard, S. Ali, *et al.*. "Tunable and high-purity room temperature single-photon emission from atomic defects in hexagonal boron nitride." *Nature Communications* 8 (1), 705, **2017**. DOI http://dx.doi.org/10.1038/s41467-017-00810-2.

[78] P. Tonndorf, S. Schwarz, J. Kern, I. Niehues, *et al.*. "Single-photon emitters in GaSe." *2D Materials* 4 (2), 021010, **2017**. DOI http://dx.doi.org/10.1088/2053-1583/aa525b.

[79] P. Tonndorf, O. Del Pozo-Zamudio, N. Gruhler, J. Kern, *et al.*. "On-chip waveguide coupling of a layered semiconductor single-photon source." *Nano Letters* 17 (9), 5446–5451, **2017**. DOI http://dx.doi.org/10.1021/acs.nanolett.7b02092.

[80] T. L. Nicholson, M. J. Martin, J. R. Williams, B. J. Bloom, *et al.*. "Comparison of two independent Sr optical clocks with $1x10^{-17}$ stability at 10^3s." *Physical Review Letters* 109 (23), 230801, **2012**. DOI http://dx.doi.org/10.1103/PhysRevLett.109.230801.

[81] A. D. Cronin, J. Schmiedmayer, and D. E. Pritchard. "Optics and interferometry with atoms and molecules." *Reviews of Modern Physics* 81 (3), 1051–1129, **2009**. DOI `http://dx.doi.org/10.1103/RevModPhys.81.1051`.

[82] S.-Y. Lan, P.-C. Kuan, B. Estey, P. Haslinger, *et al.*. "Influence of the Coriolis force in atom interferometry." *Physical Review Letters* 108 (9), 090402, **2012**. DOI `http://dx.doi.org/10.1103/PhysRevLett.108.090402`.

[83] Y. Bidel, O. Carraz, R. Charrière, M. Cadoret, *et al.*. "Compact cold atom gravimeter for field applications." *Applied Physics Letters* 102 (14), 144107, **2013**. DOI `http://dx.doi.org/10.1063/1.4801756`.

[84] T. Aoki, B. Dayan, E. Wilcut, W. P. Bowen, *et al.*. "Observation of strong coupling between one atom and a monolithic microresonator." *Nature* 443 (7112), 671–674, **2006**. DOI `http://dx.doi.org/10.1038/nature05147`.

[85] T. G. Tiecke, J. D. Thompson, N. P. de Leon, L. R. Liu, *et al.*. "Nanophotonic quantum phase switch with a single atom." *Nature* 508 (7495), 241–244, **2014**. DOI `http://dx.doi.org/10.1038/nature13188`.

[86] A. Goban, C.-L. Hung, S.-P. Yu, J. Hood, *et al.*. "Atom-light interactions in photonic crystals." *Nature Communications* 5, 3808, **2014**. DOI `http://dx.doi.org/10.1038/ncomms4808`.

[87] S. Haroche. "Nobel Lecture: Controlling photons in a box and exploring the quantum to classical boundary." *Reviews of Modern Physics* 85 (3), 1083–1102, **2013**. DOI `http://dx.doi.org/10.1103/RevModPhys.85.1083`.

[88] B. Clader, S. Hendrickson, R. Camacho, and B. Jacobs. "All-optical microdisk switch using EIT." *Optics Express* 21 (5), 6169, **2013**. DOI `http://dx.doi.org/10.1364/OE.21.006169`.

[89] L. Stern, M. Grajower, and U. Levy. "Fano resonances and all-optical switching in a resonantly coupled plasmonic-atomic system." *Nature Communications* 5, 4865, **2014**. DOI `http://dx.doi.org/10.1038/ncomms5865`.

[90] L. Stern, B. Desiatov, N. Mazurski, and U. Levy. "Strong coupling and high-contrast all-optical modulation in atomic cladding waveguides." *Nature Communications* 8, 14461, **2017**. DOI `http://dx.doi.org/10.1038/ncomms14461`.

[91] S. M. Hendrickson, C. N. Weiler, R. M. Camacho, P. T. Rakich, *et al.*. "All-optical-switching demonstration using two-photon absorption and the Zeno effect." *Physical Review A* 87 (2), 023808, **2013**. DOI `http://dx.doi.org/10.1103/PhysRevA.87.023808`.

[92] M. Hafezi, M. D. Lukin, and J. M. Taylor. "Non-equilibrium fractional quantum Hall state of light." *New Journal of Physics* 15 (6), 063001, **2013**. DOI `http://dx.doi.org/10.1088/1367-2630/15/6/063001`.

[93] M. Hafezi, S. Mittal, J. Fan, A. Migdall, *et al.*. "Imaging topological edge states in silicon photonics." *Nature Photonics* 7 (12), 1001–1005, **2013**. DOI `http://dx.doi.org/10.1038/nphoton.2013.274`.

[94] W. Yang, D. B. Conkey, B. Wu, D. Yin, *et al.*. "Atomic spectroscopy on a chip." *Nature Photonics* 1 (6), 331–335, **2007**. DOI http://dx.doi.org/10.1038/nphoton.2007.74.

[95] L. Stern, B. Desiatov, I. Goykhman, and U. Levy. "Nanoscale light-matter interactions in atomic cladding waveguides." *Nature Communications* 4, 1548, **2013**. DOI http://dx.doi.org/10.1038/ncomms2554.

[96] T. Schädle and B. Mizaikoff. "Mid-infrared waveguides: A perspective." *Applied Spectroscopy* 70 (10), 1625–1638, **2016**. DOI http://dx.doi.org/10.1177/0003702816659668.

[97] A. Katiyi and A. Karabchevsky. "Si nanostrip optical waveguide for on-chip broadband molecular overtone spectroscopy in near-infrared." *ACS Sensors* 3 (3), 618–623, **2018**. DOI http://dx.doi.org/10.1021/acssensors.7b00867.

[98] P. Rath, M. Hirtz, G. Lewes-Malandrakis, D. Brink, *et al.*. "Diamond nanophotonic circuits functionalized by dip-pen nanolithography." *Advanced Optical Materials* 3 (3), 328–335, **2015**. DOI http://dx.doi.org/10.1002/adom.201400434.

[99] A. M. Rijs and J. Oomens (editors). *Gas-Phase IR Spectroscopy and Structure of Biological Molecules*, vol. 364 of *Topics in Current Chemistry*. Springer International Publishing, Cham, **2015**. ISBN 9783319192031. DOI http://dx.doi.org/10.1007/978-3-319-19204-8.

[100] N. Gruhler. "Graphene-based optoelectronic devices embedded in nanophotonic circuits.", **2013**. Diploma thesis, AG Pernice, Institute of Nanotechnology, Karlsruhe Institute of Technology.

[101] N. Gruhler, C. Benz, H. Jang, J.-H. Ahn, *et al.*. "High-quality Si3N4 circuits as a platform for graphene-based nanophotonic devices." *Optics Express* 21 (25), 31678, **2013**. DOI http://dx.doi.org/10.1364/OE.21.031678.

[102] A. E. J. Lim, J. Song, Q. Fang, C. Li, *et al.*. "Review of silicon photonics foundry efforts." *IEEE Journal on Selected Topics in Quantum Electronics* 20 (4), 405–416, **2014**. DOI http://dx.doi.org/10.1109/JSTQE.2013.2293274.

[103] D. Thomson, A. Zilkie, J. E. Bowers, T. Komljenovic, *et al.*. "Roadmap on silicon photonics." *Journal of Optics* 18 (7), 073003, **2016**. DOI http://dx.doi.org/10.1088/2040-8978/18/7/073003.

[104] R. Soref and J. Lorenzo. "Single-crystal silicon: a new material for 1.3 and 1.6 μm integrated-optical components." *Electronics Letters* 21 (21), 953, **1985**. DOI http://dx.doi.org/10.1049/el:19850673.

[105] C. D. Salzberg and J. J. Villa. "Infrared refractive indexes of silicon germanium and modified selenium glass." *Journal of the Optical Society of America* 47 (3), 244, **1957**. DOI http://dx.doi.org/10.1364/JOSA.47.000244.

[106] I. H. Malitson. "Interspecimen comparison of the refractive index of fused silica." *Journal of the Optical Society of America* 55 (10), 1205, **1965**. DOI http://dx.doi.org/10.1364/JOSA.55.001205.

[107] B. Jalali, V. Raghunathan, R. Shori, S. Fathpour, *et al.*. "Prospects for silicon mid-IR Raman lasers." *IEEE Journal on Selected Topics in Quantum Electronics* 12 (6), 1618–1626, **2006**. DOI http://dx.doi.org/10.1109/JSTQE.2006.885340.

[108] G. P. Agrawal. *Fiber-optic communication systems.* Wiley series in microwave and optical engineering. Wiley-Interscience, New York, 4. edn., **2010**. ISBN 9780470505113.

[109] T. Miya, Y. Terunuma, T. Hosaka, and T. Miyashita. "Ultimate low-loss single-mode fibre at 1.55 μm." *Electronics Letters* 15 (4), 106–108, **1979**. DOI http://dx.doi.org/10.1049/el:19790077.

[110] S. V. Deshpande, E. Gulari, S. W. Brown, and S. C. Rand. "Optical properties of silicon nitride films deposited by hot filament chemical vapor deposition." *Journal of Applied Physics* 77 (12), 6534–6541, **1995**. DOI http://dx.doi.org/10.1063/1.359062.

[111] D. J. Moss, R. Morandotti, A. L. Gaeta, and M. Lipson. "New CMOS-compatible platforms based on silicon nitride and Hydex for nonlinear optics." *Nature Photonics* 7 (8), 597–607, **2013**. DOI http://dx.doi.org/10.1038/nphoton.2013.183.

[112] R. Soref and B. Bennett. "Electrooptical effects in silicon." *IEEE Journal of Quantum Electronics* 23 (1), 123–129, **1987**. DOI http://dx.doi.org/10.1109/JQE.1987.1073206.

[113] D. Dimitropoulos, R. Jhaveri, R. Claps, J. C. S. Woo, *et al.*. "Lifetime of photogenerated carriers in silicon-on-insulator rib waveguides." *Applied Physics Letters* 86 (7), 071115, **2005**. DOI http://dx.doi.org/10.1063/1.1866635.

[114] A. D. Bristow, N. Rotenberg, and H. M. van Driel. "Two-photon absorption and Kerr coefficients of silicon for 850-2200 nm." *Applied Physics Letters* 90 (19), 191104, **2007**. DOI http://dx.doi.org/10.1063/1.2737359.

[115] H. R. Philipp. "Optical properties of silicon nitride." *Journal of The Electrochemical Society* 120 (2), 295, **1973**. DOI http://dx.doi.org/10.1149/1.2403440.

[116] C. H. Henry, R. F. Kazarinov, H. J. Lee, K. J. Orlowsky, *et al.*. "Low loss Si3N4-SiO2 optical waveguides on Si." *Applied Optics* 26 (13), 2621–2624, **1987**. DOI http://dx.doi.org/10.1364/AO.26.002621.

[117] A. W. Elshaari, I. E. Zadeh, K. D. Jons, and V. Zwiller. "Thermo-optic characterization of silicon nitride resonators for cryogenic photonic circuits." *IEEE Photonics Journal* 8 (3), 1–9, **2016**. DOI http://dx.doi.org/10.1109/JPHOT.2016.2561622.

[118] A. Arbabi and L. L. Goddard. "Measurements of the refractive indices and thermo-optic coefficients of Si3N4 and SiOx using microring resonances." *Optics Letters* 38 (19), 3878, **2013**. DOI http://dx.doi.org/10.1364/OL.38.003878.

[119] J. Komma, C. Schwarz, G. Hofmann, D. Heinert, *et al.*. "Thermo-optic coefficient of silicon at 1550 nm and cryogenic temperatures." *Applied Physics Letters* 101 (4), 041905, **2012**. DOI http://dx.doi.org/10.1063/1.4738989.

[120] W. Stutius and W. Streifer. "Silicon nitride films on silicon for optical waveguides." *Applied Optics* 16 (12), 3218, **1977**. DOI http://dx.doi.org/10.1364/AO.16.003218.

[121] K. Ikeda, R. E. Saperstein, N. Alic, and Y. Fainman. “Thermal and Kerr nonlinear properties of plasma-deposited silicon nitride / silicon dioxide waveguides.” *Optics Express* 16 (17), 12987, **2008**. DOI http://dx.doi.org/10.1364/OE.16.012987.

[122] J. S. Levy, A. Gondarenko, M. A. Foster, A. C. Turner-Foster, *et al.*. “CMOS-compatible multiple-wavelength oscillator for on-chip optical interconnects.” *Nature Photonics* 4 (1), 37, **2009**. DOI http://dx.doi.org/10.1038/nphoton.2009.259.

[123] R. W. Boyd. *Nonlinear optics*. Elsevier, Academic Press, Amsterdam, 3. edn., **2008**. ISBN 9780123694706.

[124] P. Del Haye, A. Schliesser, O. Arcizet, T. Wilkins, *et al.*. “Optical frequency comb generation from a monolithic microresonator.” *Nature* 450 (7173), 1214–7, **2007**. DOI http://dx.doi.org/10.1038/nature06401.

[125] T. J. Kippenberg, R. Holzwarth, and S. A. Diddams. “Microresonator-based optical frequency combs.” *Science* 332 (6029), 555–559, **2011**. DOI http://dx.doi.org/10.1126/science.1193968.

[126] J. Pfeifle, V. Brasch, M. Lauermann, Y. Yu, *et al.*. “Coherent terabit communications with microresonator Kerr frequency combs.” *Nat Photon* 8 (5), 375–380, **2013**. DOI http://dx.doi.org/10.1038/NPHOTON.2014.57.

[127] P. Marin-Palomo, J. N. Kemal, M. Karpov, A. Kordts, *et al.*. “Microresonator solitons for massively parallel coherent optical communications.” *Nature* 546 (7657), 274–279, **2016**. DOI http://dx.doi.org/10.1038/nature22387.

[128] K. Kao and G. Hockham. “Dielectric-fibre surface waveguides for optical frequencies.” *Proceedings of the Institution of Electrical Engineers* 113 (7), 1151–1158, **1966**. DOI http://dx.doi.org/10.1049/piee.1966.0189.

[129] S. Kumar and M. J. Deen. *Fiber Optic Communications: Fundamentals and Applications*. John Wiley & Sons, Ltd, Chichester, UK, **2014**. ISBN 9781118684207. DOI http://dx.doi.org/10.1002/9781118684207.

[130] J.-M. Liu. *Photonic devices*. Cambridge, **2005**. ISBN 0521551951.

[131] K. Okamoto. *Fundamentals of optical waveguides*. Elsevier; AP, Amsterdam, 2. edn., **2006**. ISBN 0125250967.

[132] A. Yariv and P. Yeh. *Photonics: optical electronics in modern communications*. Oxford University Press, New York, NY [u.a.], 6. edn., **2007**. ISBN 0195179463.

[133] B. E. A. Saleh and M. C. Teich. *Fundamentals of photonics*. Wiley, Hoboken, N.J., 2. edn., **2007**. ISBN 9780471358329.

[134] A. Matsko. *Practical Applications of Microresonators in Optics and Photonics*. CRC Press, Boca Raton, **2009**. ISBN 9781420065787. DOI http://dx.doi.org/10.1201/9781420065794.

[135] G. Gagliardi and H.-P. Loock. *Cavity-enhanced spectroscopy and sensing*. Springer, Berlin, Heidelberg, **2014**. ISBN 9783642400025. DOI http://dx.doi.org/10.1007/978-3-642-40003-2.

[136] P. Grelu. *Nonlinear optical cavity dynamics: from microresonators to fiber lasers.* Wiley, Hoboken, N.J., **2016**. ISBN 3527413324.

[137] C. Reimer, L. Caspani, M. Clerici, M. Ferrera, *et al.*. "Integrated frequency comb source of heralded single photons." *Optics Express* 22 (6), 6535, **2014**. DOI `http://dx.doi.org/10.1364/OE.22.006535`.

[138] J. Leuthold, C. Koos, and W. Freude. "Nonlinear silicon photonics." *Nature Photonics* 4 (8), 535–544, **2010**. DOI `http://dx.doi.org/10.1038/nphoton.2010.185`.

[139] X. Guo, C.-l. Zou, C. Schuck, H. Jung, *et al.*. "Parametric down-conversion photon-pair source on a nanophotonic chip." *Light: Science & Applications* 6 (5), e16249, **2016**. DOI `http://dx.doi.org/10.1038/lsa.2016.249`.

[140] E. M. Purcell. "Spontaneous emission probabilities at radio frequencies." In *Physical Review*, vol. 69, 839–839, **1946**. ISBN 0031-899X. DOI `http://dx.doi.org/10.1007/978-1-4615-1963-8_40`.

[141] F. Pyatkov, V. Fütterling, S. Khasminskaya, B. S. Flavel, *et al.*. "Cavity-enhanced light emission from electrically driven carbon nanotubes." *Nature Photonics* 10 (6), 420–427, **2016**. DOI `http://dx.doi.org/10.1038/nphoton.2016.70`.

[142] T. J. Kippenberg and K. J. Vahala. "Cavity opto-mechanics." *Optics Express* 15 (25), 17172, **2007**. DOI `http://dx.doi.org/10.1364/OE.15.017172`.

[143] K. Hennessy, A. Badolato, M. Winger, D. Gerace, *et al.*. "Quantum nature of a strongly coupled single quantum dot-cavity system." *Nature* 445 (7130), 896–9, **2007**. DOI `http://dx.doi.org/10.1038/nature05586`.

[144] H. Walther, B. T. H. Varcoe, B.-G. Englert, and T. Becker. "Cavity quantum electrodynamics." *Reports on Progress in Physics* 69 (5), 1325–1382, **2006**. DOI `http://dx.doi.org/10.1088/0034-4885/69/5/R02`.

[145] C. Hood, H. Kimble, and J. Ye. "Characterization of high-finesse mirrors: Loss, phase shifts, and mode structure in an optical cavity." *Physical Review A* 64 (3), 033804, **2001**. DOI `http://dx.doi.org/10.1103/PhysRevA.64.033804`.

[146] O. Painter. "Two-dimensional photonic band-gap defect mode laser." *Science* 284 (5421), 1819–1821, **1999**. DOI `http://dx.doi.org/10.1126/science.284.5421.1819`.

[147] Y. Akahane, T. Asano, B.-S. Song, and S. Noda. "Erratum: High-Q photonic nanocavity in a two-dimensional photonic crystal." *Nature* 425 (6961), 944–947, **2003**. DOI `http://dx.doi.org/10.1038/nature02063`.

[148] K. Busch (editor). *Photonic crystals: advances in design, fabrication, and characterization.* Wiley, Weinheim, **2004**. ISBN 352760717X.

[149] K. J. Vahala. "Optical microcavities." *Nature* 424 (6950), 839–46, **2003**. DOI `http://dx.doi.org/10.1038/nature01939`.

[150] D. W. Vernooy, V. S. Ilchenko, H. Mabuchi, E. W. Streed, *et al.*. "High-Q measurements of fused-silica microspheres in the near infrared." *Optics Letters* 23 (4), 247, **1998**. DOI http://dx.doi.org/10.1364/OL.23.000247.

[151] B. Gayral, J. M. Gérard, A. Lemaître, C. Dupuis, *et al.*. "High- Q wet-etched GaAs microdisks containing InAs quantum boxes." *Applied Physics Letters* 75 (13), 1908–1910, **1999**. DOI http://dx.doi.org/10.1063/1.124894.

[152] D. K. Armani, T. J. Kippenberg, S. M. Spillane, and K. J. Vahala. "Ultra-high-Q toroid microcavity on a chip." *Nature* 421 (6926), 925–928, **2003**. DOI http://dx.doi.org/10.1038/nature01371.

[153] D. G. Rabus. *Integrated ring resonators: the compendium.* Springer, Berlin, Heidelberg, **2007**. ISBN 9783540687887.

[154] S. Ramo, J. R. Whinnery, and T. Van Duzer. *Fields and waves in communication electronics.* Wiley, New York [u.a.], **1965**. ISBN 0471707201.

[155] A. Yariv. *Quantum electronics.* Wiley, New York [u.a.], 3. edn., **1989**. ISBN 0471609978.

[156] M. L. Gorodetsky and V. S. Ilchenko. "Thermal nonlinear effects in optical whispering-gallery microresonators." *Laser Physics* 2 (6), 1004–1009, **1992**.

[157] D. S. Weiss, V. Sandoghdar, J. Hare, V. Lefèvre-Seguin, *et al.*. "Splitting of high-Q Mie modes induced by light backscattering in silica microspheres." *Optics Letters* 20 (18), 1835, **1995**. DOI http://dx.doi.org/10.1364/OL.20.001835.

[158] M. L. Gorodetsky, A. D. Pryamikov, and V. S. Ilchenko. "Rayleigh scattering in high-Q microspheres." *Journal of the Optical Society of America B* 17 (6), 1051, **2000**. DOI http://dx.doi.org/10.1364/JOSAB.17.001051.

[159] J. Čtyroký, I. Richter, and M. Šiňor. "Dual resonance in a waveguide-coupled ring microresonator." *Optical and Quantum Electronics* 38 (9-11), 781–797, **2007**. DOI http://dx.doi.org/10.1007/s11082-006-9037-5.

[160] M. Borselli, T. J. Johnson, and O. Painter. "Accurate measurement of scattering and absorption loss in microphotonic devices." *Optics Letters* 32 (20), 2954, **2007**. DOI http://dx.doi.org/10.1364/OL.32.002954.

[161] N. C. Harris, Y. Ma, J. Mower, T. Baehr-Jones, *et al.*. "Efficient, compact and low loss thermo-optic phase shifter in silicon." *Optics Express* 22 (9), 10487, **2014**. DOI http://dx.doi.org/10.1364/OE.22.010487.

[162] A. P. Ovvyan, N. Gruhler, S. Ferrari, and W. H. P. Pernice. "Cascaded Mach-Zehnder interferometer tunable filters." *Journal of Optics* 18 (6), 064011, **2016**. DOI http://dx.doi.org/10.1088/2040-8978/18/6/064011.

[163] M. Li, H. X. Tang, and M. L. Roukes. "Ultra-sensitive NEMS-based cantilevers for sensing, scanned probe and very high-frequency applications." *Nature Nanotechnology* 2 (2), 114–120, **2007**. DOI http://dx.doi.org/10.1038/nnano.2006.208.

[164] X. Sun, K. Y. Fong, C. Xiong, W. H. P. Pernice, *et al.*. "GHz optomechanical resonators with high mechanical Q factor in air." *Optics Express* 19 (22), 22316, **2011**. DOI http://dx.doi.org/10.1364/OE.19.022316.

[165] P. Rath, S. Khasminskaya, C. Nebel, C. Wild, *et al.*. "Diamond-integrated optomechanical circuits." *Nature Communications* 4, 1690, **2013**. DOI http://dx.doi.org/10.1038/ncomms2710.

[166] M. Izutsu, Y. Nakai, and T. Sueta. "Operation mechanism of the single-mode optical-waveguide Y junction." *Optics letters* 7 (3), 136–8, **1982**. DOI http://dx.doi.org/10.1364/OL.7.000136.

[167] I. Anderson. "Transmission performance of Y-junctions in planar dielectric waveguide." *Microwaves, Optics and Acoustics, IEE Journal on* 2 (1), 7–, **1978**. DOI http://dx.doi.org/10.1049/ij-moa.1978.0002.

[168] H. Yajima. "Coupled-mode analysis of anisotropic dielectric planar branching waveguides." *Journal of Lightwave Technology* 1 (1), 273–279, **1983**. DOI http://dx.doi.org/10.1109/JLT.1983.1072081.

[169] L. Soldano and E. Pennings. "Optical multi-mode interference devices based on self-imaging: principles and applications." *Journal of Lightwave Technology* 13 (4), 615–627, **1995**. DOI http://dx.doi.org/10.1109/50.372474.

[170] P. Besse, E. Gini, M. Bachmann, and H. Melchior. "New 2x2 and 1x3 multimode interference couplers with free selection of power splitting ratios." *Journal of Lightwave Technology* 14 (10), 2286–2293, **1996**. DOI http://dx.doi.org/10.1109/50.541220.

[171] D. Bonneau, E. Engin, K. Ohira, N. Suzuki, *et al.*. "Quantum interference and manipulation of entanglement in silicon wire waveguide quantum circuits." *New Journal of Physics* 14 (4), 045003, **2012**. DOI http://dx.doi.org/10.1088/1367-2630/14/4/045003.

[172] E. A. J. Marcatili. "Dielectric rectangular waveguide and directional coupler for integrated optics." *Bell System Technical Journal* 48 (7), 2071–2102, **1969**. DOI http://dx.doi.org/10.1002/j.1538-7305.1969.tb01166.x.

[173] M. Stegmaier and W. H. P. Pernice. "Broadband directional coupling in aluminum nitride nanophotonic circuits." *Optics Express* 21 (6), 7304, **2013**. DOI http://dx.doi.org/10.1364/OE.21.007304.

[174] V. R. Almeida, Q. Xu, C. A. Barrios, and M. Lipson. "Guiding and confining light in void nanostructure." *Optics Letters* 29 (11), 1209, **2004**. DOI http://dx.doi.org/10.1364/OL.29.001209.

[175] Q. Xu, V. R. Almeida, R. R. Panepucci, and M. Lipson. "Experimental demonstration of guiding and confining light in nanometer-size low-refractive-index material." *Optics Letters* 29 (14), 1626, **2004**. DOI http://dx.doi.org/10.1364/OL.29.001626.

[176] J. T. Robinson, C. Manolatou, L. Chen, and M. Lipson. "Ultrasmall mode volumes in dielectric optical microcavities." *Physical Review Letters* 95 (14), 143901, **2005**. DOI http://dx.doi.org/10.1103/PhysRevLett.95.143901.

[177] Y. C. Jun, R. M. Briggs, H. A. Atwater, and M. L. Brongersma. "Broadband enhancement of light emission in silicon slot waveguides." *Optics Express* 17 (9), 7479, **2009**. DOI http://dx.doi.org/10.1364/OE.17.007479.

[178] Q. Quan, I. Bulu, and M. Lončar. "Broadband waveguide QED system on a chip." *Physical Review A* 80 (1), 011810, **2009**. DOI http://dx.doi.org/10.1103/PhysRevA.80.011810.

[179] T. Baehr-Jones, M. Hochberg, C. Walker, and A. Scherer. "High-Q optical resonators in silicon-on-insulator-based slot waveguides." *Applied Physics Letters* 86 (8), 081101, **2005**. DOI http://dx.doi.org/10.1063/1.1871360.

[180] S. Xiao, M. H. Khan, H. Shen, and M. Qi. "Compact silicon microring resonators with ultra-low propagation loss in the C band." *Optics Express* 15 (22), 14467, **2007**. DOI http://dx.doi.org/10.1364/OE.15.014467.

[181] G. Li, J. Yao, H. Thacker, A. Mekis, *et al.*. "Ultralow-loss, high-density SOI optical waveguide routing for macrochip interconnects." *Optics Express* 20 (11), 12035, **2012**. DOI http://dx.doi.org/10.1364/OE.20.012035.

[182] J. Schindelin, I. Arganda-Carreras, E. Frise, V. Kaynig, *et al.*. "Fiji: an open-source platform for biological-image analysis." *Nature Methods* 9 (7), 676–682, **2012**. DOI http://dx.doi.org/10.1038/nmeth.2019.

[183] H. J. Levinson. *Principles of lithography.* Spie Press, Bellingham, WA, 3. edn., **2010**. ISBN 9780819483249.

[184] T. Ito and S. Okazaki. "Pushing the limits of lithography." *Nature* 406 (6799), 1027–1031, **2000**. DOI http://dx.doi.org/10.1038/35023233.

[185] C. Wagner and N. Harned. "EUV lithography: Lithography gets extreme." *Nature Photonics* 4 (1), 24–26, **2010**. DOI http://dx.doi.org/10.1038/nphoton.2009.251.

[186] C. Vieu, F. Carcenac, A. Pépin, Y. Chen, *et al.*. "Electron beam lithography: resolution limits and applications." *Applied Surface Science* 164 (1-4), 111–117, **2000**. DOI http://dx.doi.org/10.1016/S0169-4332(00)00352-4.

[187] Huiming Bu. "5 nanometer transistors inching their way into chips.", **2017**. URL https://www.ibm.com/blogs/think/2017/06/5-nanometer-transistors/, Accessed 2018/10/04.

[188] Z. Cui. *Nanofabrication: Principles, capabilities and limits.* Springer, Cham, 2. edn., **2017**. ISBN 9783319393612.

[189] H. Elsner and H.-G. Meyer. "Nanometer and high aspect ratio patterning by electron beam lithography using a simple DUV negative tone resist." *Microelectronic Engineering* 57-58, 291–296, **2001**. DOI http://dx.doi.org/10.1016/S0167-9317(01)00498-1.

[190] B.-Y. Zong, G.-C. Han, Y.-K. Zheng, L.-H. An, *et al.*. "A general approach to semimetallic, ultra-high-resolution, electron-beam resists." *Advanced Functional Materials* 19 (9), 1437–1443, **2009**. DOI http://dx.doi.org/10.1002/adfm.200800939.

[191] M. Parikh. “Corrections to proximity effects in electron beam lithography. I. Theory.” *Journal of Applied Physics* 50 (6), 4371–4377, **1979**. DOI http://dx.doi.org/10.1063/1.326423.

[192] M. Stepanova and S. Dew. *Nanofabrication: Techniques and Principles*. Springer, Vienna, **2012**. ISBN 9783709104231. DOI http://dx.doi.org/10.1007/978-3-7091-0424-8.

[193] S. J. Wind. “Accuracy and efficiency in electron beam proximity effect correction.” *Journal of Vacuum Science & Technology B: Microelectronics and Nanometer Structures* 16 (6), 3262, **1998**. DOI http://dx.doi.org/10.1116/1.590361.

[194] A. Gondarenko, J. S. Levy, and M. Lipson. “High confinement micron-scale silicon nitride high Q ring resonator.” *Optics Express* 17 (14), 11366, **2009**. DOI http://dx.doi.org/10.1364/OE.17.011366.

[195] J. W. Coburn and H. F. Winters. “Ion- and electron-assisted gas-surface chemistry - An important effect in plasma etching.” *Journal of Applied Physics* 50 (5), 3189, **1979**. DOI http://dx.doi.org/10.1063/1.326355.

[196] L. Zimmermann, T. Tekin, H. Schroeder, P. Dumon, *et al.*. “How to bring nanophotonics to application - silicon photonics packaging.” *IEEE LEOS Newsletter* 22 (6), 4–14, **2008**.

[197] D. Taillaert, P. Bienstman, and R. Baets. “Compact efficient broadband grating coupler for silicon-on-insulator waveguides.” *Optics Letters* 29 (23), 2749, **2004**. DOI http://dx.doi.org/10.1364/OL.29.002749.

[198] W. K. Burns and G. B. Hocker. “End fire coupling between optical fibers and diffused channel waveguides.” *Applied Optics* 16 (8), 2048, **1977**. DOI http://dx.doi.org/10.1364/AO.16.002048.

[199] S. McNab, N. Moll, and Y. Vlasov. “Ultra-low loss photonic integrated circuit with membrane-type photonic crystal waveguides.” *Optics Express* 11 (22), 2927, **2003**. DOI http://dx.doi.org/10.1364/OE.11.002927.

[200] S. Mahdi, M. Grehn, A. Al-Saadi, M. Höfner, *et al.*. “Facet preparation of silicol nano-waveguides by cleaving the SOI chip.” *Journal of Nonlinear Optical Physics & Materials* 20 (04), 509–523, **2011**. DOI http://dx.doi.org/10.1142/S0218863511006315.

[201] D. Sarid. “High efficiency input-output prism waveguide coupler: an analysis.” *Applied Optics* 18 (17), 2921, **1979**. DOI http://dx.doi.org/10.1364/AO.18.002921.

[202] S. Saavedra and W. Reichert. “Prism coupling into polymer integrated optical waveguides with liquid superstrates.” *Applied Spectroscopy* 44 (7), 1210, **1990**. URL https://www.osapublishing.org/as/abstract.cfm?URI=as-44-7-1210.

[203] M. L. Dakss, L. Kuhn, P. F. Heidrich, and B. A. Scott. “Grating coupler for efficient excitation of optical guided waves in thin films.” *Applied Physics Letters* 16 (12), 523, **1970**. DOI http://dx.doi.org/10.1063/1.1653091.

[204] D. Taillaert, W. Bogaerts, P. Bienstman, T. Krauss, *et al.*. “An out-of-plane grating coupler for efficient butt-coupling between compact planar waveguides and single-mode fibers.” *Quantum Electronics, IEEE Journal of* 38 (7), 949–955, **2002**. DOI http://dx.doi.org/10.1109/JQE.2002.1017613.

[205] D. Taillaert, F. Van Laere, M. Ayre, W. Bogaerts, *et al.*. "Grating couplers for coupling between optical fibers and nanophotonic waveguides." *Japanese Journal of Applied Physics* 45 (8A), 6071–6077, **2006**. DOI http://dx.doi.org/10.1143/JJAP.45.6071.

[206] C. R. Doerr, L. Chen, Y.-K. Chen, and L. L. Buhl. "Wide bandwidth silicon nitride grating coupler." *IEEE Photonics Technology Letters* 22 (19), 1461–1463, **2010**. DOI http://dx.doi.org/10.1109/LPT.2010.2062497.

[207] A. Landowski, D. Zepp, S. Wingerter, G. von Freymann, *et al.*. "Direct laser written polymer waveguides with out of plane couplers for optical chips." *APL Photonics* 2 (10), 106102, **2017**. DOI http://dx.doi.org/10.1063/1.4994806.

[208] M. Schumann, T. Bückmann, N. Gruhler, M. Wegener, *et al.*. "Hybrid 2D-3D optical devices for integrated optics by direct laser writing." *Light: Science & Applications* 3 (6), 175, **2014**. DOI http://dx.doi.org/10.1038/lsa.2014.56.

[209] N. Lindenmann, G. Balthasar, D. Hillerkuss, R. Schmogrow, *et al.*. "Photonic wire bonding: a novel concept for chip-scale interconnects." *Optics Express* 20 (16), 17667, **2012**. DOI http://dx.doi.org/10.1364/OE.20.017667.

[210] S. E. Miller. "Coupled wave theory and waveguide applications." *Bell System Technical Journal* 33 (3), 661–719, **1954**. DOI http://dx.doi.org/10.1002/j.1538-7305.1954.tb02359.x.

[211] M. Antelius, K. B. Gylfason, and H. Sohlström. "An apodized SOI waveguide-to-fiber surface grating coupler for single lithography silicon photonics." *Optics Express* 19 (4), 3592, **2011**. DOI http://dx.doi.org/10.1364/OE.19.003592.

[212] X. Chen, C. Li, C. K. Y. Fung, S. M. G. Lo, *et al.*. "Apodized waveguide grating couplers for efficient coupling to optical fibers." *IEEE Photonics Technology Letters* 22 (15), 1156–1158, **2010**. DOI http://dx.doi.org/10.1109/LPT.2010.2051220.

[213] G. Roelkens, D. V. Thourhout, and R. Baets. "High efficiency grating coupler between silicon-on-insulator waveguides and perfectly vertical optical fibers." *Optics Letters* 32 (11), 1495, **2007**. DOI http://dx.doi.org/10.1364/OL.32.001495.

[214] D. Vermeulen, S. Selvaraja, P. Verheyen, G. Lepage, *et al.*. "High-efficiency fiber-to-chip grating couplers realized using an advanced CMOS-compatible Silicon-On-Insulator platform." *Optics Express* 18 (17), 18278, **2010**. DOI http://dx.doi.org/10.1364/OE.18.018278.

[215] T. Alasaarela, D. Korn, L. Alloatti, A. Säynätjoki, *et al.*. "Reduced propagation loss in silicon strip and slot waveguides coated by atomic layer deposition." *Optics Express* 19 (12), 11529, **2011**. DOI http://dx.doi.org/10.1364/OE.19.011529.

[216] F. Ay and A. Aydinli. "Comparative investigation of hydrogen bonding in silicon based PECVD grown dielectrics for optical waveguides." *Optical Materials* 26 (1), 33–46, **2004**. DOI http://dx.doi.org/10.1016/J.OPTMAT.2003.12.004.

[217] J. Bauters, M. Heck, D. John, D. Dai, *et al.*. "Ultra-low-loss high-aspect-ratio Si3N4 wavequides." *Optics express* 19 (4), 3163–3174, **2011**. DOI http://dx.doi.org/10.1364/OE.19.003163.

[218] M.-C. Tien, J. F. Bauters, M. J. R. Heck, D. T. Spencer, *et al.*. "Ultra-high quality factor planar Si3N4 ring resonators on Si substrates." *Optics express* 19 (14), 13551–6, **2011**. DOI http://dx.doi.org/10.1364/OE.19.013551.

[219] D. T. Spencer, J. F. Bauters, M. J. R. Heck, and J. E. Bowers. "Integrated waveguide coupled Si3N4 resonators in the ultrahigh-Q regime." *Optica* 1 (3), 153, **2014**. DOI http://dx.doi.org/10.1364/OPTICA.1.000153.

[220] K. Luke, A. Dutt, C. B. Poitras, and M. Lipson. "Overcoming Si3N4 film stress limitations for high quality factor ring resonators." *Optics Express* 21 (19), 22829, **2013**. DOI http://dx.doi.org/10.1364/OE.21.022829.

[221] Q. Li, A. A. Eftekhar, M. Sodagar, Z. Xia, *et al.*. "Vertical integration of high-Q silicon nitride microresonators into silicon-on-insulator platform." *Optics Express* 21 (15), 18236, **2013**. DOI http://dx.doi.org/10.1364/OE.21.018236.

[222] Y. Xuan, Y. Liu, L. T. Varghese, A. J. Metcalf, *et al.*. "High-Q silicon nitride microresonators exhibiting low-power frequency comb initiation." *Optica* 3 (11), 1171, **2016**. DOI http://dx.doi.org/10.1364/OPTICA.3.001171.

[223] X. Cheng, J. Hong, A. M. Spring, and S. Yokoyama. "Fabrication of a high-Q factor ring resonator using LSCVD deposited Si3N4 film." *Optical Materials Express* 7 (7), 2182, **2017**. DOI http://dx.doi.org/10.1364/OME.7.002182.

[224] J.-C. Tinguely, Ø. I. Helle, and B. S. Ahluwalia. "Silicon nitride waveguide platform for fluorescence microscopy of living cells." *Optics Express* 25 (22), 27678, **2017**. DOI http://dx.doi.org/10.1364/OE.25.027678.

[225] A. Gorin, A. Jaouad, E. Grondin, V. Aimez, *et al.*. "Fabrication of silicon nitride waveguides for visible-light using PECVD: a study of the effect of plasma frequency on optical properties." *Optics Express* 16 (18), 13509, **2008**. DOI http://dx.doi.org/10.1364/OE.16.013509.

[226] A. Z. Subramanian, P. Neutens, A. Dhakal, R. Jansen, *et al.*. "Low-Loss Singlemode PECVD Silicon Nitride Photonic Wire Waveguides for 532-900nm Wavelength Window Fabricated Within a CMOS Pilot Line." *IEEE Photonics Journal* 5 (6), 2202809, **2013**. DOI http://dx.doi.org/10.1109/JPHOT.2013.2292698.

[227] E. Shah Hosseini, S. Yegnanarayanan, M. Soltani, and A. Adibi. "Ultra-High Quality Factor Microdisk Resonators for Chip-Scale Visible Integrated Photonics." In *Frontiers in Optics 2008*. OSA, Washington, D.C., **2008**. ISBN 9781557528612. DOI http://dx.doi.org/10.1364/FIO.2008.FMG4.

[228] E. Shah Hosseini, S. Yegnanarayanan, A. H. Atabaki, M. Soltani, *et al.*. "High quality planar silicon nitride microdisk resonators for integrated photonics in the visible wavelength range." *Optics Express* 17 (17), 14543, **2009**. DOI http://dx.doi.org/10.1364/OE.17.014543.

[229] R. Ritter, N. Gruhler, W. Pernice, H. Kübler, *et al.*. "Atomic vapor spectroscopy in integrated photonic structures." *Applied Physics Letters* 107 (4), 041101, **2015**. DOI http://dx.doi.org/10.1063/1.4927172.

[230] R. Ritter, N. Gruhler, W. H. P. Pernice, H. Kübler, *et al.*. "Coupling thermal atomic vapor to an integrated ring resonator." *New Journal of Physics* 18 (10), 103031, **2016**. DOI `http://dx.doi.org/10.1088/1367-2630/18/10/103031`.

[231] R. Ritter, N. Gruhler, H. Dobbertin, H. Kübler, *et al.*. "Coupling thermal atomic vapor to slot waveguides." *Physical Review X* 8 (2), 021032, **2018**. DOI `http://dx.doi.org/10.1103/PhysRevX.8.021032`.

[232] J. Meija, T. B. Coplen, M. Berglund, W. A. Brand, *et al.*. "Isotopic compositions of the elements 2013 (IUPAC Technical Report)." *Pure and Applied Chemistry* 88 (3), 293–306, **2016**. DOI `http://dx.doi.org/10.1515/pac-2015-0503`.

[233] J. R. Rumble, David R. Lide, and Thomas J. Bruno. *CRC handbook of chemistry and physics: a ready-reference book of chemical and physical data.* CRC Press, Boca Raton, 98 edn., **2017**. ISBN 9781498784542.

[234] H. Haken and H. C. Wolf. *The physics of atoms and quanta: introduction to experiments and theory.* Springer, Berlin, 7 edn., **2005**. ISBN 9783540208075.

[235] I. V. Hertel and C.-P. Schulz. *Atome, Moleküle und optische Physik 1: Atome und Grundlagen ihrer Spektroskopie.* Springer Spektrum, Berlin, Heidelberg, 2 edn., **2017**. ISBN 9783662531044.

[236] H. Friedrich. *Theoretical atomic physics.* Springer, Cham, 4 edn., **2017**. ISBN 9783319477695.

[237] D. A. Steck. "Rubidium 85 D line data." Available online at `http://steck.us/alkalidata` (revision 2.1.6, 20 September 2013).

[238] D. A. Steck. "Rubidium 87 D line data." Available online at `http://steck.us/alkalidata` (revision 2.1.5, 13 January 2015).

[239] E. Arimondo, M. Inguscio, and P. Violino. "Experimental determinations of the hyperfine structure in the alkali atoms." *Reviews of Modern Physics* 49 (1), 31–75, **1977**. DOI `http://dx.doi.org/10.1103/RevModPhys.49.31`.

[240] G. P. Barwood, P. Gill, and W. R. C. Rowley. "Frequency measurements on optically narrowed Rb-stabilised laser diodes at 780 nm and 795 nm." *Applied Physics B Photophysics and Laser Chemistry* 53 (3), 142–147, **1991**. DOI `http://dx.doi.org/10.1007/BF00330229`.

[241] J. Ye, S. Swartz, P. Jungner, and J. L. Hall. "Hyperfine structure and absolute frequency of the 87Rb 5P3/2 state." *Optics Letters* 21 (16), 1280, **1996**. DOI `http://dx.doi.org/10.1364/OL.21.001280`.

[242] S. Bize, Y. Sortais, M. S. Santos, C. Mandache, *et al.*. "High-accuracy measurement of the 87Rb ground-state hyperfine splitting in an atomic fountain." *Europhysics Letters (EPL)* 45 (5), 558–564, **1999**. DOI `http://dx.doi.org/10.1209/epl/i1999-00203-9`.

[243] S. Haroche and J.-M. Raimond. "Cavity quantum electrodynamics." *Scientific American* 268 (4), 54–62, **1993**. DOI `http://dx.doi.org/10.1038/scientificamerican0493-54`.

[244] H. J. Kimble. "Strong interactions of single atoms and photons in cavity QED." *Physica Scripta* T76 (1), 127, **1998**. DOI `http://dx.doi.org/10.1238/Physica.Topical.076a00127`.

[245] L. Essen and J. V. L. Parry. “An atomic standard of frequency and time interval: A caesium resonator.” *Nature* 176 (4476), 280–282, **1955**. DOI `http://dx.doi.org/10.1038/176280a0`.

[246] N. Ashby, T. E. Parker, and B. R. Patla. “A null test of general relativity based on a long-term comparison of atomic transition frequencies.” *Nature Physics* 1, **2018**. DOI `http://dx.doi.org/10.1038/s41567-018-0156-2`.

[247] K. M. Birnbaum, A. Boca, R. Miller, A. D. Boozer, *et al.*. “Photon blockade in an optical cavity with one trapped atom.” *Nature* 436 (7047), 87–90, **2005**. DOI `http://dx.doi.org/10.1038/nature03804`.

[248] A. Gaëtan, Y. Miroshnychenko, T. Wilk, A. Chotia, *et al.*. “Observation of collective excitation of two individual atoms in the Rydberg blockade regime.” *Nature Physics* 5 (2), 115–118, **2009**. DOI `http://dx.doi.org/10.1038/nphys1183`.

[249] E. Urban, T. A. Johnson, T. Henage, L. Isenhower, *et al.*. “Observation of Rydberg blockade between two atoms.” *Nature Physics* 5 (2), 110–114, **2009**. DOI `http://dx.doi.org/10.1038/nphys1178`.

[250] D. Jaksch, J. I. Cirac, P. Zoller, S. L. Rolston, *et al.*. “Fast quantum gates for neutral atoms.” *Physical Review Letters* 85 (10), 2208–2211, **2000**. DOI `http://dx.doi.org/10.1103/PhysRevLett.85.2208`.

[251] M. D. Lukin, M. Fleischhauer, R. Cote, L. M. Duan, *et al.*. “Dipole blockade and quantum information processing in mesoscopic atomic ensembles.” *Physical Review Letters* 87 (3), 037901, **2001**. DOI `http://dx.doi.org/10.1103/PhysRevLett.87.037901`.

[252] M. S. Safronova, C. J. Williams, and C. W. Clark. “Optimizing the fast Rydberg quantum gate.” *Physical Review A* 67 (4), 040303, **2003**. DOI `http://dx.doi.org/10.1103/PhysRevA.67.040303`.

[253] M. Saffman and T. G. Walker. “Analysis of a quantum logic device based on dipole-dipole interactions of optically trapped Rydberg atoms.” *Physical Review A* 72 (2), 022347, **2005**. DOI `http://dx.doi.org/10.1103/PhysRevA.72.022347`.

[254] M. Saffman and T. G. Walker. “Entangling single- and N -atom qubits for fast quantum state detection and transmission.” *Physical Review A* 72 (4), 042302, **2005**. DOI `http://dx.doi.org/10.1103/PhysRevA.72.042302`.

[255] E. Brion, A. S. Mouritzen, and K. Mølmer. “Conditional dynamics induced by new configurations for Rydberg dipole-dipole interactions.” *Physical Review A* 76 (2), 022334, **2007**. DOI `http://dx.doi.org/10.1103/PhysRevA.76.022334`.

[256] S. Du, M. B. Squires, Y. Imai, L. Czaia, *et al.*. “Atom-chip Bose-Einstein condensation in a portable vacuum cell.” *Physical Review A* 70 (5), 053606, **2004**. DOI `http://dx.doi.org/10.1103/PhysRevA.70.053606`.

[257] G. Bison, N. Castagna, A. Hofer, P. Knowles, *et al.*. “A room temperature 19-channel magnetic field mapping device for cardiac signals.” *Applied Physics Letters* 95 (17), 173701, **2009**. DOI `http://dx.doi.org/10.1063/1.3255041`.

[258] R. Wyllie, M. Kauer, R. T. Wakai, and T. G. Walker. "Optical magnetometer array for fetal magnetocardiography." *Optics Letters* 37 (12), 2247, **2012**. DOI http://dx.doi.org/10.1364/OL.37.002247.

[259] D. Sheng, S. Li, N. Dural, and M. V. Romalis. "Subfemtotesla scalar atomic magnetometry using multipass cells." *Physical Review Letters* 110 (16), 160802, **2013**. DOI http://dx.doi.org/10.1103/PhysRevLett.110.160802.

[260] T. W. Hänsch, I. S. Shahin, and A. L. Schawlow. "High-resolution saturation spectroscopy of the sodium D lines with a pulsed tunable dye laser." *Physical Review Letters* 27 (11), 707–710, **1971**. DOI http://dx.doi.org/10.1103/PhysRevLett.27.707.

[261] S. Knappe, V. Shah, P. D. D. Schwindt, L. Hollberg, *et al.*. "A microfabricated atomic clock." *Applied Physics Letters* 85 (9), 1460–1462, **2004**. DOI http://dx.doi.org/10.1063/1.1787942.

[262] J. Kitching. "Chip-scale atomic devices: From atomic clocks to brain imaging and beyond." In *2014 European Frequency and Time Forum (EFTF)*, 1–1. IEEE, **2014**. DOI http://dx.doi.org/10.1109/EFTF.2014.7331409.

[263] S. M. Spillane, G. S. Pati, K. Salit, M. Hall, *et al.*. "Observation of nonlinear optical interactions of ultralow levels of light in a tapered optical nanofiber embedded in a hot rubidium vapor." *Physical Review Letters* 100 (23), 233602, **2008**. DOI http://dx.doi.org/10.1103/PhysRevLett.100.233602.

[264] S. M. Hendrickson, M. M. Lai, T. B. Pittman, and J. D. Franson. "Observation of two-photon absorption at low power levels using tapered optical fibers in rubidium vapor." *Physical Review Letters* 105 (17), 173602, **2010**. DOI http://dx.doi.org/10.1103/PhysRevLett.105.173602.

[265] R. Garcia-Fernandez, W. Alt, F. Bruse, C. Dan, *et al.*. "Optical nanofibers and spectroscopy." *Applied Physics B* 105 (1), 3–15, **2011**. DOI http://dx.doi.org/10.1007/s00340-011-4730-x.

[266] A. D. Slepkov, A. R. Bhagwat, V. Venkataraman, P. Londero, *et al.*. "Spectroscopy of Rb atoms in hollow-core fibers." *Physical Review A* 81 (5), 053825, **2010**. DOI http://dx.doi.org/10.1103/PhysRevA.81.053825.

[267] G. Epple, K. S. Kleinbach, T. G. Euser, N. Y. Joly, *et al.*. "Rydberg atoms in hollow-core photonic crystal fibres." *Nature Communications* 5 (1), 4132, **2014**. DOI http://dx.doi.org/10.1038/ncomms5132.

[268] M. Giraud-Carrier, C. Hill, T. Decker, J. A. Black, *et al.*. "Perforated hollow-core optical waveguides for on-chip atomic spectroscopy and gas sensing." *Applied Physics Letters* 108 (13), 131105, **2016**. DOI http://dx.doi.org/10.1063/1.4945092.

[269] H. Schmidt and A. Hawkins. "Atomic spectroscopy and quantum optics in hollow-core waveguides." *Laser & Photonics Reviews* 4 (6), 720–737, **2010**. DOI http://dx.doi.org/10.1002/lpor.200900040.

[270] M. Xin, W. S. Leong, Z. Chen, and S.-Y. Lan. "An atom interferometer inside a hollow-core photonic crystal fiber." *Science Advances* 4 (1), e1701723, **2018**. DOI http://dx.doi.org/10.1126/sciadv.1701723.

[271] M. T. Hummon, S. Kang, D. G. Bopp, Q. Li, *et al.*. "Photonic chip for laser stabilization to an atomic vapor with 10^{-11} instability." *Optica* 5 (4), 443, **2018**. DOI `http://dx.doi.org/10.1364/OPTICA.5.000443`.

[272] Y. Millerioux, D. Touahri, L. Hilico, A. Clairon, *et al.*. "Towards an accurate frequency standard at λ778 nm using a laser diode stabilized on a hyperfine component of the Doppler-free two-photon transitions in rubidium." *Optics Communications* 108 (1-3), 91–96, **1994**. DOI `http://dx.doi.org/10.1016/0030-4018(94)90221-6`.

[273] B. Wu, J. F. Hulbert, E. J. Lunt, K. Hurd, *et al.*. "Slow light on a chip via atomic quantum state control." *Nature Photonics* 4 (11), 776–779, **2010**. DOI `http://dx.doi.org/10.1038/nphoton.2010.211`.

[274] V. Venkataraman, K. Saha, and A. L. Gaeta. "Phase modulation at the few-photon level for weak-nonlinearity-based quantum computing." *Nature Photonics* 7 (2), 138–141, **2013**. DOI `http://dx.doi.org/10.1038/nphoton.2012.283`.

[275] D. J. Fulton, S. Shepherd, R. R. Moseley, B. D. Sinclair, *et al.*. "Continuous-wave electromagnetically induced transparency: A comparison of V, Λ, and cascade systems." *Physical Review A* 52 (3), 2302–2311, **1995**. DOI `http://dx.doi.org/10.1103/PhysRevA.52.2302`.

[276] M. Anil Kumar and S. Singh. "Additional one-photon coherence-induced transparency in a Doppler-broadened V-type system." *Physical Review A* 87 (6), 065801, **2013**. DOI `http://dx.doi.org/10.1103/PhysRevA.87.065801`.

[277] J. Gea-Banacloche, Y.-Q. Li, S.-Z. Jin, and M. Xiao. "Electromagnetically induced transparency in ladder-type inhomogeneously broadened media: Theory and experiment." *Physical Review A* 51 (1), 576–584, **1995**. DOI `http://dx.doi.org/10.1103/PhysRevA.51.576`.

[278] P. M. Anisimov, J. P. Dowling, and B. C. Sanders. "Objectively discerning Autler-Townes splitting from electromagnetically induced transparency." *Physical Review Letters* 107 (16), 163604, **2011**. DOI `http://dx.doi.org/10.1103/PhysRevLett.107.163604`.

[279] B. Little, H. Haus, J. Foresi, L. Kimerling, *et al.*. "Wavelength switching and routing using absorption and resonance." *IEEE Photonics Technology Letters* 10 (6), 816–818, **1998**. DOI `http://dx.doi.org/10.1109/68.681495`.

[280] B. C. Jacobs and J. D. Franson. "All-optical switching using the quantum Zeno effect and two-photon absorption." *Physical Review A* 79 (6), 063830, **2009**. DOI `http://dx.doi.org/10.1103/PhysRevA.79.063830`.

[281] Y.-P. Huang, J. B. Altepeter, and P. Kumar. "Interaction-free all-optical switching via the quantum Zeno effect." *Physical Review A* 82 (6), 063826, **2010**. DOI `http://dx.doi.org/10.1103/PhysRevA.82.063826`.

[282] L. Pasternak and Y. Paz. "Low-temperature direct bonding of silicon nitride to glass." *RSC Advances* 8 (4), 2161–2172, **2018**. DOI `http://dx.doi.org/10.1039/C7RA08854J`.

[283] G.-W. Hsieh, C.-H. Tsai, W.-C. Lin, and C.-C. Liang. "Detailed study on anodic bonding process between glass and SiNx deposited silicon substrate and its application on waferlevel

AFM probe array integration." In *Proceedings of IEEE Sensors*, 607–610. IEEE, **2004**. DOI http://dx.doi.org/10.1109/ICSENS.2004.1426239.

[284] G.-W. Hsieh, C.-H. Tsai, and W.-C. Lin. "Anodic bonding of glass and silicon wafers with an intermediate silicon nitride film and its application to batch fabrication of SPM tip arrays." *Microelectronics Journal* 36 (7), 678–682, **2005**. DOI http://dx.doi.org/10.1016/J.MEJO.2005.04.057.

[285] K. Schjølberg-Henriksen, E. Poppe, S. Moe, P. Storås, *et al.*. "Anodic bonding of glass to aluminium." *Microsystem Technologies* 12 (5), 441–449, **2006**. DOI http://dx.doi.org/10.1007/s00542-005-0040-8.

[286] T. T. Veenstra, J. W. Berenschot, J. G. E. Gardeniers, R. G. P. Sanders, *et al.*. "Use of selective anodic bonding to create micropump chambers with virtually no dead volume." *Journal of The Electrochemical Society* 148 (2), G68, **2001**. DOI http://dx.doi.org/10.1149/1.1339873.

[287] M. Nese and A. Hanneborg. "Anodic bonding of silicon to silicon wafers coated with aluminium, silicon oxide, polysilicon or silicon nitride." *Sensors and Actuators A: Physical* 37-38, 61–67, **1993**. DOI http://dx.doi.org/10.1016/0924-4247(93)80013-7.

[288] P. E. Barclay, K. Srinivasan, O. Painter, B. Lev, *et al.*. "Integration of fiber-coupled high-Q SiNx microdisks with atom chips." *Applied Physics Letters* 89 (13), 131108, **2006**. DOI http://dx.doi.org/10.1063/1.2356892.

[289] P. Siddons, C. S. Adams, C. Ge, and I. G. Hughes. "Absolute absorption on rubidium D lines: comparison between theory and experiment." *Journal of Physics B: Atomic, Molecular and Optical Physics* 41 (15), 155004, **2008**. DOI http://dx.doi.org/10.1088/0953-4075/41/15/155004.

[290] L. Weller, R. J. Bettles, P. Siddons, C. S. Adams, *et al.*. "Absolute absorption on the rubidium D1 line including resonant dipole-dipole interactions." *Journal of Physics B: Atomic, Molecular and Optical Physics* 44 (19), 195006, **2011**. DOI http://dx.doi.org/10.1088/0953-4075/44/19/195006.

[291] G. Nienhuis, F. Schuller, and M. Ducloy. "Nonlinear selective reflection from an atomic vapor at arbitrary incidence angle." *Physical Review A* 38 (10), 5197–5205, **1988**. DOI http://dx.doi.org/10.1103/PhysRevA.38.5197.

[292] J. Guo, J. Cooper, A. Gallagher, and M. Lewenstein. "Theory of selective reflection spectroscopy." *Optics Communications* 110 (1-2), 197–208, **1994**. DOI http://dx.doi.org/10.1016/0030-4018(94)90196-1.

[293] K. Zhao and Z. Wu. "Regionally specific hyperfine polarization of Rb atoms in the vicinity (E-5 cm) of surfaces." *Physical Review A* 71 (1), 012902, **2005**. DOI http://dx.doi.org/10.1103/PhysRevA.71.012902.

[294] R. Kondo, S. Tojo, T. Fujimoto, and M. Hasuo. "Shift and broadening in attenuated total reflection spectra of the hyperfine-structure-resolved D 2 line of dense rubidium vapor." *Physical Review A* 73 (6), 062504, **2006**. DOI http://dx.doi.org/10.1103/PhysRevA.73.062504.

[295] R. Loudon. *The quantum theory of light*. Oxford University Press, **2000**. ISBN 9780198501763.

[296] P. A. Petrov, A. S. Pazgalev, M. A. Burkova, and T. A. Vartanyan. "Photodesorption of rubidium atoms from a sapphire surface." *Optics and Spectroscopy* 123 (4), 574–577, **2017**. DOI `http://dx.doi.org/10.1134/S0030400X17100204`.

[297] K.-J. Liao, M.-L. Wang, G.-Y. Zhang, and K.-F. Zhao. "Time-resolved measurements of the adsorption/desorption of Rb atoms on octadecyltrichlorosilane coated surfaces." *Chinese Physics Letters* 32 (7), 076801, **2015**. DOI `http://dx.doi.org/10.1088/0256-307X/32/7/076801`.

[298] A. Cappello, C. de Mauro, A. Bogi, A. Burchianti, *et al.*. "Light induced atomic desorption from dry-film coatings." *The Journal of Chemical Physics* 127 (4), 044706, **2007**. DOI `http://dx.doi.org/10.1063/1.2756829`.

[299] C. Klempt, T. van Zoest, T. Henninger, O. Topic, *et al.*. "Ultraviolet light-induced atom desorption for large rubidium and potassium magneto-optical traps." *Physical Review A* 73 (1), 013410, **2006**. DOI `http://dx.doi.org/10.1103/PhysRevA.73.013410`.

[300] M. Meucci, E. Mariotti, P. Bicchi, C. Marinelli, *et al.*. "Light-induced atom desorption." *Europhysics Letters (EPL)* 25 (9), 639–643, **1994**. DOI `http://dx.doi.org/10.1209/0295-5075/25/9/001`.

[301] E. Lewis. "Collisional relaxation of atomic excited states, line broadening and interatomic interactions." *Physics Reports* 58 (1), 1–71, **1980**. DOI `http://dx.doi.org/10.1016/0370-1573(80)90056-3`.

[302] M. Winger, T. D. Blasius, T. P. Mayer Alegre, A. H. Safavi-Naeini, *et al.*. "A chip-scale integrated cavity-electro-optomechanics platform." *Optics Express* 19 (25), 24905, **2011**. DOI `http://dx.doi.org/10.1364/OE.19.024905`.

[303] T. P. M. Alegre, R. Perahia, and O. Painter. "Optomechanical zipper cavity lasers: theoretical analysis of tuning range and stability." *Optics Express* 18 (8), 7872, **2010**. DOI `http://dx.doi.org/10.1364/OE.18.007872`.

[304] R. Perahia, J. D. Cohen, S. Meenehan, T. P. M. Alegre, *et al.*. "Electrostatically tunable optomechanical zipper cavity laser." *Applied Physics Letters* 97 (19), 191112, **2010**. DOI `http://dx.doi.org/10.1063/1.3515296`.

[305] J. Chan, M. Eichenfield, R. Camacho, and O. Painter. "Optical and mechanical design of a zipper photonic crystal optomechanical cavity." *Optics Express* 17 (5), 3802, **2009**. DOI `http://dx.doi.org/10.1364/OE.17.003802`.

[306] P. Lombardi, A. P. Ovvyan, S. Pazzagli, G. Mazzamuto, *et al.*. "Photostable molecules on chip: Integrated sources of nonclassical light." *ACS Photonics* 5 (1), 126–132, **2018**. DOI `http://dx.doi.org/10.1021/acsphotonics.7b00521`.

[307] S. Khasminskaya, F. Pyatkov, B. S. Flavel, W. H. Pernice, *et al.*. "Waveguide-integrated light-emitting carbon nanotubes." *Advanced Materials* 26 (21), 3465–3472, **2014**. DOI `http://dx.doi.org/10.1002/adma.201305634`.

[308] S. Khasminskaya, F. Pyatkov, K. Słowik, S. Ferrari, *et al.*. "Fully integrated quantum photonic circuit with an electrically driven light source." *Nature Photonics* 10 (11), 727–732, **2016**. DOI http://dx.doi.org/10.1038/nphoton.2016.178.

[309] F. Pyatkov, S. Khasminskaya, V. Kovalyuk, F. Hennrich, *et al.*. "Sub-nanosecond light-pulse generation with waveguide-coupled carbon nanotube transducers." *Beilstein Journal of Nanotechnology* 8 (1), 38–44, **2017**. DOI http://dx.doi.org/10.3762/bjnano.8.5.

[310] S. Ferrari, O. Kahl, V. Kovalyuk, G. N. Goltsman, *et al.*. "Waveguide-integrated single- and multi-photon detection at telecom wavelengths using superconducting nanowires." *Applied Physics Letters* 106 (15), 151101, **2015**. DOI http://dx.doi.org/10.1063/1.4917166.

[311] S. Ferrari, V. Kovalyuk, W. Hartmann, A. Vetter, *et al.*. "Hot-spot relaxation time current dependence in niobium nitride waveguide-integrated superconducting nanowire single-photon detectors." *Optics Express* 25 (8), 8739, **2017**. DOI http://dx.doi.org/10.1364/OE.25.008739.

[312] O. Kahl, S. Ferrari, V. Kovalyuk, G. N. Goltsman, *et al.*. "Waveguide integrated superconducting single-photon detectors with high internal quantum efficiency at telecom wavelengths." *Scientific Reports* 5 (1), 10941, **2015**. DOI http://dx.doi.org/10.1038/srep10941.

[313] V. Kovalyuk, S. Ferrari, O. Kahl, A. Semenov, *et al.*. "On-chip coherent detection with quantum limited sensitivity." *Scientific Reports* 7 (1), 4812, **2017**. DOI http://dx.doi.org/10.1038/s41598-017-05142-1.

[314] K. S. Novoselov, A. K. Geim, S. V. Morozov, D. Jiang, *et al.*. "Electric field effect in atomically thin carbon films." *Science* 306 (5696), 666–9, **2004**. DOI http://dx.doi.org/10.1126/science.1102896.

[315] A. H. Castro Neto, N. M. R. Peres, K. S. Novoselov, and A. K. Geim. "The electronic properties of graphene." *Reviews of Modern Physics* 81 (1), 109–162, **2009**. DOI http://dx.doi.org/10.1103/RevModPhys.81.109.

[316] K. S. Novoselov, A. K. Geim, S. V. Morozov, D. Jiang, *et al.*. "Two-dimensional gas of massless Dirac fermions in graphene." *Nature* 438 (7065), 197–200, **2005**. DOI http://dx.doi.org/10.1038/nature04233.

[317] Y. Zhang, Y.-W. Tan, H. L. Stormer, and P. Kim. "Experimental observation of the quantum Hall effect and Berry's phase in graphene." *Nature* 438 (7065), 201–4, **2005**. DOI http://dx.doi.org/10.1038/nature04235.

[318] V. Gusynin and S. Sharapov. "Unconventional integer quantum Hall effect in graphene." *Physical Review Letters* 95 (14), 146801, **2005**. DOI http://dx.doi.org/10.1103/PhysRevLett.95.146801.

[319] K. S. Novoselov, D. Jiang, F. Schedin, T. J. Booth, *et al.*. "Two-dimensional atomic crystals." *Proceedings of the National Academy of Sciences of the United States of America* 102 (30), 10451–3, **2005**. DOI http://dx.doi.org/10.1073/pnas.0502848102.

[320] A. Geim. "Graphene update." *Bulletin of the American Physical Society* 55, **2010**. DOI http://meetings.aps.org/link/BAPS.2010.MAR.J21.4.

[321] A. S. Mayorov, R. V. Gorbachev, S. V. Morozov, L. Britnell, *et al.*. "Micrometer-scale ballistic transport in encapsulated graphene at room temperature." *Nano letters* 11 (6), 2396–9, **2011**. DOI http://dx.doi.org/10.1021/nl200758b.

[322] R. Murali, Y. Yang, K. Brenner, T. Beck, *et al.*. "Breakdown current density of graphene nanoribbons." *Applied Physics Letters* 94 (24), 243114, **2009**. DOI http://dx.doi.org/10.1063/1.3147183.

[323] L. Liao, Y.-C. Lin, M. Bao, R. Cheng, *et al.*. "High-speed graphene transistors with a self-aligned nanowire gate." *Nature* 467 (7313), 305–8, **2010**. DOI http://dx.doi.org/10.1038/nature09405.

[324] L. Liao, J. Bai, R. Cheng, Y.-C. Lin, *et al.*. "Sub-100 nm channel length graphene transistors." *Nano letters* 10 (10), 3952–6, **2010**. DOI http://dx.doi.org/10.1021/nl101724k.

[325] R. Cheng, J. Bai, L. Liao, H. Zhou, *et al.*. "High-frequency self-aligned graphene transistors with transferred gate stacks." *Proceedings of the National Academy of Sciences of the United States of America* 109 (29), 11588–92, **2012**. DOI http://dx.doi.org/10.1073/pnas.1205696109.

[326] R. C. Ordonez, C. K. Hayashi, C. M. Torres, J. L. Melcher, *et al.*. "Rapid fabrication of graphene field-effect transistors with liquid-metal interconnects and electrolytic gate dielectric made of honey." *Scientific Reports* 7 (1), 10171, **2017**. DOI http://dx.doi.org/10.1038/s41598-017-10043-4.

[327] K. F. Mak, M. Y. Sfeir, Y. Wu, C. H. Lui, *et al.*. "Measurement of the optical conductivity of graphene." *Physical Review Letters* 101 (19), 196405, **2008**. DOI http://dx.doi.org/10.1103/PhysRevLett.101.196405.

[328] R. R. Nair, P. Blake, A. N. Grigorenko, K. S. Novoselov, *et al.*. "Fine structure constant defines visual transparency of graphene." *Science (New York, N.Y.)* 320 (5881), 1308, **2008**. DOI http://dx.doi.org/10.1126/science.1156965.

[329] A. Kuzmenko, E. van Heumen, F. Carbone, and D. van der Marel. "Universal optical conductance of graphite." *Physical Review Letters* 100 (11), 117401, **2008**. DOI http://dx.doi.org/10.1103/PhysRevLett.100.117401.

[330] F. Wang, Y. Zhang, C. Tian, C. Girit, *et al.*. "Gate-variable optical transitions in graphene." *Science (New York, N.Y.)* 320 (5873), 206–9, **2008**. DOI http://dx.doi.org/10.1126/science.1152793.

[331] Z. Q. Li, E. A. Henriksen, Z. Jiang, Z. Hao, *et al.*. "Dirac charge dynamics in graphene by infrared spectroscopy." *Nature Physics* 4 (7), 532–535, **2008**. DOI http://dx.doi.org/10.1038/nphys989.

[332] L. A. Falkovsky. "Optical properties of graphene." *Journal of Physics: Conference Series* 129, 012004, **2008**. DOI http://dx.doi.org/10.1088/1742-6596/129/1/012004.

[333] F. Bonaccorso, Z. Sun, T. Hasan, and a. C. Ferrari. "Graphene photonics and optoelectronics." *Nature Photonics* 4 (9), 611–622, **2010**. DOI http://dx.doi.org/10.1038/nphoton.2010.186.

[334] L. Gomez De Arco, Y. Zhang, C. W. Schlenker, K. Ryu, *et al.*. "Continuous, highly flexible, and transparent graphene films by chemical vapor deposition for organic photovoltaics." *ACS nano* 4 (5), 2865–73, **2010**. DOI `http://dx.doi.org/10.1021/nn901587x`.

[335] J. K. Wassei and R. B. Kaner. "Graphene, a promising transparent conductor." *Materials Today* 13 (3), 52–59, **2010**. DOI `http://dx.doi.org/10.1016/S1369-7021(10)70034-1`.

[336] K. Rana, J. Singh, and J.-H. Ahn. "A graphene-based transparent electrode for use in flexible optoelectronic devices." *J. Mater. Chem. C* 2 (15), 2646–2656, **2014**. DOI `http://dx.doi.org/10.1039/C3TC32264E`.

[337] Y. Xu and J. Liu. "Graphene as transparent electrodes: Fabrication and new emerging applications." *Small* 12 (11), 1400–1419, **2016**. DOI `http://dx.doi.org/10.1002/smll.201502988`.

[338] K. F. Mak, C. Lee, J. Hone, J. Shan, *et al.*. "Atomically thin MoS2: A new direct-gap semiconductor." *Physical Review Letters* 105 (13), 136805, **2010**. DOI `http://dx.doi.org/10.1103/PhysRevLett.105.136805`.

[339] A. Splendiani, L. Sun, Y. Zhang, T. Li, *et al.*. "Emerging photoluminescence in monolayer MoS2." *Nano Letters* 10 (4), 1271–1275, **2010**. DOI `http://dx.doi.org/10.1021/nl903868w`.

[340] P. Miró, M. Audiffred, and T. Heine. "An atlas of two-dimensional materials." *Chem. Soc. Rev.* 43 (18), 6537–6554, **2014**. DOI `http://dx.doi.org/10.1039/C4CS00102H`.

[341] G. R. Bhimanapati, Z. Lin, V. Meunier, Y. Jung, *et al.*. "Recent advances in two-dimensional materials beyond graphene." *ACS Nano* 9 (12), 11509–11539, **2015**. DOI `http://dx.doi.org/10.1021/acsnano.5b05556`.

[342] Z. G. Yu, Y. Cai, and Y.-W. Zhang. "Robust direct bandgap characteristics of one- and two-dimensional ReS2." *Scientific Reports* 5 (1), 13783, **2015**. DOI `http://dx.doi.org/10.1038/srep13783`.

[343] C. Gerry and P. Knight. *Introductory quantum optics*. Cambridge University Press, Cambridge, **2004**. ISBN 9780511791239. DOI `http://dx.doi.org/10.1017/CBO9780511791239`.

[344] D. J. Late, B. Liu, J. Luo, A. Yan, *et al.*. "GaS and GaSe ultrathin layer transistors." *Advanced Materials* 24 (26), 3549–3554, **2012**. DOI `http://dx.doi.org/10.1002/adma.201201361`.

[345] C. Hirlimann, J.-F. Morhange, and A. Chevy. "Excitonic resonant second harmonic in GaSe." *Solid State Communications* 69 (11), 1019–1022, **1989**. DOI `http://dx.doi.org/10.1016/0038-1098(89)90479-1`.

[346] V. Negoita, D. W. Snoke, and K. Eberl. "Harmonic-potential traps for indirect excitons in coupled quantum wells." *Physical Review B* 60 (4), 2661–2669, **1999**. DOI `http://dx.doi.org/10.1103/PhysRevB.60.2661`.

[347] O. D. Pozo-Zamudio, S. Schwarz, M. Sich, I. A. Akimov, *et al.*. "Photoluminescence of two-dimensional GaTe and GaSe films." *2D Materials* 2 (3), 035010, **2015**. DOI `http://dx.doi.org/10.1088/2053-1583/2/3/035010`.

[348] N. Kolesnikov, E. Borisenko, D. Borisenko, and V. Gartman. "Influence of growth conditions on microstructure and properties of GaSe crystals." *Journal of Crystal Growth* 300 (2), 294–298, **2007**. DOI http://dx.doi.org/10.1016/J.JCRYSGRO.2007.01.001.

[349] Y. P. Gnatenko, Z. D. Kovalyuk, P. A. Skubenko, and Y. I. Zhirko. "Emission of free and bound excitons in layered gase crystals." *physica status solidi (b)* 117 (1), 283–287, **1983**. DOI http://dx.doi.org/10.1002/pssb.2221170131.

[350] T. Basché, W. E. Moerner, M. Orrit, and H. Talon. "Photon antibunching in the fluorescence of a single dye molecule trapped in a solid." *Physical Review Letters* 69 (10), 1516–1519, **1992**. DOI http://dx.doi.org/10.1103/PhysRevLett.69.1516.

[351] R. Lettow, Y. L. A. Rezus, A. Renn, G. Zumofen, *et al.*. "Quantum interference of tunably indistinguishable photons from remote organic molecules." *Physical Review Letters* 104 (12), 123605, **2010**. DOI http://dx.doi.org/10.1103/PhysRevLett.104.123605.

[352] Y. L. A. Rezus, S. G. Walt, R. Lettow, A. Renn, *et al.*. "Single-photon spectroscopy of a single molecule." *Physical Review Letters* 108 (9), 093601, **2012**. DOI http://dx.doi.org/10.1103/PhysRevLett.108.093601.

[353] C. Brunel, B. Lounis, P. Tamarat, and M. Orrit. "Triggered source of single photons based on controlled single molecule fluorescence." *Physical Review Letters* 83 (14), 2722–2725, **1999**. DOI http://dx.doi.org/10.1103/PhysRevLett.83.2722.

[354] J. Weiss. "Fluorescence of organic molecules." *Nature* 152 (3850), 176–178, **1943**. DOI http://dx.doi.org/10.1038/152176a0.

[355] W. E. Moerner. "Single-photon sources based on single molecules in solids." *New Journal of Physics* 6 (1), 88–88, **2004**. DOI http://dx.doi.org/10.1088/1367-2630/6/1/088.

[356] B. Lounis and W. E. Moerner. "Single photons on demand from a single molecule at room temperature." *Nature* 407 (6803), 491–493, **2000**. DOI http://dx.doi.org/10.1038/35035032.

[357] M. Nothaft, S. Höhla, F. Jelezko, N. Frühauf, *et al.*. "Electrically driven photon antibunching from a single molecule at room temperature." *Nature Communications* 3 (1), 628, **2012**. DOI http://dx.doi.org/10.1038/ncomms1637.

[358] L. Zhang, Y.-J. Yu, L.-G. Chen, Y. Luo, *et al.*. "Electrically driven single-photon emission from an isolated single molecule." *Nature Communications* 8 (1), 580, **2017**. DOI http://dx.doi.org/10.1038/s41467-017-00681-7.

[359] L. Fleury, B. Sick, G. Zumofen, B. Hecht, *et al.*. "High photo-stability of single molecules in an organic crystal at room temperature observed by scanning confocal optical microscopy." *Molecular Physics* 95 (6), 1333–1338, **1998**. DOI http://dx.doi.org/10.1080/00268979809483263.

[360] A. Kiraz, M. Ehrl, T. Hellerer, Ö. E. Müstecaplıoğlu, *et al.*. "Indistinguishable photons from a single molecule." *Physical Review Letters* 94 (22), 223602, **2005**. DOI http://dx.doi.org/10.1103/PhysRevLett.94.223602.

[361] A. A. L. Nicolet, C. Hofmann, M. A. Kol'chenko, B. Kozankiewicz, *et al.*. "Single dibenzoterrylene molecules in an anthracene crystal: Spectroscopy and photophysics." *ChemPhysChem* 8 (8), 1215–1220, **2007**. DOI http://dx.doi.org/10.1002/cphc.200700091.

[362] C. Toninelli, K. Early, J. Bremi, A. Renn, *et al.*. "Near-infrared single-photons from aligned molecules in ultrathin crystalline films at room temperature." *Optics Express* 18 (7), 6577, **2010**. DOI http://dx.doi.org/10.1364/OE.18.006577.

[363] J.-B. Trebbia, H. Ruf, P. Tamarat, and B. Lounis. "Efficient generation of near infra-red single photons from the zero-phonon line of a single molecule." *Optics Express* 17 (26), 23986, **2009**. DOI http://dx.doi.org/10.1364/OE.17.023986.

[364] L. A. Nakhimovsky, M. M. Lamotte, and J. Joussot-Dubien. *Handbook of low temperature electronic spectra of polycyclic aromatic hydrocarbons*. Elsevier, **1989**. ISBN 0444874046.

[365] M. S. Dresselhaus, G. Dresselhaus, and P. Avouris. *Carbon nanotubes: synthesis, structure, properties, and applications*. Springer, **2001**. ISBN 9783540410867.

[366] J. Liu, J. Lu, X. Lin, Y. Tang, *et al.*. "The electronic properties of chiral carbon nanotubes." *Computational Materials Science* 129, 290–294, **2017**. DOI http://dx.doi.org/10.1016/J.COMMATSCI.2016.12.035.

[367] B. S. Flavel, M. M. Kappes, R. Krupke, and F. Hennrich. "Separation of single-walled carbon nanotubes by 1-dodecanol-mediated size-exclusion chromatography." *ACS Nano* 7 (4), 3557–3564, **2013**. DOI http://dx.doi.org/10.1021/nn4004956.

[368] H. Liu, D. Nishide, T. Tanaka, and H. Kataura. "Large-scale single-chirality separation of single-wall carbon nanotubes by simple gel chromatography." *Nature Communications* 2 (1), 309, **2011**. DOI http://dx.doi.org/10.1038/ncomms1313.

[369] J. R. Sanchez-Valencia, T. Dienel, O. Gröning, I. Shorubalko, *et al.*. "Controlled synthesis of single-chirality carbon nanotubes." *Nature* 512 (7512), 61–64, **2014**. DOI http://dx.doi.org/10.1038/nature13607.

[370] X. Ma, N. F. Hartmann, J. K. S. Baldwin, S. K. Doorn, *et al.*. "Room-temperature single-photon generation from solitary dopants of carbon nanotubes." *Nature Nanotechnology* 10 (8), 671–675, **2015**. DOI http://dx.doi.org/10.1038/nnano.2015.136.

[371] M. S. Hofmann, J. T. Glückert, J. Noé, C. Bourjau, *et al.*. "Bright, long-lived and coherent excitons in carbon nanotube quantum dots." *Nature Nanotechnology* 8 (7), 502–505, **2013**. DOI http://dx.doi.org/10.1038/nnano.2013.119.

[372] A. Högele, C. Galland, M. Winger, and A. Imamoğlu. "Photon antibunching in the photoluminescence spectra of a single carbon nanotube." *Physical Review Letters* 100 (21), 217401, **2008**. DOI http://dx.doi.org/10.1103/PhysRevLett.100.217401.

[373] J. Chen, V. Perebeinos, M. Freitag, J. Tsang, *et al.*. "Bright infrared emission from electrically induced excitons in carbon nanotubes." *Science (New York, N.Y.)* 310 (5751), 1171–4, **2005**. DOI http://dx.doi.org/10.1126/science.1119177.

[374] J. Gérard, B. Sermage, B. Gayral, B. Legrand, *et al.*. "Enhanced spontaneous emission by quantum boxes in a monolithic optical microcavity." *Physical Review Letters* 81 (5), 1110–1113, **1998**. DOI `http://dx.doi.org/10.1103/PhysRevLett.81.1110`.

[375] T. H. C. Hoang, E. Durán-Valdeiglesias, C. Alonso-Ramos, S. Serna, *et al.*. "Narrow-linewidth carbon nanotube emission in silicon hollow-core photonic crystal cavity." *Optics Letters* 42 (11), 2228, **2017**. DOI `http://dx.doi.org/10.1364/OL.42.002228`.

[376] E. Gaufrès, N. Izard, X. Le Roux, S. Kazaoui, *et al.*. "Optical microcavity with semiconducting single-wall carbon nanotubes." *Optics Express* 18 (6), 5740, **2010**. DOI `http://dx.doi.org/10.1364/OE.18.005740`.

[377] R. Watahiki, T. Shimada, P. Zhao, S. Chiashi, *et al.*. "Enhancement of carbon nanotube photoluminescence by photonic crystal nanocavities." *Applied Physics Letters* 101 (14), 141124, **2012**. DOI `http://dx.doi.org/10.1063/1.4757876`.

[378] R. Miura, S. Imamura, R. Ohta, A. Ishii, *et al.*. "Ultralow mode-volume photonic crystal nanobeam cavities for high-efficiency coupling to individual carbon nanotube emitters." *Nature Communications* 5 (1), 5580, **2014**. DOI `http://dx.doi.org/10.1038/ncomms6580`.

[379] M. Agio and D. M. Cano. "The Purcell factor of nanoresonators." *Nature Photonics* 7 (9), 674–675, **2013**. DOI `http://dx.doi.org/10.1038/nphoton.2013.219`.

[380] J. W. Silverstone, D. Bonneau, J. L. O'Brien, and M. G. Thompson. "Silicon quantum photonics." *IEEE Journal of Selected Topics in Quantum Electronics* 22 (6), 390–402, **2016**. DOI `http://dx.doi.org/10.1109/JSTQE.2016.2573218`.

[381] C. M. Natarajan, M. G. Tanner, and R. H. Hadfield. "Superconducting nanowire single-photon detectors: physics and applications." *Superconductor Science and Technology* 25 (6), 063001, **2012**. DOI `http://dx.doi.org/10.1088/0953-2048/25/6/063001`.

[382] R. H. Hadfield. "Single-photon detectors for optical quantum information applications." *Nature Photonics* 3 (12), 696–705, **2009**. DOI `http://dx.doi.org/10.1038/nphoton.2009.230`.

[383] G. N. Gol'tsman, O. Okunev, G. Chulkova, A. Lipatov, *et al.*. "Picosecond superconducting single-photon optical detector." *Applied Physics Letters* 79 (6), 705–707, **2001**. DOI `http://dx.doi.org/10.1063/1.1388868`.

[384] V. Kovalyuk, W. Hartmann, O. Kahl, N. Kaurova, *et al.*. "Absorption engineering of NbN nanowires deposited on silicon nitride nanophotonic circuits." *Optics Express* 21 (19), 22683, **2013**. DOI `http://dx.doi.org/10.1364/OE.21.022683`.

[385] A. J. Annunziata, O. Quaranta, D. F. Santavicca, A. Casaburi, *et al.*. "Reset dynamics and latching in niobium superconducting nanowire single-photon detectors." *Journal of Applied Physics* 108 (8), 084507, **2010**. DOI `http://dx.doi.org/10.1063/1.3498809`.

[386] P. Rath, O. Kahl, S. Ferrari, F. Sproll, *et al.*. "Superconducting single-photon detectors integrated with diamond nanophotonic circuits." *Light: Science and Applications* 4 (May), 1–8, **2015**. DOI `http://dx.doi.org/10.1038/lsa.2015.111`.

[387] O. Kahl, S. Ferrari, P. Rath, A. Vetter, *et al.*. "High efficiency on-chip single-photon detection for diamond nanophotonic circuits." *Journal of Lightwave Technology* 34 (2), 249–255, **2016**. DOI http://dx.doi.org/10.1109/JLT.2015.2472481.

[388] A. Vetter, S. Ferrari, P. Rath, R. Alaee, *et al.*. "Cavity-Enhanced and Ultrafast Superconducting Single-Photon Detectors." *Nano Letters* 16 (11), 7085–7092, **2016**. DOI http://dx.doi.org/10.1021/acs.nanolett.6b03344.

[389] J. Münzberg, A. Vetter, F. Beutel, W. Hartmann, *et al.*. "Superconducting nanowire single-photon detector implemented in a 2D photonic crystal cavity." *Optica* 5 (5), 658, **2018**. DOI http://dx.doi.org/10.1364/OPTICA.5.000658.

[390] N. Gruhler, T. Yoshikawa, P. Rath, G. Lewes-Malandrakis, *et al.*. "Diamond on aluminum nitride as a platform for integrated photonic circuits." *Physica Status Solidi (A) Applications and Materials Science* 213 (8), 2075–2080, **2016**. DOI http://dx.doi.org/10.1002/pssa.201600227.

[391] H. Lin, Z. Luo, T. Gu, L. C. Kimerling, *et al.*. "Mid-infrared integrated photonics on silicon: a perspective." *Nanophotonics* 7 (2), 393–420, **2017**. DOI http://dx.doi.org/10.1515/nanoph-2017-0085.

[392] "Extending opportunities." *Nature Photonics* 6 (7), 407–407, **2012**. DOI http://dx.doi.org/10.1038/nphoton.2012.164.

[393] J. Hu, J. Meyer, K. Richardson, and L. Shah. "Feature issue introduction: mid-IR photonic materials." *Optical Materials Express* 3 (9), 1571, **2013**. DOI http://dx.doi.org/10.1364/OME.3.001571.

[394] K.-N. Liou. *An introduction to atmospheric radiation.* Academic Press, **2002**. ISBN 9780080491677.

[395] H. R. Phillip and E. A. Taft. "Kramers-Kronig analysis of reflectance data for diamond." *Physical Review* 136 (5A), A1445–A1448, **1964**. DOI http://dx.doi.org/10.1103/PhysRev.136.A1445.

[396] H. H. Li. "Refractive index of alkaline earth halides and its wavelength and temperature derivatives." *Journal of Physical and Chemical Reference Data* 9 (1), 161–290, **1980**. DOI http://dx.doi.org/10.1063/1.555616.

[397] M. Querry. "Optical constants of minerals and other materials from the millimeter to the ultraviolet.", **1987**. URL http://www.dtic.mil/docs/citations/ADA192210.

[398] P. Dore, A. Nucara, D. Cannavò, G. De Marzi, *et al.*. "Infrared properties of chemical-vapor deposition polycrystalline diamond windows." *Applied Optics* 37 (24), 5731, **1998**. DOI http://dx.doi.org/10.1364/AO.37.005731.

[399] A. D. Rakić and M. L. Majewski. "Modeling the optical dielectric function of GaAs and AlAs: Extension of Adachi's model." *Journal of Applied Physics* 80 (10), 5909, **1998**. DOI http://dx.doi.org/10.1063/1.363586.

[400] D. Chandler-Horowitz and P. M. Amirtharaj. "High-accuracy, midinfrared (450 cm-1$\leq \omega \leq$4000cm-1) refractive index values of silicon." *Journal of Applied Physics* 97 (12), 123526, **2005**. DOI http://dx.doi.org/10.1063/1.1923612.

[401] R. Soref. "Mid-infrared photonics in silicon and germanium." *Nature Photonics* 4 (8), 495–497, **2010**. DOI http://dx.doi.org/10.1038/nphoton.2010.171.

[402] J. Kischkat, S. Peters, B. Gruska, M. Semtsiv, *et al.*. "Mid-infrared optical properties of thin films of aluminum oxide, titanium dioxide, silicon dioxide, aluminum nitride, and silicon nitride." *Applied Optics* 51 (28), 6789, **2012**. DOI http://dx.doi.org/10.1364/AO.51.006789.

[403] C. Schinke, P. Christian Peest, J. Schmidt, R. Brendel, *et al.*. "Uncertainty analysis for the coefficient of band-to-band absorption of crystalline silicon." *AIP Advances* 5 (6), 067168, **2015**. DOI http://dx.doi.org/10.1063/1.4923379.

[404] L. V. Rodríguez-de Marcos, J. I. Larruquert, J. A. Méndez, and J. A. Aznárez. "Self-consistent optical constants of SiO2 and Ta2O5 films." *Optical Materials Express* 6 (11), 3622, **2016**. DOI http://dx.doi.org/10.1364/OME.6.003622.

[405] A. Ciesielski, L. Skowronski, W. Pacuski, and T. Szoplik. "Permittivity of Ge, Te and Se thin films in the 200-1500 nm spectral range. Predicting the segregation effects in silver." *Materials Science in Semiconductor Processing* 81, 64–67, **2018**. DOI http://dx.doi.org/10.1016/J.MSSP.2018.03.003.

[406] R. Shankar, R. Leijssen, I. Bulu, and M. Lončar. "Mid-infrared photonic crystal cavities in silicon." *Optics Express* 19 (6), 5579, **2011**. DOI http://dx.doi.org/10.1364/OE.19.005579.

[407] Z. Cheng, X. Chen, C. Y. Wong, K. Xu, *et al.*. "Focusing subwavelength grating coupler for mid-infrared suspended membrane waveguide." *Optics Letters* 37 (7), 1217, **2012**. DOI http://dx.doi.org/10.1364/OL.37.001217.

[408] Y. Xia, C. Qiu, X. Zhang, W. Gao, *et al.*. "Suspended Si ring resonator for mid-IR application." *Optics Letters* 38 (7), 1122, **2013**. DOI http://dx.doi.org/10.1364/OL.38.001122.

[409] Z. Cheng, X. Chen, C. Y. Wong, K. Xu, *et al.*. "Mid-infrared suspended membrane waveguide and ring resonator on silicon-on-insulator." *IEEE Photonics Journal* 4 (5), 1510–1519, **2012**. DOI http://dx.doi.org/10.1109/JPHOT.2012.2210700.

[410] P. T. Lin, V. Singh, J. Wang, H. Lin, *et al.*. "Si-CMOS compatible materials and devices for mid-IR microphotonics." *Optical Materials Express* 3 (9), 1474, **2013**. DOI http://dx.doi.org/10.1364/OME.3.001474.

[411] P. T. Lin, V. Singh, Y. Cai, L. C. Kimerling, *et al.*. "Air-clad silicon pedestal structures for broadband mid-infrared microphotonics." *Optics Letters* 38 (7), 1031, **2013**. DOI http://dx.doi.org/10.1364/OL.38.001031.

[412] J. Chiles, S. Khan, J. Ma, and S. Fathpour. "High-contrast, all-silicon waveguiding platform for ultra-broadband mid-infrared photonics." *Applied Physics Letters* 103 (15), 151106, **2013**. DOI http://dx.doi.org/10.1063/1.4824771.

[413] J. Soler Penadés, C. Alonso-Ramos, A. Z. Khokhar, M. Nedeljkovic, *et al.*. "Suspended SOI waveguide with sub-wavelength grating cladding for mid-infrared." *Optics Letters* 39 (19), 5661, **2014**. DOI http://dx.doi.org/10.1364/OL.39.005661.

[414] J. S. Penades, A. Ortega-Moñux, M. Nedeljkovic, J. G. Wangüemert-Pérez, *et al.*. "Suspended silicon mid-infrared waveguide devices with subwavelength grating metamaterial cladding." *Optics Express* 24 (20), 22908, **2016**. DOI http://dx.doi.org/10.1364/OE.24.022908.

[415] J. Chiles and S. Fathpour. "Single-mode and single-polarization photonics with anchored-membrane waveguides." *Optics Express* 24 (17), 19337, **2016**. DOI http://dx.doi.org/10.1364/OE.24.019337.

[416] N. Hô, M. C. Phillips, H. Qiao, P. J. Allen, *et al.*. "Single-mode low-loss chalcogenide glass waveguides for the mid-infrared." *Optics Letters* 31 (12), 1860, **2006**. DOI http://dx.doi.org/10.1364/OL.31.001860.

[417] T. Lewi and A. Katzir. "Silver halide single-mode strip waveguides for the mid-infrared." *Optics Letters* 37 (13), 2733, **2012**. DOI http://dx.doi.org/10.1364/OL.37.002733.

[418] P. Ma, D.-Y. Choi, Y. Yu, X. Gai, *et al.*. "Low-loss chalcogenide waveguides for chemical sensing in the mid-infrared." *Optics express* 21 (24), 29927–37, **2013**. DOI http://www.ncbi.nlm.nih.gov/pubmed/24514544.

[419] H. Lin, L. Li, Y. Zou, S. Danto, *et al.*. "Demonstration of high-Q mid-infrared chalcogenide glass-on-silicon resonators." *Optics Letters* 38 (9), 1470, **2013**. DOI http://dx.doi.org/10.1364/OL.38.001470.

[420] Y. Yu, X. Gai, P. Ma, D.-Y. Choi, *et al.*. "A broadband, quasi-continuous, mid-infrared supercontinuum generated in a chalcogenide glass waveguide." *Laser & Photonics Reviews* 8 (5), 792–798, **2014**. DOI http://dx.doi.org/10.1002/lpor.201400034.

[421] P. Ma, D.-Y. Choi, Y. Yu, Z. Yang, *et al.*. "High Q factor chalcogenide ring resonators for cavity-enhanced MIR spectroscopic sensing." *Optics Express* 23 (15), 19969, **2015**. DOI http://dx.doi.org/10.1364/OE.23.019969.

[422] A. Gutierrez-Arroyo, E. Baudet, L. Bodiou, J. Lemaitre, *et al.*. "Optical characterization at 7.7um of an integrated platform based on chalcogenide waveguides for sensing applications in the mid-infrared." *Optics Express* 24 (20), 23109, **2016**. DOI http://dx.doi.org/10.1364/OE.24.023109.

[423] V. Mittal, N. P. Sessions, J. S. Wilkinson, and G. S. Murugan. "Optical quality ZnSe films and low loss waveguides on Si substrates for mid-infrared applications." *Optical Materials Express* 7 (3), 712, **2017**. DOI http://dx.doi.org/10.1364/OME.7.000712.

[424] B. Morrison, A. Casas-Bedoya, G. Ren, K. Vu, *et al.*. "Compact Brillouin devices through hybrid integration on silicon." *Optica* 4 (8), 847, **2017**. DOI http://dx.doi.org/10.1364/OPTICA.4.000847.

[425] Y.-C. Chang, V. Paeder, L. Hvozdara, J.-M. Hartmann, *et al.*. "Low-loss germanium strip waveguides on silicon for the mid-infrared." *Optics Letters* 37 (14), 2883, **2012**. DOI http://dx.doi.org/10.1364/OL.37.002883.

[426] A. Malik, M. Muneeb, S. Pathak, Y. Shimura, *et al.*. "Germanium-on-silicon mid-infrared arrayed waveguide grating multiplexers." *IEEE Photonics Technology Letters* 25 (18), 1805–1808, **2013**. DOI http://dx.doi.org/10.1109/LPT.2013.2276479.

[427] A. Malik, M. Muneeb, Y. Shimura, J. Van Campenhout, *et al.*. "Germanium-on-silicon planar concave grating wavelength (de)multiplexers in the mid-infrared." *Applied Physics Letters* 103 (16), 161119, **2013**. DOI http://dx.doi.org/10.1063/1.4826114.

[428] M. Nedeljkovic, J. S. Penades, C. J. Mitchell, A. Z. Khokhar, *et al.*. "Surface-Grating-Coupled Low-Loss Ge-on-Si Rib Waveguides and Multimode Interferometers." *IEEE Photonics Technology Letters* 27 (10), 1040–1043, **2015**. DOI http://dx.doi.org/10.1109/LPT.2015.2405611.

[429] C. Alonso-Ramos, M. Nedeljkovic, D. Benedikovic, J. S. Penadés, *et al.*. "Germanium-on-silicon mid-infrared grating couplers with low-reflectivity inverse taper excitation." *Optics Letters* 41 (18), 4324, **2016**. DOI http://dx.doi.org/10.1364/OL.41.004324.

[430] G. Z. Mashanovich, C. J. Mitchell, J. S. Penades, A. Z. Khokhar, *et al.*. "Germanium Mid-Infrared Photonic Devices." *Journal of Lightwave Technology* 35 (4), 624–630, **2017**. DOI http://dx.doi.org/10.1109/JLT.2016.2632301.

[431] J. Kang, Z. Cheng, W. Zhou, T.-H. Xiao, *et al.*. "Focusing subwavelength grating coupler for mid-infrared suspended membrane germanium waveguides." *Optics Letters* 42 (11), 2094, **2017**. DOI http://dx.doi.org/10.1364/OL.42.002094.

[432] T.-H. Xiao, Z. Zhao, W. Zhou, M. Takenaka, *et al.*. "Mid-infrared germanium photonic crystal cavity." *Optics Letters* 42 (15), 2882, **2017**. DOI http://dx.doi.org/10.1364/OL.42.002882.

[433] N. B. Colthup, L. H. Daly, and S. E. Wiberley. *Introduction to infrared and Raman spectroscopy.* Academic Press, **1990**. ISBN 9780080917405.

[434] F. Siebert and P. Hildebrandt. *Vibrational spectroscopy in life science.* Wiley-VCH Verlag, Weinheim, Germany, **2007**. ISBN 9783527621347. DOI http://dx.doi.org/10.1002/9783527621347.

[435] I. Aharonovich and E. Neu. "Diamond nanophotonics." *Advanced Optical Materials* 2 (10), 911–928, **2014**. DOI http://dx.doi.org/10.1002/adom.201400189.

[436] P. Rath, S. Ummethala, C. Nebel, and W. H. Pernice. "Diamond as a material for monolithically integrated optical and optomechanical devices." *Physica Status Solidi (A) Applications and Materials Science* 212 (11), 2385–2399, **2015**. DOI http://dx.doi.org/10.1002/pssa.201532494.

[437] T. Schröder, S. L. Mouradian, J. Zheng, M. E. Trusheim, *et al.*. "Quantum nanophotonics in diamond." *Journal of the Optical Society of America B* 33 (4), B65, **2016**. DOI http://dx.doi.org/10.1364/JOSAB.33.000B65.

[438] P. J. Dean. "Bound excitons and donor-acceptor pairs in natural and synthetic diamond." *Physical Review* 139 (2A), A588–A602, **1965**. DOI http://dx.doi.org/10.1103/PhysRev.139.A588.

[439] T. P. Mollart, K. L. Lewis, C. S. Pickles, and C. J. Wort. "Factors affecting the optical performance of CVD diamond infrared optics." *Semiconductor Science and Technology* 18 (3), **2003**. DOI http://dx.doi.org/10.1088/0268-1242/18/3/317.

[440] T. K. Liang and H. K. Tsang. "Role of free carriers from two-photon absorption in Raman amplification in silicon-on-insulator waveguides." *Applied Physics Letters* 84 (15), 2745–2747, **2004**. DOI http://dx.doi.org/10.1063/1.1702133.

[441] L. Yin and G. P. Agrawal. "Impact of two-photon absorption on self-phase modulation in silicon waveguides." *Optics Letters* 32 (14), 2031, **2007**. DOI http://dx.doi.org/10.1364/OL.32.002031.

[442] M. P. Hiscocks, K. Ganesan, B. C. Gibson, S. T. Huntington, *et al.*. "Diamond waveguides fabricated by reactive ion etching." *Optics Express* 16 (24), 19512, **2008**. DOI http://dx.doi.org/10.1364/OE.16.019512.

[443] C. E. Nebel and J. Ristein. *Semiconductors and Semimetals: Thin-film diamond I*. Elsevier, **2003**. ISBN 9780080541037.

[444] R. Riedel (editor). *Handbook of ceramic hard materials*. Wiley-VCH Verlag GmbH, Weinheim, Germany, **2000**. ISBN 9783527618217. DOI http://dx.doi.org/10.1002/9783527618217.

[445] T. Ruf, M. Cardona, C. S. J. Pickles, and R. Sussmann. "Temperature dependence of the refractive index of diamond up to 925K." *Physical Review B* 62 (24), 16578–16581, **2000**. DOI http://dx.doi.org/10.1103/PhysRevB.62.16578.

[446] S. Stoupin and Y. V. Shvyd'ko. "Ultraprecise studies of the thermal expansion coefficient of diamond using backscattering x-ray diffraction." *Physical Review B* 83 (10), 104102, **2011**. DOI http://dx.doi.org/10.1103/PhysRevB.83.104102.

[447] Z. G. Hu and P. Hess. "Optical constants and thermo-optic coefficients of nanocrystalline diamond films at 30-500C." *Applied Physics Letters* 89 (8), 081906, **2006**. DOI http://dx.doi.org/10.1063/1.2243863.

[448] M. D. Levenson and N. Bloembergen. "Dispersion of the nonlinear optical susceptibility tensor in centrosymmetric media." *Physical Review B* 10 (10), 4447–4463, **1974**. DOI http://dx.doi.org/10.1103/PhysRevB.10.4447.

[449] N. Vermeulen, J. Sipe, L. G. Helt, and H. Thienpont. "Opportunities for wavelength conversion with on-chip diamond ring resonators." *Laser & Photonics Reviews* 6 (6), 793–801, **2012**. DOI http://dx.doi.org/10.1002/lpor.201200066.

[450] B. J. M. Hausmann, I. Bulu, V. Venkataraman, P. Deotare, *et al.*. "Diamond nonlinear photonics." *Nature Photonics* 8 (5), 369–374, **2014**. DOI http://dx.doi.org/10.1038/nphoton.2014.72.

[451] P. Latawiec, V. Venkataraman, M. J. Burek, B. J. M. Hausmann, *et al.*. "On-chip diamond Raman laser." *Optica* 2 (11), 924, **2015**. DOI http://dx.doi.org/10.1364/OPTICA.2.000924.

[452] A. A. M. Zaitsev. *Optical properties of diamond: A data handbook*. Springer, Berlin, Heidelberg, **2001**. ISBN 9783662045480.

[453] R. Brouri, A. Beveratos, J.-P. Poizat, and P. Grangier. "Photon antibunching in the fluorescence of individual color centers in diamond." *Opt. Lett.* 25 (17), 1294–1296, **2000**. DOI http://dx.doi.org/10.1364/OL.25.001294.

[454] C. Kurtsiefer, S. Mayer, P. Zarda, and H. Weinfurter. "Stable solid-state source of single photons." *Physical Review Letters* 85 (2), 290–293, **2000**. DOI http://dx.doi.org/10.1103/PhysRevLett.85.290.

[455] K. C. Lee, B. J. Sussman, M. R. Sprague, P. Michelberger, *et al.*. "Macroscopic non-classical states and terahertz quantum processing in room-temperature diamond." *Nature Photonics* 6 (1), 41–44, **2012**. DOI http://dx.doi.org/10.1038/nphoton.2011.296.

[456] M. Leifgen, T. Schröder, F. Gädeke, R. Riemann, *et al.*. "Evaluation of nitrogen- and silicon-vacancy defect centres as single photon sources in quantum key distribution." *New Journal of Physics* 16 (2), 023021, **2014**. DOI http://dx.doi.org/10.1088/1367-2630/16/2/023021.

[457] G. Balasubramanian, P. Neumann, D. Twitchen, M. Markham, *et al.*. "Ultralong spin coherence time in isotopically engineered diamond." *Nature Materials* 8, 383, **2009**. DOI http://dx.doi.org/10.1038/nmat2420http://10.0.4.14/nmat2420.

[458] P. C. Maurer, G. Kucsko, C. Latta, L. Jiang, *et al.*. "Room-temperature quantum bit memory exceeding one second." *Science* 336 (6086), 1283 LP – 1286, **2012**. DOI http://dx.doi.org/10.1126/science.1220513.

[459] E. Togan, Y. Chu, A. S. Trifonov, L. Jiang, *et al.*. "Quantum entanglement between an optical photon and a solid-state spin qubit." *Nature* 466, 730, **2010**. DOI http://dx.doi.org/10.1038/nature09256.

[460] T. van der Sar, Z. H. Wang, M. S. Blok, H. Bernien, *et al.*. "Decoherence-protected quantum gates for a hybrid solid-state spin register." *Nature* 484, 82, **2012**. DOI http://dx.doi.org/10.1038/nature10900.

[461] N. Y. Yao, L. Jiang, A. V. Gorshkov, P. C. Maurer, *et al.*. "Scalable architecture for a room temperature solid-state quantum information processor." *Nature Communications* 3, 800, **2012**. DOI http://dx.doi.org/10.1038/ncomms1788.

[462] W. Pfaff, B. J. Hensen, H. Bernien, S. B. van Dam, *et al.*. "Unconditional quantum teleportation between distant solid-state quantum bits." *Science* 345 (6196), 532 LP – 535, **2014**. DOI http://dx.doi.org/10.1126/science.1253512.

[463] H. Najar, M.-L. Chan, H.-A. Yang, L. Lin, *et al.*. "High quality factor nanocrystalline diamond micromechanical resonators limited by thermoelastic damping." *Applied Physics Letters* 104 (15), 151903, **2014**. DOI http://dx.doi.org/10.1063/1.4871803.

[464] M. Mitchell, B. Khanaliloo, D. P. Lake, T. Masuda, *et al.*. "Single-crystal diamond low-dissipation cavity optomechanics." *Optica* 3 (9), 963, **2016**. DOI http://dx.doi.org/10.1364/OPTICA.3.000963.

[465] M. J. Burek, J. D. Cohen, S. M. Meenehan, N. El-Sawah, *et al.*. "Diamond optomechanical crystals." *Optica* 3 (12), 1404, **2016**. DOI http://dx.doi.org/10.1364/OPTICA.3.001404.

[466] M. S. Hanay, S. Kelber, A. K. Naik, D. Chi, *et al.*. "Single-protein nanomechanical mass spectrometry in real time." *Nature Nanotechnology* 7 (9), 602–608, **2012**. DOI http://dx.doi.org/10.1038/nnano.2012.119.

[467] Y. Tao, J. M. Boss, B. A. Moores, and C. L. Degen. "Single-crystal diamond nanomechanical resonators with quality factors exceeding one million." *Nature Communications* 5, 3638, **2014**. DOI http://dx.doi.org/10.1038/ncomms4638.

[468] P. Rath, S. Ummethala, S. Diewald, G. Lewes-Malandrakis, *et al.*. "Diamond electro-optomechanical resonators integrated in nanophotonic circuits." *Applied Physics Letters* 105 (25), **2014**. DOI http://dx.doi.org/10.1063/1.4901105.

[469] J. L. O'Brien, A. Furusawa, and J. Vučković. "Photonic quantum technologies." *Nature Photonics* 3 (12), 687–695, **2009**. DOI http://dx.doi.org/10.1038/nphoton.2009.229.

[470] X.-S. Ma, S. Zotter, N. Tetik, A. Qarry, *et al.*. "A high-speed tunable beam splitter for feed-forward photonic quantum information processing." *Optics Express* 19 (23), 22723, **2011**. DOI http://dx.doi.org/10.1364/OE.19.022723.

[471] E. Knill, R. Laflamme, and G. J. Milburn. "A scheme for efficient quantum computation with linear optics." *Nature* 409 (6816), 46–52, **2001**. DOI http://dx.doi.org/10.1038/35051009.

[472] H. A. Atikian, A. Eftekharian, A. Jafari Salim, M. J. Burek, *et al.*. "Superconducting nanowire single photon detector on diamond." *Applied Physics Letters* 104 (12), **2014**. DOI http://dx.doi.org/10.1063/1.4869574.

[473] R. J. Nemanich, J. A. Carlisle, A. Hirata, and K. Haenen. "CVD diamond - Research, applications, and challenges." *MRS Bulletin* 39 (6), 490–494, **2014**. DOI http://dx.doi.org/10.1557/mrs.2014.97.

[474] P. W. May. "Diamond thin films: a 21st-century material." *Philosophical Transactions of the Royal Society A: Mathematical, Physical and Engineering Sciences* 358 (1766), 473–495, **2000**. DOI http://dx.doi.org/10.1098/rsta.2000.0542.

[475] R. P. Mildren and J. Rabeau. *Optical engineering of diamond.* Wiley-VCH Verlag GmbH, **2013**. ISBN 9783527648603.

[476] N. Mizuochi, T. Makino, H. Kato, D. Takeuchi, *et al.*. "Electrically driven single-photon source at room temperature in diamond." *Nature Photonics* 6 (5), 299–303, **2012**. DOI http://dx.doi.org/10.1038/nphoton.2012.75.

[477] M. Schreck, J. Asmussen, S. Shikata, J. C. Arnault, *et al.*. "Large-area high-quality single crystal diamond." *MRS Bulletin* 39 (6), 504–510, **2014**. DOI http://dx.doi.org/10.1557/mrs.2014.96.

[478] T. Jung, L. Kreiner, C. Pauly, F. Mücklich, *et al.*. "Reproducible fabrication and characterization of diamond membranes for photonic crystal cavities." *Physica Status Solidi (A) Applications and Materials Science* 213 (12), 3254–3264, **2016**. DOI http://dx.doi.org/10.1002/pssa.201600656.

[479] B. A. Fairchild, P. Olivero, S. Rubanov, A. D. Greentree, *et al.*. "Fabrication of ultrathin single-crystal diamond membranes." *Advanced Materials* 20 (24), 4793–4798, **2008**. DOI http://dx.doi.org/10.1002/adma.200801460.

[480] H. A. Atikian, P. Latawiec, M. J. Burek, Y.-I. Sohn, *et al.*. "Freestanding nanostructures via reactive ion beam angled etching." *APL Photonics* 2 (5), 051301, **2017**. DOI http://dx.doi.org/10.1063/1.4982603.

[481] B. Khanaliloo, M. Mitchell, A. C. Hryciw, and P. E. Barclay. "High-Q/V monolithic diamond microdisks fabricated with quasi-isotropic etching." *Nano Letters* 15 (8), 5131–5136, **2015**. DOI http://dx.doi.org/10.1021/acs.nanolett.5b01346.

[482] I. Bayn, A. Bolker, C. Cytermann, B. Meyler, *et al.*. "Diamond processing by focused ion beam-surface damage and recovery." *Applied Physics Letters* 99 (18), 1–4, **2011**. DOI http://dx.doi.org/10.1063/1.3658631.

[483] A. A. Martin, M. Toth, and I. Aharonovich. "Subtractive 3d printing of optically active diamond structures." *Scientific Reports* 4, 2–5, **2014**. DOI http://dx.doi.org/10.1038/srep05022.

[484] B. Sotillo, V. Bharadwaj, J. P. Hadden, M. Sakakura, *et al.*. "Diamond photonics platform enabled by femtosecond laser writing." *Scientific Reports* 6 (October), 1–9, **2016**. DOI http://dx.doi.org/10.1038/srep35566.

[485] F. Lenzini, N. Gruhler, N. Walter, and W. H. Pernice. "Diamond as a platform for integrated quantum photonics." *Advanced Quantum Technologies* , **2018**. Accepted for publication.

[486] K. D. Jahnke, B. Naydenov, T. Teraji, S. Koizumi, *et al.*. "Long coherence time of spin qubits in 12C enriched polycrystalline CVD diamond." *Applied Physics Letters* 101 (1), 012405, **2012**. DOI http://dx.doi.org/10.1063/1.4731778.

[487] R. G. Sandstrom, O. Shimoni, A. A. Martin, and I. Aharonovich. "Study of narrowband single photon emitters in polycrystalline diamond films." *Applied Physics Letters* 105 (18), 181104, **2014**. DOI http://dx.doi.org/10.1063/1.4901083.

[488] M. Füner, C. Wild, and P. Koidl. "Novel microwave plasma reactor for diamond synthesis." *Applied Physics Letters* 72 (10), 1149, **1998**. DOI http://dx.doi.org/10.1063/1.120997.

[489] M. Füner, C. Wild, and P. Koidl. "Simulation and development of optimized microwave plasma reactors for diamond deposition." *Surface and Coatings Technology* 116-119, 853–862, **1999**. DOI http://dx.doi.org/10.1016/S0257-8972(99)00233-9.

[490] E. L. Thomas, G. W. Nelson, S. Mandal, J. S. Foord, *et al.*. "Chemical mechanical polishing of thin film diamond." *Carbon* 68, 473–479, **2014**. DOI http://dx.doi.org/10.1016/J.CARBON.2013.11.023.

[491] D. R. Selviah, H. Baghsiahi, K. Wang, R. C. A. Pitwon, *et al.*. "Optical waveguide end facet roughness and optical coupling loss." *Journal of Lightwave Technology* 31 (16), 2959–2968, **2013**. URL https://www.osapublishing.org/jlt/abstract.cfm?uri=jlt-31-16-2959.

[492] P. Rath. "Integrated optomechanics and single-photon detection in diamond photonic integrated circuits." *PhD thesis* , **2016**. URL https://publikationen.bibliothek.kit.edu/1000064004.

[493] P. Achatz, J. A. Garrido, M. Stutzmann, O. A. Williams, *et al.*. "Optical properties of nanocrystalline diamond thin films." *Applied Physics Letters* 88 (10), 101908, **2006**. DOI http://dx.doi.org/10.1063/1.2183366.

[494] F. Trojánek, K. Žídek, B. Dzurňák, M. Kozák, *et al.*. "Nonlinear optical properties of nanocrystalline diamond." *Optics Express* 18 (2), 1349, **2010**. DOI http://dx.doi.org/10.1364/OE.18.001349.

[495] B. J. M. Hausmann, I. B. Bulu, P. B. Deotare, M. McCutcheon, *et al.*. "Integrated high-quality factor optical resonators in diamond." *Nano Letters* 13 (5), 1898–1902, **2013**. DOI http://dx.doi.org/10.1021/nl3037454.

[496] M. J. Burek, Y. Chu, M. S. Z. Liddy, P. Patel, *et al.*. "High quality-factor optical nanocavities in bulk single-crystal diamond." *Nature Communications* 5, 5718, **2014**. DOI http://dx.doi.org/10.1038/ncomms6718.

[497] B. Feigel, F. Gao, H. Thienpont, J. V. Erps, *et al.*. "Low-loss millimeter-length waveguides and grating couplers in single-crystal diamond." *Journal of Lightwave Technology* 34 (23), 5576–5582, **2016**. DOI http://dx.doi.org/10.1109/JLT.2016.2622620.

[498] F. Liu, J. Z. H. Zhang, and Y. Mei. "The origin of the cooperativity in the streptavidin-biotin system: A computational investigation through molecular dynamics simulations." *Scientific Reports* 6 (1), 27190, **2016**. DOI http://dx.doi.org/10.1038/srep27190.

[499] A. Bykhovski, W. Zhang, J. Jensen, and D. Woolard. "Analysis of electronic structure, binding, and vibrations in biotin-streptavidin complexes based on density functional theory and molecular mechanics." *The Journal of Physical Chemistry B* 117 (1), 25–37, **2013**. DOI http://dx.doi.org/10.1021/jp3075833.

[500] G. L. Bratthauer. "The avidin-biotin complex (ABC) method and other avidin-biotin binding methods." In *Immunocytochemical Methods and Protocols*, 257–270. Humana Press, **2010**. ISBN 9781597453240. DOI http://dx.doi.org/10.1007/978-1-59745-324-0_26.

[501] M. Norton. "Designed self-organization for molecular optoelectronic sensors." *International Journal of High Speed Electronics and Systems* 17 (02), 311–326, **2007**. DOI http://dx.doi.org/10.1142/S0129156407004527.

[502] G. J. Mizejewski. "Alpha-fetoprotein structure and function: Relevance to isoforms, epitopes, and conformational variants." *Experimental Biology and Medicine* 226 (5), 377–408, **2001**. DOI http://dx.doi.org/10.1177/153537020122600503.

[503] T. B. Tomasi. "Structure and function of alpha-fetoprotein." *Annual Review of Medicine* 28 (1), 453–465, **1977**. DOI http://dx.doi.org/10.1146/annurev.me.28.020177.002321.

[504] J. I. Blair, R. Carachi, R. Gupta, F. G. Sim, *et al.*. "Plasma alpha fetoprotein reference ranges in infancy: effect of prematurity." *Archives of disease in childhood* 62 (4), 362–9, **1987**. DOI http://dx.doi.org/10.1136/ADC.62.4.362.

[505] D. Ball, E. Rose, and E. Alpert. "Alpha-fetoprotein levels in normal adults." *The American Journal of the Medical Sciences* 303 (3), 157–159, **1992**. DOI http://dx.doi.org/10.1097/00000441-199203000-00004.

[506] J. M. Ertle, D. Heider, M. Wichert, B. Keller, *et al.*. "A combination of α-fetoprotein and des-γ-carboxy prothrombin is superior in detection of hepatocellular carcinoma." *Digestion* 87 (2), 121–31, **2013**. DOI http://dx.doi.org/10.1159/000346080.

[507] R. Xu, Y. Jiang, L. Xia, T. Zhang, *et al.*. "A sensitive photoelectrochemical biosensor for AFP detection based on ZnO inverse opal electrodes with signal amplification of CdS-QDs." *Biosensors and Bioelectronics* 74, 411–417, **2015**. DOI http://dx.doi.org/10.1016/J.BIOS.2015.06.037.

[508] Y. Jiang, D. Liu, Y. Yang, R. Xu, *et al.*. "Photoelectrochemical detection of alpha-fetoprotein based on ZnO inverse opals structure electrodes modified by Ag2S nanoparticles." *Scientific Reports* 6 (1), 38400, **2016**. DOI http://dx.doi.org/10.1038/srep38400.

[509] Q. Wang, R. Li, K. Shao, Y. Lin, *et al.*. "A portable immunosensor with differential pressure gauges readout for alpha fetoprotein detection." *Scientific Reports* 7 (1), 45343, **2017**. DOI http://dx.doi.org/10.1038/srep45343.

[510] L. M. Wright, J. T. Kreikemeier, and C. J. Fimmel. "A concise review of serum markers for hepatocellular cancer." *Cancer Detection and Prevention* 31 (1), 35–44, **2007**. DOI http://dx.doi.org/10.1016/J.CDP.2006.11.003.

[511] H. Yu, F. Yan, Z. Dai, and H. Ju. "A disposable amperometric immunosensor for α-1-fetoprotein based on enzyme-labeled antibody/chitosan-membrane-modified screen-printed carbon electrode." *Analytical Biochemistry* 331 (1), 98–105, **2004**. DOI http://dx.doi.org/10.1016/J.AB.2004.03.042.

[512] X. Feng, G. Zhang, L. K. Chin, A. Q. Liu, *et al.*. "Highly sensitive, label-free detection of 2,4-dichlorophenoxyacetic acid using an optofluidic chip." *ACS Sensors* 2 (7), 955–960, **2017**. DOI http://dx.doi.org/10.1021/acssensors.7b00217.

[513] K. Li, G. Liu, Y. Wu, P. Hao, *et al.*. "Gold nanoparticle amplified optical microfiber evanescent wave absorption biosensor for cancer biomarker detection in serum." *Talanta* 120, 419–424, **2014**. DOI http://dx.doi.org/10.1016/J.TALANTA.2013.11.085.

[514] Q. Xie, X. Weng, L. Lu, Z. Lin, *et al.*. "A sensitive fluorescent sensor for quantification of alpha-fetoprotein based on immunosorbent assay and click chemistry." *Biosensors and Bioelectronics* 77, 46–50, **2016**. DOI http://dx.doi.org/10.1016/J.BIOS.2015.09.015.

[515] S. Ummethala, P. Rath, G. Lewes-Malandrakis, D. Brink, *et al.*. "High-Q optomechanical circuits made from polished nanocrystalline diamond thin films." *Diamond and Related Materials* 44, 49–53, **2014**. DOI http://dx.doi.org/10.1016/j.diamond.2014.02.005.

[516] V. Singh, P. T. Lin, N. Patel, H. Lin, *et al.*. "Mid-infrared materials and devices on a Si platform for optical sensing." *Science and Technology of Advanced Materials* 15 (1), 014603, **2014**. DOI http://dx.doi.org/10.1088/1468-6996/15/1/014603.

[517] M. Malmström, M. Karlsson, P. Forsberg, Y. Cai, *et al.*. "Waveguides in polycrystalline diamond for mid-IR sensing." *Optical Materials Express* 6 (4), 1286, **2016**. DOI `http://dx.doi.org/10.1364/OME.6.001286`.

[518] X. Wang, M. Karlsson, P. Forsberg, M. Sieger, *et al.*. "Diamonds are a spectroscopists best friend: Thin-film diamond mid-infrared waveguides for advanced chemical sensors/biosensors." *Analytical Chemistry* 86 (16), 8136–8141, **2014**. DOI `http://dx.doi.org/10.1021/ac5011475`.

[519] Á. I. López-Lorente, P. Wang, M. Sieger, E. Vargas Catalan, *et al.*. "Mid-infrared thin-film diamond waveguides combined with tunable quantum cascade lasers for analyzing the secondary structure of proteins." *Physica Status Solidi (A) Applications and Materials Science* 213 (8), 2117–2123, **2016**. DOI `http://dx.doi.org/10.1002/pssa.201600134`.

[520] J. Haas, E. V. Catalán, P. Piron, F. Nikolajeff, *et al.*. "Polycrystalline diamond thin-film waveguides for mid-infrared evanescent field sensors." *ACS Omega* 3 (6), 6190–6198, **2018**. DOI `http://dx.doi.org/10.1021/acsomega.8b00623`.

[521] M. Pu, L. Liu, H. Ou, K. Yvind, *et al.*. "Ultra-low-loss inverted taper coupler for silicon-on-insulator ridge waveguide." *Optics Communications* 283 (19), 3678–3682, **2010**. DOI `http://dx.doi.org/10.1016/J.OPTCOM.2010.05.034`.

[522] G. Ren, S. Chen, Y. Cheng, and Y. Zhai. "Study on inverse taper based mode transformer for low loss coupling between silicon wire waveguide and lensed fiber." *Optics Communications* 284 (19), 4782–4788, **2011**. DOI `http://dx.doi.org/10.1016/J.OPTCOM.2011.05.072`.

[523] F. Ay, I. Iñurrategui, D. Geskus, S. Aravazhi, *et al.*. "Integrated lasers in crystalline double tungstates with focused-ion-beam nanostructured photonic cavities." *Laser Physics Letters* 8 (6), 423–430, **2011**. DOI `http://dx.doi.org/10.1002/lapl.201110013`.

[524] A. Nitkowski, L. Chen, and M. Lipson. "Cavity-enhanced on-chip absorption spectroscopy using microring resonators." *Optics Express* 16 (16), 11930, **2008**. DOI `http://dx.doi.org/10.1364/OE.16.011930`.

[525] A.-K. U. Michel, D. N. Chigrin, T. W. W. Maß, K. Schönauer, *et al.*. "Using low-loss phase-change materials for mid-infrared antenna resonance tuning." *Nano Letters* 13 (8), 3470–3475, **2013**. DOI `http://dx.doi.org/10.1021/nl4006194`.

[526] K. Du, L. Cai, H. Luo, Y. Lu, *et al.*. "Wavelength-tunable mid-infrared thermal emitters with a non-volatile phase changing material." *Nanoscale* 10 (9), 4415–4420, **2018**. DOI `http://dx.doi.org/10.1039/C7NR09672K`.

[527] V. Bharadwaj, Y. Wang, T. T. Fernandez, R. Ramponi, *et al.*. "Femtosecond laser written diamond waveguides - a step towards integrated photonics in the far infrared." , **2018**. DOI `http://arxiv.org/abs/1806.05412`.

[528] B. Tatian. "Fitting refractive-index data with the Sellmeier dispersion formula." *Applied Optics* 23 (24), 4477, **1984**. DOI `http://dx.doi.org/10.1364/AO.23.004477`.

[529] C. Tan. "Determination of refractive index of silica glass for infrared wavelengths by IR spectroscopy." *Journal of Non-Crystalline Solids* 223 (1-2), 158–163, **1998**. DOI `http://dx.doi.org/10.1016/S0022-3093(97)00438-9`.

[530] T. Bååk. "Silicon oxynitride; a material for GRIN optics." *Applied Optics* 21 (6), 1069, **1982**. DOI http://dx.doi.org/10.1364/AO.21.001069.

[531] J. Pastrňák and L. Roskovcová. "Refraction index measurements on AlN single crystals." *physica status solidi (b)* 14 (1), K5–K8, **1966**. DOI http://dx.doi.org/10.1002/pssb.19660140127.

[532] A. Yariv. "Universal relations for coupling of optical power between microresonators and dielectric waveguides." *Electronics letters* 36 (4), 321–322, **2000**. DOI http://dx.doi.org/10.1049/el:20000340.

[533] W. R. McKinnon, D. X. Xu, C. Storey, E. Post, *et al.*. "Extracting coupling and loss coefficients from a ring resonator." *Optics Express* 17 (21), 18971, **2009**. DOI http://dx.doi.org/10.1364/OE.17.018971.

[534] S. K. Ghandhi. *VLSI fabrication principles: silicon and gallium arsenide*. Wiley, 2. edn., **1994**. ISBN 9780471580058.

[535] I. C. Plumb and K. R. Ryan. "Gas-phase reactions of CF3 and CF2 with atomic and molecular fluorine: Their significance in plasma etching." *Plasma Chemistry and Plasma Processing* 6 (1), 11–25, **1986**. DOI http://dx.doi.org/10.1007/BF00573818.

[536] Y. X. Li. "Selective reactive ion etching of silicon nitride over silicon using CHF3 with N2 addition." *Journal of Vacuum Science & Technology B: Microelectronics and Nanometer Structures* 13 (5), 2008, **1995**. DOI http://dx.doi.org/10.1116/1.588124.

[537] T. C. Mele. "Selective and anisotropic reactive ion etch of LPCVD silicon nitride with CHF3 based gases." *Journal of Vacuum Science & Technology B: Microelectronics and Nanometer Structures* 2 (4), 684, **1984**. DOI http://dx.doi.org/10.1116/1.582863.

[538] W. J. W. J. Thompson. *Angular momentum: an illustrated guide to rotational symmetries for physical systems*. Wiley, **1994**. ISBN 9780471552642.

[539] A. R. Edmonds. *Angular momentum in quantum mechanics*. Princeton University Press, **1996**. ISBN 9780691025896. DOI https://press.princeton.edu/titles/478.html.

[540] A. N. Nesmejanov. *Vapor pressure of the chemical elements*. Elsevier, Amsterdam [u.a.], **1963**.

Zusammenfassung in deutscher Sprache

Einleitung und Umfang der Arbeit

Die optische Datenübertragung über Glasfaserkabel ist von großer Bedeutung, um dem anhaltend stark steigenden Datenaufkommen der heutigen Informationsgesellschaft gerecht zu werden. Dies verdeutlicht den Einfluss von Lichtleitung, der Führung einer elektromagnetischen Welle in einem transparenten Material aufgrund von interner Totalreflexion, auf den aktuellen technologischen Fortschritt. Während Glasfaserkabel schon seit Jahrzehnten steigende Übertragungsraten für die Langstreckenkommunikation ermöglichen, ersetzt die optische Datenübertragung nun auch elektronische Systeme auf immer kürzeren Kommunikationsstrecken. Optische Verbindungen zwischen einzelnen Servern und Platinen gehören inzwischen zum Standard und in der Grundlagenforschung wird intensiv an optischen Verbindungen zwischen sowohl einzelnen Chips als auch zwischen einzelnen Bauteilen auf einem Chip geforscht.

Parallel zur Nutzung optischer Datenverbindungen wurden integrierte optische Schaltkreise entwickelt, die auf der Lichtleitung in dielektrischen Wellenleitern beruhen. Dadurch können komplexe optische Aufbauten, für die sonst typischerweise Freistrahloptiken verwendet werden, verkleinert und vereinfacht werden. Dies führt zu einer deutlichen Steigerung der Stabilität und Verlässlichkeit, einhergehend mit einer Senkung der Produktionskosten aufgrund der möglichen Massenproduktion skalierbarer Schaltkreise. Außerdem wird eine größere Bandbreite für die Datenübertragung innerhalb eines Chips ermöglicht. Dies geschieht bei gleichzeitiger Senkung der Wärmeentwicklung durch Verlustleistungen, was eine der gravierendsten Einschränkungen aktueller elektronischer Platinenarchitekturen darstellt.

Ein zentrales Element vieler Anwendungen, die auf integrierten optischen Schaltkreisen beruhen, ist die Kopplung geführter Moden an zusätzliche Elemente in ihrem direkten Umfeld. Aufgrund ihres evaneszenten Feldes reagieren die Moden empfindlich auf jegliche Änderung der Umgebung. Dies wird ausgenutzt, um die Eigenschaften einer geführten Welle aktiv zu kontrollieren oder um Modifikationen im Umfeld zu detektieren. Prominente Beispiele sind quantenoptische Einzelphotonenschaltkreise, in denen Einzelphotonenquellen (wie z.B. Quantenpunkte oder Farbzentren in Nanodiamanten) und -detektoren (z.B. bestehend aus supraleitenden Nanodrähten) an integrierte Wellenleiter gekoppelt werden sowie die Anbindung von Phasenwechselmaterialien an Wellenleiterstrukturen für die Herstellung volloptischer nichtflüchtiger Bauteile (z.B. als Speicherelement, Schalter oder optische Synapse).

In dieser Arbeit wird das Potential der Kopplung geführter Moden in integrierten optischen Wellenleitern an umgebende Elemente studiert mit dem Fokus auf die Anwendung dieser Systeme als

Sensoren. In Wellenleitern ist ein sehr starkes optisches Feld auf ein kleines Volumen eingeschränkt, wodurch die Empfindlichkeit für Änderungen der Umgebung maßgeblich verstärkt wird. Im Vergleich zu Detektoren, die auf wenigen Reflektionen an optischen Grenzflächen aufbauen, ermöglicht die Verwendung von Wellenleitern außerdem eine deutlich gesteigerte Interaktionslänge.

Im ersten Teil der Arbeit wird die Kopplung von Wellenleitermoden an einen umgebenden Atomdampf untersucht. Typischerweise werden ultrakalte Atome für extrem präzise Messungen, z.B. im Bereich der Metrologie oder Quantenelektrodynamik, verwendet, wofür aber sehr große Aufbauten benötigt werden. Im Gegensatz dazu ermöglicht der Einsatz thermischer Atomdämpfe aufgrund der geringen technischen Komplexität die Miniaturisierung solcher Experimente sowie die Anbindung an integrierte Strukturen. Die Kopplung zwischen Wellenleitermoden und einem Atomdampf kann beispielsweise ausgenutzt werden, um schnelle volloptische Modulatoren, Routenführungen und Schalter zu realisieren (z.B. auf der Basis von elektromagnetisch induzierter Transparenz oder von Zweiphotonenabsorption bei Ringresonatoren). Ein weiterer wichtiger Anwendungsbereich ist die Verwendung als Doppler-freie Frequenzreferenz zur Stabilisierung optischer Systeme auf Chipgröße. Dazu kommt die Erfassung fundamentaler Absorptionsspektren, was von zentraler Bedeutung für die Verwendung eines integrierten Schaltkreises als Sensorelement ist. Konkret wird hier die Kopplung an einen Rubidium-Atomdampf untersucht, wobei die Elektronenanregung innerhalb der Rb D2 Linie bei einer Wellenlänge von 780 nm verwendet wird.

Die Aufzeichnung von Absorptionsspektren stellt einen wichtigen Bereich der Analyseverfahren mithilfe integrierter optischer Strukturen dar. Dies betrifft nicht nur die Atomspektroskopie vor allem im sichtbaren Wellenlängenbereich, sondern insbesondere auch die chemische Analyse von Molekülen im mittel- und langwelligen Infrarotbereich (MIR, LWIR). In diesen Wellenlängenbereichen von 2 µm bis 20 µm liegen die Absorptionsbänder vieler chemischer Bindungen sowie die einzigartigen Absorptionsspektren vieler Moleküle und funktioneller Gruppen. Um aber integrierte optische Sensoren zu realisieren, wird eine neuartige Materialplattform benötigt, die in diesem Spektralbereich sowohl transparent ist als auch interne Totalreflektion ermöglicht. Die Entwicklung solch einer Materialplattform wird im zweiten Teil dieser Arbeit vorgestellt.

Drei unterschiedliche Materialsysteme werden im Verlauf der Arbeit eingeführt, um die Anforderungen der einzelnen Anwendungen zu erfüllen. Siliziumnitrid (Si_3N_4) wird als fundamentale Plattform für Anwendungen im sichtbaren und nah-infraroten (NIR) Spektralbereich verwendet. Eine sehr niedrige Absorption und ein Transparenzfenster von 0.3-5.3 µm ermöglichen hochqualitative integrierte optische Schaltkreise. Silizium ist im Gegensatz dazu aufgrund seiner Bandlücke auf ein Wellenlängenintervall oberhalb von 1.1 µm begrenzt. Allerdings reicht das nutzbare Spektrum bis zu einer Wellenlänge von ca. 8.5 µm und daher wird Silizium als Referenzmaterial für die Leistungsfähigkeit der integrierten Bauteile in diesem Spektralbereich verwendet. Im Bezug auf den nutzbaren Wellenlängenbereich werden aber alle Materialien von Diamant weit übertroffen. Das Transparenzfenster beginnt nahe des ultravioletten (UV) Bereichs und reicht bis hin zu einer Wellenlänge um die 500 µm im fern-infraroten (FIR) Bereich. Dadurch wird die Herstellung integrierter optischer Bauteile für den sichtbaren ($\lambda \approx 650$ nm),

NIR ($\lambda \approx 1550\,\text{nm}$) und LWIR ($\lambda \approx 8\,\mu\text{m}$) Bereich auf ein und derselben Probe ermöglicht. Aufgrund der mechanischen Stabilität und der chemischen Inaktivität, eignet sich Diamant außerdem hervorragend als Material für Sensoren in biowissenschaftlichen Anwendungen. Dies wird ausgenutzt, um den optischen Nachweis der Proteinbindung an die funktionalisierte Diamantoberfläche zu testen.

Durchführung und Ergebnisse

Integrierte optische Schaltkreise aus Si_3N_4 dienen als Grundlage für die Mehrzahl der Forschungsprojekte in unserer Arbeitsgruppe. Daher war die die Entwicklung dieser Materialplattform von besonderer Bedeutung und durch die Optimierung des Herstellungsprozess wurden hochqualitative Schaltkreise ermöglicht. Dies zeigt sich in der Evaluation der Transmissionspektren integrierter Ringresonatoren bei einer Wellenlänge von 1550 nm. Für schwach gekoppelte Ringe wird ein Qualitätsfaktor von über 1×10^6 erreicht, was einem sehr geringen Verlust von 21 dB/m entspricht. Damit wird für kritisch gekoppelte Ringe ein Qualitätsfaktor von 5×10^5 ermöglicht. Durch die Verwendung ausgeglichener integrierter Strahlteiler können Mach-Zehnder Interferometern (MZIs) mit einem sehr guten Extinktionsverhältnis von 40 dB hergestellt werden. Diese sind insbesondere für die Erkennung kleinster Phasenverschiebungen innerhalb eines Wellenleiters geeignet. Ebenso wurden die Bauteile im sichtbaren Spektralbereich charakterisiert. Für kritisch gekoppelte Ringresonatoren (Extinktionsverhältnis von 12 dB) wurde ein Qualitätsfaktor von 9.6×10^4 gemessen, was einem Verlust von 1.1 dB/cm im Wellenleiter entspricht. Damit gehören diese integrierten optischen Schaltkreisen zu den besten Si_3N_4 Strukturen, die je hergestellt wurden. Niedrigere Verluste wurden bisher nur erreicht, indem die Schaltkreise zum einen komplett in eine Glasschicht eingebettet wurden (was die Streuverluste an Oberflächenrauigkeiten verringert) und zum anderen indem sie nach der Herstellung bei Temperaturen um die 1200 °C ausgeglüht wurden (was eine Reduzierung von absorbierenden Wasserstoffbindungen im Material zur Folge hat).

Die oben beschriebene Si_3N_4 Plattform wurde für die Realisierung integrierter optischer Strukturen verwendet, die mit einem Rubidium-Atomdampf wechselwirken. Typischerweise wird Licht über Gitterkoppler in die optischen Schaltkreise eingekoppelt, indem direkt oberhalb des Kopplers ein Faserende platziert wird. Da die Strukturen im Falle der Rubidium-Kopplung von einem Atomdampf umgeben sind, musste dieses Schema modifiziert werden. Ein transparentes Substrat ermöglicht die Einkopplung von Licht in die photonischen Strukturen durch die Rückseite des Chips, indem ein Laserstrahl durch das Substrat auf die Gitterkoppler fokussiert wird. Durch die Verwendung der Gitterkoppler zum Ein- und Auskoppeln kann weiterhin die komplette Probenfläche optimal für die integrierten Strukturen genutzt werden. Auf der Probenoberfläche wurde ein Großteil der Strukturen von einer Wasserstoffsilsesquioxan-Schicht (engl. hydrogen silsesquioxane (HSQ), glasartig) abgedeckt, wodurch eine präzise Interaktionsregion für die Atomdampfkopplung definiert wird. Die Proben wurden mithilfe von anodischem Bonden mit einer kleinen Dampfzelle verbunden, an die ein Rubidiumreservoir angeschlossen ist. Dadurch wurde eine sehr kompakte und damit gut handhabbare Zelle für die Ankopplung

von Wellenleitermoden an einen thermischen Atomdampf geschaffen.

Lineare Absorptionspektren der Rb D2 Linie wurden aufgenommen, um die Interaktionsstärke zu charakterisieren und um die grundlegende Eignung dieser Strukturen für spektroskopische Analysen aufzuzeigen. Die Elektronenanregung der Rubidiumatome führt aber nicht nur zur Absorption eines Lichtstrahls, sondern auch zur Beeinflussung des Realteils des effektiven Brechungsindex einer geführten Mode. Dies verursacht eine Phasenverschiebung der Mode im Spektralbereich des Elektronenübergangs. Um diesen Effekt quantitativ auszuwerten, wurden integrierte MZIs verwendet, bei denen ein Arm des Interferometers dem Atomdampf ausgesetzt ist. Durch die Bestimmung der Absorption sowie der Phasenverschiebung konnte die Kopplung des Rb Atomdampfes an einen Wellenleiter umfassend beschrieben werden. Zusätzlich wurde ein theoretisches Modell der Wechselwirkung eingeführt und mittels numerischer Methoden der Einfluss der Atome auf die Wellenleitermoden simuliert. Dieses Modell zeigt eine sehr gute Übereinstimmung mit den experimentell bestimmten Daten und eignet sich daher gut für die Beschreibung der Kopplung und um Prognosen bezüglich weiterer Bauteile abzugeben. Das Zusammenspiel der Absorption und Phasenverschiebung zeigt sich insbesondere bei der Verwendung von Ringresonatoren, die zur Verstärkung der Wechselwirkung verwendet wurden. Abhängig von der relativen spektralen Position sowie der Breite der Ringresonanz und der Absorptionslinien, tragen die beiden Einflussfaktoren unterschiedlich stark zum resultierenden Spektrum bei. Abschließend wurde der Einsatz von Spaltwellenleitern zur Verstärkung der Wechselwirkung studiert. In diesen Wellenleitern sitzt der Hauptteil des optischen Feldes in einem Spalt zwischen zwei dielektrischen Streifen. Dadurch kann ein extrem hoher Anteil der Strahlungsintensität außerhalb der massiven Streifen erreicht werden. Da dieser Bereich für den umgebenden Atomdampf direkt zugänglich ist, wird die Kopplung signifikant verstärkt.

Das Potential integrierter Strukturen als optische Sensoren wurde durch die Entwicklung von Schaltkreisen für den LWIR Bereich stark erweitert. Durch den Einsatz schwebender Siliziumstrukturen (gehalten von Brücken in einer dünnen Siliziummembran) wurden die Einschränkung einer absorbierenden Pufferschicht umgangen. Dadurch konnten Bauteile für den Einsatz im NIR und LWIR Breich auf der selben Materialplattform realisiert werden. Anhand von Ringresonatoren mit einem Qualitätsfaktor von bis zu 1×10^5 wurde bei einer Wellenlänge von 1550 nm ein Propagationsverlust von 0.5 dB/mm bestimmt. Im LWIR Bereich, bei einer Wellenlänge von 8 µm, wurde die Transmission durch Wellenleiter mit einer Länge von 9 mm gemessen und ein Verlust von 1 dB/mm abgeschätzt. Damit wurde die erstmalige Verwendung integrierte Siliziumstrukturen in diesem Spektralbereich prÃd'sentiert. Vorherige Anwendungen reichten bis zu einer maximalen Wellenlänge von 5.2 µm.

Um den nutzbaren Spektralbereich darüber hinaus zu erweitern, wurde Diamant als dritte Materialplattform eingeführt. Polykristalline Diamantschichten, die per chemischer Gasphasenabscheidung hergestellt werden, dienen als Grundlage für die Fertigung integrierter Schaltkreise. Erste Diamantstrukturen für Anwendungen im NIR Bereich wurden auf einer Glaspufferschicht hergestellt. Dabei wurde ein Propagationsverlust von 4.3 dB/mm erreicht. Diese Plattform wurde verwendet, um die optische Detektierung der Proteinbindung an eine funktionalisiert Oberfläche zu testen. Hierbei wurde

die Bindung zwischen Strepdavidin und Biotin, sowie zwischen Alphafetoprotein (AFP) und dessen Antikörper untersucht. Der Nachweis von AFP spielt insbesondere bei der Früherkennung bestimmter Krebsarten eine tragende Rolle.

Um Diamant als Plattform für die spektroskopische Analyse von Molekülen und chemischen Bindungen im LWIR Bereich zu verwenden, muss die darunterliegende Glasschicht ersetzt werden. Es wurde beispielsweise eine Aluminiumnitridschicht (AlN) als Puffer verwendet, was erste Diamantschaltkreise bei einer Wellenlänge von 8 µm ermöglicht hat. Die Absorption der verwendeten AlN Schicht verursacht allerdings ebenfalls hohe Propagationsverluste und es bedarf einer Optimierung der AlN Abscheidung, um diese Plattform tatsächlich konkurrenzfähig zu machen. Stattdessen wurden auch hier schwebende Diamantstrukturen eingeführt, die von schmalen Brücken in einer Diamantmembran gehalten werden. Damit konnten Bauteile für den sichtbaren ($\lambda = 650\,\text{nm}$), NIR ($\lambda = 1550\,\text{nm}$, 8.9 dB/mm Verlust), sowie LWIR ($\lambda = 8\,\mu\text{m}$, 9.8 dB/mm Verlust) Bereich verwirklicht werden. Diese einzigartige Verbindung verschiedener Spektralbereiche innerhalb einer kompakten Materialplattform eröffnet ungeahnte Möglichkeiten für die Kombination unterschiedlichster Sensorsysteme. Dabei sind die Diamantstrukturen sogar noch erweiterbar für die Nutzung im kurzwelligen (nahezu bis zum UV Bereich), sowie im langwelligen Bereich (bis tief in den FIR Bereich). Sowohl auf der Silizium- als auch auf der Diamantplattform wurde die Ein- und Auskopplung von Licht mithilfe von Gitterkopplern und über die Wellenleiterfacette ermöglicht. In Kombination mit kompakten Wellenleitern (ca. 1.5 µm x 4.5 µm Querschnitt) können somit komplexe optische Schaltungen, die die komplette Chipfläche ausnutzen, hergestellt werden.

Ausblick

Die Ergebnisse dieser Arbeit zeigen, dass integrierte optische Strukturen vielversprechend für die zukünftige Entwicklung hochempfindlicher Sensoren in unterschiedlichsten Wellenlängenbereichen sind. Dabei kann die Kopplung durch die Verwendung integrierter optischer Resonatoren und Spaltwellenleitern verstärkt werden. Dies wurde beispielsweise anhand der Kopplung zu einem Rubidium-Atomdampf aufgezeigt. Eine Vestärkung des Effekt kann durch die Verwendung hochqualitativer Kavitäten weiter untersucht werden. Indem ein Zweiphotonenübergang verwendet wird (z.B. der Rb Übergang $5^2S_{1/2} \rightarrow 5^2P_{3/2} \rightarrow 4^3D_{3/2}$, der aus der D2 Linie besteht, gefolgt von einer Anregung bei einer Wellenlänge von 1529 nm), kann die Wechselwirkung in den NIR Bereich verschoben werden. Damit wird die Kopplung an Si_3N_4 Ringresonatoren mit extrem hohen Qualitätsfaktoren bis zu 1×10^6 ermöglicht. Um andererseits das Kopplungsvolumen deutlich zu verkleinern, können photonische Kristallkavitäten verwendet werden. Diese können auch mit Spaltwellenleitern kombiniert werden, um eine extrem große optische Intensität im Bereich der Atome mit einem sehr kleinen Modenvolumen des Resonators zu verbinden.

Für die zukünftige Entwicklung optischer Schaltkreise im LWIR Bereich steht die Weiterentwicklung des Messaufbaus an erster Stelle. Dadurch wird die Aufnahme von Transmissionsspektren ermöglicht,

mit denen die Leistungsfähigkeit der Strukturen exakt vermessen werden kann. Dies ist außerdem eine Voraussetzung für die Erfassung von Molekülspektren zur chemischen Analyse. Darauf folgend können sowohl integrierte Mikrokavitäten verwendet werden, um die Spektroskopie zu unterstützen, als auch mögliche Phasenverschiebungen mithilfe von MZIs erfasst werden. Die Implementierung integrierter, hochempfindlicher Einzelphotonendetektoren für den LWIR Bereich stellt einem weiterer Entwicklungsschritt hin zur Verkleinerung des gesamten optischen Aufbaus dar. Dadurch würde das Erfassen des Transmissionssignals außerhalb des Chips entfallen. Die hier gezeigten Diamantbauteile wurden in polykristallinen Schichten realisiert. Da die Korngrenzen zwischen den einzelnen Kristallen ein Hauptgrund sowohl für Streuverluste als auch für Materialabsorption sind, ist ein Transfer der Strukturen auf einkristalline Diamantschichten hochinteressant. Dies geht zwar einher mit komplexeren Herstellungsverfahren und die verfügbaren Schichten sind in ihrer Fläche stark begrenzt, die Qualität der Schaltkreise kann dadurch aber deutlich gesteigert werden. Daher gehört dies sicherlich zu den zukünftigen Entwicklungen der integrierten Diamantphotonik auch im LWIR Bereich. Die Erschließung des langwelligen Spektralbereichs ist nicht nur von großem Interesse für die Molekülspektroskopie, sondern auch generell für die chipbasierte Integration optischer Systeme. Damit stellt die Erweiterung des nutzbaren Spektralbereichs eine enorme Wachstumschance für das Feld der integrierten Optik dar.

List of Publications

[1] F. Lenzini, **N. Gruhler**, N. Walter, and W. H. P. Pernice, "Diamond as a Platform for Integrated Quantum Photonics," *Adv. Quantum Technol.*, *accepted for publication*, 2018.

[2] J. von Keitz, J. Feldmann, **N. Gruhler**, C. Ríos, C. D. Wright, H. Bhaskaran, and W. H. P. Pernice, "Reconfigurable nanophotonic cavities with nonvolatile response," *ACS Photonics*, *submitted*, 2018.

[3] R. Ritter, **N. Gruhler**, H. Dobbertin, H. Kübler, S. Scheel, W. H. P. Pernice, T. Pfau, and R. Löw, "Coupling Thermal Atomic Vapor to Slot Waveguides," *Phys. Rev. X* 8 (2), 021032, May 2018.
DOI: `http://dx.doi.org/10.1103/PhysRevX.8.021032`

[4] P. Lombardi, A. P. Ovvyan, S. Pazzagli, G. Mazzamuto, G. Kewes, O. Neitzke, **N. Gruhler**, O. Benson, W. H. P. Pernice, F. S. Cataliotti, and C. Toninelli, "Photostable Molecules on Chip: Integrated Sources of Nonclassical Light," *ACS Photonics* 5 (1), 126-132, Jan. 2018.
DOI: `http://dx.doi.org/10.1021/acsphotonics.7b00521`

[5] J. Feldmann, M. Stegmaier, **N. Gruhler**, C. Ríos, H. Bhaskaran, C. D. Wright, and W. H. P. Pernice, "Calculating with light using a chip-scale all-optical abacus," *Nat. Commun.* 8 (1), 1256, Dec. 2017.
DOI: `http://dx.doi.org/10.1038/s41467-017-01506-3`

[6] P. Tonndorf, O. Del Pozo-Zamudio, **N. Gruhler**, J. Kern, R. Schmidt, A. I. Dmitriev, A. P. Bakhtinov, A. I. Tartakovskii, W. H. P. Pernice, S. Michaelis de Vasconcellos, and R. Bratschitsch, "On-Chip Waveguide Coupling of a Layered Semiconductor Single-Photon Source," *Nano Lett.* 17 (9), 5446-5451, Sep. 2017.
DOI: `http://dx.doi.org/10.1021/acs.nanolett.7b02092`

[7] S. Checcucci, P. Lombardi, S. Rizvi, F. Sgrignuoli, **N. Gruhler**, F. B. C. Dieleman, F. S. Cataliotti, W. H. P. Pernice, M. Agio, and C. Toninelli, "Beaming light from a quantum emitter with a planar optical antenna," *Light Sci. Appl.* 6 (4), e16245-e16245, Apr. 2017.
DOI: `http://dx.doi.org/10.1038/lsa.2016.245`

[8] R. Ritter, **N. Gruhler**, W. H. P. Pernice, H. Kübler, T. Pfau, and R. Löw, "Coupling thermal atomic vapor to an integrated ring resonator," *New J. Phys.* 18 (10),103031, Oct. 2016.
DOI: `http://dx.doi.org/10.1088/1367-2630/18/10/103031`

[9] **N. Gruhler**, T. Yoshikawa, P. Rath, G. Lewes-Malandrakis, E. Schmidhammer, C. Nebel, and W. H. P. Pernice, "Diamond on aluminum nitride as a platform for integrated photonic circuits," *Phys. status solidi A* 213 (8), 2075-2080, Aug. 2016.
DOI: `http://dx.doi.org/10.1002/pssa.201600227`

[10] A. P. Ovvyan, **N. Gruhler**, S. Ferrari, and W. H. P. Pernice, “Cascaded Mach-Zehnder interferometer tunable filters,” *J. Opt.* 18 (6), 064011, Jun. 2016.
DOI: `http://dx.doi.org/10.1088/2040-8978/18/6/064011`

[11] R. Ritter, **N. Gruhler**, W. Pernice, H. Kübler, T. Pfau, and R. Löw, “Atomic vapor spectroscopy in integrated photonic structures,” *Appl. Phys. Lett.* 107 (4), 041101, Jul. 2015.
DOI: `http://dx.doi.org/10.1063/1.4927172`

[12] M. Schumann, T. Bückmann, **N. Gruhler**, M. Wegener, and W. Pernice, “Hybrid 2D-3D optical devices for integrated optics by direct laser writing,” *Light Sci. Appl.* 3 (6), e175-e175, Jun. 2014.
DOI: `http://dx.doi.org/10.1038/lsa.2014.56`

[13] **N. Gruhler**, C. Benz, H. Jang, J.-H. Ahn, R. Danneau, and W. H. P. Pernice, “High-quality Si_3N_4 circuits as a platform for graphene-based nanophotonic devices,” *Opt. Express* 21 (25), 31678, Dec. 2013.
DOI: `http://dx.doi.org/10.1364/OE.21.031678`

[14] P. Rath, **N. Gruhler**, S. Khasminskaya, C. Nebel, C. Wild, and W. H. P. Pernice, “Waferscale nanophotonic circuits made from diamond-on-insulator substrates,” *Opt. Express* 21 (9), 11031, May 2013.
DOI: `http://dx.doi.org/10.1364/OE.21.011031`

Curriculum Vitae

Acknowledgments

It is my very great pleasure to thank everyone who supported and helped me on my way towards the PhD. Without your encouragement and advice the successful completion of the present work would not have been accomplished.

First of all, I am immensely grateful to my advisor Prof. Dr. Wolfram Pernice for the opportunity to work on this exciting topic. Thank you for letting me join your research group already for my Diploma thesis and enabling me to carry out my dissertation. It is very special that your door was always open to ask for advice and to discuss the current proceedings. Your unshakable optimism, the provision of the experimental equipment as well as the freedom to explore own ideas motivated me to work on and revise my research projects until their successful implementation. I also want to thank Prof. Dr. Rudolf Bratschitsch for co-refereeing this work and for the opportunity to collaborate with his PhD students.

Special thanks go to the many people I had the chance to work with for their immense support and for sharing their experience and knowledge. In particular I would like to thank Dr. Matthias Stegmaier for your help in assembling several measurement setups and for the discussion we had during work and many enjoyable evenings, which often produced new ideas. I want to thank Simone Ferrari for your huge efforts in setting up and the maintenance of all kinds of fabrication facilities and systems in Karlsruhe and Münster. Thank you for your readiness to share your broad expertise and your steady commitment to the group.

In addition I would like to thank the following group members: Dr. Svetlana Khasminskaya for the introduction to several fabrication systems at the KIT and your support in the development of the basic Si_3N_4 platform. Dr. Patrik Rath for the fundamental work on diamond integrated photonic circuits setting the basics for parts of my experiments. Anna Ovvyan for the joint work on circuit development for the integration of molecular single-photon sources and the shared time in our offices in Karlsruhe and Münster. Johannes Feldmann for the opportunity to talk about work and life in our shared office and your immediate willingness to help with the fabrication and even with the evaluation of some samples in Münster towards the end of my work. Nicolai Walter and Wladick Hartmann for many scientific discussions, your invaluable care for details and your pragmatic approach to any challenge. Fabian Beutel for your dedication to the optimization of EBL processes in Münster and the exposure of several of my samples. Corinna Kaspar for the never-ending maintenance of the RIE system in Münster. Matthias Blaicher for the development of a clever software solution for the circuit design. Nicole Altmann and in particular Johanna Köster for your straightforward help with all

administrative matters that occurred. Also, I am thankful that Maik Stappers continues the research on integrated photonics in the LWIR regime.

Furthermore, I am grateful for the lively discussions about research opportunities, joint efforts in the fabrication procedures, the pleasant work atmosphere and the countless table football matches I had with all members of the research groups of Prof. Dr. Wolfram Pernice and Jun.-Prof. Dr. Carsten Schuck.

During my work I had the opportunity to work with many talented physicists. The successful collaboration and the exchange of knowledge between different groups who share a common vision is the foundation for modern scientific research. This enables the combination of several research fields for the realization of new ideas and the exploration of unexpected possibilities. In this way it is my pleasure to thank the following people; without their efforts this thesis would not have been the same.

Ralf Ritter at the University of Stuttgart for your expansive work on rubidium atoms and your dedication to the detailed description and analysis of the light-atom interaction. Thanks are also due to Dr. Robert Löw and Prof. Dr. Tilman Pfau for enabling this collaboration. Georgia Lewes-Malandrakis at the Fraunhofer Institute for Applied Solid State Physics (IAF) Freiburg for the growth and optimization of diamond layers. Taro Yoshikawa for the work on diamond-on-AlN layers, Dietmar Brink for the polishing of the diamond layers and Dr. Christoph Nebel for leading the collaboration. Pietro Lombardi in the group of Dr. Costanza Tonielli at the European Laboratory for Non-Linear Spectroscopy (LENS) Florence for the joint work with Anny Ovvyan on the coupling of single-photon emission from DBT molecules to integrated circuits. Philipp Tonndorf at the University of Münster for the great work on single-photon sources in layered materials and for our collaboration on the integration of the sources with nanophotonic circuits. Thanks are also due to Prof. Dr. Bratschitsch for enabling this project. Mahdi Dadfar and Dr. Dr. Michael Hirtz at the Karlsruher Institute for Technology for your dedicated work on surface functionalization, click-chemistry binding and dip-pen nanolithography. Thank you for the close collaboration and the opportunity to expand the field of integrated optics to life-science applications.

This work would not have been possible without many technical and scientific support. In particular, I want to thank Dr. Silvia Diewald from the Center of Functional Nanostructures (CFN) for your continuous support at the EBL system, which simplified the device fabrication considerably. Lucas Radtke, also from the CFN, for your efforts at the wafer-dicing saw. Simone Dehm at the INT for advice and assistance concerning the SEM and RIE. I would like to thank everyone who proof-read parts of this thesis: Johannes Feldmann, Nicolai Walter, Wladick Hartmann, Fabian Beutel, Corinna Kaspar, Dr. Francesco Lenzini, Matthias Stegmaier and Barbara Gruhler.

Last but not least I would like to thank my friends and family for their tremendous support. In particular Johannes, Katja, Nico and Julia for heartily welcoming me to Münster. Together with Wladick, Corinna, Fabian, Francesco and many others you made every time I stayed there a most enjoyable occasion! Biggest thanks to Meme, Hannes, Marlene, Lena, Andi, Martine and Clemens, my second family. A huge thank you to my dad, Gerhard, for sharing your scientific enthusiasm and

excitement; to my mom, Gesine, for being the supportive, kind-hearted soul in every situation of my life; to my siblings, Miri, Jup and Stef for the fantastic time we had and still have. Finally, I want to thank my wife Barbara for your unlimited support, for giving me strength during frustrating and stressful hours, for celebrating the little successes, for every shared moment, for your love. I am endlessly thankful for our son Nils, the greatest gift there is.

Wohl dem Menschen, der Weisheit erlangt, und dem Menschen, der Einsicht gewinnt! Denn es ist besser, sie zu erwerben, als Silber, und ihr Ertrag ist besser als Gold. Sie ist edler als Perlen, und alles, was du wünschen magst, ist ihr nicht zu vergleichen.

Sprüche 3, 13-15